

# Branching ratios of charmed baryons in the LHCb experiment

Stephen Ogilvy



University of Glasgow | Experimental  
Particle Physics

University of Glasgow  
Department of Physics and Astronomy

*Submitted in fulfilment of the requirements  
for the degree of Doctor of Philosophy*

Jan 2015

© Stephen Ogilvy, Jan 2015



# Abstract

LHCb is the dedicated heavy flavour experiment on the LHC accelerator ring. An analysis measuring the relative branching fractions of  $\Lambda_c^+ \rightarrow phh'$  decays, where  $hh' \in \{K^- \pi^+, K^- K^+, \pi^- \pi^+, \pi^- K^+\}$ , is presented using  $1024.8 \pm 35.9 \text{ pb}^{-1}$  of  $pp$  collisions gathered by LHCb during 2011. Independent measurements are made using samples of  $\Lambda_c$  produced from the primary interaction and from those produced in semileptonic decays of  $\Lambda_b^0 \rightarrow \Lambda_c^+ \mu^- \bar{\nu}_\mu$ . The measured relative branching ratios in the prompt analysis are

$$\begin{aligned} \mathcal{B}(\Lambda_c^+ \rightarrow pK^- K^+)/\mathcal{B}(\Lambda_c^+ \rightarrow pK^- \pi^+) &= (2.03 \pm 0.07 \text{ (stat)} \pm 0.10 \text{ (syst)}) \times 10^{-2}, \text{ and} \\ \mathcal{B}(\Lambda_c^+ \rightarrow p\pi^- \pi^+)/\mathcal{B}(\Lambda_c^+ \rightarrow pK^- \pi^+) &= (7.04 \pm 0.19 \text{ (stat)} \pm 0.34 \text{ (syst)}) \times 10^{-2}, \end{aligned}$$

while in the semileptonic analysis they are measured to be

$$\begin{aligned} \mathcal{B}(\Lambda_c^+ \rightarrow pK^- K^+)/\mathcal{B}(\Lambda_c^+ \rightarrow pK^- \pi^+) &= (1.68 \pm 0.03 \text{ (stat)} \pm 0.04 \text{ (syst)}) \times 10^{-2}, \text{ and} \\ \mathcal{B}(\Lambda_c^+ \rightarrow p\pi^- \pi^+)/\mathcal{B}(\Lambda_c^+ \rightarrow pK^- \pi^+) &= (7.45 \pm 0.06 \text{ (stat)} \pm 0.24 \text{ (syst)}) \times 10^{-2}. \end{aligned}$$

In the semileptonic analysis we make the first observation of the decay mode  $\Lambda_c^+ \rightarrow p\pi^- K^+$ , with a significance of  $11.1\sigma$ . We measure the ratio:

$$\mathcal{B}(\Lambda_c^+ \rightarrow p\pi^- K^+)/\mathcal{B}(\Lambda_c^+ \rightarrow pK^- \pi^+) = (1.62 \pm 0.15 \text{ (stat)} \pm 0.05 \text{ (syst)}) \times 10^{-3} .$$

Charged hadron discrimination in LHCb is provided by two ring imaging Cherenkov detectors. A data-driven study on the performance of the aerogel Cherenkov radiator is presented. Particle identification information is used to construct variables describing the likelihood of hadronic particle hypotheses of reconstructed tracks, on which cuts are placed in typical physics analyses. The preparation of new data samples allowing for the data-driven efficiency correction of particle identification cuts on proton tracks is described.

# Declaration

The research results presented in this thesis are the product of my own work. Appropriate references are provided when results of third parties are mentioned. The research presented here was not submitted for another degree in any other department or university.

Stephen Ogilvy

# Preface

This thesis documents the candidate's work, carried out within the LHCb collaboration, in measuring the relative branching fractions of  $\Lambda_c$  decays using data gathered in 2011 with the LHCb detector. It also details studies performed by the candidate on PID calibration and the performance of the LHCb RICH system aerogel.

In Chapter 1, we review the theory behind the Standard Model of particle physics, referring to the original research that underpins its development and formalism. We review in particular the development of the Quark model, and the Cabibbo-Kobayashi-Maskawa mixing matrix governing the weak couplings of the quarks. We then provide a review of some current phenomenology results from lattice QCD and HQET, before detailing some of the recent experimental results in charmed baryon spectroscopy. We conclude the chapter with a review of recent results, and motivate several potential analyses of  $\Lambda_c^+ \rightarrow phh'$  decays at LHCb, where  $hh' \in \{K^-\pi^+, K^-K^+, \pi^-\pi^+, \pi^-K^+\}$ .

In Chapter 2, we describe the design and operation of the Large Hadron Collider beauty (LHCb) detector at the Large Hadron Collider (LHC). We describe the systems responsible for particle tracking, particle identification, and calorimetry. We outline the trigger system at LHCb, concluding the chapter with a brief description of the Monte Carlo (MC) generators used by LHCb to simulate  $p - p$  interactions and heavy-flavour decays.

In Chapter 3 we outline in more detail the particle identification (PID) at LHCb, with particular focus on the performance and design of the RICH system. We then detail a data-driven efficiency correction for the selection of tracks using PID discriminants, which has been developed at LHCb by a number of people within the collaboration over recent years. The method relies on the reconstruction of decays which are identified unambiguously through kinematic constraints and decay topology. The candidate identified a lack of high transverse momentum protons in the calibration data, and prepared new calibration samples using several sources of  $\Lambda_c^+ \rightarrow pK^-\pi^+$  decays. The candidate optimised the selections using the helicity information of the  $\Lambda_c$  decay to acquire samples with far

greater purity than selections developed by others within the collaboration. The candidate then conducted a series of stability checks to evaluate the sources of systematic uncertainty associated with the extraction of the signal kinematics. We conclude the chapter by describing a study by the candidate to evaluate the performance of the aerogel in a data-driven way. The results acquired in this study were influential in the decision by the LHCb collaboration to remove the aerogel for the LHC run II.

In Chapters 4 – 5 we detail an original analysis conducted by the candidate in measuring the branching ratios of decays of the form  $\Lambda_c^+ \rightarrow phh'$  decays, where  $hh' \in \{K^-\pi^+, K^-K^+, \pi^-\pi^+, \pi^-K^+\}$ , using data gathered in 2011 by the LHCb detector. The work in these chapters was almost entirely carried out and implemented by the candidate in consultation with Paul Soler and Patrick Spradlin. The exceptions to this are the optimisation of the “stripping” selection algorithms, which were implemented by Patrick Spradlin in consultation with the candidate, the production of the simulation and data files from the reconstructed data, which was implemented by Patrick Spradlin, and the development of the  $\Lambda_c$   $IP\chi^2$  fit model for prompt and secondary  $\Lambda_c$  discrimination in the analysis of  $\Lambda_c$  produced at the primary interaction, which was implemented by Patrick Spradlin.

In Chapter 6 we present the evaluation of systematic uncertainties and the final results from this analysis. All work in this chapter was carried out and implemented by the candidate in consultation with Paul Soler and Patrick Spradlin. The results given correspond to the most precise measurements to date on the branching ratios  $\mathcal{B}(\Lambda_c^+ \rightarrow pK^-K^+)/\mathcal{B}(\Lambda_c^+ \rightarrow pK^-\pi^+)$  and  $\mathcal{B}(\Lambda_c^+ \rightarrow p\pi^-\pi^+)/\mathcal{B}(\Lambda_c^+ \rightarrow pK^-\pi^+)$ . We provide the first observation of the decay mode  $\Lambda_c^+ \rightarrow p\pi^-K^+$ , which is the first observation of a doubly-Cabibbo suppressed decay mode of a charmed baryon and the lowest recorded charm baryon branching fraction to date. We provide the relative branching ratio of this mode relative to the Cabibbo-favoured mode,  $\mathcal{B}(\Lambda_c^+ \rightarrow p\pi^-K^+)/\mathcal{B}(\Lambda_c^+ \rightarrow pK^-\pi^+)$ .

# Contents

<b>Abstract</b>	<b>i</b>
<b>Declaration</b>	<b>ii</b>
<b>Preface</b>	<b>iii</b>
<b>Contents</b>	<b>ix</b>
<b>List of figures</b>	<b>xiii</b>
<b>List of tables</b>	<b>xv</b>
<b>1 Theory review</b>	<b>1</b>
1.1 The Standard Model . . . . .	2
1.1.1 The fermions and bosons . . . . .	3
1.1.2 The mathematics of the SM . . . . .	4
1.2 The Quark Model . . . . .	5
1.2.1 From hadrons to quarks . . . . .	5
1.2.2 The $u, d, s$ and $c$ hadrons . . . . .	7
1.3 The CKM matrix and CP-violation . . . . .	10
1.3.1 Quark mixing with two generations . . . . .	10
1.3.2 The third generation . . . . .	11
1.3.3 The CKM matrix . . . . .	12
1.4 Charm baryon phenomenology . . . . .	14
1.4.1 Predictions from HQET and the lattice . . . . .	14
1.4.2 Recent experimental results . . . . .	15
1.4.3 $\Lambda_c^+ \rightarrow phh'$ decays . . . . .	19
1.5 Summary . . . . .	21

<b>2</b>	<b>The LHCb experiment at the LHC</b>	<b>23</b>
2.1	The Large Hadron Collider . . . . .	23
2.2	The LHCb detector . . . . .	25
2.2.1	Tracking . . . . .	29
2.2.2	Particle Identification . . . . .	34
2.2.3	Calorimetry . . . . .	36
2.2.4	Muon system . . . . .	37
2.3	The LHCb trigger . . . . .	40
2.3.1	Level 0 trigger . . . . .	40
2.3.2	High Level Trigger . . . . .	41
2.4	Simulation of particle production and decay . . . . .	43
<b>3</b>	<b>Proton identification at low momentum and PID calibration</b>	<b>45</b>
3.1	Charged particle identification at LHCb . . . . .	45
3.2	The RICH system . . . . .	47
3.2.1	RICH1 . . . . .	47
3.2.2	RICH2 . . . . .	49
3.2.3	Radiators . . . . .	50
3.2.4	Hybrid photon detectors . . . . .	52
3.3	RICH reconstruction and PID discriminant estimators . . . . .	54
3.3.1	Global Cherenkov detector reconstruction . . . . .	54
3.3.2	Track PID estimators . . . . .	56
3.4	Efficiency correction for PID selections . . . . .	57
3.4.1	The PIDCalib technique . . . . .	57
3.4.2	Calibration datasets . . . . .	59
3.4.3	RICH performance with calibration datasets . . . . .	60
3.5	Development of heavy flavour proton calibration samples . . . . .	63
3.5.1	Kinematic coverage of $\Lambda^0 \rightarrow p\pi^-$ calibration samples . . . . .	63
3.5.2	A heavy flavour proton calibration sample . . . . .	65
3.5.3	Triggering and stripping of $\Lambda_c$ decays . . . . .	66
3.5.4	Considerations in developing $\Lambda_c$ selections . . . . .	68
3.5.5	Eliminating $D \rightarrow hhh$ misreconstructions . . . . .	69
3.5.6	Resonant characteristics of $\Lambda_c^+ \rightarrow phh'$ decays . . . . .	70
3.5.7	Selection Optimisation . . . . .	73
3.5.8	Final data sample . . . . .	76

3.5.9	Cross checks and associated systematics . . . . .	81
3.5.10	Summary . . . . .	84
3.6	Data-driven metrics of aerogel performance . . . . .	85
3.6.1	The RICH aerogel . . . . .	85
3.6.2	Targetting the aerogel performance . . . . .	86
3.6.3	Results . . . . .	87
3.6.4	Summary . . . . .	88
3.7	Chapter summary . . . . .	91
<b>4</b>	<b><math>\Lambda_c^+ \rightarrow phh'</math> relative branching fractions</b>	<b>92</b>
4.1	Introduction . . . . .	92
4.2	Data and processing . . . . .	93
4.2.1	LHCb data set . . . . .	93
4.2.2	Monte Carlo samples . . . . .	94
4.3	Selection . . . . .	95
4.3.1	Stripping and trigger of prompt data . . . . .	95
4.3.2	Stripping and trigger of semileptonic data . . . . .	97
4.3.3	Offline selection . . . . .	100
4.3.4	Mass spectra . . . . .	110
4.4	Prompt backgrounds . . . . .	114
4.4.1	$D_s^+ \rightarrow hhh/D^+ \rightarrow hhh$ mis-reconstructions . . . . .	114
4.4.2	Mis-ID in $\Lambda_c$ decays . . . . .	124
4.4.3	Reassigning mass hypotheses in data . . . . .	127
4.4.4	Summary . . . . .	128
4.5	Semileptonic backgrounds . . . . .	129
4.5.1	Mis-ID in $\Lambda_c$ decays . . . . .	129
4.5.2	Reassigning mass hypotheses in data . . . . .	129
4.5.3	Summary . . . . .	130
<b>5</b>	<b><math>\Lambda_c^+ \rightarrow phh'</math> selection efficiencies and yield extractions</b>	<b>133</b>
5.1	Efficiencies and efficiency corrections . . . . .	133
5.1.1	Overview . . . . .	133
5.1.2	MC efficiencies and resonance modelling . . . . .	135
5.1.3	Trigger efficiencies . . . . .	138
5.1.4	Generator level efficiencies . . . . .	139

5.1.5	Stripping efficiencies . . . . .	144
5.1.6	PID efficiencies from a fully data-driven PIDCalib . . . . .	151
5.1.7	BDT efficiency . . . . .	159
5.1.8	Full selection efficiencies and summary . . . . .	159
5.2	Yield extraction . . . . .	161
5.2.1	Prompt . . . . .	161
5.2.2	Semileptonic . . . . .	164
5.2.3	Raw and adjusted yields . . . . .	167
5.2.4	Planned update to prompt fits . . . . .	167
<b>6</b>	<b><math>\Lambda_c^+ \rightarrow phh'</math> branching fraction systematic uncertainties and results</b>	<b>171</b>
6.1	Systematic uncertainties . . . . .	171
6.1.1	PID calibration uncertainty . . . . .	171
6.1.2	Selection efficiency uncertainty . . . . .	174
6.1.3	Uncertainty due to fit model . . . . .	174
6.1.4	Uncertainty from input parameters . . . . .	175
6.1.5	Systematic uncertainties summary . . . . .	176
6.2	$\Lambda_c^+ \rightarrow p\pi^-K^+$ significance extraction and confidence intervals . . . . .	179
6.3	$\Lambda_c^+ \rightarrow p\pi^-K^+$ results . . . . .	179
6.3.1	Yield extractions . . . . .	179
6.3.2	Efficiency corrections . . . . .	179
6.3.3	Systematic uncertainties . . . . .	180
6.3.4	Signal significance extractions . . . . .	182
6.4	Relative branching fraction results . . . . .	184
6.5	Extraction of absolute branching fractions . . . . .	184
<b>7</b>	<b>Summary and conclusions</b>	<b>186</b>
7.1	Summary . . . . .	186
7.2	Outlook . . . . .	188
<b>A</b>	<b>Optimum descriptions of efficiency spaces</b>	<b>190</b>
A.1	Systematics in efficiency re-weightings . . . . .	190
A.1.1	Limited MC statistics - inflation of error . . . . .	191
A.1.2	Variations in efficiency over individual bins . . . . .	192
A.1.3	The $\kappa$ statistic . . . . .	193
A.1.4	The $\kappa$ bin boundary parameter . . . . .	193

A.1.5	Optimum $\kappa$ distributions . . . . .	195
A.1.6	Practical $\kappa$ distributions . . . . .	195
A.1.7	A practical case in 2D . . . . .	196
A.2	Concluding remarks . . . . .	197
<b>B</b>	<b>Biases in efficiency re-weightings from limited simulated/calibration statistics</b>	<b>201</b>
B.1	Stripping efficiency correction . . . . .	201
B.2	Source of bias . . . . .	202
B.3	Toy estimations . . . . .	204
B.3.1	PIDCalib . . . . .	205
B.3.2	Prompt stripping efficiencies . . . . .	205
B.3.3	SL Cabibbo-suppressed stripping efficiencies . . . . .	206
B.3.4	SL $\Lambda_c^+ \rightarrow pK^-\pi^+$ stripping efficiencies . . . . .	206
B.4	Summary . . . . .	207
	<b>Bibliography</b>	<b>216</b>

# List of Figures

1.1	The pseudoscalar mesons in $SU(4)$ . . . . .	8
1.2	The baryons in $SU(4)$ . . . . .	9
1.3	Unitarity angles . . . . .	14
1.4	Heavy-flavour baryon masses from lattice QCD . . . . .	16
1.5	The known singly-charmed baryons . . . . .	17
1.6	Baryon exchange and spectator decays . . . . .	18
2.1	The LHC accelerator complex. Reproduced from [93]. . . . .	24
2.2	Recorded integrated luminosity at LHCb . . . . .	26
2.3	$b\bar{b}$ angular production at LHCb . . . . .	27
2.4	Vertical cross section of LHCb detector . . . . .	28
2.5	VELO cross section . . . . .	30
2.6	VELO sensor schematic . . . . .	31
2.7	VELO $IP$ and $PV$ resolution . . . . .	32
2.8	Division of inner and outer trackers . . . . .	32
2.9	Tracker Turicensis schematic . . . . .	33
2.10	Inner Tracker schematic . . . . .	34
2.11	Magnet schematic . . . . .	35
2.12	Calorimeter segmentation . . . . .	37
2.13	Muon system side view . . . . .	39
2.14	LHCb trigger schema . . . . .	40
2.15	L0 muon and dimuon trigger efficiency . . . . .	42
2.16	HLT2 inclusive charm trigger efficiency . . . . .	43
3.1	PID selection in $B^0 \rightarrow \pi^+ \pi^-$ . . . . .	46
3.2	RICH1 side-on schematic . . . . .	48
3.3	RICH2 top-down schematic . . . . .	50

3.4	Track momentum vs. emitted Cherenkov angle . . . . .	51
3.5	HPD pixel schematic . . . . .	53
3.6	Calibration data mass fits . . . . .	61
3.7	2011 DLL responses for charged tracks . . . . .	62
3.8	Charged hadron efficiency and mis-ID rates vs momentum in 2012 data . .	62
3.9	Proton kinematics in $\Lambda^0 \rightarrow p\pi^-$ calibration sample . . . . .	64
3.10	$\Lambda_c^+$ mass spectra after stripping selection . . . . .	68
3.11	$\Lambda_c^+$ candidate mass spectra for $\Lambda_b^0 \rightarrow \Lambda_c^+(pK^-\pi^+)\mu^-\bar{\nu}_\mu$ under rival proton mass hypotheses . . . . .	71
3.12	$\Lambda_c$ resonant variable geometry . . . . .	72
3.13	$\Lambda_c$ candidate mass spectra at different levels of selection procedure . . . .	73
3.14	$\Lambda_c$ mass fits after stripping, trigger and $D \rightarrow hhh$ vetoes . . . . .	74
3.15	Signal and combinatoric $\cos \phi_p$ distributions . . . . .	76
3.16	$\Lambda_c$ mass fits for final selection . . . . .	77
3.17	Proton momentum distributions for final calibration samples . . . . .	78
3.18	Proton $p_T$ distributions for final calibration samples . . . . .	78
3.19	Proton $p - \eta$ distributions for final calibration samples . . . . .	79
3.20	Inclusive $\Lambda_c^+ \rightarrow pK^-\pi^+$ proton PID DLL distributions . . . . .	80
3.21	$\Lambda_b^0 \rightarrow \Lambda_c^+(pK^-\pi^+)\mu^-\bar{\nu}_\mu$ proton PID DLL distributions . . . . .	80
3.22	Fit-and-count signal yield residuals . . . . .	83
3.23	Proton PID efficiency with momentum . . . . .	84
3.24	Calibration sample $\log(\mathcal{L}_p/\mathcal{L}_K)$ distributions . . . . .	88
3.25	$\log(\mathcal{L}_p/\mathcal{L}_K)$ receiver operating characteristics . . . . .	89
3.26	$\log(\mathcal{L}_p/\mathcal{L}_K)$ receiver operating characteristics versus occupancy . . . . .	90
4.1	$\Lambda_c^+ \rightarrow phh'$ prompt stripped mass distributions . . . . .	101
4.2	$\Lambda_c^+ \rightarrow phh'$ semileptonic stripped mass distributions . . . . .	102
4.3	Mass sidebands from data of the prompt $\Lambda_c^+ \rightarrow pK^-\pi^+$ and $\Lambda_c^+ \rightarrow p\pi^-K^+$ . . . . .	103
4.4	Application of DecayTreeFitter to promptly selected $\Lambda_c^+ \rightarrow pK^-\pi^+$ . . . . .	103
4.5	Vetoed proton track kinematics. . . . .	104
4.6	BDT input variable distributons for signal and combinatoric background. . . . .	106
4.7	ROC curve and classifier output distributions from final BDT . . . . .	108
4.8	Prompt $\Lambda_c^+ \rightarrow pK^-\pi^+$ prompt mass spectra . . . . .	111
4.9	Prompt $\Lambda_c^+ \rightarrow pK^-K^+$ prompt mass spectra . . . . .	111
4.10	Prompt $\Lambda_c^+ \rightarrow p\pi^-\pi^+$ prompt mass spectra . . . . .	112

4.11	SL $\Lambda_c^+ \rightarrow pK^- \pi^+$ SL mass spectra . . . . .	112
4.12	SL $\Lambda_c^+ \rightarrow pK^- K^+$ SL mass spectra . . . . .	113
4.13	SL $\Lambda_c^+ \rightarrow p\pi^- \pi^+$ SL mass spectra . . . . .	113
4.14	MC11a $D^+ \rightarrow K^- \pi^+ \pi^+$ , $\pi^+$ mis-ID as $p$ - wide mass window . . . . .	122
4.15	MC11a $D^+ \rightarrow K^- \pi^+ \pi^+$ , $\pi^+$ mis-ID as $p$ - $\Lambda_c$ mass window . . . . .	123
4.16	MC11a single mis-ID of $\Lambda_c^+ \rightarrow phh'$ modes . . . . .	125
4.17	Simulated double mis-ID of $\Lambda_c^+ \rightarrow pK^- \pi^+$ . . . . .	126
4.18	Data mass reassignment - prompt $\Lambda_c^+ \rightarrow pK^- \pi^+ - p \rightarrow K$ . . . . .	127
4.19	MC11a single mis-ID of $\Lambda_c^+ \rightarrow phh'$ modes . . . . .	130
4.20	MC11a double mis-ID of $\Lambda_c^+ \rightarrow phh'$ modes . . . . .	131
4.21	Data mass reassignment - SL $\Lambda_c^+ \rightarrow pK^- \pi^+ - p \rightarrow K$ . . . . .	132
5.1	$\Lambda_c$ resonant variable geometry . . . . .	136
5.2	Prompt $\Lambda_c^+ \rightarrow pK^- \pi^+$ resonant variable comparisons . . . . .	137
5.3	Generator level acceptances . . . . .	139
5.4	Generator level acceptances . . . . .	141
5.5	Generated $\Lambda_c$ $\eta$ and $\Lambda_c$ charge . . . . .	143
5.6	Stripping acceptance variations in SL $\Lambda_c^+ \rightarrow pK^- \pi^+$ . . . . .	145
5.7	$\Lambda_c^+ \rightarrow phh'$ event nTrack distributions . . . . .	155
5.8	$\Lambda_c^+ \rightarrow phh'$ prompt PID efficiencies . . . . .	156
5.9	$\Lambda_c^+ \rightarrow phh'$ prompt PID efficiencies . . . . .	157
5.10	Semileptonic $\Lambda_c^+ \rightarrow p\pi^- \pi^+$ $\pi$ efficiencies . . . . .	158
5.11	$\Lambda_c^+ \rightarrow pK^- \pi^+$ prompt mass fit . . . . .	162
5.12	$\Lambda_c^+ \rightarrow pK^- K^+$ prompt mass fit . . . . .	162
5.13	$\Lambda_c^+ \rightarrow p\pi^- \pi^+$ prompt mass fit . . . . .	163
5.14	$\Lambda_c^+ \rightarrow pK^- \pi^+$ SL mass fit . . . . .	165
5.15	$\Lambda_c^+ \rightarrow pK^- K^+$ SL mass fit . . . . .	165
5.16	$\Lambda_c^+ \rightarrow p\pi^- \pi^+$ SL mass fit . . . . .	166
5.17	$\Lambda_c^+$ $IP\chi^2$ distributions in $\Lambda_c^+ \rightarrow pK^- \pi^+$ . . . . .	168
6.1	PID Calibration statistical systematic - toy yields . . . . .	172
6.2	Prompt PID binning systematics . . . . .	174
6.3	SL PID binning systematics . . . . .	175
6.4	$\Lambda_c^+ \rightarrow p\pi^- K^+$ prompt mass fit . . . . .	180
6.5	$\Lambda_c^+ \rightarrow p\pi^- K^+$ semileptonic mass fit . . . . .	181
6.6	Semileptonic $-\Delta$ Log-likelihood Log-likelihood scan . . . . .	183

6.7	Prompt $-\Delta$ Log-likelihood Log-likelihood scan . . . . .	183
A.1	Extremes of $\kappa$ distributions . . . . .	198
A.2	$\kappa$ distributions example . . . . .	199
A.3	$\kappa$ distributions example . . . . .	200
B.1	Bin efficiencies - PIDCalib systematics . . . . .	208
B.2	Efficiency bias vs number of bins - PIDCalib systematics . . . . .	209
B.3	Bin efficiencies - prompt stripping . . . . .	209
B.4	Efficiency bias vs number of bins - prompt stripping . . . . .	211
B.5	Bin efficiencies - SL CS stripping . . . . .	211
B.6	Efficiency bias vs number of bins - SL CS stripping . . . . .	213
B.7	Bin efficiencies - SL $\Lambda_c^+ \rightarrow pK^-\pi^+$ stripping . . . . .	213
B.8	Efficiency bias vs number of bins - SL $\Lambda_c^+ \rightarrow pK^-\pi^+$ stripping . . . . .	215

# List of Tables

1.1	PDG branching ratios for $\Lambda_c^+ \rightarrow phh'$ modes . . . . .	20
2.1	LHCb running conditions in run 1 . . . . .	25
3.1	Branching fractions of relevant $D$ decays . . . . .	69
3.2	Selection training variables . . . . .	75
3.3	Final signal yields and purities for calibration datasets . . . . .	76
3.4	Fit-and-count residuals and associated systematics . . . . .	82
3.5	Pion, kaon and proton Cherenkov radiator momentum thresholds . . . . .	86
3.6	Pion, kaon and proton Cherenkov radiator momentum thresholds . . . . .	87
4.1	PDG branching ratios for $\Lambda_c^+ \rightarrow phh'$ modes . . . . .	93
4.2	Prompt $\Lambda_c^+ \rightarrow phh'$ Stripping17b selection criteria . . . . .	97
4.3	Semileptonic $\Lambda_c^+ \rightarrow phh'$ Stripping17b selection criteria . . . . .	98
4.4	Kinematically vetoed regions of the P and $\eta$ phase space . . . . .	104
4.5	Default and optimum BDT architecture variables . . . . .	108
4.6	Final PID cuts in offline selection . . . . .	109
4.7	$D^+$ kaon to proton mis-ID decays . . . . .	115
4.8	Simulated charged $D$ decays for background studies - populations . . . . .	118
4.9	Simulated charged $D$ decays for background studies - efficiencies . . . . .	119
4.10	Charged $D$ yields in 2011 . . . . .	120
5.1	Average trigger efficiencies. . . . .	139
5.2	Prompt generator level efficiencies . . . . .	142
5.3	Semileptonic generator level efficiencies . . . . .	142
5.4	Average generator level efficiencies. . . . .	143
5.5	MC stats passing no-PID stripping selection. . . . .	146
5.6	Final stripping efficiencies . . . . .	152

5.7	Phase-space averages vs re-weighted stripping efficiencies . . . . .	152
5.8	Binning schemas used in PID calibration . . . . .	155
5.9	Average PID efficiencies. . . . .	155
5.10	Prompt BDT efficiencies in simulation . . . . .	159
5.11	Total selection efficiencies. . . . .	160
5.12	$\Lambda_c^+ \rightarrow phh'$ raw yields . . . . .	167
5.13	Prompt and secondary stripping efficiencies in prompt simulation . . . . .	168
6.1	Prompt $\mathcal{B}(\Lambda_c^+ \rightarrow pK^- K^+)/\mathcal{B}(\Lambda_c^+ \rightarrow pK^- \pi^+)$ systematics . . . . .	177
6.2	Prompt $\mathcal{B}(\Lambda_c^+ \rightarrow p\pi^- \pi^+)/\mathcal{B}(\Lambda_c^+ \rightarrow pK^- \pi^+)$ systematics . . . . .	177
6.3	SL $\mathcal{B}(\Lambda_c^+ \rightarrow pK^- K^+)/\mathcal{B}(\Lambda_c^+ \rightarrow pK^- \pi^+)$ systematics . . . . .	178
6.4	SL $\mathcal{B}(\Lambda_c^+ \rightarrow p\pi^- \pi^+)/\mathcal{B}(\Lambda_c^+ \rightarrow pK^- \pi^+)$ systematics . . . . .	178
6.5	$\Lambda_c^+ \rightarrow p\pi^- K^+$ stripping efficiencies. . . . .	181
6.6	$\Lambda_c^+ \rightarrow p\pi^- K^+$ PID efficiencies. . . . .	181
6.7	$\Lambda_c^+ \rightarrow p\pi^- K^+$ selection efficiencies. . . . .	182
6.8	SL $\mathcal{B}(\Lambda_c^+ \rightarrow p\pi^- K^+)/\mathcal{B}(\Lambda_c^+ \rightarrow pK^- \pi^+)$ systematics . . . . .	182
6.9	Final relative branching fractions . . . . .	184
6.10	Final absolute branching fractions . . . . .	185
B.1	Re-weighting biases - PIDCalib systematics . . . . .	208
B.2	Re-weighting biases - prompt stripping . . . . .	210
B.3	Re-weighting biases - SL CS stripping . . . . .	212
B.4	Re-weighting biases - SL $\Lambda_c^+ \rightarrow pK^- \pi^+$ stripping . . . . .	214

# Chapter 1

## Theory review

Few things are as satisfying to the human mind, and to human curiosity, as a good mystery. My generation of physicists have grown up with the wonders of the internet and personal computers, making possible research our forebears could only dream of. Still, I cannot help but feel envy for those forebears who lived through the first developments of quantum theory and electrodynamics, into what would eventually become the Standard Model (SM) of particle physics. The twentieth century arguably saw some of humanity's deepest reappraisals of nature's most fundamental aspects.

While the golden days of theory and experiment informing each other quite so keenly has arguably passed, thus far this century has had several surprises in store for experimentalists. One of the most prominent being the first model-independent observation of neutrino oscillations by the Super-Kamiokande experiment [1]. As an undergraduate student I recall particularly recent texts asserting that neutrinos were massless - suddenly we were inundated with proof that this was not the case.

In 2015, we eagerly await the LHC run II to see what it might bring. The Standard Model is in rude health - with the independent discovery of the long-theorised Higgs boson by both the ATLAS [2] and CMS [3] collaborations it is arguably too robust to experimental scrutiny. Despite the Standard Model's inability to explain gravity and dark matter on the cosmological scale (among other problems), it stands up to the most rigorous experimental tests the particle physics community can level against it.

For all the wonderfully elegant extensions to the Standard Model conceived by the theory community over the past 50 or more years to remedy this incompleteness, the experimental community has not found empirical evidence to definitively favour any particular one. The LHCb collaboration has made great strides to inform this discussion - the first evidence

for the decay  $B_s^0 \rightarrow \mu^+ \mu^-$  found in parallel with CMS [4–6] has already placed powerful constraints on two Higgs doublet models, a category including many supersymmetric models, informing discussion from the theoretical community on observables that may be sensitive to new physics at LHCb in rare  $B$  decays with more data [7–9].

The LHCb detector is suited to performing a wide variety of heavy-flavour physics measurements with unprecedented precision. While it is primarily designed to record the decays of  $b\bar{b}$ , it has also proven adept at recording the vast volumes of  $c\bar{c}$  production occurring in LHC collisions. This includes the ability to cleanly reconstruct a wide variety of charmed baryon decays. This is a field in which theoretical and experimental knowledge has seen recent and vast improvements, but one in which a great many results are still to be found. To this end the candidate conducted an analysis to measure the branching fractions of the  $\Lambda_c$  baryon to hadrons without hyperon mediation, given in Chapters 4 – 6. Better understanding of these decays than is available presently is vital to conducting a wide variety of LHCb analyses with charmed baryon decays. These include searches for rare decays that are sensitive to new physics, and complementary searches of CP-violation to those conducted in the  $B$  and  $D$  meson systems being conducted at LHCb.

We first review the fundamental theory underpinning the Standard Model in Section 1.1. We then discuss the quark model in Section 1.2, leading to a brief overview of the CKM matrix and CP-violation in Section 1.3. We conclude the chapter in Section 1.4 by reviewing recent results in charmed baryon experiment and theory, and describing the phenomenology of  $\Lambda_c$  decays and branching fraction predictions.

## 1.1 The Standard Model

The Standard Model describes the most basic building blocks of matter and how they interact with one another. The fermions are spin-half particles comprising the quarks and leptons, which make up the vast majority of everyday matter. They interact via the exchange of gauge bosons, integer-spin particles that mediate the four fundamental forces. The mathematics of the theory are best described as a gauge theory, obeying certain precise symmetries which imbue the model with extraordinary predictive power. In this section we outline the fundamentals of the standard model, with the particles and forces it describes.

### 1.1.1 The fermions and bosons

The leptons consist of three generations of doublets, each of which contains a charged and neutral particle. The charged particles are the electron ( $e$ ), the muon ( $\mu$ ) and the tauon ( $\tau$ ). Each of these has a neutrino counterpart, respectively the  $\nu_e$ , the  $\nu_\mu$  and the  $\nu_\tau$ . Every charged lepton has an anti-matter counterpart with an opposite electric charge, while for the neutrinos there exist both the possibilities that they too have anti-matter counterparts, or that they are themselves their own antiparticles.

The remaining fermions in the SM are the quarks, again corresponding to three generations. In each generation there is a quark with an electric charge  $+\frac{2}{3}e$ , and one with charge  $-\frac{1}{3}e$ . The type of quark is referred to as the “flavour”. The positively charged quarks are the up ( $u$ ), charm ( $c$ ) and top ( $t$ ), while the negatively charged are the down ( $d$ ), strange ( $s$ ) and bottom ( $b$ ). Each quark has a property referred to as colour, with three possible colour states. Like the charged leptons, each quark has an anti-matter counterpart with the opposite electric charge.

The quarks and leptons interact with one another via the four fundamental forces in the universe. These are the force of gravitation, electromagnetism, the nuclear strong and the nuclear weak forces. The gravitational force is many orders of magnitude weaker than the other forces, and when making calculations at the high energy scales of the LHC collisions, gravity may be safely neglected.

Each of the remaining forces is understood to be mediated by the exchange of gauge bosons. The electromagnetic force is mediated by exchange of the massless photon ( $\gamma$ ). All electrically charged particles interact via electromagnetism, meaning that all fermions in the standard model experience this force except the neutrinos. The photon does not possess mass or electrical charge, and as such cannot couple to itself or decay to other particles. Consequently, the force’s range is infinite, and its effects are easily observable at the energy and length scales that humans inhabit.

The nuclear weak force was first recognised in beta decay of radioactive particles. It is mediated by the massive  $W^\pm$  and  $Z$  bosons, which have world-average measured masses of  $80.385 \pm 0.015 \text{ GeV}/c^2$  and  $91.188 \pm 0.002 \text{ GeV}/c^2$  respectively [10]. This high mass results in the force possessing a very short range  $\mathcal{O}(10^{-18} \text{ m})$ . The weak gauge bosons couple to all fermions which conform to certain helicity conditions <sup>1</sup>.

The final and most powerful force is the nuclear strong force, which is mediated by

---

<sup>1</sup>Helicity refers to the projection of a particle’s spin onto its momentum. If the spin is aligned with the momentum, it is referred to as right-handed. If the two are antiparallel it is referred to as left-handed. The weak bosons only couple to left-handed particles.

the massless gluon ( $g$ ). The gluon interacts only with particles possessing a color charge, and as such the quarks feel the strong force while the leptons do not. Despite the force's mediation by a massless gauge boson, it has a short interaction range of  $\mathcal{O}(10^{-15} \text{ m})$ . This is because unlike the massless photon, which is neutral, the gluon itself carries colour charge, and is therefore able to couple to itself. This self interaction leads to the phenomenon of asymptotic freedom [11], giving rise to the confinement of colour-charged particles. Free quarks are not observed, and instead they must exist in combinations which are colour-neutral.

One final particle in the Standard Model firmament remains. The symmetry of the weak force should dictate that in order for the electroweak gauge to be renormalisable, its gauge bosons should be massless. However, as described, they are found experimentally to have masses which in relation to most other fundamental particles are huge. The concept of spontaneous symmetry breaking, as had been used in theories of superconductivity by Anderson in 1958 [12], was known to be capable of providing the weak bosons with mass in the theory, but work by Nambu [13] and Goldstone [14] had shown that for every spontaneously broken symmetry in a quantum field theory, there must be an additional massive vector boson. In 1964 three distinct teams of researchers published papers which showed that when a field which spontaneously breaks the symmetry of a gauge theory, massive vector bosons arise [15–17]. This field is now referred to popularly as the Higgs field, and through its excitations it was predicted that another boson may be observed. This particle, termed the Higgs boson, was finally observed by the ATLAS and CMS experiments at CERN in 2012 [2, 3], such that every fundamental particle in the Standard Model has now been observed.

### 1.1.2 The mathematics of the SM

The Standard Model is a gauge theory, or a field theory that obeys a gauge symmetry. Such a symmetry occurs whereby the equations describing the field remain constant after an operation to all fields in space. The gauge transformations comprise a Lie group, termed the symmetry group of the theory. When the field theory is quantised it acquires gauge bosons, the quanta of the gauge fields. A Special Unitary group of order  $n$  ( $SU(n)$ ) has  $n^2 - 1$  generators, which can be interpreted as a fundamental force with  $n^2 - 1$  vector bosons. Electromagnetism is mediated only by the photon, while the weak force is mediated by three heavy bosons. As such, they were originally expected to correspond to a  $U(1)$  group and a  $SU(2)$  group respectively. One of the great achievements underlining the SM was

the realisation by Glashow, Salam and Weinberg that the electromagnetic and weak forces may be unified, similarly to the unification of electricity and magnetism in the 19<sup>th</sup> century. They realised the gauge group for the unified electroweak force is  $SU(2) \times U(1)_Y$  [18–20]<sup>2</sup>. The gluons mediate the strong force, and carry colour charge. The allowed permutations of colour are given in the next section, but we note for now that there are eight gluon colour states generated by the  $SU(3)$  group.

An elegant representation of the dynamics of a system is the Lagrangian. Classically it is given as

$$\mathcal{L} = T - V \tag{1.1}$$

where  $T$  is the kinetic energy of the system and  $V$  is the potential energy. The Lagrangian can be substituted into the Euler-Lagrange equation through application of the principle of least action:

$$\frac{\partial \mathcal{L}}{\partial \phi} - \partial_\mu \left( \frac{\partial \mathcal{L}}{\partial (\partial_\mu \phi)} \right) = 0 \tag{1.2}$$

where  $\partial_\mu$  is the covariant derivative. In a many-particle system the Lagrangian for the system is then the summation of the Lagrangians for the particles and their interactions. The full standard model Lagrangian is then

$$\mathcal{L} = \mathcal{L}_{boson\ kinetic} + \mathcal{L}_{fermion\ kinetic} + \mathcal{L}_{fermion\ masses} + \mathcal{L}_{Higgs}. \tag{1.3}$$

This dictates all the interactions between fundamental particles in the Standard Model.

## 1.2 The Quark Model

### 1.2.1 From hadrons to quarks

In the early-mid twentieth century wide variety of what are now known to be hadrons were discovered, such that few at the time believed that they could all be fundamental particles. The discovery of the charged pion in 1947 [21] was originally seen as a candidate for the mediator of the strong force, predicted by Yukawa in 1935 to explain the strong attraction between the proton and neutron [22]. The observation of the  $\Delta$  particles presented new questions - these particles were unstable, decaying into nucleons and pions with short

---

<sup>2</sup>We note that the gauge bosons of this group are not the photon and weak bosons, but instead the  $W^{1,2,3}$  and the  $B$ , which in the formalism give rise to the  $\gamma$ ,  $W^\pm$  and  $Z$  found in nature, after spontaneous symmetry breaking.

lifetimes. The discovery of new particles which were longer-lived prompted Gell-Mann [23] and Nishijima [24] to propose a new concept of *strangeness*.

This was eventually extended into the eightfold way [25], which is described by the  $SU(3)$  group. This model, while incomplete, was a radical leap forward in our understanding of the spectrum of observed hadrons, and a vital step towards our current understanding of the Standard Model. The model placed the nucleons with total angular momentum  $J = 1/2$  into an octet representation. Any two generators of the group which commute can, in addition to the dimensionality of the group, characterise the representation. Usually these are taken to be the third component of the isospin,  $I_3$ , and the hypercharge, defined as  $Y = B + S$  where  $B$  is the baryon number and  $S$  is the strangeness. The  $SU(3)$  symmetry is only an approximate symmetry - the different masses of the particles and their different weak interactions break it.

At the time the eightfold way was proposed, only nine of the baryons of  $J = 3/2$  had been identified. The model's earliest success was Gell-Mann's prediction that these would fit very well into a similar decuplet representation following  $SU(3)$ , predicting the existence of one further particle with  $S = -3$ . This was observed at the Brookhaven Laboratory in 1963 [26], with the mass predicted correctly to be approximately  $1.67 \text{ GeV}/c^2$  by the roughly linear mass spacing of the baryons with increasing strangeness. Gell-Mann suspected that a triplet, corresponding to the fundamental representation, existed in the form of three more fundamental particles, which he dubbed "quarks". These came to be known as the  $u$ ,  $d$  and  $s$ . All hadrons were thought to be bound states of these quarks.

The relation of strangeness-violating decays to these quarks came from Cabibbo in 1963 [27]. He posited that the weak eigenstates of quarks are rotated from the mass eigenstates, by an angle, now known by his name, which dictates the strength of coupling between quark flavours. This presented a new problem - under this formalism, Flavour Changing Neutral Currents (FCNCs) would be allowed at tree level, when experimentally such decays were known to be highly suppressed. The Glashow-Illiopoulos-Maiani (GIM) mechanism, postulated in 1970 [28], demonstrated that with the addition of a fourth quark these tree level amplitudes would cancel <sup>3</sup>.

In November of 1974, two experiments independently discovered a narrow resonance at  $3.1 \text{ GeV}/c^2$  [29, 30]. This resonance had the narrow width and approximate mass of the expected bound state of  $c\bar{c}$ , and was subsequently named the  $J/\psi$  as a compromise between the two proposed names of  $J$  and  $\psi$ . This was rapidly followed by the discovery in 1975

---

<sup>3</sup>Not precisely, due to the mass difference between the up and charm quarks.

of the first charmed baryon candidates [31] (one of which was the  $\Lambda_c$ ), and observations of the  $D^0$  [32] and  $D^+$  [33] followed in 1976. This quick series of discoveries led to the widespread acceptance of the quark model.

The discovery of the muon in 1937 [34] and the tauon in 1975 [35] had given us three generations of leptons. It was therefore predicted that nature's tendency towards symmetries would lead to the observation of a third generation of quarks. This was confirmed in 1978 when the  $\Upsilon$  was discovered [36] and interpreted as a  $b\bar{b}$  bound state. Searches for the predicted  $t\bar{t}$  quarkonium continued without success, until it was realised that if its mass was high enough, its lifetime would be so low it would decay prior to hadronisation [37]. The top quark was not discovered until 1995, when both the CDF [38] and D0 [39] detectors at the Tevatron accelerator independently observed its decays.

### 1.2.2 The $u$ , $d$ , $s$ and $c$ hadrons

Free quarks are never seen due to colour confinement. The only way to access their properties is by studying the hadrons they form. In this section we review the configurations of quarks in the mesons and baryons, and describe in particular the  $SU(4)$  multiplets of baryons composed of  $u$ ,  $d$ ,  $s$  and  $c$ .

The discovery of the  $\Omega^-$  at first appeared to violate the Pauli exclusion principle, which states no two fermions can possess the same quantum numbers. Two distinct spin configurations allow for two of the strange quarks to coexist in the hadron, while in the  $\Omega^-$  there are three. To resolve this, the existence of a new quantum number, the colour charge, was postulated. Colour is never observed freely - combinations of quarks in hadrons must be colour-neutral. By a convenient analogy with visible light, the colour charges are named red, blue and green, with anti-red, anti-blue and anti-green for the antiquarks. Colour is neutral in the event that a colour is bound with its anti-colour counterpart, or in the event that a red, blue and green charge are bound.

Colour confinement therefore dictates that quarks can hadronise together in two configurations. The first is a bound quark and antiquark, or a  $q\bar{q}$  state whereby the colour charges of the quarks are equal and opposite - this is termed a meson. The second is when three quarks, or a  $qqq$  state, of different colour charges are bound, resulting in a hadron that is colourless - this is termed a baryon. An equivalent statement of the Pauli exclusion principle is that the wavefunction for a fermion state must be antisymmetric

under exchange of two quarks of equal mass. For the baryons this can be written as

$$|qqq\rangle_A = |\text{colour}\rangle_A \times |\text{space, spin, flavour}\rangle_S \quad (1.4)$$

with  $A$  and  $S$  denoting the components which are symmetric or anti-symmetric under the described transformation. Without colour, the overall wavefunction would be symmetric under such transforms and forbidden for fermions.

The configurations of the lightest four quarks are represented by a  $SU(4)$  symmetry, albeit one which is badly broken because the mass of the charm quark is significantly higher than the three light quarks. The configurations of mesons made of  $u$ ,  $d$ ,  $s$  and  $c$  quarks form a 15-plet and a singlet:

$$4 \otimes \bar{4} = 15 \oplus 1 \quad (1.5)$$

while for the baryons the configurations form three twentyplets and a quartet:

$$4 \otimes 4 \otimes 4 = 20 \oplus 20'_1 \oplus 20'_2 \oplus \bar{4}. \quad (1.6)$$

For the four lightest quarks, the pseudoscalar (spin-parity assignment  $J^P = 0^+$ ) meson states are shown in Figure 1.1. It should be noted that while every charmed meson in the

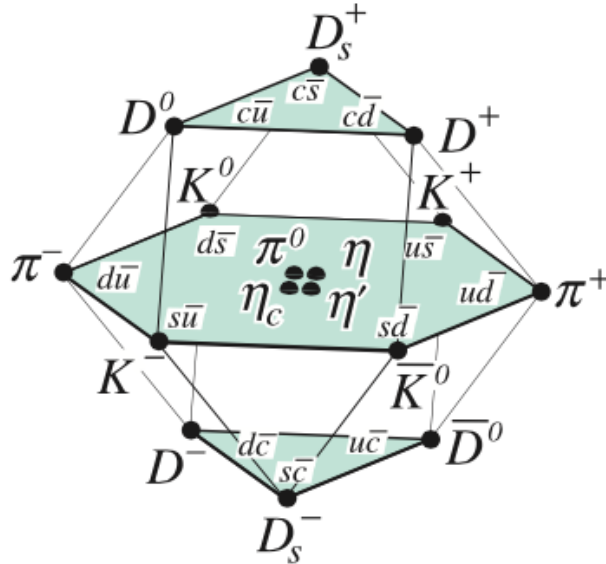


Figure 1.1: The 16-plet for the pseudoscalar  $J^P = 0^+$  mesons made from the four lightest quarks. Reproduced from [10].

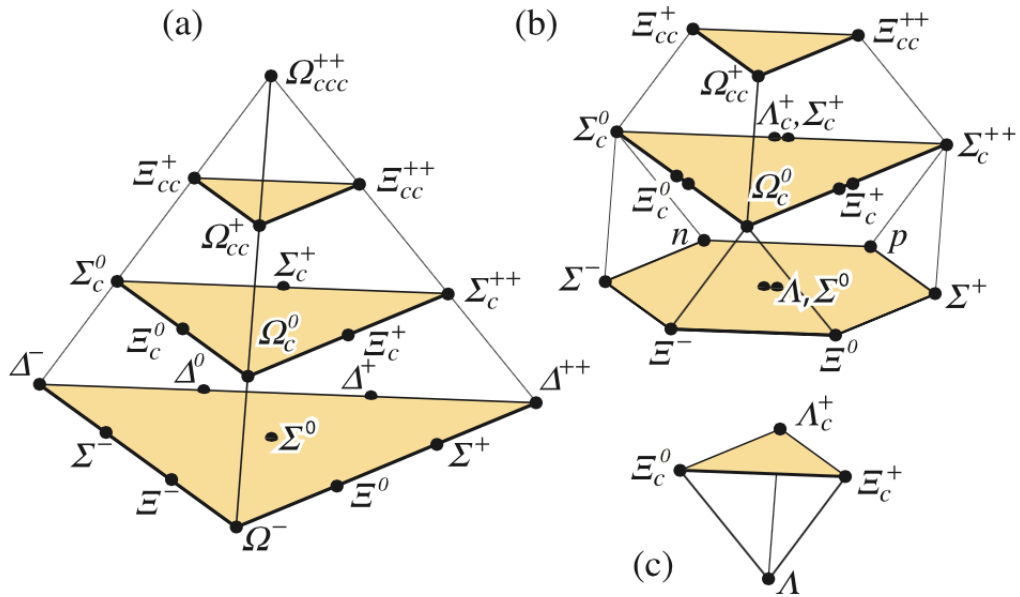


Figure 1.2: The 20-plet corresponding to the  $J^P = \frac{1}{2}^+$  baryons, the  $20_1$ -plet corresponding to the  $\frac{3}{2}^+$  baryons and the  $\bar{4}$ -plet corresponding to the  $\frac{1}{2}^-$  baryons, all corresponding to the baryons from the  $SU(4)$  representation of the four lightest quarks. Reproduced from [10].

$SU(4)$  formalism has been observed, a number of charmed baryons remain unobserved. The spectra of charmed baryons in the  $SU(4)$  formalism is given in Figure 1.2. As will be more fully reviewed in Section 1.4, evidence for doubly-charmed baryon production has only been found in one experiment, and no triple-charm production has ever been observed.

The particles given correspond to those particles which are ground-state systems of bound quarks. They are arranged into multiplets based on their spin-parity assignments  $J^P$ , where  $P$  is the parity quantum number,  $J = L + S$  is the total angular momentum, and  $S$  and  $L$  are the spin and angular momentum quantum numbers respectively. The alignment of the quark spins, which are all of magnitude  $1/2$  and may be either parallel or antiparallel, result in the ground state multiplets corresponding to ground-state assignments of  $J^P = 1/2^+$  for the hadrons with the quark spins as  $\uparrow\downarrow\uparrow$  and  $J^P = 3/2^+$  for hadrons with quark spins  $\uparrow\uparrow\uparrow$ .

Further excitations of the quark system are possible in the quark model. Radial and angular excitations of the quarks result in resonant states which can decay strongly with short lifetimes ( $\mathcal{O}(10^{-23})$  s). Knowledge of the charm meson spectra are very well understood, and in recent years many of the predicted excitations have been observed. LHCb has even

recently observed the first heavy-flavour spin-3 meson in decays of  $B_s^0 \rightarrow \bar{D}^0 K^- \pi^+$  [40]. However, knowledge of the charmed baryon spectra has proceeded more slowly. The current state of the field is outlined in Section 1.4.

## 1.3 The CKM matrix and CP-violation

### 1.3.1 Quark mixing with two generations

As stated in the previous section, the phenomena of strangeness-violating decays was first explained by Cabibbo in 1963 [27]. He posited that the flavour eigenstates and mass eigenstates were rotated from one another by an angle. In the context of the quark model with  $u$ ,  $d$  and  $s$  quarks, this interpretation means that the  $u$  couples via the weak interaction to a superposition of  $d$  and  $s$ . This rotation angle is parameterised as

$$\begin{pmatrix} u \\ d' \end{pmatrix} = \begin{pmatrix} u \\ d \cos \theta_c + s \sin \theta_c \end{pmatrix} \quad (1.7)$$

This was first measured by taking the ratio of branching fractions

$$\frac{\mathcal{B}(K^+ \rightarrow \mu^+ \nu_\mu)}{\mathcal{B}(\pi^+ \rightarrow \mu^+ \nu_\mu)} \propto \frac{m_K \sin^2 \theta_c}{m_\pi \cos^2 \theta_c} \quad (1.8)$$

where the kaon/pion in the decay undergoes annihilation, with the  $u$  coupling to the down-type quark and a  $W$  boson. The current best measurement of the Cabibbo angle is  $13.02^\circ$  [10]. The GIM mechanism [28] extended this to four quarks, predicting the existence of the charm quark  $c$ . The weak eigenstates  $q'$  are related to the mass eigenstates  $q$  by:

$$d' = V_{ud}d + V_{us}s \quad (1.9)$$

$$s' = V_{cd}d + V_{cs}s \quad (1.10)$$

where  $|V_{ij}|^2$  is the probability of quark  $j$  decaying to quark  $i$ . In matrix notation, with four quarks we find:

$$\begin{pmatrix} d' \\ s' \end{pmatrix} = \begin{pmatrix} V_{ud} & V_{us} \\ V_{cd} & V_{cs} \end{pmatrix} \begin{pmatrix} d \\ s \end{pmatrix}, \quad (1.11)$$

or using the Cabibbo angle:

$$\begin{pmatrix} d' \\ s' \end{pmatrix} = \begin{pmatrix} \cos \theta_c & \sin \theta_c \\ -\sin \theta_c & \cos \theta_c \end{pmatrix} \begin{pmatrix} d \\ s \end{pmatrix}, \quad (1.12)$$

where the  $2 \times 2$  matrix is called the Cabibbo matrix. Using just one parameter, the Cabibbo angle, the mixing between the four lightest quark states can be parameterised.

The smallness of the off-diagonal terms in the CKM matrix gives rise to the concept of Cabibbo suppression. Hadronic decays involving transitions corresponding to the off-diagonal elements are suppressed due to the  $\sin \theta_c$  term.. Considering the hadronic decays of the  $D^0$ , we expect abundant decays of  $D^0 \rightarrow K^- \pi^+$ , where the  $c$  decays via  $W$  emission to a  $s$ . In the case of the decay  $D^0 \rightarrow \pi^+ \pi^-$ , where the  $c$  decays via  $W$  emission to a  $d$ , we expect from the small value of  $V_{cd}$  relative to  $V_{cs}$  that this rate should be suppressed, despite the larger  $Q$ -value for the latter decay. Indeed, the world-averages of these decays are currently [10]:

$$\mathcal{B}(D^0 \rightarrow K^- \pi^+) = (3.88 \pm 0.05) \times 10^{-2} \quad (1.13)$$

$$\mathcal{B}(D^0 \rightarrow \pi^- \pi^+) = (1.40 \pm 0.03) \times 10^{-3}. \quad (1.14)$$

We therefore refer to the former as a Cabibbo-favoured (CF) decay, and the latter as a Cabibbo-suppressed (CS) decay. Depending on the structure of a decay there can be multiple Cabibbo-suppressed transitions in a single decay mode. For example, the two-body doubly-Cabibbo suppressed decay  $D^0 \rightarrow K^+ \pi^-$  has the branching fraction [10]:

$$\mathcal{B}(D^0 \rightarrow K^+ \pi^-) = (1.38 \pm 0.03) \times 10^{-4}. \quad (1.15)$$

As such, the observation of highly Cabibbo-suppressed decays can be experimentally challenging due to their low branching fractions.

### 1.3.2 The third generation

Few concepts in particle physics are as important as symmetry. Symmetries dictate all conservation laws in physics - for example, translational symmetry underpins the conservation of momentum. Certain discrete symmetries in physics are of key importance in particle physics. These are charge conjugation ( $C$ ), parity ( $P$ ) and time reversal ( $T$ ).

Originally these were thought to be conserved in all interactions. In 1957, an experiment

led by Wu found that parity was violated in the weak decays of  $^{60}\text{Co}$  atoms [41]. The combined symmetry  $CP$  was shown to be broken in the decays of neutral kaons by Cronin and Fitch in 1964 [42].

This is incompatible with a quark model with only two generations. To conserve probability, the Cabibbo matrix must be unitary<sup>4</sup>. For an  $N \times N$  unitary matrix, the number of free parameters is  $(n - 1)^2$ , and the number of complex phases, through which  $CP$ -violation can enter the theory, is  $(N - 1)(N - 2)/2$ . Therefore in a two generation quark model, there are no complex phases and  $CP$ -violation cannot occur. The minimal dimensionality of any quark mixing matrix that permits  $CP$ -violation in weak interactions is  $N = 3$ . This was one of the earliest indications that there should be an as-yet unobserved third generation of quarks.

### 1.3.3 The CKM matrix

The Cabibbo matrix was generalised to the three dimensional case by Kobayashi and Maskawa, into what is now referred to as the Cabibbo-Kobayashi-Maskawa quark mixing matrix [43]. The weak eigenstates are now related to the mass eigenstates as:

$$\begin{pmatrix} d' \\ s' \\ b' \end{pmatrix} = \begin{pmatrix} V_{ud} & V_{us} & V_{ub} \\ V_{cd} & V_{cs} & V_{cb} \\ V_{td} & V_{ts} & V_{tb} \end{pmatrix} \begin{pmatrix} d \\ s \\ b \end{pmatrix}. \quad (1.16)$$

With the three rotation angles  $\theta_{ij}$ , and a complex phase  $\delta$ , we can parameterise the matrix in what has come to be termed the the standard parameterisation [44]:

$$V_{\text{CKM}} = \begin{pmatrix} c_{12}c_{13} & s_{12}c_{13} & s_{13}e^{-i\delta} \\ -s_{12}c_{23} - c_{12}s_{23}s_{13}e^{i\delta} & c_{12}c_{23} - s_{12}s_{23}s_{13}e^{i\delta} & s_{23}c_{13} \\ s_{12}s_{23} - c_{12}c_{23}s_{13}e^{i\delta} & -c_{12}c_{23} - s_{12}s_{23}s_{13}e^{i\delta} & c_{23}c_{13} \end{pmatrix} \quad (1.17)$$

where  $s_{ij} = \sin \theta_{ij}$  and  $c_{ij} = \cos \theta_{ij}$  and  $\delta$  is the  $CP$ -violating phase. The sizes of these parameters are not dictated by the theory, and must be measured experimentally. The

---

<sup>4</sup>Mathematically, a unitary matrix is one which when multiplied by its conjugate transpose yields the identity matrix.

current world-average measurements [10] of the parameters are

$$V_{\text{CKM}} = \begin{pmatrix} 0.97427 \pm 0.00014 & 0.22536 \pm 0.00061 & 0.00355 \pm 0.00015 \\ 0.22522 \pm 0.00061 & 0.97343 \pm 0.00015 & 0.0414 \pm 0.0012 \\ 0.00886^{+0.00033}_{-0.00032} & 0.0405^{+0.0011}_{-0.0012} & 0.99914 \pm 0.00005 \end{pmatrix}. \quad (1.18)$$

We have already noted that the CKM matrix is unitary, and therefore its on-diagonal components must obey the relation:

$$\sum_i |V_{ij}|^2 = \sum_j |V_{ij}|^2 = 1 \quad (1.19)$$

where  $i$  is the set of up-type quarks and  $j$  the down-type quarks. This is necessary in that the probability of coupling of any given up type quark to the down type quarks is unity (and vice-versa for down-type coupling to up-type). Unitarity requires that the off-diagonal elements obey the relation

$$\sum_k V_{ki} V_{kj}^* = 0 \quad (1.20)$$

where the sum over  $k$  is over the up-type quarks and fixed, and  $i, j$  are over the down-type quarks where  $i \neq j$ . This gives rise to six different relations dependent on the looping index, such as:

$$V_{ud} V_{ub}^* + V_{cd} V_{cb}^* + V_{td} V_{tb}^* = 0, \quad (1.21)$$

each of which gives rise to a triangle in the complex plane. The triangle area is constant, and relates to  $\delta$ . The relation in Equation 1.21 is the most commonly referred to of the six, and the angles of the triangle it describes are:

$$\alpha = \arg \left( \frac{V_{td} V_{tb}^*}{V_{ud} V_{ub}^*} \right) \quad (1.22)$$

$$\beta = \arg \left( \frac{V_{td} V_{tb}^*}{V_{cd} V_{cb}^*} \right) \quad (1.23)$$

$$\gamma = \arg \left( \frac{V_{ud} V_{ub}^*}{V_{cd} V_{cb}^*} \right) \quad (1.24)$$

These are referred to as the unitarity angles, and the current state of our knowledge on these parameters is shown in Figure 1.3. One of the key aims of LHCb is to make high-precision measurements of the angle  $\gamma$  through analysis of  $B$  meson decays.

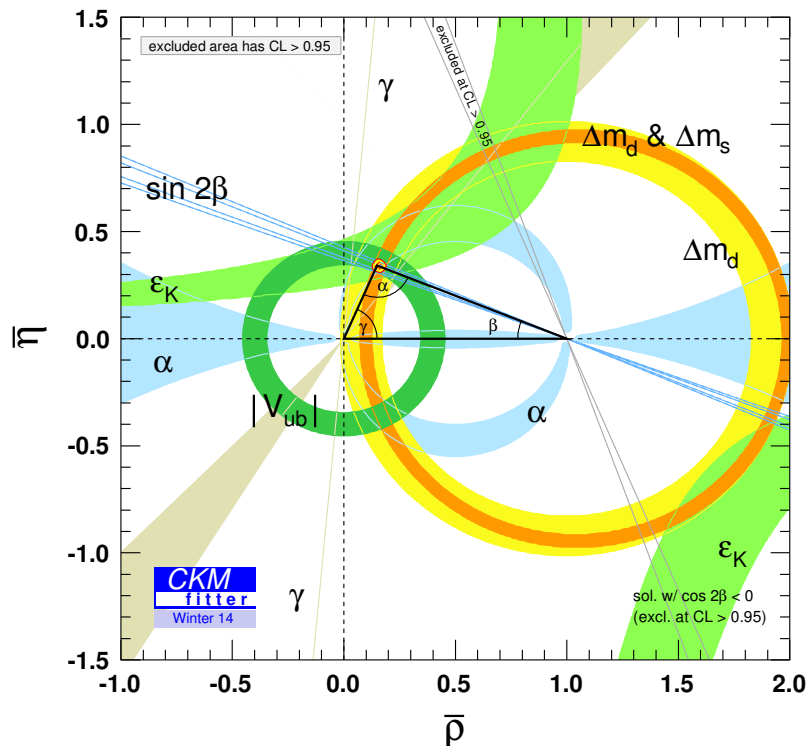


Figure 1.3: The current knowledge of and constraints on the unitary angle  $CP$ -violation parameters. Reproduced from [45].

## 1.4 Charm baryon phenomenology

While recent years have seen some advancement in our understanding of charm baryon spectra and decays, there is still much in this field to be measured and discovered. In this section we will review some selected phenomenology and results, and describe some of the more interesting questions facing the field, which remain unanswered.

### 1.4.1 Predictions from HQET and the lattice

While the underlying theory of Quantum Chromodynamics (QCD) is a very precise one, the manifestations of QCD in nature are often very complex. Making predictions on the bound states of quarks is therefore challenging, and a number of powerful methods of performing QCD calculations have been developed by the theory community. While the heavy  $b$  mass enables results on bottom baryons to be calculated from the application of

non-relativistic QCD (NRQCD) [46], the  $c$  mass is too light for relativistic effects to be removed from the calculations.

The use in physics of effective theories, where one integrates out effects not relevant at the scales involved in a theory, is common. One of the most successful in recent years in the Heavy Quark Effective Theory (HQET) [47–49], a QCD expansion in the inverse powers of the mass of the heavy quark,  $1/m_Q$ . In the case of single heavy-quark baryons this corresponds to the approximation of a stationary heavy quark interacting with a light quark dipole, used to simplify calculations. This is possible when the heavy quark  $Q$  is a charm or beauty quark, which are much heavier than the scale of the strong interaction,  $\Lambda_{QCD} \approx 400$  MeV. For the past two decades, results in this field have been extensively produced to predict a wide variety of heavy baryon properties. These include the baryon masses [50, 51], their decay widths [51–53] and their lifetimes [54–56]. For the singly-charmed baryons, these predictions have been generally in good agreement with experiment, however there still remain many unmeasured charmed baryon properties to test HQET against.

Another powerful method by which charm baryon calculations are produced is lattice QCD [57], where space-time is discretised to a grid, with quark fields located at the grid sites and gluon fields operating on the links between neighbouring sites. This technique has proven particularly adept at predicting the masses of heavy quark baryon states [58–61]. The masses of baryons containing at least one  $c$  or  $b$  quark, as calculated in a recent study by Brown *et al.* [62], are given in Figure 1.4. This figure should emphasise not only the power of lattice calculations, as evident in the fine agreement with experiment, but also the daunting task facing experimentalists to populate this menagerie of states.

## 1.4.2 Recent experimental results

### Excited charm baryon states

The  $B$ -factories, in particular BELLE and BaBar, have been very successful in making a plethora of first observations of excited singly-charmed baryons [65–72]. Our best knowledge of the spectra of singly-charmed baryons is given in Figure 1.5. The spin-parity assignments of many of the observed states are still unknown, requiring angular analysis with larger datasets.

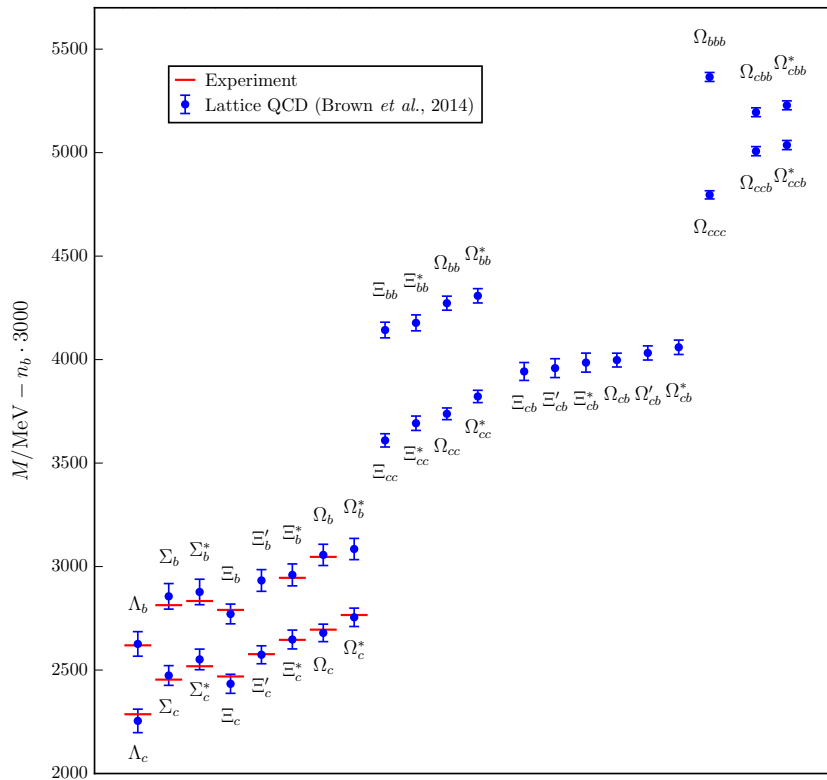


Figure 1.4: The masses of the heavy-flavour baryons from lattice QCD calculations. Where such states have been observed by experiment (red solid lines) a good agreement is demonstrated [10, 63, 64]. We note that the masses of baryons containing beauty quarks have been offset by  $-n_b \cdot 3 \text{ GeV}/c^2$  such that they may be shown with the much lighter charmed baryons. Reproduced from [62].

## Doubly charmed baryons

We take particular note of the search for doubly-charmed baryon production. In the  $SU(4)$  formalism we find states corresponding to  $ccd$  ( $\Xi_{cc}^+$ ),  $ccu$  ( $\Xi_{cc}^{++}$ ) and  $ccs$  ( $\Omega_{cc}^+$ ). Theoretical calculations generally agree that the  $C = 1$  states should have lifetimes between 100 – 250 fs, with the  $C = 2$  state having a lifetime between 500 – 700 fs [73, 74]. Evaluations for the particle mass generally predict that the  $\Xi_{cc}$  isodoublet should have a mass between 3.5 – 3.7  $\text{GeV}/c^2$ , with the mass of the  $\Omega_{cc}^+$  predicted to be between 3650 – 3800  $\text{GeV}/c^2$  [75–78].

The SELEX collaboration has reported the observation of the  $\Xi_{cc}^+$  in its decays to  $\Lambda_c K^- \pi^+$  [79] and to  $p D^+ K^-$  [80]. The reported state had a measured mass that, at  $3519 \pm 2 \text{ MeV}/c^2$ , was consistent with predictions from the theory community. Its measured lifetime, however, was consistent with zero, and less than 33 fs at the 90 % confidence

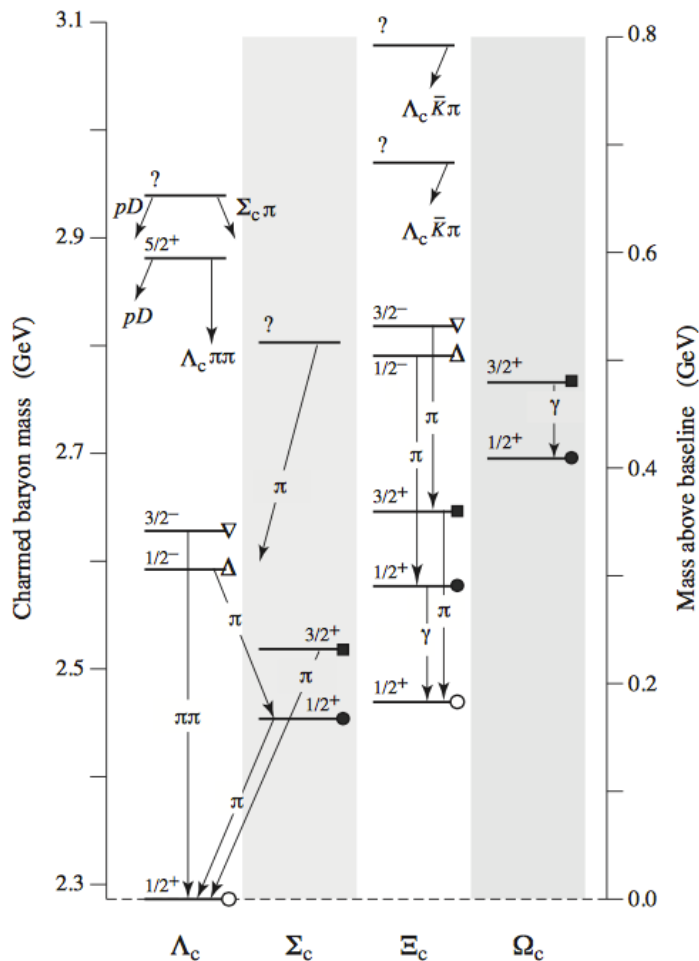


Figure 1.5: The spectra of known singly-charmed baryons and their mass splittings. Reproduced from [10].

level. This is in strong disagreement with the theory predictions, and is in stark contrast with the lifetime of the  $\Lambda_c$  ( $\tau \approx 200$  fs).

If such an observation is legitimate, then much can be learned from the study of the baryon, and why its lifetime is so uncharacteristically short. Subsequent searches at BELLE [65], BaBar [81] and most recently at LHCb [82] have not shown evidence for doubly-charmed baryon production. As such, the matter is still very much open to

discussion, and the theory community eagerly awaits a second experimental observation of the state.

### Amplitude analysis

In hadronic multibody decays, intermediate and strongly decaying particles can be produced, such that the final state is topologically similar were the decay to proceed in a non-resonant fashion. These resonances are of vital importance in the study of heavy-flavour baryons. In charmed mesons, spectator diagrams are the dominant form of weak decays, where the heavy quark emits a  $W$  and the light quark remains unchanged. Exchange diagrams, whereby the  $W$  emission of the heavy quark couples to the light quark in the hadron, are suppressed in meson decays due to helicity and form factor concerns [83]. In baryons, due to the three-body decay topology, these effects do not inhibit exchange contributions. Quark diagrams illustrating exchange and spectator diagrams are shown for a number of singly-charmed baryons in Figure 1.6.

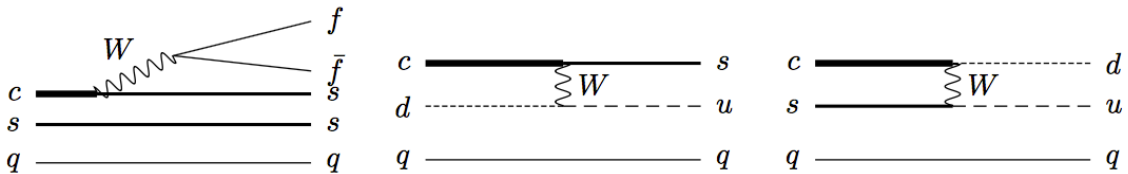


Figure 1.6: Quark diagrams of baryon decays, where the form of weak decay is  $W$  emission and  $s\bar{s}$  interference (left), Cabibbo-favoured  $W$  exchange (mid) and Cabibbo-suppressed  $W$  exchange (right). Reproduced from [84].

In particular, decays of  $\Lambda_c$  to hadrons without hyperon mediation ( $\Lambda_c^+ \rightarrow phh'$  where  $hh' \in \{K^-\pi^+, K^-K^+, \pi^-\pi^+, \pi^-K^+\}$ ) are particularly useful for studying the relative importance of spectator and exchange diagrams in enhancing charm baryon decay rates. The large number of strongly decaying intermediate resonances in these decays allow the isolation of exchange and spectator effects. For example, in the decay  $\Lambda_c^+ \rightarrow pK^-\pi^+$ , the decay can proceed non-resonantly, or via intermediate processes like  $pK^*(892)$  and  $\Lambda(1520)\pi^-$ . At first order the decay  $\Lambda_c^+ \rightarrow \Delta^{++}(1232)K^-$  can only proceed via exchange decays. With analysis of the  $\Lambda_c^+ \rightarrow phh'$  modes, the amplitudes of these decays can be measured to inform calculations of charmed baryon decay rates and lifetimes.

The first amplitude analysis of a charmed baryon decay was recently carried out by the E791 Collaboration [83]. Where the amplitudes of meson resonances are entirely described by the resonant mass pairings of the daughters (for example in  $D^+ \rightarrow h_1h_2h_3$ , the variables

$m(h_1h_2)$  and  $m(h_1h_3)$  are sufficient to fully characterise the decay), this is not true for baryons. This is because the  $\Lambda_c$  and the proton in the decay carry spin, and as such there are angular considerations in the resonant characters. The non-resonant amplitude is assumed to be uniform across the phase space. The full decay amplitude including resonant components is given by:

$$\begin{aligned} d\Gamma \sim & \frac{1 + \mathbf{P}_{\Lambda_c}}{2} \left( \left| \sum_r B_r(m_r) \alpha_{r, \frac{1}{2}, \frac{1}{2}} \right|^2 + \left| \sum_r B_r(m_r) \alpha_{r, \frac{1}{2}, -\frac{1}{2}} \right|^2 \right) \\ & + \frac{1 - \mathbf{P}_{\Lambda_c}}{2} \left( \left| \sum_r B_r(m_r) \alpha_{r, -\frac{1}{2}, \frac{1}{2}} \right|^2 + \left| \sum_r B_r(m_r) \alpha_{r, -\frac{1}{2}, -\frac{1}{2}} \right|^2 \right) \end{aligned} \quad (1.25)$$

where  $\mathbf{P}_{\Lambda_c}$  is the  $\Lambda_c$  polarization.  $\alpha_{r,m,\lambda_p}$  is the complex decay amplitude for resonance  $r$  with spin  $m$  (the  $\Lambda_c$  spin projection onto the  $z$ -axis) and a proton helicity  $\lambda_p$  in the rest frame of the  $\Lambda_c$ .  $B_r$  is the Breit-Wigner amplitude, and its form is given in [85].

To fully parameterise the resonant character of a  $\Lambda_c^+ \rightarrow phh'$  decay, 5 variables are required, two characterising the resonant mass pairings and 3 helicity angles. These angles and their definitions will be detailed in Section 3.5.8, where they are used in the selection of  $\Lambda_c$  decays in an analysis conducted by the candidate. The E791 study used a statistical sample of approximately 1000  $\Lambda_c^+ \rightarrow pK^-\pi^+$  decays. With the high statistics of charm decays at LHCb, the experiment can be the first to perform amplitude analyses of the Cabibbo-suppressed decay modes. Provided systematic uncertainties can be controlled, it can also improve the precision of the Cabibbo-favoured fit, and in doing so fit for more resonant components in the decay.

### 1.4.3 $\Lambda_c^+ \rightarrow phh'$ decays

There are still many unanswered questions about  $\Lambda_c^+ \rightarrow phh'$  decay rates and amplitudes. Table 1.1 reproduces the current knowledge of the relative branching ratios of  $\Lambda_c^+ \rightarrow phh'$  decays.

We note that in the errors quoted, a significant external component enters through the absolute branching fraction of  $\Lambda_c^+ \rightarrow pK^-\pi^+$ , which at the time of writing in the PDG is an average of a series of model-dependent results, with a high error of 26 % [10]. The current best measurement on the relative branching fractions of  $\Lambda_c^+ \rightarrow pK^-K^+$  to  $\Lambda_c^+ \rightarrow pK^-\pi^+$

Mode	BF	Refs	Note
$\Lambda_c^+ \rightarrow pK^- \pi^+$	$(5.0 \pm 1.3) \times 10^{-2}$	[86–88]	Derived from $\mathcal{B}(\bar{B} \rightarrow \Lambda_c^+ X)$
$\rightarrow p\bar{K}^*(892)^0$	$(1.6 \pm 0.5) \times 10^{-2}$		Inclusive $\bar{K}^*(892)^0$
$\rightarrow \Delta(1232)^{++}K^-$	$(8.6 \pm 3.0) \times 10^{-3}$		
$\rightarrow \Lambda(1520)^0\pi^+$	$(1.8 \pm 0.6) \times 10^{-2}$		Inclusive $\Lambda(1520)^0$
$\rightarrow pK^- \pi^+$ nonresonant	$(2.8 \pm 0.8) \times 10^{-2}$		
$\Lambda_c^+ \rightarrow p\pi^- \pi^+$	$(3.5 \pm 2.0) \times 10^{-3}$	[89]	
$\rightarrow pf_0(980)$	$(2.8 \pm 1.9) \times 10^{-3}$		Inclusive $f_0(980)$
$\Lambda_c^+ \rightarrow pK^- K^+$	$(7.7 \pm 3.5) \times 10^{-4}$	[90, 91]	
$\rightarrow p\phi$	$(8.2 \pm 2.7) \times 10^{-4}$		Inclusive $\phi$
$\rightarrow pK^- K^+$ non- $\phi$	$(3.5 \pm 1.7) \times 10^{-4}$		
$\Lambda_c^+ \rightarrow p\pi^- K^+$	$< 2.3 \times 10^{-4}$	[92]	CL = 90%

Table 1.1: World-average branching fractions for  $\Lambda_c^+ \rightarrow phh'$  decays as recorded in the 2012 PDG Review of Particle Properties [10]. Where noted, the PDG has adjusted the branching fractions for resonant decays to include all final states of the indicated resonances, not just the  $phh'$  final state of interest.

are from BELLE [90], measuring:

$$\mathcal{B}(\Lambda_c^+ \rightarrow pK^- K^+)/\mathcal{B}(\Lambda_c^+ \rightarrow pK^- \pi^+) = 0.014 \pm 0.002 (\text{stat}) \pm 0.002 (\text{syst}) \quad (1.26)$$

where the first errors are from limited signal statistics and the second are from systematic uncertainties. The current best measurement on the ratio of  $\Lambda_c^+ \rightarrow p\pi^- \pi^+$  to  $\Lambda_c^+ \rightarrow pK^- \pi^+$  is from NA32 [89], and has a considerably lower precision:

$$\mathcal{B}(\Lambda_c^+ \rightarrow p\pi^- \pi^+)/\mathcal{B}(\Lambda_c^+ \rightarrow pK^- \pi^+) = 0.069 \pm 0.036. \quad (1.27)$$

We note that the doubly-Cabibbo suppressed decay  $\Lambda_c^+ \rightarrow p\pi^- K^+$  has not yet been observed.

The massive production of  $c\bar{c}$  at LHCb has allowed the experiment to gather unprecedented high-statistics datasets on a number of charmed baryon decays. The primary experimental challenges to making high precision measurements of these relative branching fractions are the selection of promptly produced, hadronic  $\Lambda_c$  decays over the high hadronic combinatoric background. The short lifetime of the  $\Lambda_c$  relative to other charmed hadrons makes the rejection of background a key requirement to produce a precise result. The lack of amplitude models for the Cabibbo-suppressed decays also presents significant challenges, in that the simulation of the  $\Lambda_c^+ \rightarrow phh'$  decay kinematics, and mitigating systematic

uncertainties from any model-dependence, becomes more difficult. However, with the high statistics gathered by the LHCb machine, the statistical uncertainties in any such analyses will invariably be small.

Such a measurement is also a gateway to other LHCb analyses. Better understanding the branching fractions and resonant character of the  $\Lambda_c^+ \rightarrow phh'$  decays can inform the theory community considerably. Within the  $\Lambda_c^+ \rightarrow phh'$  decay modes, a considerable number of intermediate resonances may occur (at the very least, the  $K^*$ ,  $\Lambda(1520)$  and  $\Delta^{++}$  are all accessible in the Cabibbo-favoured decay). High statistics studies of these resonances and their interference effects can provide valuable insight into the nature of the spectator and exchange decays which are thought to give the charmed baryons their lifetime hierarchies. Better understanding of the acceptances and kinematics of the decay  $\Lambda_c^+ \rightarrow pK^-\pi^+$  can lead to improvements in searches for doubly and triply charmed baryon decays, many of which proceed via intermediary  $\Lambda_c^+ \rightarrow pK^-\pi^+$  decays with relatively high branching fractions.

Charmed baryons, while not as much a focus of LHCb activity as searches for  $CP$ -violation and new-physics sensitive rare decays, can still provide a considerable number of new experimental results and observations. These can not only inform the theory community in their modelling of heavy-quark hadronisation, but provide robust checks against the predictions of the quark model, the CKM matrix, and the Standard Model in general.

## 1.5 Summary

The Standard Model of particle physics has enjoyed unparalleled success in describing the fundamental constituents of the universe. We have outlined the concepts underpinning the SM, and given a brief description of its mathematical formalism. We have discussed the quark model, with particular emphasis on the multiplets of baryons comprised of the four lightest quarks predicted in the  $SU(4)$  formalism. We have described the mechanisms of quark mixing, and shown how the  $CKM$  matrix gives rise to the suppression and enhancement of certain weak decays of heavy-flavour hadrons. A summary of recent theoretical and experimental results on charmed baryons was given, remarking on a variety of open questions in the field of charmed baryon spectroscopy. We concluded with a motivation of an analysis of the relative branching fractions of  $\Lambda_c^+ \rightarrow phh'$  decays at LHCb. This analysis was conducted by the candidate, with the experimental methods outlined in

Chapters 4 – 5, with the results given in Chapter 6.

# Chapter 2

## The LHCb experiment at the LHC

The LHCb beauty (LHCb) experiment at the Large Hadron Collider (LHC) is a dedicated forward-arm spectrometer designed to conduct precision heavy-flavour physics measurements. We first describe the LHC accelerator complex, and the conditions under which the LHCb experiment gathers data. We then provide a description of the detector, including all subsystems necessary to its operation. This chapter concludes with a discussion of the LHCb trigger system.

### 2.1 The Large Hadron Collider

The CERN accelerator complex is home to the LHC collider, an accelerator with the highest centre-of-mass energy to date, with a nominal centre of mass energy ( $\sqrt{s}$ ) for  $p$ - $p$  collisions of 14 TeV.<sup>1</sup>

The protons accelerated by the collider originate from a source of hydrogen gas, progressing through a series of accelerators at the CERN site as depicted in Figure 2.1. The hydrogen gas is then ionised through the application of an electric field, and the resultant protons accelerated to 50 MeV by Linac2, which uses radio frequency (RF) cavities to impart energy to the protons. Protons from pulses of up to 100 ns are injected into the Proton Synchrotron Booster (PSB), which is composed of four superimposed synchrotron rings that accelerate the protons to 1.4 GeV.

The PSB then injects the protons into the Proton Synchrotron (PS), which accelerates the protons to 25 GeV. The protons are then injected into the Super Proton Synchrotron

---

<sup>1</sup>The LHC has not yet achieved 14 TeV collisions. For 2010–2011 the collider ran at  $\sqrt{s} = 7$  TeV, and at  $\sqrt{s} = 8$  TeV in 2012.

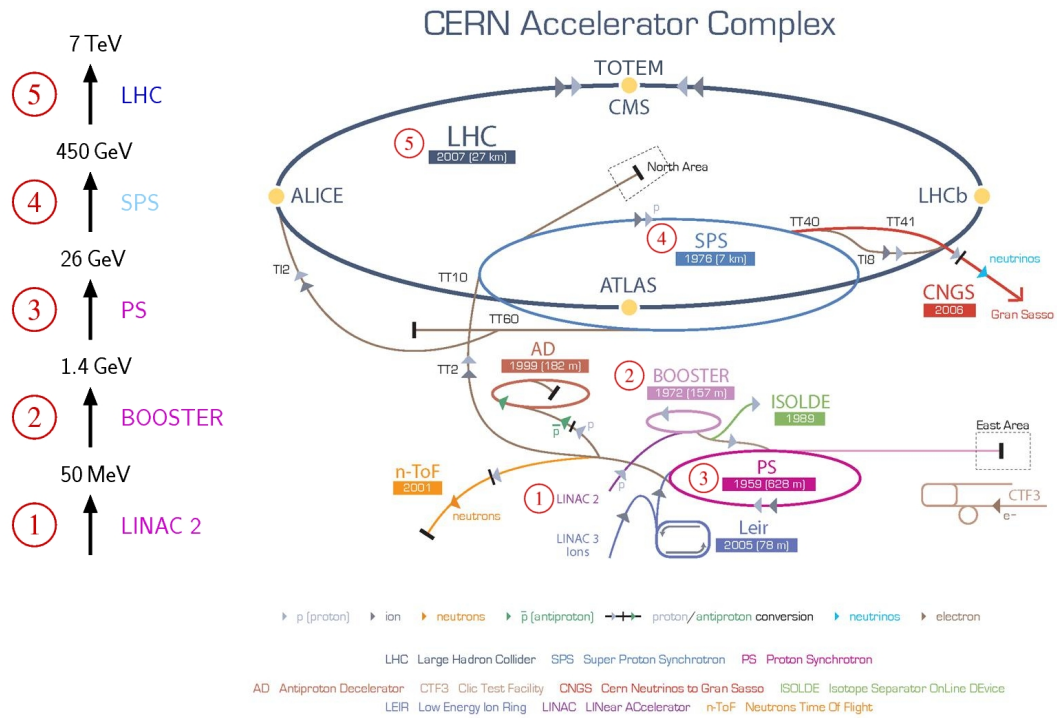


Figure 2.1: The LHC accelerator complex. Reproduced from [93].

(SPS), accelerating the protons to 450 GeV. Finally, the protons are then injected into the LHC collider and divided into two beams circulating in opposite directions.

The protons travel through the LHC in a vacuum of better than  $10^{-8}$  mbar. The accelerator utilises 1232 copper-clad niobium–titanium dipole magnets to curve the protons around the ring, each of which produce a peak magnetic field of 8.4 T when the protons reach 7 TeV. The bunches of protons are focussed by 392 quadrupole magnets. The magnets are cooled to a temperature of 1.9 K to a super-conducting state through the use of liquid helium. Sixteen RF cavities accelerate the protons from their injection energy to the required  $\sqrt{s}$ , and are housed in cryomodules that cool their temperature lower than 4.5 K. Full details of the LHC design are provided in [94].

There are four detectors in which the beams collide, the general purpose detectors CMS [95] and ATLAS [96], the heavy-ion optimised ALICE [97], and LHCb. Amongst their aims are the discovery of new particles, particularly the previously unobserved particles predicted by Higgs theory and supersymmetry, precision measurements of Standard Model quantities and searches for new physics outside of the Standard Model.

The LHC first successfully collided 3.5 TeV beams in March 2010, breaking the record

for highest energy particle collision previously held by Fermilab’s TeVatron at 1.96 TeV. This record was again broken in 2012 as the LHC ramped up to 4 TeV beams for its 2012 run. Data taking at this energy continued until the end of 2012, when the collider was shut down to enable upgrades to take the LHC to its design luminosity and beam energy. In 2015 data taking will begin at beam energies of 6.5 TeV enabling even higher energy scales to be explored.

The LHCb experiment has gathered large volumes of data under varying operating conditions in 2010, 2011 and 2012. In 2010 an integrated luminosity  $\int \mathcal{L} = 0.04 \text{ fb}^{-1}$  at  $\sqrt{s} = 7 \text{ TeV}$  was recorded. In 2011  $\int \mathcal{L} = 1.10 \text{ fb}^{-1}$  at  $\sqrt{s} = 7 \text{ TeV}$  was recorded, with an instantaneous luminosity twice that of the nominal design value. In 2012 the centre-of-mass energy was increased to  $\sqrt{s} = 8 \text{ TeV}$ , with  $\int \mathcal{L} = 2.08 \text{ fb}^{-1}$  recorded. These operating conditions over the years are summarised in Table 2.1. The nominal design value for the average number of  $p - p$  interactions per visible bunch crossing  $\mu = 0.4$  was chosen to be low to allow a sufficiently clean environment for the event reconstruction due to the planned 25 ns interval between bunch crossings. The LHC was instead operated with a bunch spacing of 50 ns, such that the trigger and reconstruction software was able to function in a higher pileup environment. The recorded luminosity for each year as a function of time is shown in Figure 2.2, along with the delivered absolute luminosity in 2012. The data-taking efficiency, the ratio of recorded luminosity over the delivered luminosity, has been around 90 % throughout operation.

Year	$\sqrt{s}$ [TeV]	Instantaneous $\mathcal{L}$ [ $\text{cm}^2 \text{ s}^{-1}$ ]	Bunches	$\mu$
2010	7	$1 \times 10^{32}$	344	0.5 – 2.5
2011	7	$4 \times 10^{32}$	1380	1.5
2012	8	$4 \times 10^{32}$	1380	1.6
Nominal	14	$2 \times 10^{32}$	2808	0.4

Table 2.1: The LHCb running conditions in 2010, 2011, 2012 and the nominal conditions. The pileup,  $\mu$ , is the average number of  $p - p$  collisions in each visible bunch crossing.

## 2.2 The LHCb detector

The LHCb detector [98] is a dedicated heavy-flavour forward-arm spectrometer operating at the LHC. Its physics aspirations include precision measurements of CP-violation, the search for rare heavy-flavour decays and to search for indications of new physics beyond the Standard Model. The key aspects of the detector’s design are:

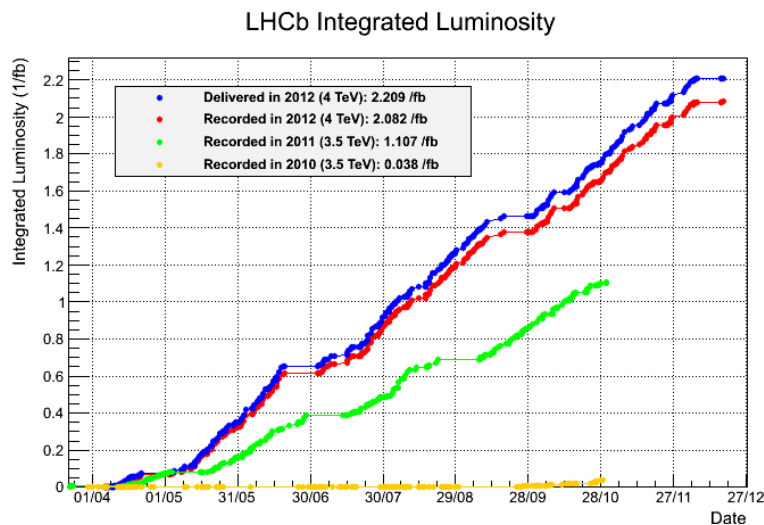


Figure 2.2: The recorded integrated luminosity at LHCb for 2010, 2011 and 2012 as a function of time. The delivered luminosity in 2012 is also given, demonstrating the 90 % data-taking efficiency achieved. From the LHCb collaboration.

- A powerful discrimination of secondary vertices from the decays of heavy-flavour particles produced in the primary interaction. Heavy flavour particles typically live long enough to fly around 1 cm from the location of the primary interaction. LHCb exploits a high-quality vertex resolution to isolate these particles from the production of lighter hadrons, which are of limited physics interest. The tracking system at LHCb provides a lifetime resolution of the order of 50 fs, precise enough to enable the study of the rapidly oscillating  $B_s^0$  meson.
- The discrimination of interesting signals from the high backgrounds present in a hadronic production environment requires a precise mass resolution, which in turn requires a precise momentum resolution. The tracking system at LHCb provides a momentum resolution of  $\delta p/p \approx 0.4 - 0.6 \%$ , which for example in the case of the decay  $B_s^0 \rightarrow D_s^+ K^-$  provides a mass resolution of 16 MeV/ $c^2$  [99].
- Many decays of heavy-flavour hadrons of particular interest have a variety of topologically identical final states, obeying different CP symmetries. The discrimination of these final states is vital to LHCb's goal to study CP-violation in the beauty and charm sectors, and also key to the search for rare decays such as  $B_s^0 \rightarrow \mu^+ \mu^-$ . The discrimination between different species of charged particle is therefore of crucial importance. The particle identification (PID) system at LHCb is able to provide

strong discrimination over the momentum range 1 – 100 GeV.

The major production processes underlying the production of heavy quarks at the LHC are gluon – gluon fusion and quark – antiquark annihilation to produce quark pairs of  $c\bar{c}$  and  $b\bar{b}$ . The low mass of charm and beauty quarks relative to the momentum of the partons in hard scattering processes result in  $c\bar{c}$  and  $b\bar{b}$  being produced dominantly in a highly boosted region. The LHCb detector uses a right-handed Cartesian coordinate system, with the  $z$ -axis pointing along the beampipe, the  $y$ -axis defined as vertical and the  $x$ -axis horizontal. The detector’s acceptance lies only in the forward region, covering an angle with respect to the  $z$ -axis 10 mrad to 250 (300) mrad vertical (horizontal). The angular production of  $b\bar{b}$  pairs at LHCb is shown in Figure 2.3 in terms of the angles between the  $b$  and  $\bar{b}$  momenta and the  $z$ -axis. This demonstrates that even with a low fraction of overall coverage around the interaction region the detector is still able to detect 27 % of  $b$  and  $\bar{b}$  production, with 25 % of  $b\bar{b}$  pairs falling in the detector acceptance.

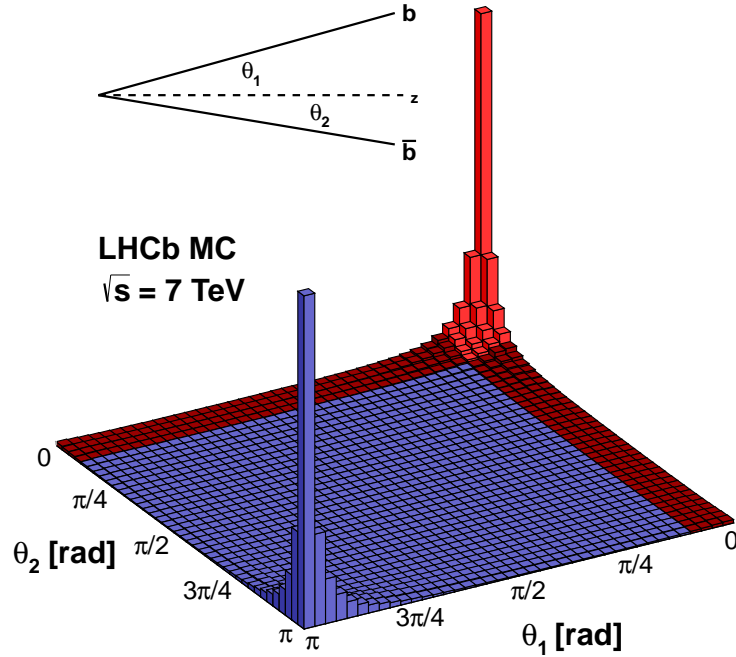


Figure 2.3: The angular production of  $b\bar{b}$  at LHCb for  $\sqrt{s} = 7 \text{ TeV}$  collisions. Shown in red is the LHCb acceptance. From the LHCb collaboration.

A vertical cross-section of the LHCb detector is given in Figure 2.4. The proton collisions take place at  $z = 0$  within the VERtice LOcator (VELO). Particles travelling within the acceptance then traverse the first of two Ring-Imaging Cherenkov detectors (RICH) before passing through the Tracker Turicensis (TT). The particles then pass through the magnet and three tracking stations (T1 – T3) before traversing the second RICH detector. We note that points that are located at relatively higher positions in  $z$  than some other reference point are said to be “downstream” of the reference point, while points with lower  $z$  are “upstream” of the reference point. The muon and calorimetry systems are the furthest components from the interaction point. Each of these subsystems will now be detailed, collected loosely into the tracking, the RICH detectors, the calorimetry, muon system and the trigger.

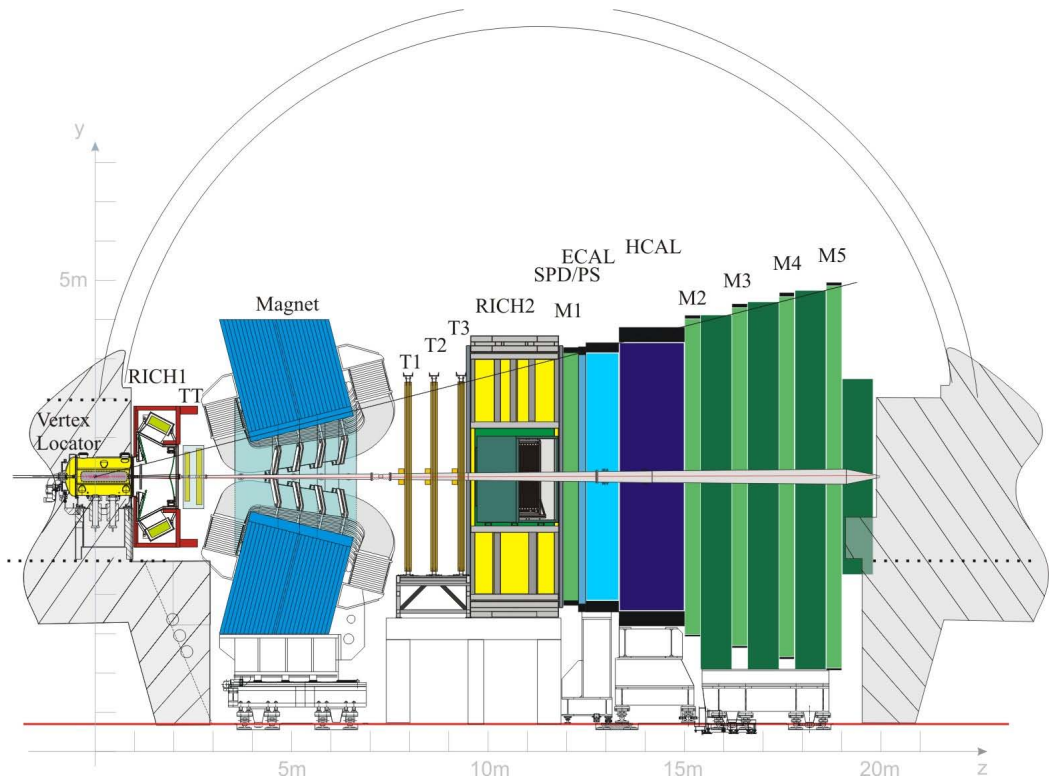


Figure 2.4: The vertical cross section of the LHCb detector. The projection is in the  $y z$  plane at  $x = 0$ . From the LHCb collaboration.

### 2.2.1 Tracking

The tracking of particles at LHCb is provided by the VELO, the four tracking stations and the dipole magnet. The tracking system has the job of reconstructing the trajectory of particles traversing the detector with a high spatial resolution and to determine their momenta. Powerful tracking is key to the acquisition of precise measurements of particle masses and lifetimes, and is one of the cornerstones of the physics programme at LHCb.

#### VELO

The VELO is a silicon microstrip detector with the job of locating primary vertices (PV) from  $p - p$  collisions and secondary vertices (SV) from the decays of long lived heavy flavour hadrons. The majority of beauty mesons in the LHCb acceptance produced in  $p$ - $p$  collisions fly very close to the beam axis, therefore the VELO has been designed to operate as close to the beamline as possible. The VELO is composed of two halves so that the detector may be retracted from the beamline during beam injection and then centred around the beam when stable beams are circulated. During beam injection the beams are unstable, and the VELO must be retracted by 29 mm from the beam axis during fills. Under data-taking conditions the VELO is closed around the beam with a circular 7 mm aperture in the centre to allow the LHC beams to pass through without interacting with and damaging the detector material. A top-down cross section of the VELO is given in Figure 2.5.

Each half is composed of 21 modules, each housing two semi-circular sensors with a cylindrical geometry, with a  $R$  sensor to measure the radial coordinate of tracks and a  $\phi$  sensor to measure the azimuthal coordinate. With this geometry the VELO can be used in the trigger to provide a first reconstruction of tracks and vertices using 2-dimensional  $R - z$  tracking. This allows high impact parameter ( $IP$ ) tracks, those tracks with a large distance of closest approach with respect to the reconstructed primary vertex, to be identified early in the reconstruction procedure. The modules are bunched together more closely near the interaction region to ensure a low extrapolation distance from the first registered hit of a track to its primary vertex for optimum  $IP$  and PV resolution.

Schematics of the  $r$  and  $\phi$  sensors are given in Figure 2.6 The VELO sensors are made from 300  $\mu\text{m}$  thick silicon, with active areas from a radius of 8 mm to 42 mm. The sensors are subdivided into four 45° sections to reduce both the capacitance of the sensors and their occupancy. For the  $R$  sensors, the strip pitch, or the distance between sensor strips, is at a minimum of 38  $\mu\text{m}$  in the central region, which increases linearly to 101.6  $\mu\text{m}$ .

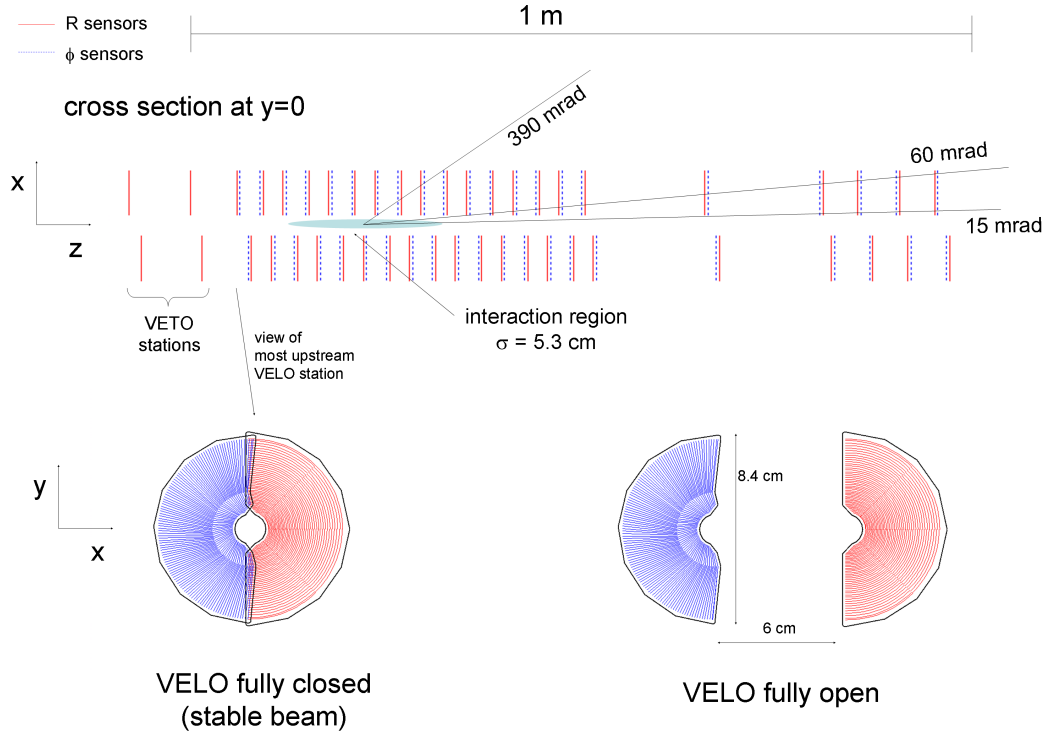


Figure 2.5: A cross section in the  $xz$  plane of the VELO stations. Shown bottom is a diagram of a VELO stations closed, left, and open. From the LHCb collaboration.

This gradient ensures that measurements along the track contribute to the precision of the  $IP$  with approximately equal weights. The  $\phi$  sensors are subdivided into an inner and outer region to keep the strip occupancy in the outer region sufficiently low. The inner strips have a pitch of  $78.3 \mu\text{m}$ , running from the innermost point of the sensor to a radius of  $17.25 \text{ mm}$ , where the outer strips begin. The outer strips have a pitch roughly half that of the inner strips of  $39.8 \mu\text{m}$ . The inner strips are skewed roughly  $20^\circ$  to the radial and the outer strips are skewed roughly  $10^\circ$  from the radial in the opposite direction. Adjacent  $\phi$  sensors have the opposite skew, providing adjacent stations with an enhanced ability to suppress the reconstruction of ghost tracks by providing a stereo view.

The halves are encased in a  $300 \mu\text{m}$  aluminium foil to shield the detector against radiofrequency pickup from the beam and to protect the LHC vacuum from outgassing of the detector modules. The foil must be thin to minimise multiple scattering, making it subject to deformations under pressure differences of as low as  $20 \text{ mbar}$ . The pressure in the LHC vacuum is kept better than  $10^{-8} \text{ mbar}$ , while the VELO is kept in a separate

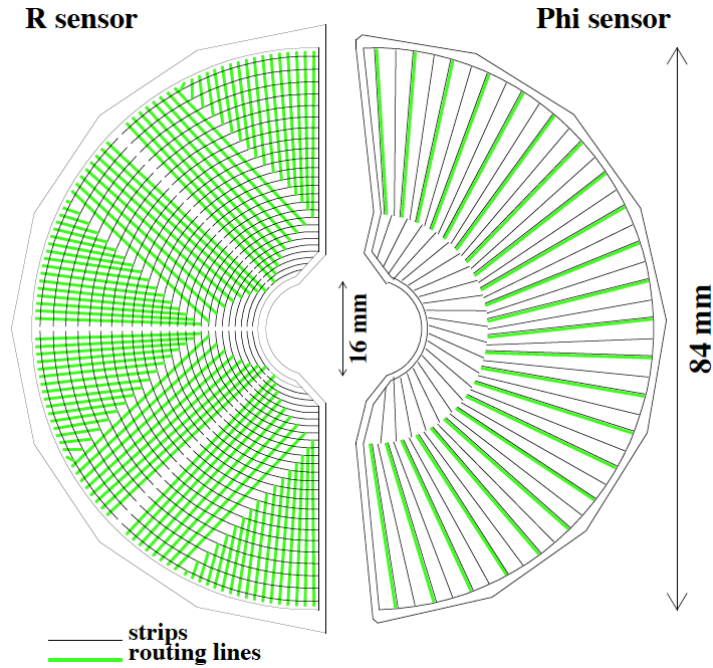


Figure 2.6: Schematic of the VELO  $R$  and  $\phi$  sensors. The routing lines are oriented perpendicularly to the strips in the  $R$  sensors and parallel to the strips in the  $\phi$  sensors. From the LHCb collaboration.

vacuum of approximately  $10^{-7}$  mbar to prevent foil deformation. The foil is corrugated such that the modules in each half can overlap in order to achieve a gapless acceptance in  $\phi$ . This overlap region is also of use in the relative alignment of the two VELO halves. The RF foil contributes the majority of the VELO's material budget, which is on average 17.5 % of a radiation length in total.

The impact parameter as a function of  $1/p_T$  and the vertex resolution as a function of event multiplicity are shown in Figure 2.7. For high transverse-momentum tracks an  $IP$  resolution of as low as  $11.6 \mu\text{m}$  may be achieved. The vertex resolution for a typical event multiplicity is between  $10 - 20 \mu\text{m}$ , which is the most precise vertex location of any LHC experiment.

### Tracking detectors

The tracking detector system is composed of the Tracker Turicensis (TT) [101], and the three tracking stations located downstream of the magnet (T1 – T3) [102]. The inner regions of T1 – T3 and the TT are subject to a much higher particle flux than the outer regions of the detector, and are therefore built with the same radiation-hard silicon strip

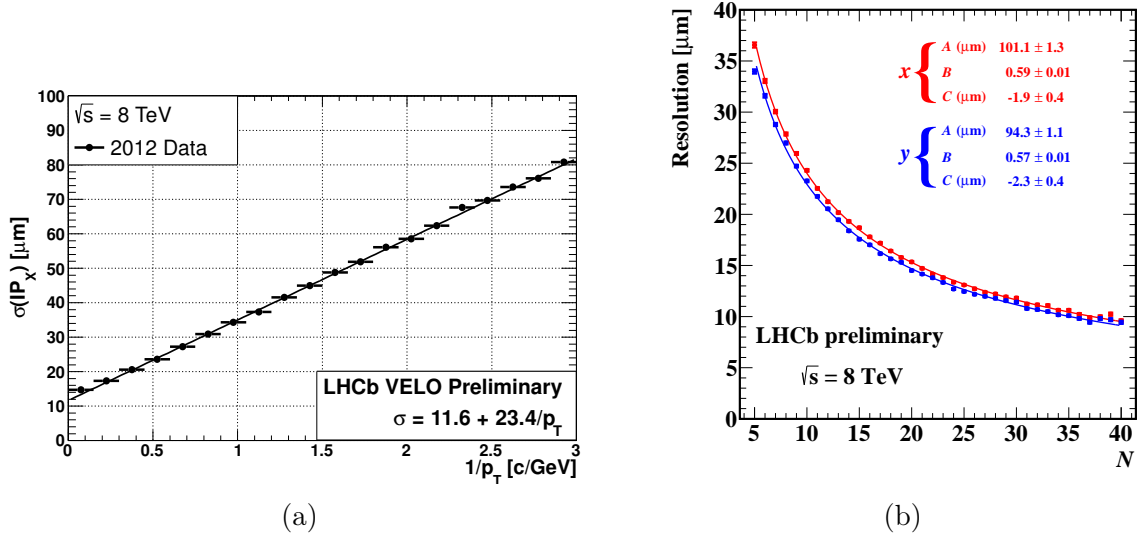


Figure 2.7: The VELO  $IP_x$  resolution as a function of  $1/p_T$  (a) and PV vertex resolution in  $x$  and  $y$  as a function of event multiplicity (b), taken with 2012 data. The vertex resolution achieved is the most powerful at the LHC. From [100].

design with high granularity for efficient pattern reconstruction. These are collectively referred to as the Silicon Tracker (ST). The outer regions of T1 – T3 are referred to as the Outer Tracker (OT), and are drift-time detectors. The division between the inner and outer trackers throughout T1 – T3 is shown in Figure 2.8.

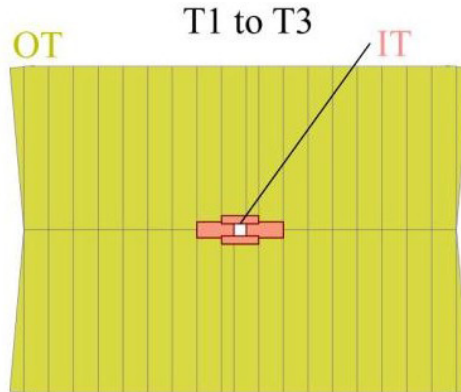


Figure 2.8: The division of the inner and outer trackers in the T1 – T3 stations. From the LHCb collaboration.

The TT is shown in Figure 2.9. It is composed of four layers of 500  $\mu\text{m}$  thick silicon microstrip sensors with a 183  $\mu\text{m}$  strip pitch. The TT is 1.5 m wide and 1.3 m tall

covering the LHCb acceptance. The first and fourth layers have their sensors oriented vertically while the middle two sensors are oriented at  $\pm 5^\circ$  from horizontal in opposing directions, to give a  $(x - u - v - x)$  layout, providing a stereo view of particles traversing the detector and allowing all cooling and support infrastructure for the detector to be located outside of the active area and the detector acceptance. Each detection layer is separated by approximately 27 cm in  $z$ .

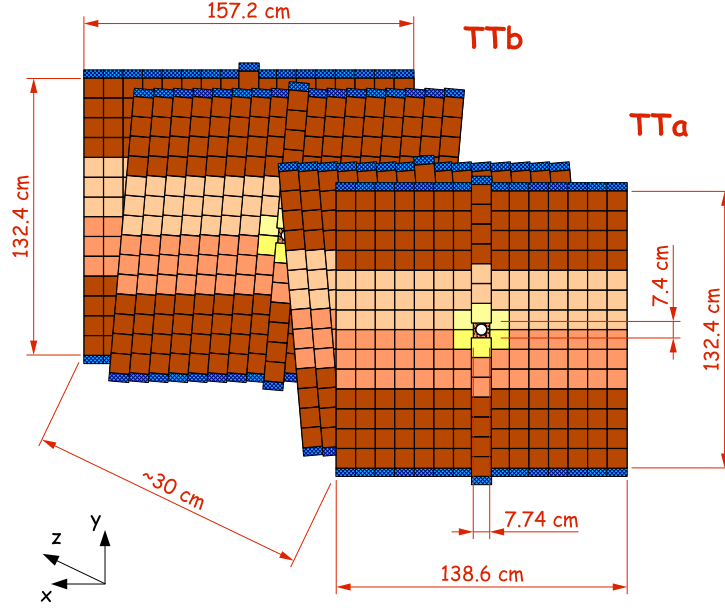


Figure 2.9: Schematic of the Tracker Turicensis. From the LHCb collaboration.

The inner tracker stations are located in the high luminosity region close to the beampipe, and their design must maintain a low occupancy for an effective reconstruction. The stations are composed of four detector boxes, two located above and two located adjacent to the beampipe. The stations are arranged in a cross shape as depicted in Figure 2.10, with a greater horizontal coverage than vertical to account for the bending of particles in the dipole magnetic field.

The outer tracker is a drift-time detector, and comprises the remainder of the T1 – T3 stations [103]. The detector modules are straw-tubes with a gas-tight design, each comprising two monolayers of 4.9 mm drift-tubes. Each of these is filled with a gas mixture of 70 % Argon and 30 %  $\text{CO}_2$  that becomes ionised when charged particles traverse the drift-tube. The tubes are constructed by winding two thin foil strips together, which have a voltage applied upon them to form an anode and cathode. The ionisation of the gas

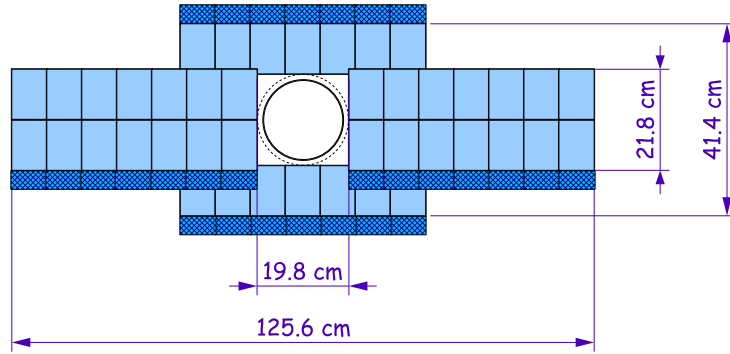


Figure 2.10: Schematic of the inner tracker layout. From the LHCb collaboration.

releases electrons which fly to the cathode, recording a signal. The specific gas mixture is chosen such that a low drift-time of 50 ns, and a precise spatial drift-resolution of 200  $\mu\text{m}$ , can be achieved. Like the TT modules, the OT modules in each tracker station are also aligned in a  $(x - u - v - x)$  formation, with the outer modules layered vertically and the inner modules tilted by  $\pm 5^\circ$  providing a stereo view of particle trajectories. The total material budget of the Outer Tracker is 9.6 % of  $X_0$ .

### Dipole magnet

The detector makes use of a warm dipole magnet to bend charged tracks for purposes of momentum measurements [104]. Its design weighed the need for a high overall field integral and for a sizeable field integral between the VELO and TT with the requirement that the field inside the RICH detectors be negligible. The magnet is comprised of a 1500 ton iron yoke and two 27 ton Al – 99.7 coil in a saddle-shape. The magnet has an integrated field strength of approximately 4 Tm and a peak field strength of 1.1 T. A precise knowledge of the magnetic field is required to ensure the desired momentum resolution can be achieved. The field integral was measured through the use of an array of Hall probes to a precision of order  $10^{-4}$  to this end. The main component of the magnetic field lies in the  $y$ -axis, and the magnet’s polarity is periodically flipped such that a variety of systematic uncertainties in charged particle tracking may be understood. A schematic of the LHCb magnet is given in Figure 2.11.

### 2.2.2 Particle Identification

The precise determination of the identity of charged particles traversing the detector is of key importance to the physics aspirations of the experiment. This is accomplished through

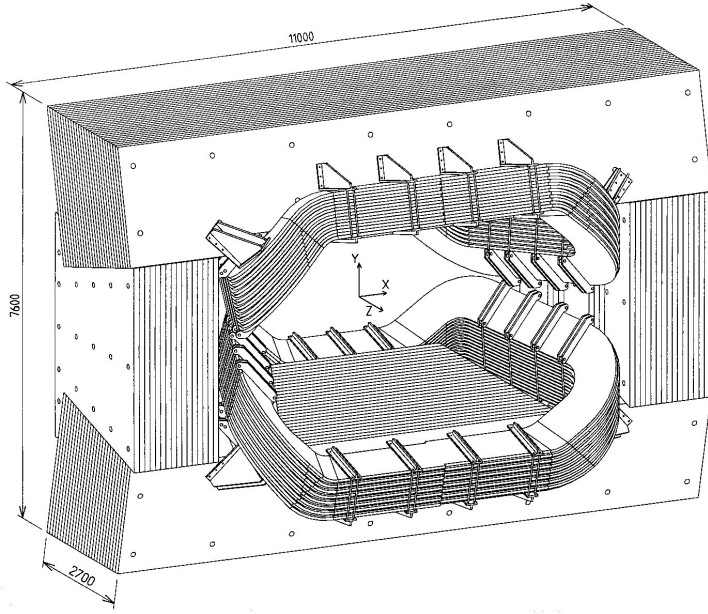


Figure 2.11: Schematic of the LHCb magnet. From the LHCb collaboration.

the use of two ring imaging Cherenkov detectors (RICH), which provide LHCb with strong particle identification (PID). RICH1 is located immediately downstream of the VELO while RICH2 is located downstream of T3. RICH1 contains two radiator materials; an aerogel block which provides particle discrimination in the range 1 – 15 GeV/ $c$  and a gas radiator providing discrimination up to momenta of 60 GeV/ $c$ . RICH2 contains a CF<sub>4</sub> gas radiator which provides discrimination for particles up to and above 100 GeV/ $c$ .

The detector's functionality exploits the emission of Cherenkov radiation from charged particles when they traverse a medium with a speed faster than the phase velocity of light in the medium. The light is emitted in a cone with a Cherenkov angle  $\cos \theta_C$  given by:

$$\cos \theta_C = \frac{1}{n\beta} \quad (2.1)$$

where  $n$  is the refractive index of the material and  $\beta$  is the ratio of the particle's velocity over the speed of light,  $v/c$ . By utilising the expression:

$$\beta = \frac{pc}{E} \quad (2.2)$$

it is possible to re-express the Cherenkov angle in terms of the particle energy:

$$\cos \theta_C = \frac{E}{npc} \quad (2.3)$$

which can in turn be expressed in the rest mass of the emitting particle:

$$\cos \theta_C = \frac{1}{n} \sqrt{1 + \left(\frac{mc}{p}\right)^2}. \quad (2.4)$$

If the momentum and Cherenkov angle of a particle can be measured, then the rest mass of the particle can be calculated.

The candidate's work in PID at low momentum and in developing new PID calibration samples necessitates a thorough discussion of the RICH detectors and their reconstruction algorithms. As such, we present this information more thoroughly in Section 3.2 as an introduction to the work conducted.

### 2.2.3 Calorimetry

The calorimetry at LHCb has multiple functionalities. It contributes to the PID of hadrons, electrons and photons, and enables the identification of high transverse energy particles, which are characteristic signatures of heavy-flavour decays. It also provides measurements of the energies and positions of particles. The calorimeter system is located immediately downstream of RICH2. Both calorimeters function by absorbing all energy of incident particles through interaction with the calorimeter material, producing cascade showers of other particles in the calorimetric system. From upstream to downstream, the calorimeter is comprised of a scintillator pad detector (SPD), a preshower detector (PS), the electromagnetic calorimeter (ECAL) and the hadronic calorimeter (HCAL).

All calorimeters have a similar operation, in which scintillation light is transferred to PhotoMultipliers (PMT) through wavelength-shifting (WLS) fibres. While the fibres for the SPD and PS are read out with the use of multianode photomultiplier tubes (MAPMT), those in the ECAL and HCAL are read out with individual phototubes.

The SPD and PS are comprised of a 15 mm lead converter of  $2.5 X_0$  located between two planes of high-granularity scintillator pads, with 12032 detection channels in total. The detector's active area is 7.6 m wide and 6.2 m tall. Electrons possess electric charge, and so will interact with the SPD producing an electromagnetic shower, whereas the neutral photons may only interact through their Bremsstrahlung emission, which has a much

lower probability of occurring in the SPD. The majority of photons instead convert in the iron prior to entering the PS, providing a differentiation between charged and neutral electromagnetic objects.

The ECAL utilises 66 modules, each with 2 mm of lead in front of 4 mm of scintillator material to capture the shower produced in the lead. The ECAL's thickness corresponds to  $25 X_0$ , where  $X_0$  is the radiation length, to ensure that all energy from incident photons and electrons is captured. The HCAL modules are also comprised of alternating lead and scintillator tiles, but unlike the ECAL they are aligned in parallel to the  $z$ -axis. The HCAL is  $5.6 \lambda_{int}$  deep, where  $\lambda_{int}$  is the hadronic interaction length. To account for the higher multiplicity environments close to the beampipe, and to maintain a manageable sensor occupancy, both the HCAL and ECAL are segmented such that the inner regions of the detector have higher granularity, as shown in Figure 2.12. The energy resolution achieved in the ECAL is  $\frac{8\%}{\sqrt{E(\text{GeV})}} \oplus 0.8\%$ , while that achieved in the HCAL is  $\frac{69\%}{\sqrt{E(\text{GeV})}} \oplus 9\%$ .

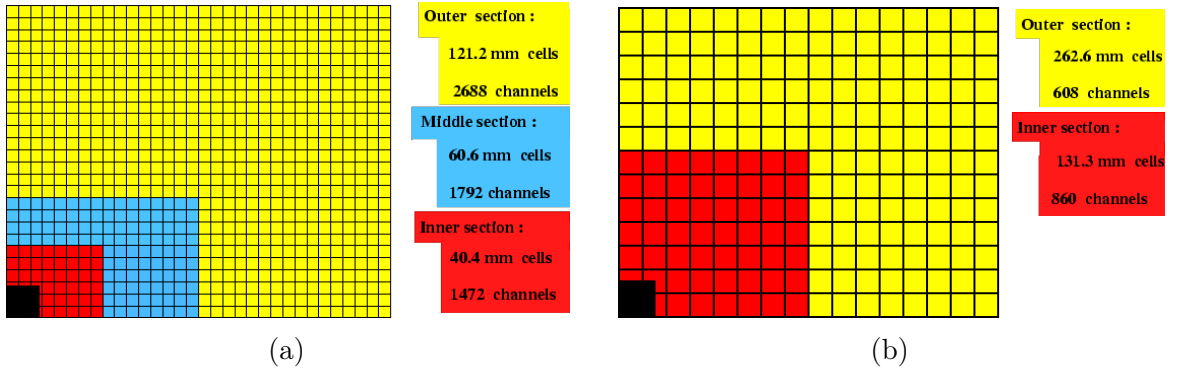


Figure 2.12: The segmentation of the SPD, PS and ECAL (a) and HCAL (b) calorimetry. From the LHCb collaboration.

## 2.2.4 Muon system

A high detection efficiency for muons is of key importance to the physics programme at LHCb. They are part of the final states of many decays that are sensitive to CP-violation, such as  $B_s^0 \rightarrow J/\psi \phi$ . They are of use in tagging the flavours at production of neutral heavy-flavour mesons, which enables studies of meson oscillation. Finally, they are present in the final states of a number of rare decay processes, in particular the new-physics sensitive  $B \rightarrow \mu^+ \mu^-$  decays.

The muon system is comprised of five rectangular stations (M1 – M5) on the beam axis. The system has an angular acceptance of  $20 - 306$  ( $16 - 258$ ) mrad in the horizontal

(vertical) planes. The resultant acceptance for muons from semileptonic decays of  $b$ -hadrons is approximately 20 % [98]. The M2 – M5 stations are located at the most downstream part of the detector, between which are sandwiched iron absorbers to absorb any remaining hadrons and electrons to isolate the muons. The M1 station is located in front of the calorimetry, and is used to improve measurements of  $p_T$  in the lowest trigger levels. The total depth of the muon system corresponds to approximately 20 interaction lengths, and as such, muons must have a minimum momentum of 6 GeV/ $c$  to traverse all five stations.

A side view of the muon system is provided in Figure 2.13. The stations are divided into four regions of roughly equivalent particle flux and occupancy, labelled R1 – R4. The detector regions are comprised of multi-wire proportional chambers (MWPC) in all but the inner region of M1, where the particle flux is above the limit for ageing via radiation damage. In this region triple-GEM detectors are utilised instead. The muon trigger algorithm requires all five stations to record hits in a track, and so the detection efficiency in each station must be excellent, with the timing resolution of 25 ns to unambiguously determine from which bunch crossing the track originated.

To this end, a MWPC design is adopted using a wire plane of 2 mm spacing, symmetrically placed in a 5 mm gas gap. A fast, non-flammable gas mixture of Ar / CO<sub>2</sub> / CF<sub>4</sub> in a mixture ratio of (40:55:5) is used. The logical OR of two adjacent gas gaps is taken, resulting in an efficiency better than 95 % for a time of 20 ns, with an order 10<sup>5</sup> gain acquired through the application of a voltage of 2700 V [105].

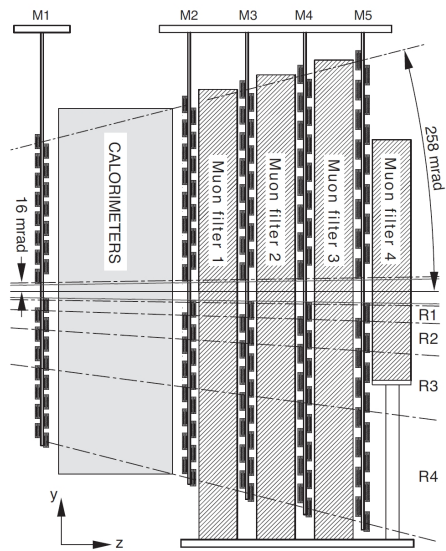


Figure 2.13: A side view of the muon system, indicating the four segmented regions of approximately equal occupancy. From the LHCb collaboration.

## 2.3 The LHCb trigger

The maximum bunch collision frequency at the LHC is 40 MHz, while only 15 % of these events will include a  $B$  meson with all decay products produced in the detector acceptance. At the LHCb interaction point the proton beams are defocussed such that the number of collisions per bunch is lower than is the case at the GPDs, but to record each event would still amount to an overwhelming accumulation of data. For the reasons outlined, the rate of visible interactions at LHCb is reduced to 10 MHz. It is the trigger's job to reduce this rate to about 5 kHz, which can be written to storage for physics analysis. This is accomplished via the use of a two-stage hardware and software trigger [106]. The Level-0 (L0) trigger is a hardware trigger, built with custom electronics, while the High Level Trigger (HLT) is a software trigger, and is executed on a computer farm. A simplified diagram of the LHCb trigger schema is shown in Figure 2.14.

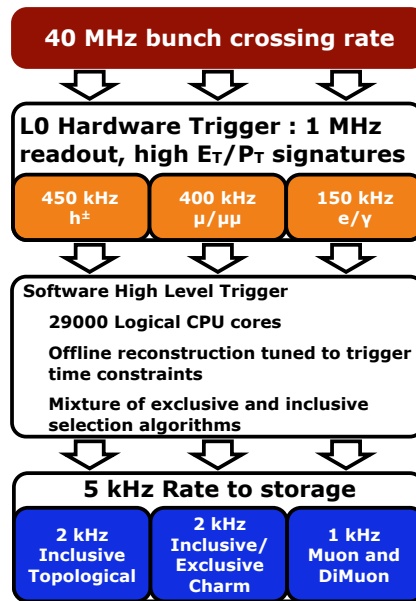


Figure 2.14: The schema of the LHCb trigger, showing the processing of events through the various alleys of the L0 and HLT levels. From the LHCb collaboration.

### 2.3.1 Level 0 trigger

The L0 trigger must bring the event rate from 10 MHz to 1 MHz, the rate at which the full event can be read out to perform a more sophisticated event selection. It is fully

implemented in hardware, and runs synchronously with the 40 MHz bunch crossing of the LHC. Heavy flavour hadrons decay into particles that typically have a significantly higher transverse energy and momentum than particles produced in soft interactions, which are not of interest. The L0 trigger exploits this by attempting to reconstruct the highest  $p_T$  hadron, electron and photon clusters (formed from the sum of  $2 \times 2$  adjacent calorimeter cells), and the two highest  $p_T$  muons in the muon system.

A pile-up system in the VELO also creates an estimate for the number of  $p - p$  collisions in the bunch crossing. Together with an estimate of the number of tracks in the event taken from the number of hits in the SPD, this information is used to reject events that may have been triggered due to a large number of combinatorics. The muon chambers are able to provide a first reconstruction with a transverse momentum resolution of approximately 20 %. The tracks corresponding to the calorimeter clusters are identified with information from the SPD, PS, ECAL and HCAL as either electrons, photons or hadrons.

The two muon candidates and the electron, hadron and photon clusters with the highest energy are checked against a series of simple logical cuts. The results of the individual decisions are passed onto the Level-0 Decision Unit (DU), which arrives at the final L0 trigger decision for the bunch crossing. Provided one of the requirements are met, the event is sent to the HLT. The time between the  $p - p$  interaction and the receipt of the decision by the front-end electronics is fixed to 4  $\mu\text{s}$ , and is independent of event-variable quantities like the detector occupancy. The L0 decision must then be reached within 2  $\mu\text{s}$ . As an example, the efficiency of certain L0 requirements with respect to the decay products of reconstructed  $B_s^0 \rightarrow J/\psi \phi$  as a function of the  $p_T$  of the  $B$  meson are shown in Figure 2.15. Taking the logical OR of the muon and dimuon trigger decisions, the efficiency across the full  $p_T$  range exceeds 75 %.

### 2.3.2 High Level Trigger

The output of the L0 trigger is passed to the Event Filter Farm (EFF), comprised of up to 2000 computing nodes, on which the HLT C++ applications run. The HLT has access to the full information on the event, but given the high 1 MHz input it is more practical to make a decision using only part of the event data. The HLT is split into two stages. HLT1 is responsible for reconstructing charged tracks in the VELO and trackers that match the objects which fired the L0 trigger, or for photons and pions to verify the lack of a charged track. HLT1 reduces the retention rate of events to approximately 30 kHz, allowing the HLT2 component of the trigger to perform a full reconstruction on the surviving events.

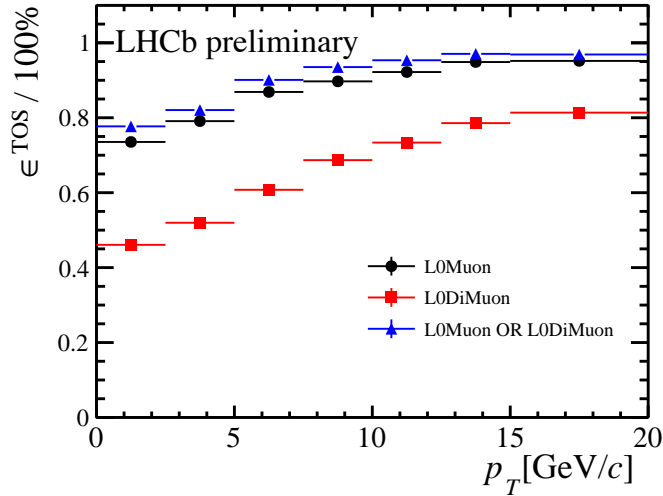


Figure 2.15: The L0 muon and dimuon trigger efficiency with respect to the decay  $B_s^0 \rightarrow J/\psi \phi$ , as a function of the  $p_T$  of the  $B$  meson. The TOS efficiency is the efficiency of the L0 trigger when applied to the tracks resulting from the decay of the  $B$  meson. From [107].

HLT2 comprises a variety of exclusive and inclusive lines, which impose a variety of selection criteria on the candidates surviving HLT1. These most commonly include cuts on the invariant mass of reconstructed heavy-flavour hadrons, quality requirements on reconstructed secondary vertices and pointing directions on the reconstructed hadrons with respect to the location of the related primary interaction. Information from the RICH PID discrimination may also be used at this juncture. <sup>2</sup>

Shown in Figure 2.16 are the efficiencies of various  $D$  decays with respect to an inclusive charm hadron HLT2 trigger line as a function of the  $D$  lifetime. Despite being optimised for the decays of  $b\bar{b}$  pairs, these high efficiencies demonstrate that LHCb successfully acquires information on a considerable number of charm hadron decays.

For many physics analyses at LHCb the efficiency of a trigger selection must be known to high precision. Finding the absolute efficiency of the entire trigger's selection of a decay mode is often problematic. It can also be advantageous to assign trigger requirements based on individual tracks in the event. We therefore classify all reconstructed tracks and particles resulting from combinations of such tracks as dependent or independent of every algorithm in the trigger, at both L0 and HLT. If a given signal candidate, either a track or some reconstructed heavy-flavour particle, is sufficient to trigger the event then the signal is classed as Triggered On Signal (TOS). If the signal candidate falls in an

<sup>2</sup>PID information has not yet been used in the trigger for Run I, but will be used in 2015 for Run II.

event which could have been triggered by other tracks or candidates in the event it is classified as Trigger Independently of Signal (TIS). Events can be both TOS and TIS simultaneously, and are designated as TIS and TOS with respect to each trigger line in the L0 and HLT. In the candidate's studies of  $\Lambda_c^+ \rightarrow phh'$  decays, which are detailed in Chapter 4, the classification of promptly-selected events as TIS with respect to a suite of HLT lines ensures a convenient trigger selection efficiency cancellation between the decay modes under consideration.

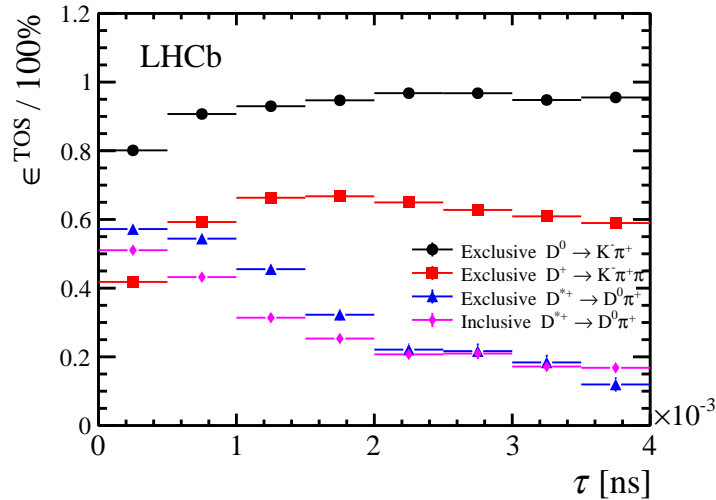


Figure 2.16: The HLT2 trigger efficiency with respect to a variety of hadronic  $D$  decays, as a function of the  $D$  lifetime. The TOS efficiency is the efficiency of the trigger line when applied to  $D$  candidate specifically, ignoring the rest of the event. From [107].

## 2.4 Simulation of particle production and decay

It is of utmost importance that a robust and accurate simulation of particle production and decay at LHCb is available, allowing the collaboration to better understand a wide variety of detector and physics effects. This is performed in the GAUSS package, detailed in [108], [109]. The simulation is broadly split into two phases, the generation of the primary interaction and decaying particles, and the transport of the particles through the detector.

For the former the HEPMC event record [110] is utilised as a format for the generated event. The primary interaction is simulated with the PYTHIA general purpose generator [111], simulating the  $p$ - $p$  collision and the production of particles. The PHOTOS

package [112] is interfaced to PYTHIA to account for Final State Radiation (FSR). To account for complex and time dependent decay properties of heavy flavour neutral mesons, the EVTGEN [113] package, designed by the BaBar collaboration [114] for the study of heavy-flavour meson decays, is utilised. Finally, the simulation of the particle interaction with the detector, and the approximation of the detector itself, are handled by GEANT4 [115], [116].

# Chapter 3

## Proton identification at low momentum and PID calibration

Key to the heavy-flavour physics aspirations of LHCb is the ability to accurately identify final state particles. This is accomplished with the use of the RICH particle identification (PID) system. In this chapter, the need for powerful PID at LHCb is first outlined in Section 3.1. A brief overview of the RICH technical specifications follows in Section 3.2. The reconstruction algorithms used in the RICH to assign particle hypotheses are then detailed in Section 3.3. The candidate's work on using the particle hypothesis information to measure the performance of the RICH aerogel is then given in Section 3.6. A data-driven correction to PID selection efficiency is commonly used on LHCb, which uses data of decays that can be reconstructed unambiguously through the use of kinematic information alone and without the use of PID discriminants. This technique is described in detail in Section 3.4. The candidate's work on preparing a sample of proton tracks from  $\Lambda_c^+$  decays is then given in Section 3.5.

### 3.1 Charged particle identification at LHCb

The need to accurately identify charged particles produced in heavy-flavour decays or from the underlying event is of paramount importance to the physics goals of LHCb. The majority of particles produced in the proton – proton collisions are pions, while many decays relevant to heavy-flavour physics contain pions, kaons and protons in the final state. In each event, typically of the order of one hundred tracks are reconstructed. The ability to distinguish between these particle hypotheses is vital to suppressing combinatoric

backgrounds in reconstructing the masses of heavy-flavour particles.

The ability to discriminate between different species of charged particles is also required to distinguish between topologically identical decays with different daughters. Without PID discrimination, any signal extraction using kinematic and vertex information is a sum over all possible modes. An example of this is given in Figure 3.1 from the decay  $B^0 \rightarrow \pi^+\pi^-$ , which is indistinguishable from all other  $B \rightarrow h^+h'^-$  modes without PID information. This is especially crucial for measurements of  $CP$ -violation, where the different final states possess different  $CP$  symmetries. Also of interest to  $CP$ -violation studies is the accurate tagging of neutral meson decays, where knowledge of the meson flavour at production is required. This may be accomplished in the identification of associated-production particles. By exploiting the high particle identification efficiencies over a wide momentum range of the RICH system, decay modes of interest may be isolated and studied more effectively. The LHCb trigger system [106] also makes use of the charged particle identification systems. The RICH reconstruction is fast enough so that it can be deployed online, and as such can be used to reduce the trigger retention rate while improving the signal purity for a variety of modes.

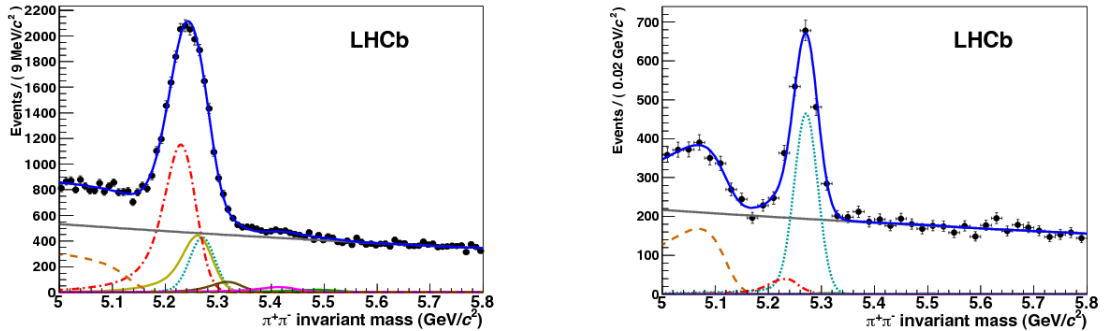


Figure 3.1: The effects of applying PID selection on the mass spectrum of  $B \rightarrow h^+h'^-$  decays, from [117]. Shown left is the reconstructed  $B^0 \rightarrow \pi^+\pi^-$  mass spectrum before PID selection, right is after PID selection. The correctly identified signal component (dashed blue) is much more emphasised after selection. Of the mis-reconstructed backgrounds ( $B^0 \rightarrow K^+\pi^-$  dotted red,  $B_s^0 \rightarrow K^+K^-$  solid yellow,  $B^0 \rightarrow 3$ -body dashed orange,  $B_s^0 \rightarrow \pi^+K^-$  solid brown,  $\Lambda_b^0 \rightarrow pK^-$  solid purple,  $\Lambda_b^0 \rightarrow p\pi^-$  solid green), all but two are eliminated entirely. The combinatoric background (solid grey) is also markedly reduced.

## 3.2 The RICH system

There is a need to accurately identify both high-momentum charged particles from heavy flavour decays and low-momentum particles from associated production for tagging. As such the RICH system is composed of two detectors to cover the full momentum range. RICH1 is located upstream of the magnet and is capable of PID in the range 1 – 60 GeV/ $c$ , and has aerogel and C<sub>4</sub>F<sub>10</sub> radiators. RICH2 is located downstream of the magnet, and contains a CF<sub>4</sub> radiator which covers the momentum range from 15 – 100 GeV/ $c$ . RICH1 covers the acceptance range 25 mrad – 300 mrad (horizontal)/ 250 mrad (vertical), while RICH2 covers the narrower acceptance range of 15 mrad – 120 mrad (horizontal)/ 100 mrad (vertical) corresponding to higher momentum tracks. In each, the Cherenkov light is focussed using both spherical and flat mirrors and guided out of the LHCb acceptance and onto Hybrid Photon Detectors (HPDs) which are capable of detecting photons with wavelength of 200 – 600 nm.

### 3.2.1 RICH1

The RICH1 detector is immediately downstream of the VELO and immediately upstream of the Trigger Tracker. It covers the approximate momentum range 1 – 60 GeV/ $c$ , and contains aerogel and C<sub>4</sub>F<sub>10</sub> radiators. Its general design is influenced by the need to minimise the material budget in the detector acceptance. The total radiation length, including the radiators of the full RICH1, is 8 %  $X_0$ . The magnetic field at the detector's location is approximately 60 mT, while the HPDs operate at peak efficiency up to 3 mT. Local MuMetal alloy shields and iron boxes are used to reduce the magnetic field at the HPD plane to 2.4 mT. A side-view schematic of the RICH1 detector is given in Figure 3.2.

Simulation has been used to optimise the optical design of the detector. Charged tracks passing through the RICH1 are generated, and Cherenkov photons are emitted uniformly along the length of the tracks in the radiators. The photons are ray-traced through the system to the HPDs. The Cherenkov angle at emission is then calculated for each photon under the assumption that the emission point lies halfway along the track's path through the radiator. The error in reconstructed Cherenkov angle due to the true emission point of the photon along the track is made by design to be smaller than other sources of finite angular resolution, for example the chromatic dispersion of the radiators. The simulation also determines the necessary coverage of the HPD planes. Close to full HPD coverage is required for photons emitted by the gas radiator, while photons emitted from the aerogel

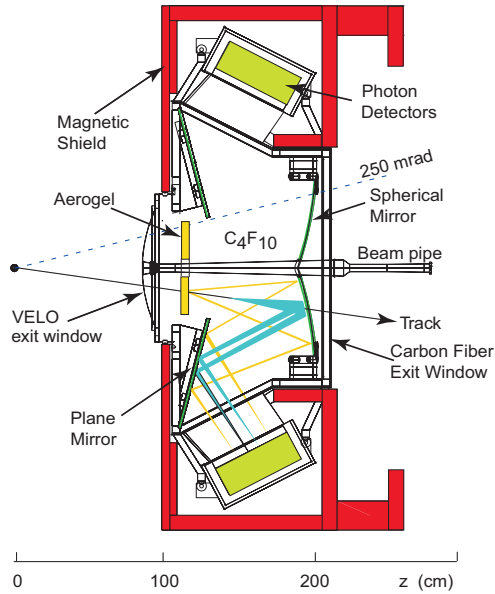


Figure 3.2: Side-view schematic of the RICH1 detector.

have a HPD coverage of 68 % due to cost restrictions, although this does not affect the detector performance significantly.

As the spherical mirrors fall within the detector acceptance, minimising the material budget is a concern. As such, they are made of a carbon fibre reinforced polymer (CFRP) substrate, keeping their contribution to the material budget below 2 %. There are four spherical mirrors in the assembly, each with an area of 830 mm by 630 mm projected into the  $x - y$  plane. The reflectivity of the mirrors is improved with thin coatings of Al (80 nm) and  $\text{MgF}_2$  (160 nm), such that the reflectivity of glass substrates can be improved at all wavelengths of interest. The flat mirrors are located outside the detector acceptance, and so glass can be used in their construction without increasing the material budget. Two planes are used, one above and one below the beampipe. In each plane, eight 380 mm by 347.5 mm mirrors of Simax glass are used.

The  $\text{C}_4\text{F}_{10}$  gas is contained in a gas enclosure which also provides a light-tight environment for the optical components. A pressure differential of  $\pm 300$  Pa must be maintained between the gas box and its surroundings. The enclosure's upstream boundary is attached to stainless steel bellows 300  $\mu\text{m}$  thick providing a gas-tight seal to the downstream end of the VELO vacuum tank. The downstream end is bounded by an exit window made of two 0.5 mm thick CFRP membranes on either side of a 16 mm thick polymethacrylimid (PMI) foam, which contributes 0.6 %  $X_0$  to the material budget. The sides of the enclosure

are open, allowing full access to the optical components, and closed by 10 mm thick aluminium panels. 8 mm thick quartz windows with an antireflective coating allow the Cherenkov light to reach the HPDs.

The shield boxes are designed with the considerations of maintaining the magnetic field integral within the fiducial volume, while allowing the HPDs to be sufficiently shielded that their efficiency is not adversely affected. The HPD planes are located in the upstream tails of the field, where the field strength is approximately 60 mT, while the HPDs operate at full efficiency in magnetic fields up to a strength of 3 mT. The shield is constructed from iron plates, with final dimensions of 1950 mm by 4000 mm by 1175 mm. Measurements made while the magnetic field is at full strength show the field at the HPD plane show that the field is reduced to 2.4 mT, and the field integral between the IP and TT is 0.12 Tm. Each shield box weighs 75 kN while the forces on the box at full field are approximately 50 kN. The design of the shield and its mountings ensures that the HPD displacement is no greater than 0.5 mm while the magnet is operational.

### 3.2.2 RICH2

The RICH2 detector is responsible for PID at high momentum, and is located downstream of the final tracking station and upstream of the first muon station. The detector uses a CF<sub>4</sub> radiator, which provides particle discrimination between 15 – 100 GeV/*c* in the acceptance  $\pm 120$  mrad horizontal and  $\pm 100$  mrad vertical, with a minimum radial acceptance of 15 mrad required by the thermal insulation around the beampipe. The detector is oriented with the mirrors and HPDs offset horizontally. Like the RICH1, the spherical mirrors must be located within the detector acceptance, while the flat mirrors and HPDs are located outwith. The radiation length of the detector, including the radiator, is 15 %  $X_0$ . A schematic of the detector is given in Figure 3.3.

As for the RICH1, the optical layout is optimised with simulation. The emission-point error is found to be small compared to other sources of finite angular resolution, including the dominant contribution from the chromatic dispersion of the CF<sub>4</sub>, which results in an uncertainty of 0.42 mrad. The spherical and flat mirrors are composed of 6 mm thick Simax glass substrate.

The gas enclosure has a volume of 95 m<sup>3</sup>. The upstream boundary is an entrance window made of two 1 mm thick carbon fibre reinforced epoxy membranes bounding 28 mm thick PMI foam. The downstream boundary is the exit window, with two 1 mm thick aluminium membranes bounding 30 mm PMI foam. Their contributions to the

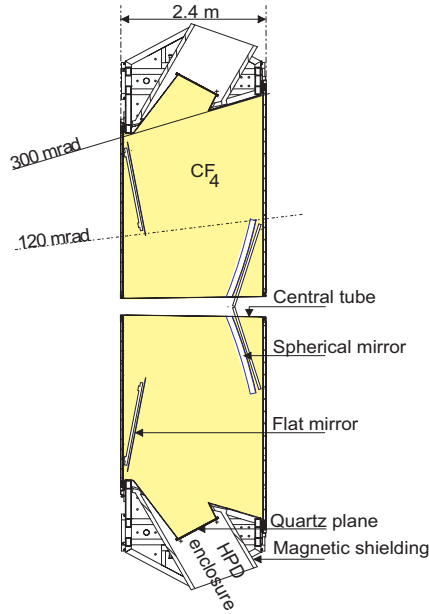


Figure 3.3: Top-down schematic of the RICH2 detector.

material budget are 1 %  $X_0$  and 2.5 %  $X_0$  respectively. As with RICH1, quartz windows with antireflective coating separate the HPDs from the gas enclosure. The magnetic field in the region of the RICH2 HPD planes is complex, with a field strength of more than 15 mT. The magnetic shielding is performed with the use of boxes made from 60 mm thick iron plates. The measured field at the locations of the HPD planes is from 0.2 – 0.6 mT, allowing the HPDs to operate at peak efficiency.

### 3.2.3 Radiators

In order to provide particle identification in the full momentum range 2 – 100 GeV/ $c$ , three radiators are used in the RICH detectors. The aerogel and  $C_4F_{10}$  are housed in RICH1, providing discrimination from 2 – 60 GeV/ $c$ . The  $CF_4$  is housed in RICH2, and provides discrimination from 15 – 100 GeV/ $c$ . Particle discrimination for all common charged particles produced in LHCb collisions is required. The Cherenkov angles against track momentum for electrons, muons, kaons, protons and pions are given in Figure 3.4 for each radiator. The different photon emission angles across the full momentum range allow for discrimination between different charged particle hypotheses.

The range of refractive indices between typical liquids and gases is well covered by  $SiO_2$  aerogel, which has a refractive index which is tuneable between 1.01 – 1.10. Any

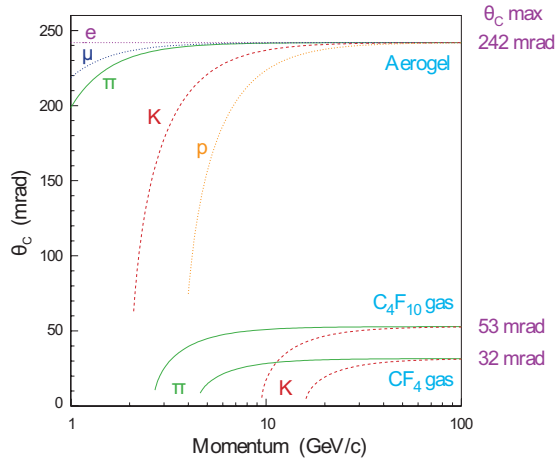


Figure 3.4: Track momentum vs. emitted photon Cherenkov angle for each radiator.

Cherenkov radiator should have minimal scatter of the photons produced by charged particles passing through their volume. Any such scattering would reduce the precision of the reconstructed Cherenkov angle, and degrade the imaging quality available at the HPD plane. The dominant mechanism of scatter at low photon energy is Rayleigh scattering. As such, the transmission of light  $T$  for a given length of radiator  $L$  and photon wavelength  $\lambda$  is well-described by

$$T = Ae^{-CL/\lambda^4} \quad (3.1)$$

where  $A$  is the high-wavelength transmission and  $C$  is the clarity coefficient. High purity aerogel samples with a low clarity coefficient have been developed for the high multiplicity LHC environment [118]. The clarity coefficient of the final aerogel samples used in the RICH1 detector is below  $0.0054 \mu\text{m}^4/\text{cm}$  at  $\lambda = 400 \text{ nm}$ . A 30 mm glass window is placed at the downstream end of the aerogel to absorb photons at higher than 3.5 eV, where the effects of multiple scatter significantly affect the photon resolution.

At this wavelength the refractive index of the material is 1.03. The predicted number of photo-electrons produced in the aerogel and detected at the HPDs is around 6.8. It is measured in data in [119], by calculating the distribution of  $\Delta\theta_C = \theta_C - \theta_0$ , where  $\theta_C$  is the reconstructed Cherenkov angle and  $\theta_0$  is the Cherenkov angle which is calculated using the track momentum and the refractive index of the medium. Taking only those photoelectron hits falling in a ring of width  $\pm 5 \sigma$  of the angular resolution of the system, the photoelectron yields are measured to be  $5.0 \pm 3.0$  in tagged  $D^0 \rightarrow \pi^+ K^-$  decays and  $4.3 \pm 0.9$  in  $pp \rightarrow pp\mu^+\mu^-$  decays, where the dominant errors are from uncertainties in the

fit to the  $\Delta\theta_C$  spectrum and the high background photoelectrons.

The gas radiators were chosen because of the suitability of their refractive indices to providing discrimination in the momentum range of heavy-flavour decays at LHCb, as well as their low chromatic dispersion. The RICH1 is filled with 4 cm<sup>3</sup> of C<sub>4</sub>F<sub>10</sub> gas, the RICH2 is filled with 100 m<sup>3</sup> of CF<sub>4</sub> gas. During operational conditions both are kept at a relative pressure stability of less than 0.5 mbar. The refractive index of a gas as a function of wavelength can be taken from a Sellmeier approximation [120]. For the C<sub>4</sub>F<sub>10</sub> gas at a temperature of 0 °C and a pressure of approximately 1 mbar this is

$$(n - 1) \times 10^6 = \frac{0.25324}{73.2 - \lambda^{-2}} \quad (3.2)$$

and for the CF<sub>4</sub> gas is

$$(n - 1) \times 10^6 = \frac{0.12489}{61.8 - \lambda^{-2}} \quad (3.3)$$

for a wavelength measured in nm. The low chromatic dispersion of the fluorocarbons results in a very low contribution to the angular resolution of the system.

The presence of water and oxygen in the radiator gases are kept below 200 ppm to prevent formation of HF. Nitrogen contamination in the radiators has the effect of altering the refractive indices of the gases and so is kept below 1 %. CO<sub>2</sub> is transparent above 180 nm, and so can be used as a pressure balancing gas without affecting the photon yield significantly. The high price of the fluorocarbons makes a reclamation and purification system vital to the RICH operation, such that nitrogen contamination can be controlled. The gas circulation in RICH1 is run in a closed loop, with inline liquifaction to eliminate volatile impurities and a molecular sieve to eliminate water impurities. In RICH2, the circulation is also run in a closed loop but without liquefaction, using filters to remove water impurities. Full information on the reclamation and purification system may be found in [121].

A Laser Alignment Monitoring System (LAMS) was used to check the stability of the RICH2 mirrors throughout data taking [122]. It has been shown that the mirror stability is affected by small temperature variations, but their effect on the Cherenkov angle reconstruction, of less than 80 mrad, does not affect the RICH performance [123].

### 3.2.4 Hybrid photon detectors

Once photons are produced in the radiators, their positions must be recorded at the detection plane. Any photon detection system used in the RICH must satisfy several

challenging design considerations. The active area of the pixel arrays must be a high proportion of their surface area, to ensure minimal loss of Cherenkov photons. The granularity must be sufficiently high that the spatial resolution of the array is high enough to meet the RICH requirements. In the high luminosity LHCb environment, the detector must be high speed with a timing resolution of 25 ns. These are all accomplished via the use of pixel arrays of hybrid photon detectors (HPDs), which have been designed in collaboration with industry [124].

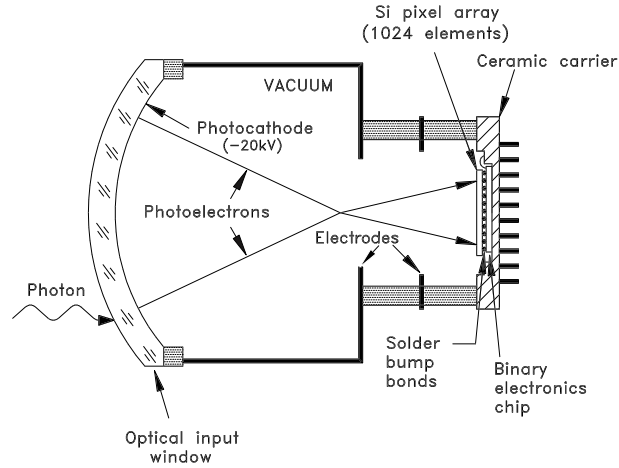


Figure 3.5: A schematic of a pixel HPD from the RICH detector.

A schematic of an HPD pixel is given in Figure 3.5. Incident photons pass into the pixels through a 7 mm thick spherical quartz window, with an inner radius of curvature of 55 mm. A thin multialkali photocathode is coated upon the window’s inner surface. Photoelectrons are released from the photocathode by the incident photons, which are then accelerated through the vacuum tube by a high voltage of approximately 20 kV onto a reverse-biased silicon detector. This produces around 5000 electrons in the silicon per photon, with an energy of 3.6 eV being required to create an electron-hole pair. The silicon detector in each tube has 8192 square of area  $500 \mu\text{m} \times 62.5 \mu\text{m}$ , in a 32 by 256 array, and during operation groups of 8 pixels are logically “ORed” to make a  $32 \times 32$  array of  $500 \mu\text{m} \times 500 \mu\text{m}$  square super-pixels, with no drop in performance compared to reading out all pixels individually. The HPD tubes are very tightly packed, leading to a ratio of active to total area of 64 %, and a total area of around  $3.5 \text{ m}^2$ . 196 tubes are used in the RICH1 and 288 in the RICH2, for a total of 484 HPDs used in the system.

The final quantum efficiency (QE), or ratio of incident photons to converted electrons produced, is maximal in the HPDs at an incident photon wavelength of 270 nm, with an

average QE of approximately 31 %. The dark count due to thermionic electron emission in the photocathode is an important consideration. These have been measured, and are typically below the specification value of 5 kHz. The vacuum quality is also key to the HPD operation. The presence of gas atoms in the HPD chambers can result in the production of ions, which then drift to the photocathode where they release electrons that are detected several hundred nanoseconds after the arrival of the initial Cherenkov photon. The ion feedback rate in the testing stage was measured to be lower than the specification value of 1 %. During operation, outgassing from the detector elements inside the HPD gradually deteriorates the vacuum. When HPDs reach ion feedback levels of 5 %, they are replaced. In Run I more than one hundred HPDs have been replaced for this reason.

### **3.3 RICH reconstruction and PID discriminant estimators**

The job of the reconstruction is to take the information from the RICH detectors and the tracking system and to identify charged hadrons passing through the RICH. A global reconstruction algorithm that simultaneously determines the identities of all charged particles in an event is employed, which culminates in a global likelihood calculation. This algorithm can successfully account for sources of background, and has a running time low enough that it may be practically used online. It is desirable to compare particle hypotheses for each track, such that particles are assigned not just a mass hypothesis but relative strengths for each charged particle hypothesis. These are assigned for each charged track in the event such that the purity of any PID selection can be varied.

#### **3.3.1 Global Cherenkov detector reconstruction**

A typical Cherenkov detector reconstruction algorithm first determines from which track detected photons were emitted. Then, the photons associated with each track are fitted with a ring of width determined by the angular resolution of the photon detector. The Cherenkov angle of the ring is then calculated, and the mass of the original particle may be extracted from this angle and momentum information from a tracking system. The reconstruction of Cherenkov photons and their association with a given track on a track-by-track basis is described as a local approach to the reconstruction problem. The

high number of charged tracks in a typical event, and the presence of backgrounds from Cherenkov photons scattered in the aerogel and from dark counts in the HPDs, make a practical implementation of this approach problematic.

Instead, an approach has been developed to determine the particle hypotheses for each charged track in the event in a global way. Instead of assigning photons to tracks, the problem is abstracted to the HPD detector plane. The charged tracks reconstructed by the tracking system are used as seeds, and the photon yield at the HPD plane may be extrapolated assuming different particle hypotheses. This is then compared to the observed photon yield and a likelihood is calculated. The difference to the global likelihood when individual track hypotheses are altered may be used as a powerful and flexible discriminant for practical physics analysis.

We consider the global event hypothesis  $\vec{h} = (h_1, \dots, h_N)$ . where  $h_j$  is the mass-hypothesis corresponding to track  $j$ . For a given event hypothesis  $\vec{h}$  the expected signal  $v_i(\vec{h})$  in each pixel  $i$  in the HPD plane as

$$v_i(\vec{h}) = \sum_{j=1}^N a_{ij}(h_j) \quad (3.4)$$

where  $a_{ij}(h_j)$  is the expected number of photoelectrons detected from source  $j$  under hypothesis  $h_j$  in pixel  $i$ . The likelihood for the full event is then

$$\mathcal{L}(\vec{h}) = \prod_{i=1}^M \mathcal{P}_{v_i(\vec{h})}(n_i) \quad (3.5)$$

where  $M$  is the total number of pixels in the HPD plane, and  $\mathcal{P}_{v_i(\vec{h})}(n_i)$  is the Poisson probability to observe a signal  $n_i$  when we expect  $v_i(\vec{h})$ , and is expressed as

$$\mathcal{P}_{v_i(\vec{h})}(n_i) = \frac{e^{-v_i(\vec{h})} v_i(\vec{h})^{n_i}}{n_i!}. \quad (3.6)$$

More complete information on the likelihood and the prediction of pixel contents under different hypotheses may be found in [125].

For each track the likelihood of each of the five common charged tracks ( $p$ ,  $K$ ,  $\pi$ ,  $e$ ,  $\mu$ ) must be tested. For  $N$  tracks in an event this results in  $5^N$  permutations of track identities. This exponential growth in possible combinations results in prohibitively long reconstruction times - for 50 charged tracks in an event this results in  $10^{35}$  possible

combinations and likelihood calculations. The reconstruction instead exploits the high abundance of pions in LHCb events relative to any other charged tracks. As such, the starting point for the algorithm is to assume that all charged tracks are pions. Each track in the event then has its mass hypothesis changed to each of the other four common hypotheses, assuming all other tracks in the event are pions. The change in hypothesis in all tracks which results in the biggest increase to the likelihood is made and retained. For all other tracks the process is re-iterated until no increases in likelihood can be made. Consequently, the number of combinations is reduced from  $5^N$  to  $4(N - 1)$ .

The high number of HPD pixels and the high multiplicity of LHCb events results in this algorithm being highly CPU intensive, even with these improvements in speed. In order to increase the speed of the algorithm such that it may be run online, some further optimisations are made to reduce the number of possible combinations while yielding the same final result. After the iteration over all tracks to find the largest increase in likelihood, these are sorted by their largest change in likelihood from the previous iteration. If the first sorted track has a likelihood increase under some rival hypothesis above a tuneable threshold, its identity is changed and the algorithm proceeds to the next iteration. If a track shows a strong preference for any particular likelihood, it is set to that hypothesis and removed from future iterations. These optimisations improve the speed considerably, which makes an implementation in the heavily time-constrained online reconstruction possible.

### 3.3.2 Track PID estimators

Instead of simply assigning the maximum likelihood hypothesis identities to tracks in an event, it is useful to examine the difference in likelihoods when different hypotheses are imposed on the tracks. This allows examination of the relative strengths of rival hypotheses for a given track, and for the application of selections with variable purity. The discriminant between two rival hypotheses  $x$  and  $y$  is given as:

$$DLL(x - y) = \sqrt{2\Delta \ln \mathcal{L}} \quad (3.7)$$

where  $\Delta \ln \mathcal{L}$  is the difference in log-likelihood between the two hypotheses. This discriminant may be used to preferentially select tracks on which the strongest identification hypotheses can be placed, allowing for flexibility of selection purity depending on the needs of any given analysis.

In addition to these discriminants, the development of a neural net enables the DLL information from the RICH detectors to be combined with other information in the detector on the tracks specifically kinematic information from the track and the track quality. These can offer greater discrimination than the DLL information alone. PID selections using DLL information and neural net information have been implemented and published in a wide variety of LHCb results.

## 3.4 Efficiency correction for PID selections

The aforementioned PID discriminants may be used to enhance the purity of selections. It is usually vital in HEP analyses to understand the efficiency of a given selection on a dataset. This is typically performed with the aid of simulation. The response of LHCb's PID estimators is well understood to be poorly modelled. The simulation assumes an average refractive index based on idealised conditions. However, since the refractive indices of the gas radiators depend on environmental conditions such as temperature and pressure, the simulation can never fully account for the variations in reality. Additionally, the simulated LHCb events are typically of lower multiplicity than in real data.

As such, a data-driven method to measure the efficiency of any PID selection is commonly deployed on LHCb. This exploits the use of decays which can be reconstructed with kinematic and displaced vertex information, and without the use of PID discriminants. The method of extracting efficiencies from data is detailed in Section 3.4.1, while information on the decay modes used to perform the efficiency re-weighting are provided in Section 3.4.2.

### 3.4.1 The PIDCalib technique

The variation of the PID response necessitates a data-driven approach to extract efficiencies of PID selections. A centrally maintained software package, `PIDCalib`, is the most commonly utilised tool on LHCb for performing such efficiency calculations. The procedure recognises that the poorly modelled PID response of any given track may be fully characterised by a suite of variables that are well modelled in the LHCb simulation. A track's trajectory through the detector determines which radiators the track traverses. The pseudorapidity in particular is related to the RICH occupancy in that boosted tracks fall in regions of the detector with higher multiplicity regions, where there is a greater incidence of overlapping rings, which add ambiguity to the RICH reconstruction. The track momentum determines in which radiators a given track will emit Cherenkov photons. The

difference in expected Cherenkov angle of emitted photons for different mass hypotheses is varied across the momentum range. Finally, the overall multiplicity of a given event determines the occupancy of the HPDs - more isolated tracks generally lead to greater differences in global likelihood when particle hypotheses are interchanged.

The PIDCalib technique utilises data samples of decays whereby the daughter particles are reconstructed unambiguously without PID information, purely using kinematic and vertex-based selection. Pure samples of each of the five common charged species are attained - these are referred to as the calibration samples. A full suite of kinematic and event variables on which the PID response depends is assembled - this is usually the track's momentum, one of either the track's transverse momentum or its pseudorapidity, and a variable indicative of the RICH occupancy such as the number of reconstructed tracks in the event.

The calibration samples are then split into multidimensional bins in these variables, with a binning schema chosen to be fine enough so that the PID response to any given selection should be approximately uniform across each bin of the schema. We now compare an ensemble of tracks from some signal mode in one bin to the tracks from the corresponding calibration sample falling in the same bin. If the same PID selection is applied to a given track type in the two datasets, the efficiency of the selection should be uniform between the calibration and signal datasets in each particular bin, regardless of the ancestry of the track. For decays involving multiple daughters on which PID selection is placed, we must also take into account the kinematic correlations between the daughter particles.

To do so, we first determine a PID selection to be placed upon a signal mode of interest, and prepare a sample of simulated signal data on which no PID selection has been placed. For each species in the signal decay on which PID selection is placed, we must consult the corresponding calibration datasets for the species. We then bin the calibration dataset in those variables characterising the PID response, and apply the determined PID selection to the calibration dataset to determine efficiencies for each bin. The efficiency in bin  $j$  is then simply

$$\epsilon_j = \frac{k_j}{l_j} \quad (3.8)$$

where  $l_j$  is the total number of calibration tracks in bin  $j$ , and  $k_j$  is the number of calibration tracks in bin  $j$  surviving the selection. For each signal event in the simulation, we then take each daughter track and match its kinematics, along with the event occupancy, to the corresponding calibration efficiency bin. Each daughter track  $t$  from candidate  $i$  is assigned an efficiency  $\epsilon_{t,i}$ . The signal efficiency for candidate  $i$  is then simply the product

of all its daughter track efficiencies:

$$\epsilon_i = \prod_t \epsilon_{t_i}. \quad (3.9)$$

In such a fashion each signal candidate is assigned an efficiency weight. The signal per-mode average efficiency to the PID selection is then simply the mean efficiency of the  $n$  signal candidates:

$$\epsilon_{PID} = \frac{\sum \epsilon_i}{n}. \quad (3.10)$$

Therefore the efficiency of a PID selection can be corrected in a data-driven way which can intrinsically account for kinematic correlations between final state tracks.

### 3.4.2 Calibration datasets

The `PIDCalib` method requires the acquisition of data modes that can be reconstructed unambiguously with the use of kinematic and vertex constraints alone, without utilising PID information. This involves identifying a hadronic decay mode of a particle into charged daughters with a distinct topology. Where ambiguity is introduced by the existence of other topologically identical decays, selections can utilise vetoes on the invariant mass of reconstructed candidates where different hypotheses are enforced on the daughters such that contamination is eliminated. Any remaining combinatoric backgrounds arising due to mis-reconstructions or combinations of unrelated tracks may be subtracted using the `sPlots` method [126]. This is a technique which uses the results of a maximum Likelihood fit to a discriminating variable to extract from a sample containing several species the distributions of the individual species, and is widely used in HEP to efficiency correct selections on an event-by-event basis.

Samples of kaons and pions are attained from decays of  $D^{*+} \rightarrow D^0(K^-\pi^+)\pi_s^+$ , where the slow pion is not recorded as a calibration probe track but instead is used to tag the flavour of the  $D^0$  meson at production. The  $D^0$  daughters are recorded as the calibration probe tracks; the  $D^0$  daughter with the same charge as the slow pion is taken as the pion probe and the daughter with the opposite charge as the slow pion is taken as the probe kaon. To remove any  $D^0$  reflection backgrounds, candidates are vetoed if their mass is within 25 MeV/ $c^2$  of the nominal  $D^0$  mass when reconstructed as a wrong sign  $K^+\pi^-$ , or as  $\pi^+\pi^-$ ,  $K^+K^-$ . This is of course necessary as any PID selection would bias the calibration dataset in obvious ways.

To improve the selection purity with respect to combinatoric backgrounds, further selection is employed. The candidate  $D^0$  must have a transverse momentum greater than 1.5 GeV/ $c$ , and a reconstructed mass within 75 MeV/ $c$  of the nominal. It must also have a vertex  $\chi^2 < 13$  and a flight distance  $\chi^2 > 49$ . The  $IP\chi^2$  w.r.t. the PV, or the improvement to the PV's vertex  $\chi^2$  when the candidate  $D^0$  is excluded, must be less than 30. The cosine of the angle between the  $D^0$  momentum and the displacement vector from the PV to the  $D^0$  must exceed 0.9999. The slow pion must have a momentum less than 150 MeV/ $c$  and a track  $\chi^2$  lower than 5. The  $D^{*+}$  candidate must have a vertex  $\chi^2 < 13$ .

The signal extraction is performed as a simultaneous 2D fit to the reconstructed  $D^0$  mass and the mass difference between the  $D^0$  and the  $D^{*+}$ , called the  $\delta m$ . The  $\delta m$  must be within the range 130 – 155 MeV/ $c^2$ . Both the  $D^0$  mass and  $\delta m$  signal shapes are parameterised by a double Gaussian function constrained such that both means are equal. For the  $D^0$  mass, the combinatoric background component is characterised by a first order polynomial. As can be seen from the mass fit in Figure B.7b, a very high signal purity can be achieved in this decay.

Samples of protons are acquired in the decay  $\Lambda \rightarrow p\pi^-$ . The long  $\Lambda$  lifetime results in a high separation from the primary vertex with a two-body hadronic decay which is easy to reconstruct with high purity. To eliminate contamination from the decay  $K_S^0 \rightarrow \pi^+\pi^-$ , which has a similar lifetime and separation from the primary vertex, candidates which reconstruct within 20 MeV/ $c^2$  of the  $K_S^0$  nominal mass under the  $\pi^-\pi^+$  hypothesis are vetoed.

To further suppress the combinatoric background the  $\Lambda^0$  candidate has several further requirements enforced. The relatively high  $\Lambda^0$  lifetime compared to heavy flavour decays is exploited by requiring the product  $c\tau$  is greater than 5 mm. Its vertex  $\chi^2$  must also be less than 16.

The signal is extracted from a fit to the reconstructed  $\Lambda$  mass. The fit model utilised is a double Gaussian function with a shared mean for the signal with a first order polynomial combinatoric background. An example mass fit from the 2011 data is shown in Figure 3.6b, again demonstrating the high purity of the final selection.

### 3.4.3 RICH performance with calibration datasets

With the calibration datasets, the measurement of the RICH performance in a data-driven way is now possible. The DLL responses of protons, kaons and pions are shown in Figure 3.7 for the 2011 calibration datasets. Strong discrimination between the species of charged

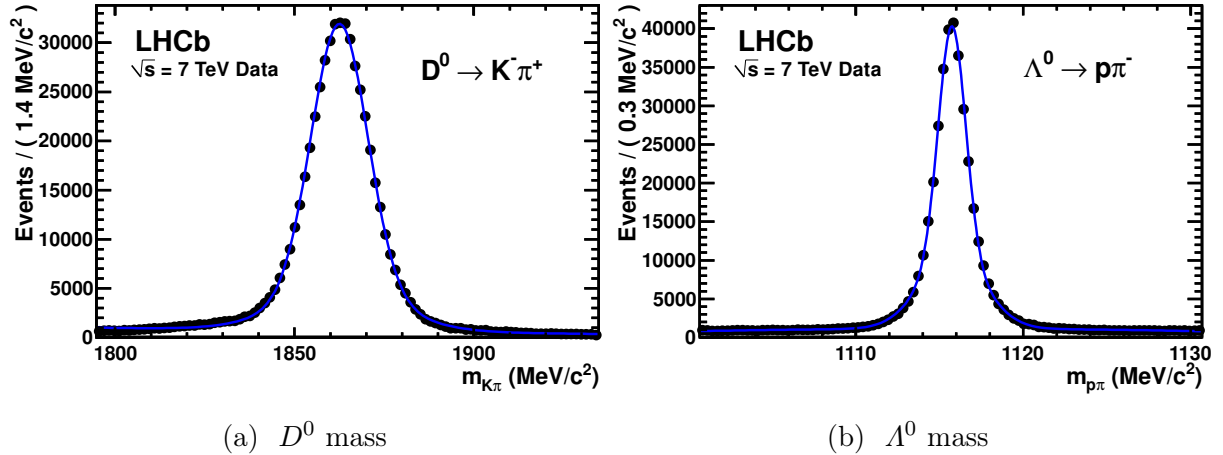


Figure 3.6:  $D^0$  (a) and  $\Lambda^0$  (b) mass fits from 2011 calibration data. Solid blue lines indicate the combined fit from the signal and combinatoric components.

hadrons can be achieved using the PID estimators.

By examining the PID responses of the various purely reconstructed track types we can derive the receiver operating characteristics of the DLL estimators. The kinematics of the calibration samples are of course unique - other signal decays will produce tracks with different kinematics. As such it is more useful and more illustrative of the general LHCb performance to measure the characteristics as a function of momentum. To do so we subdivide samples of two different track types into momentum bins and scan across the appropriate PID estimator which provides discrimination between the two track types. This is demonstrated in Figure 3.8 for the 2012 calibration data, illustrating the achievable separation for pion and kaon tracks as a function of momentum.

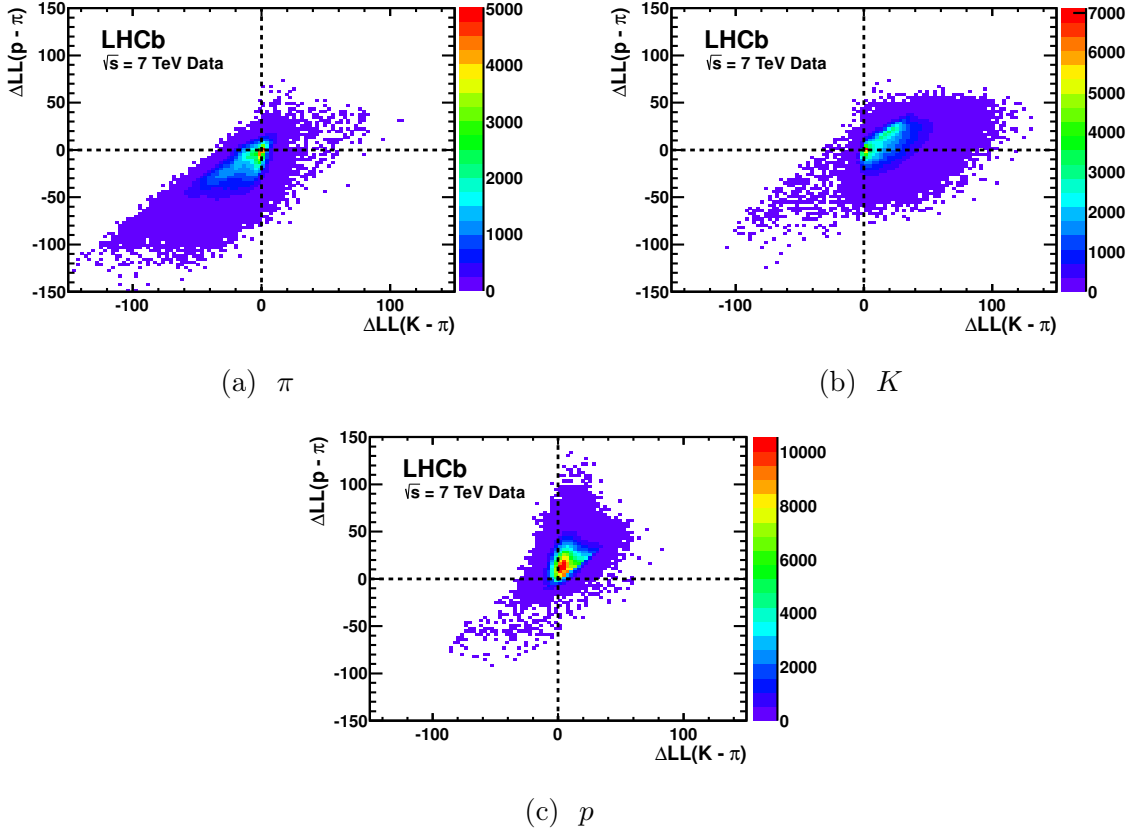


Figure 3.7: DLL responses for pions (a), kaons (b) and protons (c), from the 2011 calibration datasets, demonstrating the strong discriminatory power that the RICH provides.

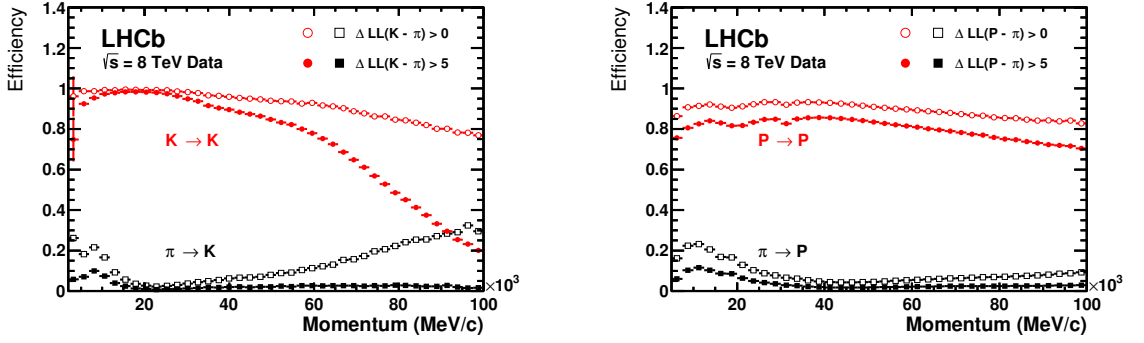


Figure 3.8: The charged hadron identification and misidentification rates as a function of momentum for kaons against pions (left) and protons against pions (right). In each figure the rates are shown for two commonly utilised DLL cuts. The distributions are taken from the calibration datasets for the 2012 data.

## 3.5 Development of heavy flavour proton calibration samples

As outlined in the previous section, pure samples of protons are acquired from the  $\Lambda^0 \rightarrow p\pi^-$  calibration mode to allow for a data-driven efficiency correction for PID selections. The long  $\Lambda^0$  lifetime makes the decay mode a good candidate for selection, as the large separation of the  $\Lambda^0$  decay vertex from the primary interaction allows for a high purity selection, even without the use of PID discrimination. For the `PIDCalib` technique to be utilised, the samples are binned in a suite of variables characterising the PID response to derive local efficiencies in the variable space. This necessitates the calibration sample to have good coverage in these variables with respect to the protons produced in heavy flavour decays. The relatively low mass of the  $\Lambda^0$  compared to the heavy flavour particles of interest to LHCb leads to only partial coverage in these variables of the calibration sample. As such, for a considerable region of the variable space it is impossible to calculate efficiencies for PID selection on protons. In collaboration with others in the LHCb collaboration's PID working group, the candidate developed a new proton calibration sample based on hadronic decays of  $\Lambda_c$  particles. In this section the work performed in developing selections for the datasets is outlined. Work on the signal extraction is given, followed by a series of stability tests performed by the candidate to ratify the new samples.

### 3.5.1 Kinematic coverage of $\Lambda^0 \rightarrow p\pi^-$ calibration samples

The samples of protons acquired from  $\Lambda^0 \rightarrow p\pi^-$  decays have a typically lower momentum and a lower transverse momentum than those originating from decays of heavy-flavour particles. High momentum protons produced from these decays also tend to be produced in the higher pseudorapidity range. This leads to the high momentum, low eta region - corresponding to high  $p_T$ - being largely unpopulated in  $\Lambda^0 \rightarrow p\pi^-$  decays - although this region is often highly populated by protons originating in heavy-flavour decays of interest to LHCb. This makes the efficiency correction for proton tracks falling in this high  $p_T$  region of the variable space impossible utilising just the  $\Lambda^0 \rightarrow p\pi^-$  sample. The proton track kinematics are given in Figure 3.9.

Several workarounds have been implemented when calculating efficiency corrections for proton tracks. The central processing and selection of data at LHCb is referred to as “stripping”. In this procedure, PID selections are very commonly deployed, and the events failing the selection are discarded. In doing so, access to the unbiased PID distributions is

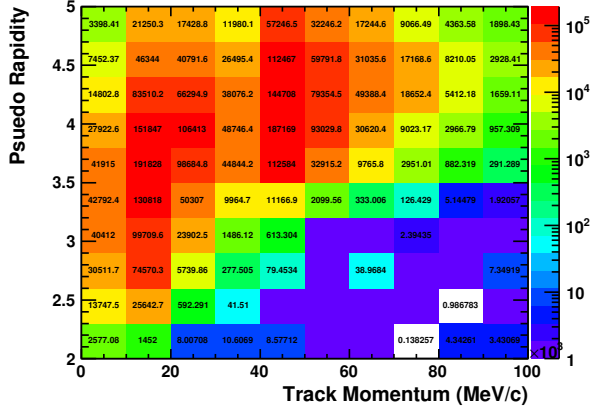


Figure 3.9: The  $p - \eta$  spectrum for proton tracks in the  $\Lambda^0 \rightarrow p\pi^-$  calibration sample. The dataset corresponds to a small fraction of the data gathered in 2012 with the magnet polarity down. The high  $p_T$  region at the bottom right of the plot is not populated by protons from these decays. The signal kinematics have been extracted through use of the  $sPlots$  technique.

lost. This is often necessary to reduce the retention of the selection due to limited storage capacity and bandwidth. If no PID cuts are employed in the stripping selection of a decay mode, PID cuts can then be placed only in regions of the PIDCalib kinematic space in which proton calibration tracks have been acquired. This ensures no signal is lost, but the overall power of the selection to reduce backgrounds is reduced.

If PID cuts are included in the stripping selection for a given decay mode, this is not feasible as the selection has already been uniformly applied to all tracks in the variable space. In such a case, one possible workaround is to veto signal candidates whose protons fall in the region of the variable space not populated by calibration data. The efficiency of the veto, provided the variables in the variable space are well modelled, may be safely evaluated with the use of simulation. This has the very unfortunate effect of reducing the signal statistics.

In analysis of rare or hitherto unobserved decays, it is also possible to impose very large kinematic bins at the boundary of the variable space which is populated by calibration data. This results in an efficiency being attainable due to the presence of calibration data in all bins in the schema, but leads to the potential for biases in the efficiency correction, as the efficiencies in the large bins at the kinematic fringes of the calibration dataset are likely to have large variations in PID response over the bin - in samples with different proton kinematics from the calibration sample the average PID efficiency can be significantly different in such large bins. As such, the systematic uncertainty of the efficiency correction

increases accordingly.

### 3.5.2 A heavy flavour proton calibration sample

The described workarounds to the poor kinematic coverage of the calibration sample either result in higher backgrounds, lower signal statistics or higher systematic uncertainties on the efficiency correction. As such, it was highly desirable to find a new decay mode with a proton in the final state which could be cleanly reconstructed without the use of PID, but could also populate the higher momentum regions the existing  $\Lambda^0 \rightarrow p\pi^-$  sample could not.

This raises the question of which heavy flavour decays can be exploited in this fashion. The desirable traits of such a mode are:

- That it be possible to select the mode in abundance. The efficiency calculation involves binning the sample in up to three dimensions, with a sufficient granularity to account for the variation in efficiency in the variable space. Consequently, high statistics of calibration tracks are desirable.
- That it be possible to select the mode with a high purity. The extraction of the signal should be pure, as any contamination from other species of charged tracks in the final sample will bias the PID response distributions. This is especially of concern given the inability to utilise the information from the RICH detector on the proton probe track.
- That the kinematics of the decay are such that the proton is produced over a wide range of the variable spaces used in PIDCalib. Given the limitations of the  $\Lambda^0 \rightarrow p\pi^-$  sample, it is desirable that the proton kinematics should populate the high momentum, low pseudorapidity region which is unpopulated by the existing calibration protons.

No decays of the  $\Lambda_b^0$  with a direct proton daughter have been measured to have branching fractions higher than  $10^{-3}$  [10]. The most common direct  $\Lambda_b^0$  decays to protons are via the decays  $\Lambda_b^0 \rightarrow pK^-$  and  $\Lambda_b^0 \rightarrow p\pi^-$ . These have been measured at CDF [127] and LHCb [128] to have branching fractions of the order  $10^{-6}$ . The high abundance of a large range of other  $B \rightarrow h^+h'^-$  decays which are kinematically indistinguishable presents difficulties in preventing contamination from other charged species. Without the use of PID discriminants, the only way to ensure that peaking backgrounds from other  $B \rightarrow h^+h'^-$

decays are eliminated is to place vetoes on the  $B$  candidate mass when reconstructed under rival particle hypotheses - a measure which lowers the signal efficiency considerably.

Unlike the  $\Lambda_b^0$ , the  $\Lambda_c$  decays to final states with protons in channels which have high measured branching fractions. The Cabibbo-favoured decay  $\Lambda_c^+ \rightarrow pK^-\pi^+$  has a measured branching fraction of approximately 5 % [129]. Additionally, the  $\Lambda_c$  is produced copiously in LHCb interactions, with a measured cross section at  $\sqrt{s} = 7$  TeV of approximately 233  $\mu\text{b}$  [130]. While the mode is abundant, the short  $\Lambda_c$  lifetime (with a PDG average of 200 ps [10]) relative to that of the  $\Lambda^0$  and  $D^0$  presents some difficulty in developing a pure selection. A further concern is that the decay is topologically identical to decays of the form  $D \rightarrow hhh$ , which necessitates the use of vetoes on the candidate mass when reconstructed under rival daughter mass hypotheses to ensure an uncontaminated selection.

The low separation of promptly-produced  $\Lambda_c$  decay vertices from the primary interaction results in a very high combinatoric background from pairings of unrelated tracks. This background is considerably reduced when instead of reconstructing promptly-produced  $\Lambda_c$ , the decay  $\Lambda_b^0 \rightarrow \Lambda_c^+(pK^-\pi^+)\mu^-\bar{\nu}_\mu$  is reconstructed. Unlike direct  $\Lambda_b^0$  decays to protons, this decay has a high branching fraction of approximately 10 % [10]. The  $\Lambda_b^0$  lifetime is considerably higher than that of the  $\Lambda_c$ , with a PDG averaged lifetime of approximately 1.45 ps [10] (of which the most accurate contribution to said average is an LHCb measurement [131]). As such, the  $\Lambda_c$  decay vertex is at a considerably larger distance on average from the primary interaction than in those  $\Lambda_c$  that are produced promptly, and the combinatorics are lower. While the neutrino is not reconstructed, leading to a non-peaking  $\Lambda_b^0$  mass, the bachelor muon in the  $\Lambda_b^0$  decay can fire the muon-based triggers, which operate with a high efficiency relative to the triggering of purely hadronic modes.

As such, it was decided to reconstruct both prompt  $\Lambda_c^+ \rightarrow pK^-\pi^+$  decays and  $\Lambda_b^0 \rightarrow \Lambda_c^+(pK^-\pi^+)\mu^-\bar{\nu}_\mu$  decays, with selections that utilise no PID information on the protons in the decays, to produce new PID calibration samples.

### 3.5.3 Triggering and stripping of $\Lambda_c$ decays

In this selection the stripping selections developed by collaborators are given. The trigger requirements that must be placed on the datasets to ensure an unbiased selection with respect to the proton PID are also detailed.

### Inclusive $\Lambda_c^+ \rightarrow pK^-\pi^+$

The prompt selection reconstructs the pattern  $\Lambda_c^+ \rightarrow pK^-\pi^+$ , which will reconstruct  $\Lambda_c$  decays from prompt and secondary decays. The stripping selection requires the momentum of all  $\Lambda_c$  daughters to exceed 2 GeV/c, with a transverse momentum of greater than 250 MeV/c. All daughters must also have an  $IP\chi^2$  with respect to the primary vertex of greater than 8. The reconstructed  $\Lambda_c$  must have a transverse momentum greater than 1 GeV/c and satisfy certain vertex quality cuts based on the greatest distance of closest approach between the  $\Lambda_c$  daughter tracks and the vertex  $\chi^2$ . If the proton mass hypothesis in the decay is changed to a pion, the reconstructed mass must fall outside of the range 1800 – 1890 MeV/c<sup>2</sup> to suppress  $D^+$  and  $D^0$  contamination.

To ensure an unbiased selection of protons, certain triggering requirements are enforced on the decays. The  $\Lambda_c$  decay itself must have fired triggers that cannot have placed PID requirements on the proton. At HLT2 the  $\Lambda_c$  candidate must have fired a trigger line dedicated to reconstructing three-body hadronic decays of charm.

$$\Lambda_b^0 \rightarrow \Lambda_c^+(pK^-\pi^+)\mu^-\bar{\nu}_\mu$$

The stripping line to select this mode accepts only those events with fewer than 250 reconstructed long tracks in the event. All  $\Lambda_c$  daughters must have a transverse momentum exceeding 300 MeV/c. The daughter kaon must have a  $\log(\mathcal{L}_K/\mathcal{L}_\pi)$  greater than 8 while the daughter pion must have a  $\log(\mathcal{L}_K/\mathcal{L}_\pi)$  less than -2. The reconstructed  $\Lambda_c$  candidate must have a transverse momentum exceeding 2 GeV/c and have a reconstructed mass within 80 MeV/c<sup>2</sup> of the nominal. The  $\Lambda_c$  vertex must have a reduced vertex  $\chi^2$  of less than 3. The  $\Lambda_c$ 's flight distance  $\chi^2$  must exceed 20. The angle between the momentum vector of the reconstructed  $\Lambda_c$  and the displacement vector of the  $\Lambda_c$  to the primary vertex should have a cosine greater than 0.99. The bachelor muon must have a transverse momentum greater than 1 GeV/c and a  $\log(\mathcal{L}_\mu/\mathcal{L}_\pi)$  greater than 0. The reconstructed  $\Lambda_b^0$  must fall in a wide mass window of 3 – 5 GeV/c to account for the unreconstructed neutrino. The  $\Lambda_b^0$  vertex must have a reduced vertex  $\chi^2$  lower than 3. The angle between the  $\Lambda_b^0$  momentum vector and the displacement vector between the  $\Lambda_b^0$  and the primary vertex must have a cosine greater than 0.999. The distance along the beamline between the  $\Lambda_b^0$  and  $\Lambda_c$  decay vertices must exceed 0.5 mm.

The  $\Lambda_b^0$  decay must either be selected by a trigger selection that is known to place no PID on the proton. To this end the  $\Lambda_b^0$  candidate must be selected by an algorithm in the high level trigger exploiting the topology of the decays and the presence of a muon in the

decay.

### 3.5.4 Considerations in developing $\Lambda_c$ selections

The reconstructed  $\Lambda_c$  mass spectra for the PID stripping output for the magnet-down data gathered in 2012 after the trigger selections are given in Figure 3.10. While  $\Lambda_c$  peaks

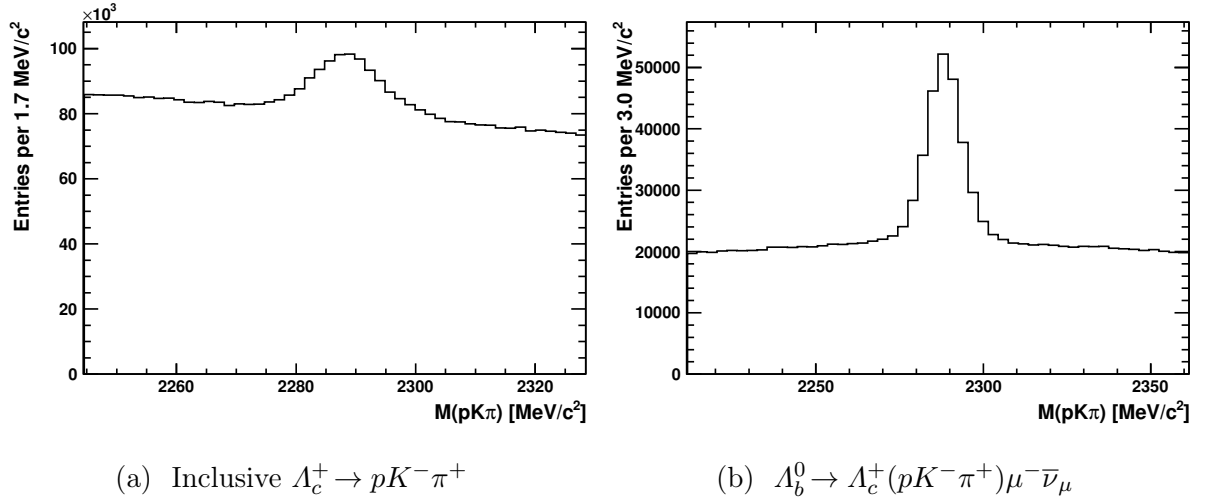


Figure 3.10: The mass spectra for the  $\Lambda_c^+$  calibration modes after the stripping selection. The data presented here corresponds to the full dataset gathered in 2012 with the magnet-down polarity.

are clearly visible, the presence of a high combinatoric and the indistinguishability of  $\Lambda_c^+ \rightarrow pK^- \pi^+$  decays from  $D \rightarrow hhh$  decays present challenges in deriving a pure selection. The aim of the candidate's work was to further develop the existing selections put in place by others to create samples that could be reliably be used by physics analyses as part of the PIDCalib package to calculate PID selection efficiencies on protons. Several key considerations were taken into account when developing selections:

1. The PIDCalib technique entails fitting the candidate mass distribution to extract signal weights with the *sPlot* method once, before PID cuts. The PID cuts are then enforced and the sum of weights before and after cuts are used to derive selection efficiencies. The validity of signal weights derived with *sPlot* is only retained after some selection if the selection applies to each species uniformly in the discriminating variable. In this case, the validity of the weights is only retained after the PID selection if said selection applies uniformly in the  $\Lambda_c$  mass to each individual species.

For simplicity, the fit model for the  $\Lambda_c$  mass should have only components for the signal and a component for the combinatoric. The presence of any “reflection” backgrounds from misidentified protons will result in preferential sculpting of the  $\Lambda_c$  mass in regions where the reflections manifest, invalidating the signal weights. As such the elimination of any backgrounds originating from proton misidentifications is vital.

2. The overall motivation behind creating heavy flavour samples of proton calibration data was to enable the derivation of PID efficiencies in the kinematic space not covered by the extant  $\Lambda^0 \rightarrow p\pi^-$  sample. As such, any selection should endeavour to preserve the high momentum protons preferentially.
3. The combinatoric backgrounds in  $\Lambda_c$  decays are much higher than those in  $D^{*+} \rightarrow D^0(K^-\pi^+)\pi_s^+$  or  $\Lambda^0 \rightarrow p\pi^-$  decays. To control the statistical uncertainties arising from the  $\Lambda_c$  mass fit attempts should be made to improve the signal purity over the stripping output.

### 3.5.5 Eliminating $D \rightarrow hhh$ misreconstructions

The proton mass hypothesis is varied to probe for reflections from the topologically indistinguishable  $D \rightarrow hhh$  decays. The most obvious to eliminate are the decays  $D^+ \rightarrow K^+K^-\pi^+$  and  $D^+ \rightarrow \pi^+K^-\pi^+$  (and the  $D_s^+$  equivalent decays), whereby only a mis-identification of the proton is necessary to be reconstructed in the  $\Lambda_c^+ \rightarrow pK^-\pi^+$  spectrum. The cross sections of the  $D^+$  and  $D_s^+$  at LHCb have been measured to be  $(676 \pm 137)$   $\mu\text{b}$  and  $(194 \pm 38)$   $\mu\text{b}$  respectively [130], compared to 233  $\mu\text{b}$  for the  $\Lambda_c$ . The branching fractions for the  $D \rightarrow hhh$  decays are provided in Table 3.1. From the high branching fractions and high production cross sections we expect all listed decays to be copiously produced at LHCb.

Mode	$\mathcal{B}$ [%]
$D^+ \rightarrow K^+K^-\pi^+$	$9.13 \pm 0.19$
$D^+ \rightarrow \pi^+K^-\pi^+$	$9.54 \pm 0.26$
$D^{*+} \rightarrow D^0\pi^+$	$67.7 \pm 0.5$
$D^0 \rightarrow K^-\pi^+$	$3.88 \pm 0.05$

Table 3.1: The branching fractions for the  $D$  decays relevant to the suppression of reflection backgrounds.

To investigate the presence of  $D$  reflections we calculate the candidate mass when the mass hypothesis of the proton is changed to either a kaon or pion. The mass distributions of the candidate mass in these cases for the raw stripping output of  $\Lambda_b^0 \rightarrow \Lambda_c^+(pK^-\pi^+)\mu^-\bar{\nu}_\mu$  are given in Figure 3.11. Large peaks from the decays  $D^+ \rightarrow K^+K^-\pi^+$  and  $D^+ \rightarrow \pi^+K^-\pi^+$  are observed. Centred at 2010 MeV/ $c^2$  in the  $M(\pi\pi K)$  spectrum a smaller peak corresponding to  $D^{*+} \rightarrow D^0(\pi^+K^-\pi^+$ , where the intermediate  $D^0$  decays with a short lifetime such that the  $K^-$  and  $\pi^+$  from the  $D^0$  decay form a common vertex with the bachelor  $\pi^+$ , can be observed. While not sharply peaking in the  $\Lambda_c^+ \rightarrow pK^-\pi^+$  candidate mass, they are a large component of the combinatoric background. If the response of the combinatoric background to PID cuts differs from that of the reflection background, their inclusion in any fit will result in the loss of weight normalisation when PID cuts are applied to the sample.

To prevent this contamination vetoes are placed on candidates when reconstructed under rival mass hypotheses. The  $M(KK\pi)$  must not be between 1860 MeV/ $c^2$  and 1890 MeV/ $c^2$  to exclude  $D^+ \rightarrow K^+K^-\pi^+$  decays. The  $M(\pi K\pi)$  must not be between 1800 MeV/ $c^2$  and 1900 MeV/ $c^2$  to exclude  $D^+ \rightarrow \pi^+K^-\pi^+$  decays. We also impose that the  $M(\pi K\pi)$  must be greater than 2025 MeV/ $c^2$  or lower than 1990 MeV/ $c^2$  to exclude reconstructions of  $D^{*+} \rightarrow D^0(\pi^+K^-\pi^+$ . The vetoed regions are shown in Figure 3.11. It should be noted that the broad structures in the  $M(KK\pi)$  spectrum in the high mass region are dominated by the reflections of  $D^+ \rightarrow \pi^+K^-\pi^+$  and  $D^{*+} \rightarrow D^0(\pi^+K^-\pi^+$ , and once the  $M(\pi K\pi)$  vetoes are applied they are no longer present.

### 3.5.6 Resonant characteristics of $\Lambda_c^+ \rightarrow phh'$ decays

In accordance with the helicity formalism described in [86] the resonant structure of  $\Lambda_c^+ \rightarrow phh'$  decays can be parameterised by 5 variables, shown in Figure 3.12<sup>1</sup>. These variables are:

$M(ph_1)(h_1h_2)$  - The invariant mass of the proton and opposite sign meson, and the invariant mass of the meson pair. Decays through intermediate resonances (such as  $K^*$ ,  $\Lambda(1520)$ ,  $\phi$ ,  $f^0(980)$  etc.) will result in local enhancements in these quantities not present in a phase-space generated distribution.

---

<sup>1</sup>We note the caption from the original paper contains an error in the definition of  $\phi_{h_1h_2}$ . This is defined by the angle between the plane containing the meson daughter momenta, and the plane containing the  $p$  momentum and the  $\Lambda_c^+$  polarisation vector, not the plane containing the  $p$  momentum and the x-axis.

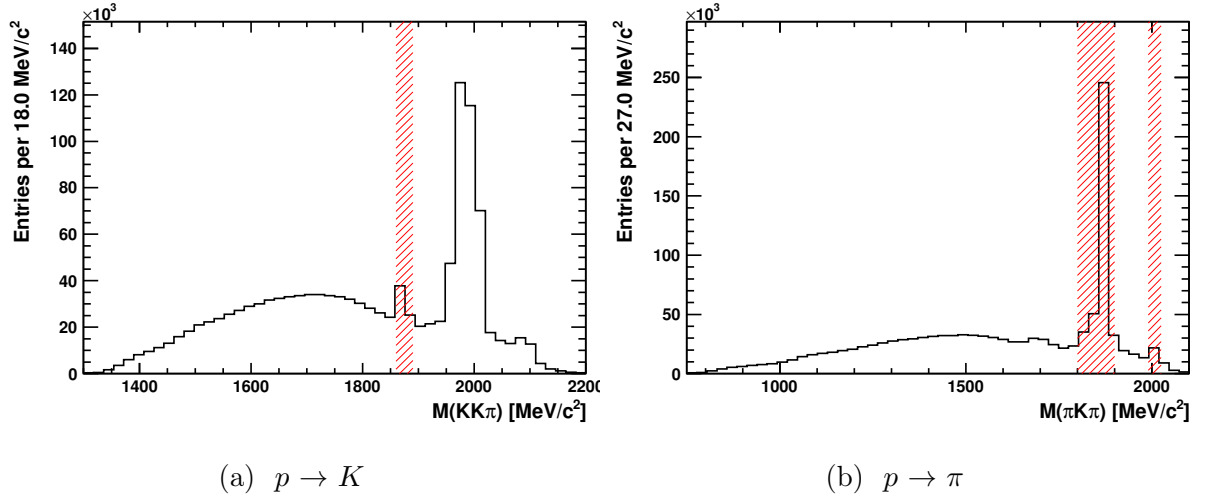


Figure 3.11: The mass spectra for the  $\Lambda_c^+$  candidates in the  $\Lambda_b^0 \rightarrow \Lambda_c^+(pK^-\pi^+)\mu^-\bar{\nu}_\mu$  stripping output when the proton is reconstructed as a kaon or pion. The data presented here corresponds to the full dataset gathered in 2012 with the magnet-down polarity. The shaded areas illustrate the vetoed regions where the  $KK\pi$  background (left) and the  $\pi\pi K$  backgrounds (right) may be found.

$\cos \theta_p$  - In the  $\Lambda_c$  rest frame, the angle between the proton momentum vector and the polarisation axis of the  $\Lambda_c$ .

$\cos \phi_p$  - In the  $\Lambda_c$  rest frame, the angle between the component of proton momentum perpendicular to the  $\Lambda_c$  polarisation and the direction of the lab frame  $\Lambda_c$  momentum vector.

$\phi_{h_1 h_2}$  - In the  $\Lambda_c$  rest frame, the angle between the plane containing the proton momentum vector and the  $\Lambda_c$  polarisation vector, and the plane containing the two meson momentum vectors.

The  $\Lambda_c$  in  $p - p$  collisions [132] is predicted to be polarised.  $\Lambda_c$  produced in target experiments with a  $\pi$  beam have demonstrated increasingly negative polarisation of the  $\Lambda_c$  with increasing transverse momentum [83]. If the production at LHCb is indeed highly polarized, sping of the  $\Lambda_c$  and the  $p$  in the decay should mean that these variables can be of use in isolating signal from the unpolarised combinatoric background.

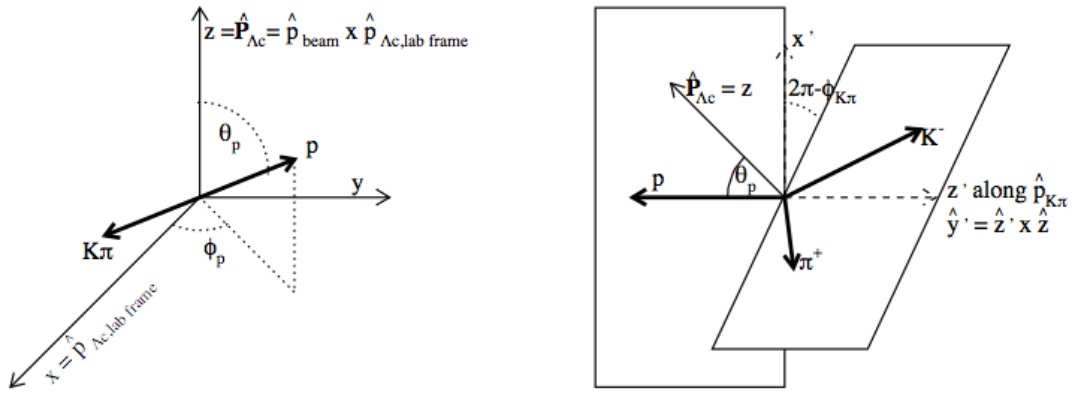


Figure 3.12: The angular variables characterising the  $\Lambda_c$  resonance structure. From [86].

### 3.5.7 Selection Optimisation

A study was performed to further optimise the selection of  $\Lambda_c$  candidates with respect to combinatoric background. Some moderate PID cuts are first placed on the kaon and pion in the  $\Lambda_c$  decay to ensure that contributions from other misidentifications are suppressed, such that the only species in the  $\Lambda_c$  mass spectrum are the combinatoric background and the  $\Lambda_c$  signal. These PID cuts are  $\log(\mathcal{L}_K/\mathcal{L}_\pi) > 5$  for the kaon and  $\log(\mathcal{L}_K/\mathcal{L}_\pi) < -5$  for the pion.

The  $\Lambda_c$  mass distributions for varying stages of the selection are shown in Figure 3.13. These include the raw mass distributions from the stripping output, the mass distributions after application of the trigger selection and  $D$  reflection vetoes, and the full training suite of cuts.

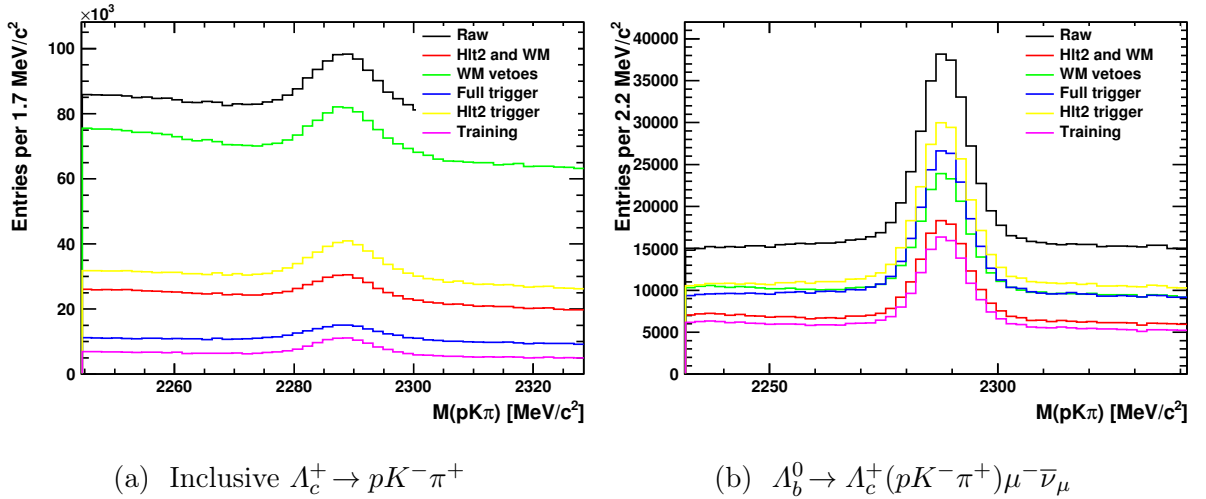


Figure 3.13: The mass spectra for the  $\Lambda_c$  candidates in each of the calibration modes for each stage of selection.

#### Optimisation procedure

The goals of the procedure were to improve the purity of the selection by removing combinatoric backgrounds, while minimising the uncertainty on the signal yield. Any selection developed must endeavour to preserve as many of the high-momentum protons in the sample as possible.

Fits were generated to the  $\Lambda_c$  mass spectra of the four calibration modes. The datasets used corresponded to 20 % of the magnet down data. In all cases the signal is parameterised

by two Gaussian functions with their means constrained to be equal and both widths allowed to vary. The combinatoric background in all cases is parameterised by a natural exponential function with the exponent allowed to vary. An unbinned extended maximum Likelihood fit was performed to the spectrum to extract a set of signal weights using the *sPlots* technique. The fit models are shown in Figure 3.14.

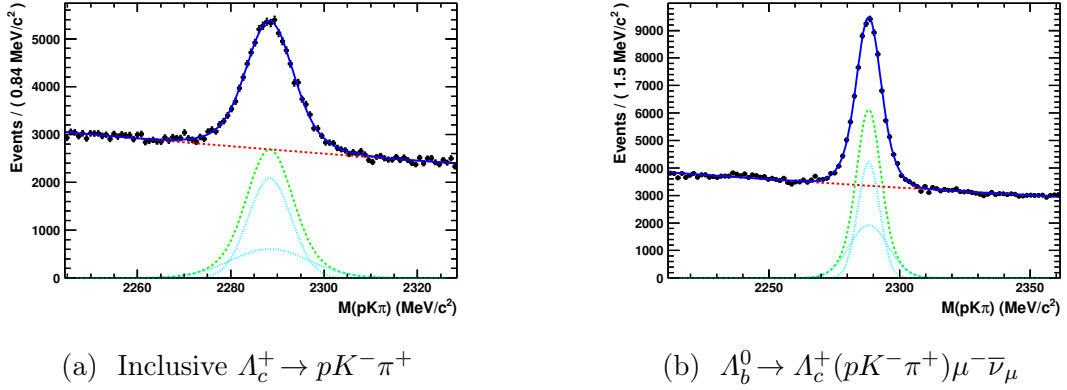


Figure 3.14: The mass fits for the  $\Lambda_c$  calibration data used in the selection optimisation. The data presented here corresponds to one fifth of the dataset gathered in 2012 with the magnet-down polarity. Solid blue is the total Probability Density Function (PDF), dotted cyan are the individual signal Gaussians, dashed green is the combined signal PDF, dashed red is the combinatoric background.

The signal weights were used to disentangle the kinematic and event distributions for the signal and combinatoric components for a variety of variables. Examination of these distributions enables the identification of variables that may be used to discriminate between signal and combinatoric background.

Variables for which the distributions differ were included in a recursive selection optimisation algorithm developed by Conor Fitzpatrick. The algorithm uses the figure of merit for the significance  $\sigma$

$$\sigma = \frac{S}{\sqrt{S+B}} \quad (3.11)$$

where  $S$  is the sum of the signal weights and  $B$  is the sum of the background weights. For each specified variable a valid range and a step size is set. The algorithm then performs an optimisation for each variable individually, finding the optimum cut and using this as a seed value for the recursive optimisation. The cuts are ordered by the sum of the fractional signal efficiency and fractional background rejection to identify the most powerful discriminants. The cuts are then re-optimised together, using the seed values found in the

previous step. The cuts are then individually scanned over in the designated order, with the cut order and the signal significance recorded. This reoptimisation is then repeated an arbitrary number of times until the cut order and signal significance converge. At this point a local maximum in signal significance has been achieved. A cross check is employed to check for other maxima in the cutspace by altering the order in which the cuts are employed, but in all cases the local maxima found proved to be the global maxima.

### Optimisation results

The investigations of the signal and background distributions of the kinematics and event variables were used to inform which should be used in the recursive optimisation procedure. The resonant variable  $\cos \phi_p$  was found to display excellent separation power between signal and background. In the signal, the proton is produced with a momentum in the  $\Lambda_c$  rest frame which is preferentially parallel or anti-parallel with the direction of  $\Lambda_c$  travel in the lab frame. For the combinatoric background, the particle reconstructed as the proton has a very strong preference for a momentum in the  $\Lambda_c$  rest frame which is antiparallel with the  $\Lambda_c$  direction of travel in the lab frame. The signal and background distributions for  $\cos \phi_p$  in the  $\Lambda_b^0 \rightarrow \Lambda_c^+(pK^-\pi^+)\mu^-\bar{\nu}_\mu$  training sample are provided in Figure 3.15. By placing a minimum cut on this variable the purity of the sample may be enhanced significantly.

The final training results for those variables found to have strong discriminatory power are provided in Table 3.2. We note that some variables which have discriminatory power in one mode did not display such discrimination between the signal and background species in other decay modes. This is attributable to the markedly different selections placed on the samples at the stripping and HLT2 level.

Cut	Incl. $\Lambda_c^+ \rightarrow pK^-\pi^+$	$\Lambda_b^0 \rightarrow \Lambda_c^+(pK^-\pi^+)\mu^-\bar{\nu}_\mu$
$\min \cos \phi_p$	-0.3	-0.45
$\min  \cos \theta_p $	-	0.1
$\min m(pK)$	1.7 GeV/c <sup>2</sup>	-
$\min M(K\pi)$	-	0.8 GeV/c <sup>2</sup>
$\max \log(\Lambda_c IP\chi^2)$	8	-

Table 3.2: The optimum cuts placed on the samples as found in the selection optimisation procedure to optimise the signal significance.

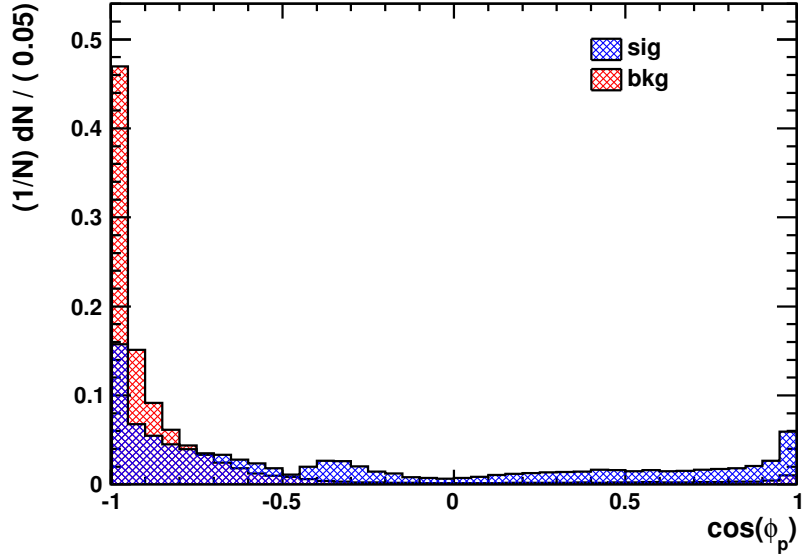


Figure 3.15: The distributions for the signal and combinatoric background of the resonant variable  $\cos \phi_p$  in the  $\Lambda_b^0 \rightarrow \Lambda_c^+(pK^-\pi^+)\mu^-\bar{\nu}_\mu$  training sample. Strong discrimination is afforded between the signal and combinatoric.

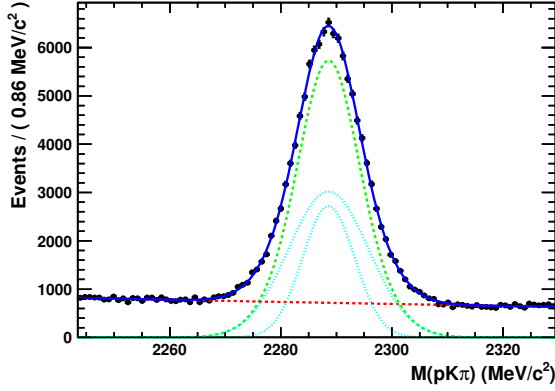
### 3.5.8 Final data sample

#### Final $\Lambda_c$ mass fits

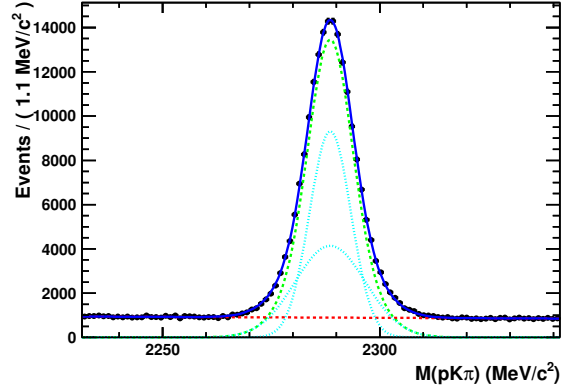
The fit model used is the same as for the training samples. All parameters in the fit are permitted to vary. The fits to the  $\Lambda_c$  mass spectrum after the final selections are given in Figure 3.16. The signal yields, selection purities and the candidate efficiency with respect to the training samples are given in Table 3.3.

Mode	Polarity	Polarity $N_{\text{sig}}$	Total $N_{\text{sig}}$	Purity	$\epsilon_{\text{final training}}$
Inclusive $\Lambda_c^+ \rightarrow pK^-\pi^+$	MagDown	$100521 \pm 433$	$196400 \pm 600$	80 %	34 %
	MagUp	$95879 \pm 415$			
$\Lambda_b^0 \rightarrow \Lambda_c^+(pK^-\pi^+)\mu^-\bar{\nu}_\mu$	MagDown	$177576 \pm 517$	$338002 \pm 716$	88 %	54 %
	MagUp	$160426 \pm 495$			

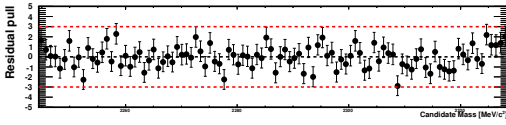
Table 3.3: The final signal yields ( $N_{\text{sig}}$ ) for each mode by polarity, with the combined signal yield for each mode. The signal efficiency,  $\epsilon_{\text{final|training}}$ , of the selection with respect to the training sample is also provided. The purity is defined as  $\frac{S}{S+B}$ , where  $S$  and  $B$  are the signal and background yields respectively within a 30 MeV/ $c^2$  window centred on the nominal  $\Lambda_c$  mass.



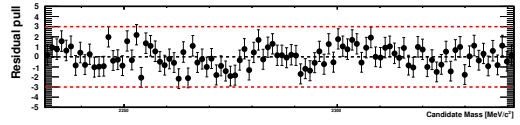
(a) Inclusive  $\Lambda_c^+ \rightarrow pK^-\pi^+$  mass fit



(b)  $\Lambda_b^0 \rightarrow \Lambda_c^+(pK^-\pi^+)\mu^-\bar{\nu}_\mu$  mass fit



(c) Inclusive  $\Lambda_c^+ \rightarrow pK^-\pi^+$  residual pull

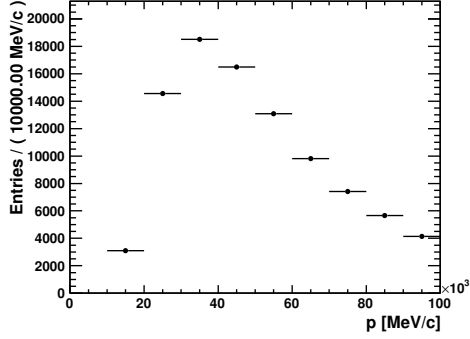


(d)  $\Lambda_b^0 \rightarrow \Lambda_c^+(pK^-\pi^+)\mu^-\bar{\nu}_\mu$  residual pull

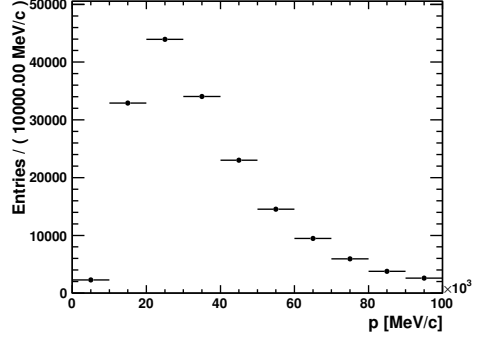
Figure 3.16: The mass fits for the  $\Lambda_c$  calibration data after the final selection. The datasets correspond to the full dataset in 2012 gathered with the magnet polarity down. Solid blue is the total PDF, dotted cyan are the individual signal Gaussians, dashed green is the combined signal PDF, dashed red is the combinatoric background.

## Proton kinematics

The final distributions for the proton kinematics are provided herein. Again we use the full dataset taken in 2012 with the magnet polarity down. The momentum distributions are given in Figure 3.17, the transverse momentum distributions provided in Figure 3.18 and the 2D distributions of momentum and pseudo-rapidity given in Figure 3.19. In all cases, the coverage in the high  $p_T$  region is vastly improved compared to the  $\Lambda^0 \rightarrow p\pi^-$  calibration samples. This enables for the first time a data-driven PID correction for protons in the high  $p_T$  region.

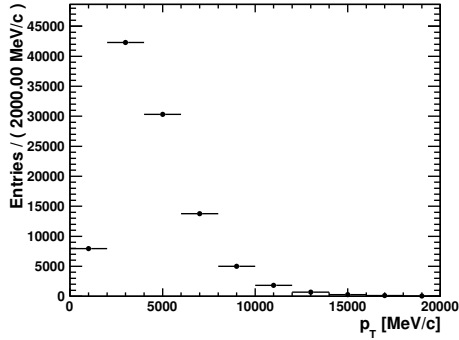


(a) Inclusive  $\Lambda_c^+ \rightarrow p K^- \pi^+ p$

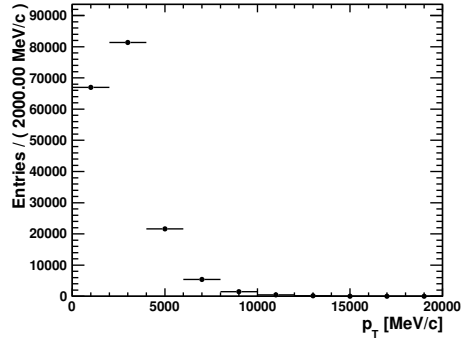


(b)  $\Lambda_b^0 \rightarrow \Lambda_c^+ (p K^- \pi^+) \mu^- \bar{\nu}_\mu p$

Figure 3.17: The proton momentum distributions in the final calibration samples. The dataset corresponds to the full data taken in 2012 with the magnet polarity down.

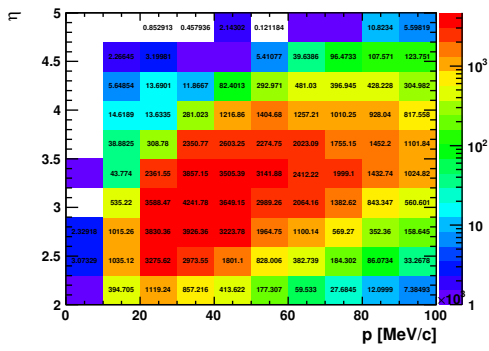


(a) Inclusive  $\Lambda_c^+ \rightarrow p K^- \pi^+ p_T$

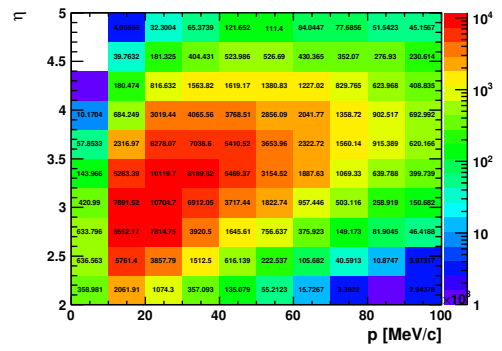


(b)  $\Lambda_b^0 \rightarrow \Lambda_c^+ (p K^- \pi^+) \mu^- \bar{\nu}_\mu p_T$

Figure 3.18: The proton transverse momentum distributions in the final calibration samples. The dataset corresponds to the full data taken in 2012 with the magnet polarity down.



(a) Inclusive  $\Lambda_c^+ \rightarrow pK^-\pi^+ p - \eta$



(b)  $\Lambda_b^0 \rightarrow \Lambda_c^+(pK^-\pi^+)\mu^-\bar{\nu}_\mu p - \eta$

Figure 3.19: The proton  $p - \eta$  distributions in the final calibration samples. The dataset corresponds to the full data taken in 2012 with the magnet polarity down.

## PID discriminant distributions

The sideband-subtracted  $\log(\mathcal{L}_p/\mathcal{L}_\pi)$  and  $\log(\mathcal{L}_p/\mathcal{L}_K)$  distributions are provided in Figure 3.20 for the inclusive  $\Lambda_c^+ \rightarrow pK^-\pi^+$  sample and in Figure 3.21 for the  $\Lambda_b^0 \rightarrow \Lambda_c^+(pK^-\pi^+)\mu^-\bar{\nu}_\mu$  sample (in both cases the distributions shown are from the data gathered with the magnet polarity down). We note that due to kinematic differences in the proton tracks the distributions are not expected to be compatible between the samples.

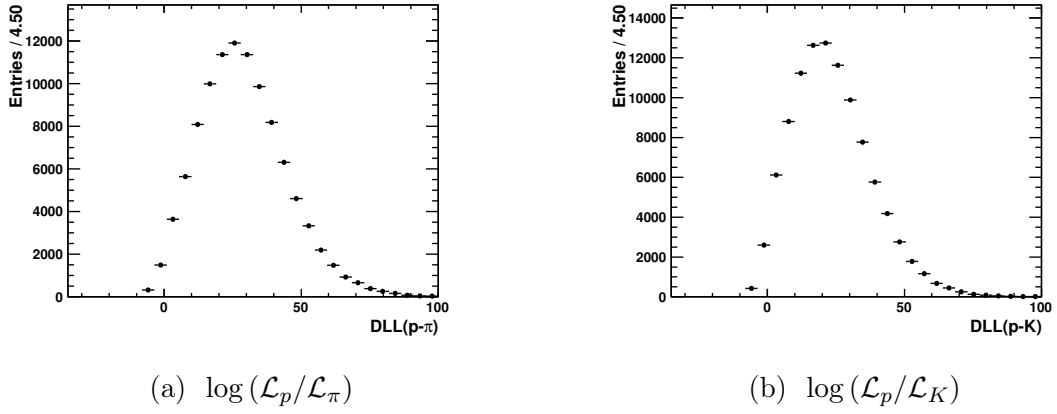


Figure 3.20: The inclusive  $\Lambda_c^+ \rightarrow pK^-\pi^+$  proton DLL distributions. The dataset corresponds to the full data taken in 2012 with the magnet polarity down.

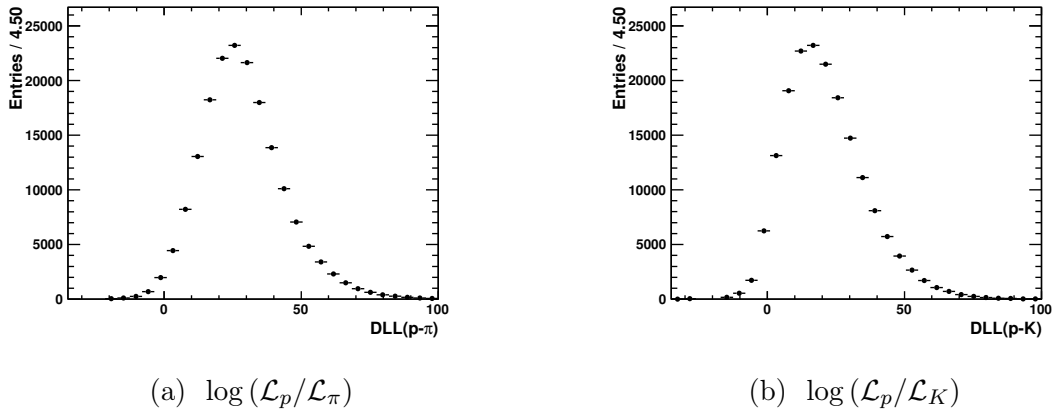


Figure 3.21: The  $\Lambda_b^0 \rightarrow \Lambda_c^+(pK^-\pi^+)\mu^-\bar{\nu}_\mu$  proton DLL distributions. The dataset corresponds to the full data taken in 2012 with the magnet polarity down.

### 3.5.9 Cross checks and associated systematics

The PID selection efficiencies calculated using these samples must undergo certain quality checks before they may be utilised to evaluate PID efficiencies of other decay modes in the `PIDCalib` package. The first of these is the evaluation of a systematic uncertainty to be associated with the yield given by the sum of weights after the PID selection, and is a check of the *sPlot* weight normalisation. The second is that the local efficiencies in the variable space on which the PID performance of tracks depends between the samples is compatible.

#### Fit-and-count systematic

In the PID correction using the `PIDCalib` package, the calibration sample has a signal extraction performed on the entire sample of data. Signal weights are assigned to each candidate in the distribution from this signal extraction using the *sPlots* technique, such that the sum of the weights is equal to the extracted yield. The sample then has the PID selection applied to it, and the sums of signal weights before and after the selection are used to extract the efficiency of the selection.

In the case of the  $\Lambda_c$  based samples, we find that a significantly higher combinatoric background is present in the sample than is found in the existing calibration samples (see Figure 3.6). This background is assumed to be composed only of combinations of unrelated tracks, which should have a uniform response to any PID selection with respect to the  $\Lambda_c$  mass. This uniformity is required such that the normalisation of the weights extracted using the *sPlots* method is preserved. If there is any particular physics background which is preferentially sculpted by the PID selection then the signal weights will no longer be properly normalised once PID selection is applied.

This is explicitly tested using a “fit-and-count” method. A particular PID variable is cut at various values, at each point finding the following:

- The signal yield surviving the selection as given by the sum of signal weights for those candidates surviving selection.
- The signal yield surviving the selection as calculated from a new fit to the surviving data.

Any non-combinatoric backgrounds in the sample will result in observable differences between the two samples. The signal shape in the fits is constrained to be the same as the

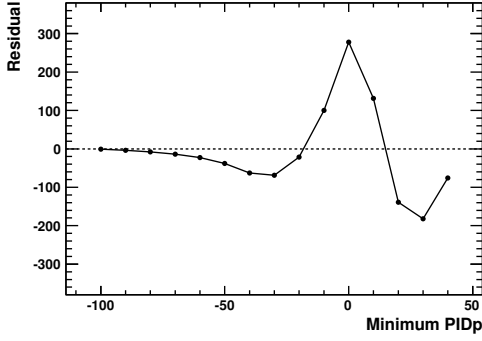
signal shape found from the fits to the full dataset. The specific parameters that are fixed are the widths and relative fractions of the two Gaussians used in the signal.

Example plots of the residual, defined as the difference between the extracted signal yield from the fit and the yield from the sum of signal weights surviving selection, are provided in Figure 3.22, where we demonstrate a broad scan over a wide range of minimum values of  $\log(\mathcal{L}_p/\mathcal{L}_\pi)$  (-100, -40) and a fine scan over those  $\log(\mathcal{L}_p/\mathcal{L}_\pi)$  values typically used in selections in heavy flavour physics analyses (-10, -20).

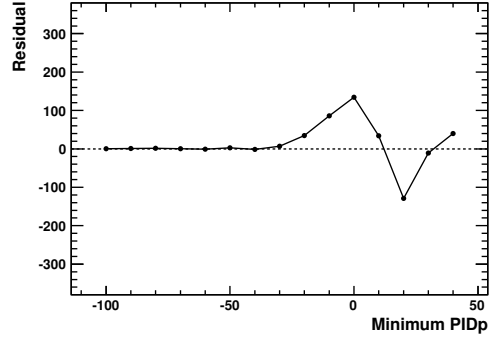
A structure is observed whereby the residual gradually increases as the PID selection is tightened until  $\log(\mathcal{L}_p/\mathcal{L}_\pi) = 2$  and then rapidly falls off, becoming negative. This structure in the residuals is observed in all the decay modes. This seems indicative that there is some physics background under the combinatoric background, which leads to a bias in the extracted signal yield as attained through counting the signal weights surviving PID selection. It is not possible to identify any physics backgrounds through investigation of the  $\Lambda_c$  mass spectrum with the available statistics. We note that the effect is minor - with a maximum systematic uncertainty in the extracted yield of 0.34 % in the inclusive  $\Lambda_c^+ \rightarrow pK^-\pi^+$  and 0.2 % in the  $\Lambda_b^0 \rightarrow \Lambda_c^+(pK^-\pi^+)\mu^-\bar{\nu}_\mu$ . The size of the systematic error, however, is smaller in size than other systematic uncertainties associated with the PIDCalib technique in the case of protons; systematic uncertainties arising from variations in efficiency over individual calibration bins are commonly of the order of 1 %. The maximum residuals on the extracted signal yields by polarity are given in Table 3.4, where we also provide the corresponding fractional systematic error arising from the weighting procedure by polarity.

Mode	Polarity	Polarity $N_{\text{sig}}$	Max residual	Max syst [%]
Inclusive $\Lambda_c^+ \rightarrow pK^-\pi^+$	MagDown	$100521 \pm 433$	295	0.2
	MagUp	$95879 \pm 415$	321	0.3
$\Lambda_b^0 \rightarrow \Lambda_c^+(pK^-\pi^+)\mu^-\bar{\nu}_\mu$	MagDown	$177576 \pm 517$	139	0.1
	MagUp	$160426 \pm 495$	235	0.2

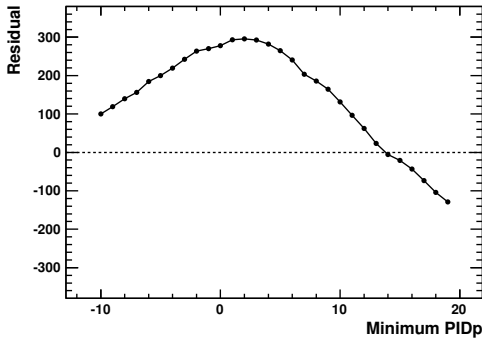
Table 3.4: The maximum residuals and associated systematic errors from the fit-and-count study. The maximum absolute value of the residual is given. The associated systematic is the maximum residual over the extracted signal yield after PID selection corresponding to the maximum residual.



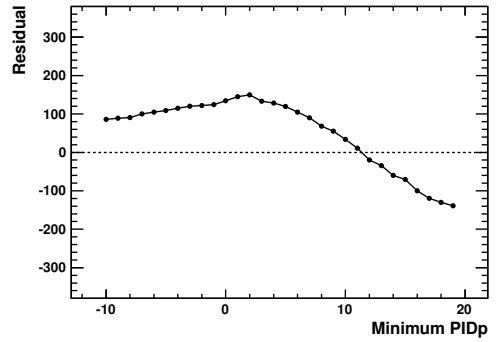
(a) Inclusive  $\Lambda_c^+ \rightarrow pK^- \pi^+$



(b)  $\Lambda_b^0 \rightarrow \Lambda_c^+(pK^- \pi^+) \mu^- \bar{\nu}_\mu$



(c) Inclusive  $\Lambda_c^+ \rightarrow pK^- \pi^+$



(d)  $\Lambda_b^0 \rightarrow \Lambda_c^+(pK^- \pi^+) \mu^- \bar{\nu}_\mu$

Figure 3.22: The signal yield residuals from the fit-and-count systematic check. The datasets correspond to the magent down data taken in 2012. The residual is defined as the difference in extracted signal yield from the fits to the  $\Lambda_c$  mass spectra after PID selection and from counting the signal weights surviving PID selection from the fit to the full dataset. Top are coarse scans over  $\log(\mathcal{L}_p/\mathcal{L}_\pi)$  over a wide range of cut values, bottom are fine scans over the range of typically utilised  $\log(\mathcal{L}_p/\mathcal{L}_\pi)$  cuts.

## Efficiency comparisons

As a cross check we compare the recorded efficiencies across the variable space as calculated with each individual sample. By binning finely in the variable space, the differences in the kinematics between the samples, and the difference in the global number of reconstructed tracks, may be mitigated. Generally, good agreement is observed across the phase space. Such a comparison is shown in Figure 3.23, corresponding to a fairly common PID selection of  $\log(\mathcal{L}_p/\mathcal{L}_\pi) > 10$ . In this plot we show the PID efficiency for the samples as a function of the proton momentum for events which have an event number of tracks between 200 – 400, and a proton pseudorapidity between 3 – 3.5.

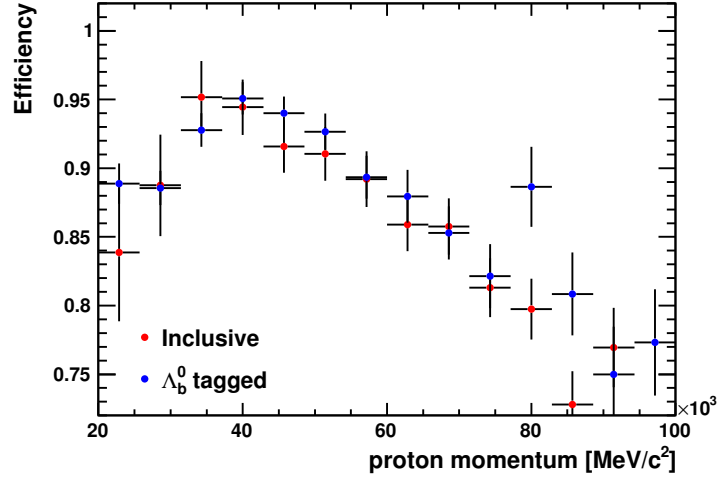


Figure 3.23: The proton PID efficiency in the inclusive  $\Lambda_c^+ \rightarrow pK^-\pi^+$  and the  $\Lambda_b^0 \rightarrow \Lambda_c^+(pK^-\pi^+)\mu^-\bar{\nu}_\mu$  as a function of momentum, for candidates which have an event number of tracks between 200 – 400, and a proton pseudorapidity between 3 – 3.5. Generally a good agreement between the sample efficiencies can be observed. The bins with poor agreement at high momentum correspond to regions where the sample kinematics are very different from one another.

### 3.5.10 Summary

To summarise, new data samples of proton tracks were prepared from  $\Lambda_c^+ \rightarrow pK^-\pi^+$  decays to be used in a data-driven efficiency correction for PID selections on protons. These proton tracks have typically higher transverse momenta than those from previously available proton calibration samples based on  $\Lambda^0 \rightarrow p\pi^-$  decays, enabling for the first time a data-driven calibration for high  $p_T$  protons at LHCb.

## 3.6 Data-driven metrics of aerogel performance

As described in Section 3.2.3, the aerogel Cherenkov radiator housed in RICH1 is responsible for the particle identification of charged hadrons at low momentum. It is designed to provide discrimination between charged hadrons in the momentum range 1 – 15 GeV/ $c$ . Prompted by discussion within the LHCb collaboration of the value of the aerogel’s contribution to particle identification at the experiment, the candidate utilised the calibration datasets outlined in Section 3.4.2 to evaluate the performance of the aerogel in a data-driven fashion.

### 3.6.1 The RICH aerogel

The aerogel is responsible for very-low momentum PID discrimination at LHCb. Particles in heavy-flavour decays at LHCb have momentum distributions which tend to be higher than the momentum range in which the aerogel can provide discrimination. The particles for which discrimination at this momentum range becomes important are those used in tagging procedures. For example, in decays of  $D^{*+} \rightarrow D^0(\pi^+K^-)\pi^+$  the slow pion produced in the decay of the  $D^{*+}$  has a momentum range in which the aerogel may provide significant discrimination. Particles produced in association with heavy-flavour particles also have lower momenta than those in heavy-flavour decays, and can provide significant tagging power of the heavy-flavour particle’s flavour at production - which is especially important in the analysis of neutral mesons that can change flavour in flight through mixing.

In 2011 the aerogel enclosure was not gas-tight, and as such the aerogel was operated in contact with the  $C_4F_{10}$  gas. At the end of the year studies revealed that the aerogel photon yield had fallen throughout the year as a consequence of  $C_4F_{10}$  gas leeching. This also altered the refractive index of the material, leading to an increase in the  $\theta_C$  by approximately 11 %. To prevent such a degradation in performance in 2012, the aerogel was placed in a gas-tight carbon fiber enclosure filled with  $CO_2$ .

To better evaluate the aerogel performance, such that we might better understand what discrimination is afforded by the RICH system to low momentum particles, the candidate attempted to measure the PID discrimination produced by the aerogel radiator in a data-driven fashion. This would also provide more information on the efficacy of the RICH aerogel box in preventing the degradation of the aerogel performance.

### 3.6.2 Targetting the aerogel performance

The evaluation of the aerogel performance using real data presents problems, as no data was collected using just the aerogel and without the gas radiators which also provide PID discrimination. As such, we must exploit a region of the momentum space whereby the gas radiators cannot provide discrimination, but the aerogel can. The radiator momentum thresholds for pions, kaons and protons in the aerogel,  $\text{CF}_4$  and  $\text{C}_4\text{F}_{10}$  are provided in Table 3.5. The low pion threshold in the  $\text{C}_4\text{F}_{10}$  results in a very low momentum range for pions for which the particle identification only uses information from the aerogel. For kaons below 9.3 GeV/ $c$  and protons below 17.7 GeV/ $c$  the only Cherenkov radiation emitted by the particle will be in the aerogel. Comparisons to the pion hypothesis in this momentum range cannot be made as pions would radiate in the gases, and the presence or absence of radiation associated with the tracks results in a non-zero contribution to  $\log(\mathcal{L}_p/\mathcal{L}_\pi)$  and  $\log(\mathcal{L}_K/\mathcal{L}_\pi)$  using information from the gas radiators.

Instead, we examine the distributions of  $\log(\mathcal{L}_p/\mathcal{L}_K)$  for kaons and protons below 9.3 GeV/ $c$ . In this range, any discrimination from the RICH between the kaon and proton mass hypotheses must necessarily come from photons radiated in the aerogel. By examining the distributions of  $\log(\mathcal{L}_p/\mathcal{L}_K)$  for genuine kaon and proton tracks we can quantitatively ascertain the aerogel performance.

Pure samples of proton and kaon tracks with momenta below 9.3 GeV/ $c$  were taken from the calibration datasets outlined in Section 3.4.2 for these studies. Some preselection is applied to tracks in this momentum range to ensure each track used in the study should have been able to radiate in the radiator under the kaon mass hypothesis. We require that the reconstructed particle passed through the aerogel volume with sufficient path length to have radiated photons. We also require that the track has a momentum above 2.0 GeV/ $c$ , the kaon momentum threshold in the aerogel. This is to ensure that we only include tracks for which the aerogel can differentiate between the kaon and proton mass hypotheses.

	$\text{CF}_4$	$\text{C}_4\text{F}_{10}$	Aerogel
$\pi$ threshold [ GeV/ $c$ ]	4.4	2.6	0.6
$K$ threshold [ GeV/ $c$ ]	15.6	9.3	2.0
$p$ threshold [ GeV/ $c$ ]	29.7	17.7	3.8

Table 3.5: The momentum thresholds for pions, kaons and protons in each radiator in the RICH system.

### 3.6.3 Results

The numbers of proton and kaon tracks used in the study are provided in Table 3.6. For these tracks the normalised  $\log(\mathcal{L}_p/\mathcal{L}_K)$  distributions are provided in Figure 3.24. There is a significant separation between the low momentum kaon and proton tracks in 2012 which is not present in 2011. Scanning across the  $\log(\mathcal{L}_p/\mathcal{L}_K)$  distributions and counting the fractions of the surviving species, we can derive identification and mis-identification rates for the protons and kaons.

These receiver operating characteristics are provided in Figure 3.25 for the full datasets, both for low momentum and for the momentum range covered by the gas for comparison. In 2011 the low momentum discrimination is consistent with random guessing (indicated by the dashed red line). In 2012 there is a significant improvement in the discrimination between the proton and kaon species at low momentum. However, the discrimination is seen in all cases to be far less powerful at low momentum than at high momentum, for the data gathered in 2011 and 2012. This is to be expected due to the significantly higher photon yield in the gas radiators and the much lower  $\theta_C$  of the gas radiators. The Cherenkov rings are more distinct due to the higher photon yield and due to the lower radius of the rings, which cover a lower area and are subject to lower backgrounds from false detections and intersections with other rings.

As the RICH performance is dependent on occupancy, the distributions are split by the number of tracks in the global event. The resultant receiver operating characteristics for ranges of detector occupancy are shown in Figure 3.26. The expected improvement in discrimination at lower levels of detector occupancy is observed in 2012, but in all cases the 2011 distributions of the low momentum sample are consistent with random guessing.

Year	Species	N (2.0 – 9.3 GeV/c)	N (9.3 – 100 GeV/c)
2012	$p$	$5.4 \times 10^6$	$145 \times 10^6$
	$K$	$2.5 \times 10^6$	$63 \times 10^6$
2011	$p$	$5.9 \times 10^6$	$108 \times 10^6$
	$K$	$2.0 \times 10^6$	$49 \times 10^6$

Table 3.6: The momentum thresholds for pions, kaons and protons in each radiator in the RICH system.

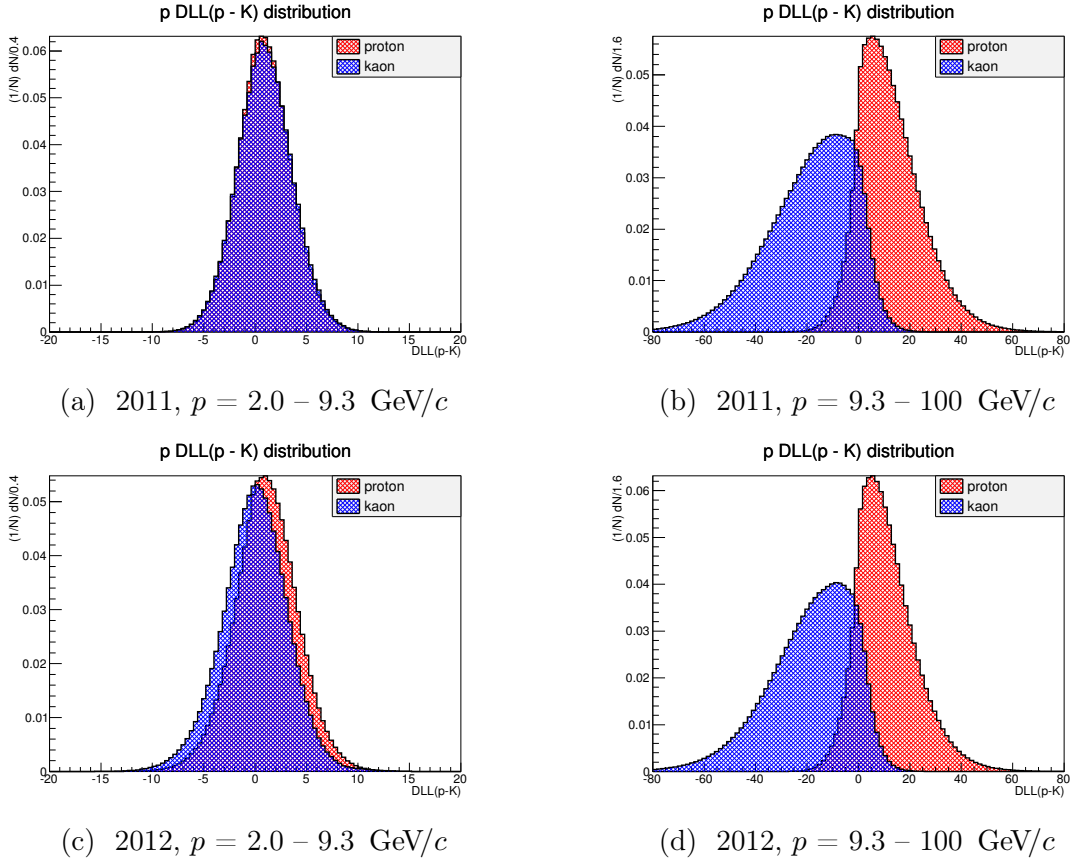


Figure 3.24: The  $\log(\mathcal{L}_p/\mathcal{L}_K)$  distributions of the kaons and protons used in the studies of aerogel performance. A notable improvement in the separation of the low momentum distributions is observed in 2012 compared to 2011.

### 3.6.4 Summary

The aerogel performance was investigated through examination of the  $\log(\mathcal{L}_p/\mathcal{L}_K)$  response of proton and kaon tracks at low momentum, where the only possible discrimination to the RICH information on these tracks is provided by the aerogel. The resultant receiver operating characteristics which were derived were the first data-driven metric of the aerogel performance, using pure datasets of charged tracks with very high statistics. This quantitatively demonstrated that the introduction of the aerogel box in 2012 markedly improved the aerogel performance.

Even with this increase in performance, the discrimination is extremely limited compared to that afforded by the gas radiators. Under the best possible conditions, with the number of tracks in the global event below 100, the efficiency of a proton enhancing cut of

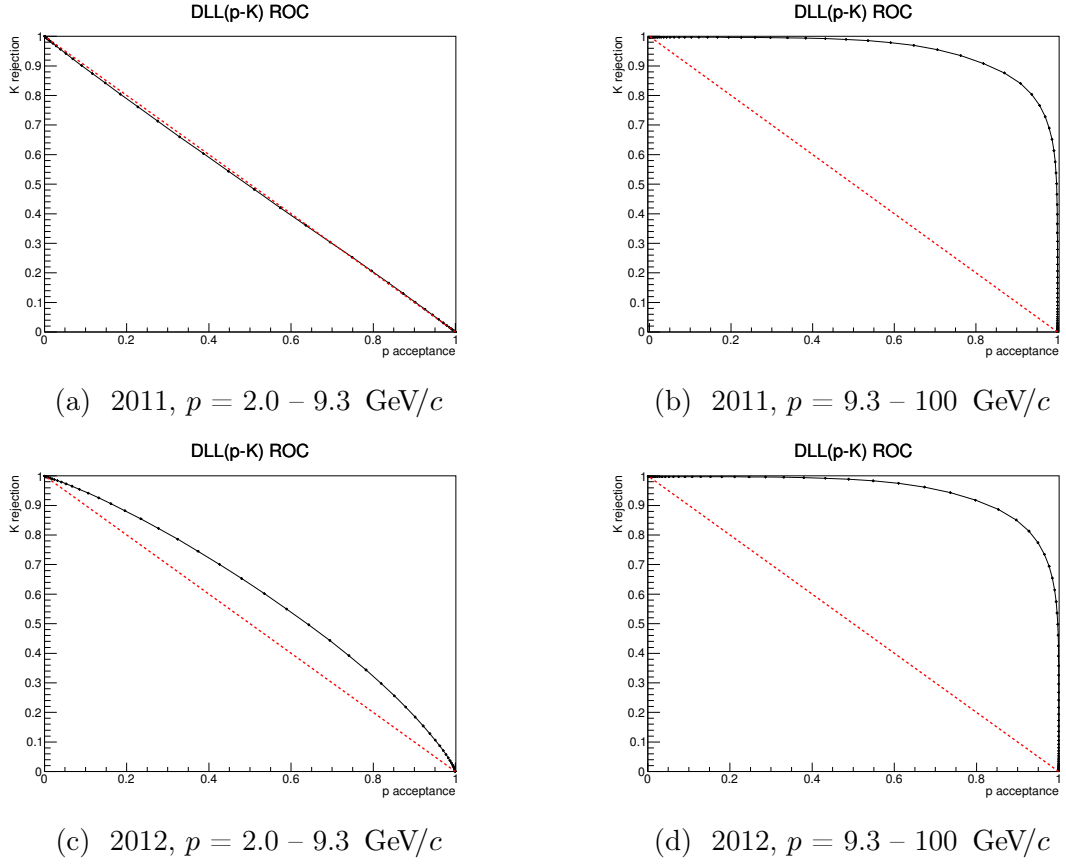
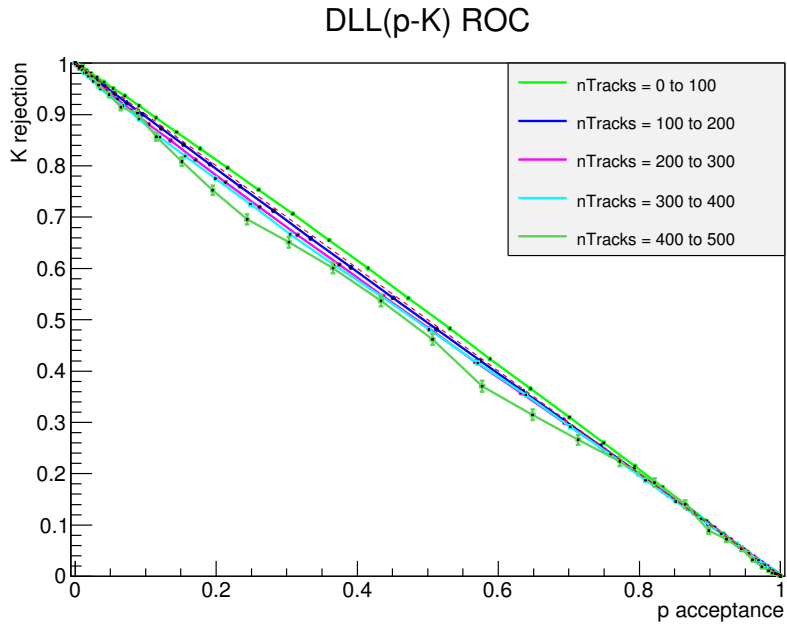
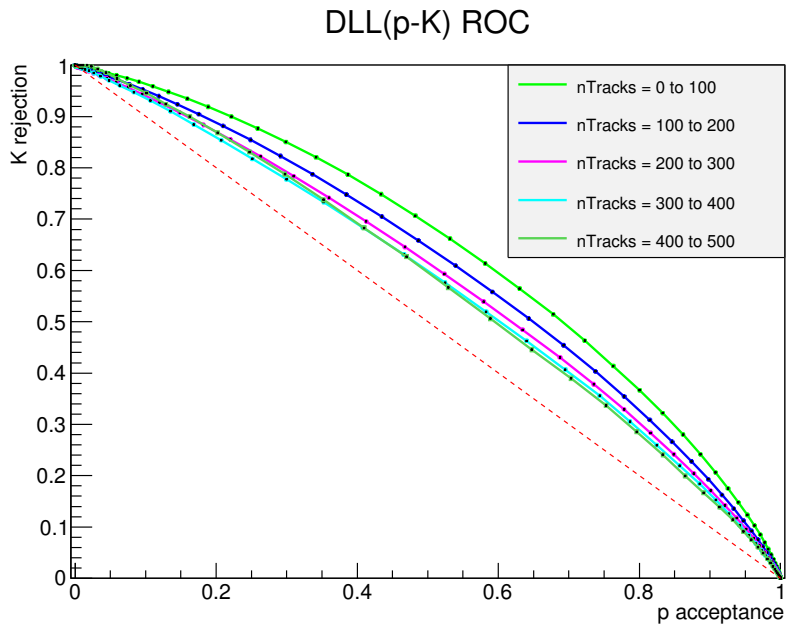


Figure 3.25: The receiver operating characteristics of the kaons and proton discrimination using the  $\log(\mathcal{L}_p/\mathcal{L}_K)$  estimator, shown in the black continuous line. The dashed red lines indicate the rates expected from random guessing. A notable improvement in the discrimination of the low momentum protons and kaons is observed in 2012 compared to 2011.

$\log(\mathcal{L}_p/\mathcal{L}_K) > 0$  has an efficiency of 59.1 % with a kaon misidentification rate of 44.2 %. The information derived from this study helped inform the LHCb Collaboration's eventual decision to remove the aerogel from the RICH system for the LHC run III, which will commence in 2015. This will reduce the material budget of the RICH system considerably, and with a higher volume of  $C_4F_{10}$  in the active area the photon yield from the RICH1 gas will be accordingly higher.



(a) 2011,  $p = 2.0 - 9.3 \text{ GeV}/c$



(b) 2012,  $p = 2.0 - 9.3 \text{ GeV}/c$

Figure 3.26: The receiver operating characteristics of the kaon and proton discrimination using the  $\log(\mathcal{L}_p/\mathcal{L}_K)$  estimator, shown in the black continuous line, split by the number of tracks in the global event. Shown in (a) is the characteristic for 2011 data, shown in (b) the characteristic for 2012 data. The dashed red lines indicate the rates expected from random guessing. The expected improvement in discrimination at lower levels of detector occupancy is observed.

## 3.7 Chapter summary

The particle identification system at LHCb provides powerful discrimination between different species of charged hadrons, with a high identification efficiency and low mis-identification rates. PID selections at LHCb are powerful, but given that the LHCb simulation of PID discriminant estimators generated from the RICH information only includes average parameters that are different to the actual parameters of the RICH gases determined by the environmental conditions during data taking, a data-driven approach is favoured for the efficiency correction of such selections.

Presented is a new calibration dataset of pure proton tracks derived from  $\Lambda_c^+ \rightarrow pK^- \pi^+$  decays to supplement existing proton calibration samples from  $\Lambda^0 \rightarrow p\pi^-$  decays. These new calibration tracks have higher transverse momenta than those previously available, which allows for the first time the data-driven calibration of PID selections on protons with high  $p_T$ , as is the case with protons from heavy-flavour decays. Helicity information on the  $\Lambda_c^+ \rightarrow pK^- \pi^+$  decay is used to veto combinatoric background and drastically improve the purities of the selected samples.

The datasets of tracks of different species gathered to aid in PID calibration were used to evaluate the performance of the aerogel radiator in the RICH system, by exploiting the momentum range where the aerogel can provide discrimination between kaons and protons but the gas radiators may not. These results were the first unbiased, data-driven metric of the aerogel performance available to the collaboration, and were influential in the decision to remove the aerogel from the RICH1 detector during run II data taking.

# Chapter 4

## $\Lambda_c^+ \rightarrow phh'$ relative branching fractions

### 4.1 Introduction

The  $\Lambda_c$  is a charmed baryon of mass  $2286.46 \pm 0.14$  MeV [10]. The decays of charmed baryons can be used to study colour suppression of  $W^+$  exchange diagrams. Table 4.1 reproduces the current knowledge of the relative branching ratios of  $\Lambda_c^+ \rightarrow phh'$  decays, where  $hh' \in \{K^-\pi^+, K^-K^+, \pi^-\pi^+, \pi^-K^+\}$ , as collected by the Particle Data Group (PDG) [10]. In 2011, LHCb collected significantly larger samples of the three hitherto observed  $\Lambda_c$  decays than those gathered in previous measurements.

The candidate led an analysis to measure the branching fractions of  $\Lambda_c$  to a proton and two charged hadrons, without hyperon mediation. The aim of the analysis was to measure the branching ratios of the three suppressed modes with respect to the Cabibbo-favored (CF) mode  $\Lambda_c^+ \rightarrow pK^-\pi^+$  with the best statistical precision to date. This goal entails the first observation of the doubly Cabibbo-suppressed (DCS) decay mode  $\Lambda_c^+ \rightarrow p\pi^-K^+$ . This search was conducted blindly by remaining ignorant of all  $\Lambda_c^+ \rightarrow p\pi^-K^+$  candidates reconstructed with a mass within  $\pm 25$  MeV of the world-average  $\Lambda_c^+$  mass until the analysis procedure was finalised.

The need to finalise the analysis procedure prior to unblinding the DCS mode requires the analysis procedure to be developed utilising control modes. The singly-Cabibbo suppressed (SCS) modes  $\Lambda_c^+ \rightarrow pK^-K^+$  and  $\Lambda_c^+ \rightarrow p\pi^-\pi^+$  are good candidates for control modes, however, as indicated in Table 4.1, the relative branching fractions of these modes are known with poor precision. We worked to obtain the requisite confidence in our analysis methods by simultaneously examining samples of  $\Lambda_c^+ \rightarrow phh'$  decays where the  $\Lambda_c$  is produced at the primary interaction vertex (PV) and where it is produced in semileptonic

Mode	BF	Refs	Note
$\Lambda_c^+ \rightarrow pK^- \pi^+$	$(5.0 \pm 1.3) \times 10^{-2}$	[86–88]	Derived from $\mathcal{B}(\bar{B} \rightarrow \Lambda_c^+ X)$
$\rightarrow p\bar{K}^*(892)^0$	$(1.6 \pm 0.5) \times 10^{-2}$		Inclusive $\bar{K}^*(892)^0$
$\rightarrow \Delta(1232)^{++}K^-$	$(8.6 \pm 3.0) \times 10^{-3}$		
$\rightarrow \Lambda(1520)^0\pi^+$	$(1.8 \pm 0.6) \times 10^{-2}$		Inclusive $\Lambda(1520)^0$
$\rightarrow pK^- \pi^+$ nonresonant	$(2.8 \pm 0.8) \times 10^{-2}$		
$\Lambda_c^+ \rightarrow p\pi^- \pi^+$	$(3.5 \pm 2.0) \times 10^{-3}$	[89]	
$\rightarrow pf_0(980)$	$(2.8 \pm 1.9) \times 10^{-3}$		Inclusive $f_0(980)$
$\Lambda_c^+ \rightarrow pK^- K^+$	$(7.7 \pm 3.5) \times 10^{-4}$	[90, 91]	
$\rightarrow p\phi$	$(8.2 \pm 2.7) \times 10^{-4}$		Inclusive $\phi$
$\rightarrow pK^- K^+$ non- $\phi$	$(3.5 \pm 1.7) \times 10^{-4}$		
$\Lambda_c^+ \rightarrow p\pi^- K^+$	$< 2.3 \times 10^{-4}$	[92]	CL = 90%

Table 4.1: World-average branching fractions for  $\Lambda_c^+ \rightarrow phh'$  decays as recorded in the 2012 PDG Review of Particle Properties [10]. Where noted, the PDG has adjusted the branching fractions for resonant decays to include all final states of the indicated resonances, not just the  $phh'$  final state of interest.

$\Lambda_b^0$  decays. The two samples are statistically independent and have different production, triggering, and selection mechanisms.

In this thesis, Chapter 4 outlines the datasets and simulated samples used, the selection of candidates and the investigation of peaking backgrounds. Chapter 5 then outlines the efficiency corrections and yield extractions in the analyses. Chapter 6 then provides the sources of systematic uncertainty in the analysis. We then give the methods utilised for extracting confidence intervals for the yield of  $\Lambda_c^+ \rightarrow p\pi^- K^+$  and gives the final branching fraction results in the analysis.

## 4.2 Data and processing

### 4.2.1 LHCb data set

The measurements described here are based on  $1024.8 \pm 35.9 \text{ pb}^{-1}$  of  $\sqrt{s} = 7 \text{ TeV}$   $p - p$  collisions observed with the full LHCb detector [98]. The data was collected throughout 2011 under varying beam, detector, and trigger conditions. We use all of the available data that has been marked OK by data quality checks. For the prompt analysis, we find  $588.2 \pm 20.6 \text{ pb}^{-1}$  with the magnet polarity down (MagDown) and  $435.7 \pm 15.2 \text{ pb}^{-1}$  for the magnet polarity up (MagUp). For the SL analysis, we find  $589.4 \pm 20.6 \text{ pb}^{-1}$  for the MagDown polarity and  $435.5 \pm 15.2 \text{ pb}^{-1}$  for the MagUp polarity.

## 4.2.2 Monte Carlo samples

We use Monte Carlo (MC) events from the LHCb full event and detector simulation for signal and background studies and to estimate reconstruction and selection efficiencies. To replicate the selections applied to the real data we use modified versions of the stripping selections which have all PID selection criteria removed, such that the PID selection may be replicated without reliance on the poorly modelled PID discriminants in the simulation. All other selection criteria remain the same as those in the version of the stripping run on real data.

The simulation utilised in the analyses employ one of two generator-level cuts, applied at the EVTGEN level. These are:

**DaughtersInLHCb** - This requires all charged daughters in the generated decay to be produced in the range  $0.01 \text{ rad} < \theta_{\text{charged}} < 0.4 \text{ rad}$  of the  $z$ -axis and all neutral daughters to be produced in the range  $0.005 \text{ rad} < \theta_{\text{neutral}} < 0.4 \text{ rad}$  of the  $z$ -axis.

**LHCbAcceptance** - This requires the head particle/mother of the specified signal decay to be produced in the range  $0 < \theta_{\text{signal}} < 0.4 \text{ rad}$  of the  $z$ -axis.

All generated MC samples utilise the **DaughtersInLHCb** cut, with the exception of the semileptonic CF  $\Lambda_c^+ \rightarrow pK^-\pi^+$  which utilises the **LHCbAcceptance** cut.

The prompt  $\Lambda_c^+ \rightarrow phh'$  MC samples were generated without a resonance structure. All decays in the simulation for both analyses proceed via the PHSP EVTGEN decay model [113]. The generated decays accordingly populate the phase space uniformly. A fraction of the prompt MC events contain only  $\Lambda_c^+$  produced in  $b$ -hadron decays. In order to ensure that the efficiencies computed from the prompt MC samples are well defined, we process these samples with a filter that retains only events that contain a promptly produced signal decay. The filter traces the ancestry of the generated signal  $\Lambda_c^+$ . If any of its ancestors has a mean lifetime longer than 0.1 fs then it is classified as not-prompt.

The semileptonic simulation used for the CF mode  $\Lambda_c^+ \rightarrow pK^-\pi^+$  include an admixture of pure phase-space and pseudo-resonance structure of the decay generated according to the following fragment of EvtGen code:

```
Decay MyLambda_c+
  0.02800      p+      K-      pi+      PHSP;
  0.01065      p+      Myanti-K*0    PHSP;
  0.00860      Delta++ K-      PHSP;
```

0.00414                      MyLambda(1520)0 pi+                      PHSP;  
 Enddecay

The semileptonic samples of the SCS decays  $\Lambda_c^+ \rightarrow pK^-K^+$  and  $\Lambda_c^+ \rightarrow p\pi^-\pi^+$  also include an admixture of pure phase-space and pseudo-resonance structure. In the sample used for  $\Lambda_c^+ \rightarrow pK^-K^+$  48.4% of the signal  $\Lambda_c^+$  undergo a pure phase space decay  $\Lambda_c^+ \rightarrow pK^-K^+$  and the remaining 51.6% decay through an intermediate  $\phi$  resonance,  $\Lambda_c^+ \rightarrow p\phi(K^-K^+)$ . In the sample used for  $\Lambda_c^+ \rightarrow p\pi^-\pi^+$ , 55.6% of the signal  $\Lambda_c^+$  undergo a pure phase space decay  $\Lambda_c^+ \rightarrow p\pi^-\pi^+$  and the remaining 44.4% decay through an intermediate  $f_0(980)$  resonance,  $\Lambda_c^+ \rightarrow pf_0(980)(\pi^-\pi^+)$ .

### 4.3 Selection

Herein we outline the selection of candidate  $\Lambda_c^+ \rightarrow phh'$  decays in the prompt and semileptonic analyses. Selection takes place at several levels: at the stripping, trigger and offline selections. The central gathering of interesting decays is known as the “stripping” selection, and its purpose is to gather decays of interest in a general fashion, such that several different measurements may be performed using the same decay mode. In the central processing of data, the stripping lines have a finite bandwidth. They must therefore make an initial selection of the decays for general purpose which preserves as much signal as possible while keeping the retention of candidates within acceptable limits. A rigid selection of trigger requirements is enforced in this analysis such that the efficiency of the trigger selections can be reliably measured. Finally, a further selection is made to adapt the selection in the stripping for the specific needs of this analysis, called the “offline” selection. This includes a multi-variate selection for use in selecting the rare decays of  $\Lambda_c^+ \rightarrow p\pi^-K^+$ .

#### 4.3.1 Stripping and trigger of prompt data

##### Stripping

The stripping selection reconstructs the general pattern  $\Lambda_c^+ \rightarrow phh'$ . Table 4.2 lists the selection criteria applied at the stripping level. The main goals of the selection are to preserve signal while vetoing combinatoric backgrounds and backgrounds from other charm decays. The multiplicity of LHCb events is high due to the hadronic production environ-

ment. Consequently, cuts on the impact parameter ( $IP$ ) of reconstructed heavy-flavour particles are often a useful discriminant in rejecting the large combinatoric backgrounds from unrelated tracks. Due to the short  $\Lambda_c$  lifetime (approximately 200 fs) relative to the  $D$  and  $B$  mesons, this approach provides less discriminatory power over the rejection of combinatorics.

We therefore utilise a suite of tight cuts on the momenta ( $p$ ) and transverse momenta ( $p_T$ ) of the candidate daughters. The requirement is made that all candidate daughters have a significant impact parameter with respect to the primary interaction. A cut is specifically placed upon the minimum daughter  $IP\chi^2$ , which is the increase in the associated primary vertex  $\chi^2$  when the daughter track is included in the primary vertex fit. PID selection is also employed at this stage to reduce the retention of the stripping line while vetoing a large number of candidates which are combinations of unrelated tracks. Requirements are made that the reconstructed tracks are of a high quality, specifically that the maximum normalised track  $\chi^2$  be below a given threshold and that the ‘‘Clone distance’’, a quantity based on the Kullback-Liebler distance between tracks [133], must exceed a given value to remove clone tracks which do not share common hits.

All permutations of pairs of the daughter tracks should have a reconstructed distance of closest approach ( $DoCA$ ) no greater than a maximum threshold. Requirements are placed on the  $\Lambda_c$  vertex quality and on the distance between the  $\Lambda_c$  decay vertex and the primary vertex. We require that the  $\Lambda_c$  candidate points back to the primary interaction by placing a minimum requirement on the cosine of the angle between the reconstructed  $\Lambda_c$  momentum and the displacement vector between the primary vertex and the  $\Lambda_c$  decay vertex, a quantity referred to as the  $DIRA$ . We require that the reconstructed candidate has a computed lifetime below 1.2 ps, which preserves most  $\Lambda_c$  signal while vetoing significant amounts of meson decays which are misreconstructed. Finally we require the candidate mass to be within 90 MeV/ $c^2$  of the nominal PDG  $\Lambda_c$  mass.

## Trigger

While a dedicated HLT2 trigger line operated in 2011 for the  $\Lambda_c^+ \rightarrow pK^-\pi^+$  mode, there were no such lines for the prompt SCS and DCS  $\Lambda_c$  decays for 2011. In order to have a consistent trigger chain for the four modes we adopt the trigger requirement that the event was triggered independently of the  $\Lambda_c$  candidate, or Triggered Independently of Signal (TIS). The efficiencies of TIS chains are typically very low, but a TIS chain provides the benefit of trigger efficiency cancellation between the  $\Lambda_c^+ \rightarrow phh'$  modes. The specific

	Variable name	Stripping
$h^\pm$	Track $\chi^2/N_{\text{ndf}}$	$< 5$
	Clone distance	$> 5000$
	$IP \chi^2$	$> 4, 8$
	$p_T$	$> 400, 1200 \text{ MeV}/c$
	$ \vec{p} $	$> 3.2 \text{ GeV}/c$
$p$	$\log(\mathcal{L}_p/\mathcal{L}_\pi)$	$> 5$
$K$	$\log(\mathcal{L}_K/\mathcal{L}_\pi)$	$> 5$
$\pi$	$\log(\mathcal{L}_K/\mathcal{L}_\pi)$	$< 0$
$h_i h_j$	$DoCA$	$< 0.10 \text{ mm}$
$\Lambda_c^+$	Vertex $\chi^2/N_{\text{ndf}}$	$< 20$
	$VD \chi^2$	$> 16$
	$DIRA$	$> 0.9999$
	Proper time $\tau$	$\in [0, 1.2] \text{ ps}$
	$ m_{phh'} - m_{\Lambda_c^+ \text{PDG}} $	$< 90 \text{ MeV}/c^2$

Table 4.2: Selection criteria for prompt  $\Lambda_c^+ \rightarrow phh'$  candidates in the stripping selection.  $h$  denotes the pion, kaon, or proton product of a  $\Lambda_c^+$  decay and is used to indicate cuts that are applied to all three. Where two values for the daughter  $h$   $p_T$  lower limit are indicated, all three daughters are required to satisfy the looser cut and at least one of the daughters must satisfy the tighter cut.  $h_i h_j$  denotes every pairing of the daughters.

requirements are that any L0 trigger was fired independently of the  $\Lambda_c$  candidate, and that the event was triggered by at least one of a collection of physics analysis trigger algorithms in the HLT independently of the  $\Lambda_c$  candidate.

### 4.3.2 Stripping and trigger of semileptonic data

#### Stripping

Each of the stripping lines in the semileptonic analysis reconstruct candidates according to the pattern  $\Lambda_b^0 \rightarrow \Lambda_c^+ \mu^\pm$ ,  $\Lambda_c^+ \rightarrow phh'$ . Table 4.3 lists the selection criteria applied at the stripping level. The selection requirements on the  $\Lambda_c^+ \rightarrow phh'$  component of the reconstruction are broadly similar to that used in the prompt analysis, but with looser momentum requirements placed upon the daughters. The relaxation of these cuts is possible due to the additional discrimination acquired from information on the  $\Lambda_b^0$  decay. The minimum requirement on the  $\Lambda_c$  daughter  $IP\chi^2$  is raised, as the daughters of the semileptonically-produced  $\Lambda_c$  decays have higher impact parameters than for daughters of those  $\Lambda_c$  which are produced promptly at the primary interaction. Similar selection

criteria are applied to the reconstructed  $\Lambda_c$  candidates as are applied to those in the prompt analysis.

	Variable name	Stripping
$h^\pm$	Track $\chi^2/N_{\text{ndf}}$	$< 4$
	Clone distance	$> 5000$
	$IP \chi^2$	$> 9$
	$p_T$	$> 300$
	$ \vec{p} $	$> 2 \text{ GeV}/c$
$p$	$\log(\mathcal{L}_p/\mathcal{L}_\pi)$	$> 4$
	$\log(\mathcal{L}_p/\mathcal{L}_K)$	$> 10^{-10}$
$K$	$\log(\mathcal{L}_K/\mathcal{L}_\pi)$	$> 4$
$\pi$	$\log(\mathcal{L}_K/\mathcal{L}_\pi)$	$< 10$
$\pi$ for $\Lambda_c^+ \rightarrow p\pi^-\pi^+$	$\log(\mathcal{L}_K/\mathcal{L}_\pi)$	$< 0$
$h_i h_j$	$DoCA \chi^2$	$< 20$
$\Lambda_c^+$	Vertex $\chi^2/N_{\text{ndf}}$	$< 6$
	$p_{T_p} + p_{T_h} + p_{T_{h'}}$	$> 1800 \text{ MeV}/c$
	$VD \chi^2$	$> 100$
	$DIRA$	$> 0.99$
	$ m_{phh'} - m_{\Lambda_c^+ \text{PDG}} $	$< 80 \text{ MeV}/c^2$
$\mu$	Track $\chi^2/N_{\text{ndf}}$	$< 4$
	$IP \chi^2$	$> 9$
	$p_T$	$> 800 \text{ MeV}/c$
	$ \vec{p} $	$> 3 \text{ GeV}/c$
	$\log(\mathcal{L}_\mu/\mathcal{L}_\pi)$	$> 0$
$\Lambda_b^0$	Vertex $\chi^2/N_{\text{ndf}}$	$< 6$
	$z_{\Lambda_c^+} - z_{\Lambda_b^0}$	$> -9999 \text{ mm}$
	$DIRA$	$> 0.999$
	$m_{\Lambda_c^+ \mu}$	$\in (2.5, 6) \text{ GeV}/c^2$

Table 4.3: Stripping selection criteria for the semileptonic  $\Lambda_b^0 \rightarrow \Lambda_c^+ \mu^\pm$ ,  $\Lambda_c^+ \rightarrow phh'$  candidates in the analysis.  $h$  denotes the pion, kaon, or proton product of a  $\Lambda_c^+$  decay and is used to indicate cuts that are applied to all three.  $h_i h_j$  denotes every pairing of the daughters.

Muon candidates are required to pass a series of track quality and kinematic requirements. The tracks are also required to have associated hits in all muon stations. The  $\Lambda_c$  candidates and muon candidates together form  $\Lambda_b^0$  candidates which are required to form a common vertex which is significantly displaced in  $z$  from the primary vertex. The  $\Lambda_b^0$  candidate is also required to point back to the primary interaction. As the neutrino in the decay is not reconstructed, the mass of the reconstructed  $\Lambda_c \mu$  system is allowed to be significantly lower than the  $\Lambda_b^0$  nominal mass, with a permitted  $m_{\Lambda_c \mu}$  range of

2.5 – 6.0 GeV/ $c$ .

### **Trigger**

For the semileptonic decays we use a trigger requirement that focuses on the muon in the  $\Lambda_b^0$  decay and thus reduces the relative bias on the  $\Lambda_c^+$  decay phase space. The muon in the  $\Lambda_b^0$  decay is required to have triggered the L0 muon trigger for that event. The  $\Lambda_b^0$  candidate is required to have triggered at least one of a series of algorithms in the HLT, designed to select decays of heavy-favour hadrons to final states including muons by exploiting the decay topology.

### 4.3.3 Offline selection

The offline selection is designed to tailor the output of the general-purpose datasets from the stripping selection output and adopt the selection for the specific purposes of our analysis. All offline selections are trained using 10% of the  $\Lambda_c^+ \rightarrow pK^-\pi^+$  data from each respective analysis. The *sPlots* method [126] is used to extract the signal and background distributions from the data. This data is then excluded from the remainder of the analysis, with an appropriate scaling factor included in the final branching fraction calculations. It is desirable to utilise the same offline cuts in the selection of all four modes for the cancellation of systematic uncertainties. The selections therefore are all trained to maximise sensitivity to the unobserved doubly-Cabibbo suppressed mode. To this end an additional global signal weighting of

$$\frac{|V_{us}|^2|V_{cd}|^2}{|V_{cs}|^2|V_{ud}|^2} \approx 0.003, \quad (4.1)$$

which is a crude indication of the expected relative rate of  $\Lambda_c^+ \rightarrow p\pi^-K^+$  over  $\Lambda_c^+ \rightarrow pK^-\pi^+$ , was applied in the trainings. Examination of the sidebands of the Cabibbo-favoured and doubly-Cabibbo suppressed data indicate that the combinatoric background in the doubly-Cabibbo suppressed mode is approximately 33 % lower than that in the Cabibbo favoured mode, as shown in Figure 4.3. This is taken into account in the selection training by applying a global combinatoric background weight of 0.67.

The output from the stripping lines contain a high combinatoric component, which must be further reduced in order to accurately fit the mass distributions. The mass distributions at stripping level for the modes which are not blinded are shown in Figure 4.1 for the promptly selected candidates and Figure 4.2 for the semileptonically selected candidates. This necessitates the use of cuts on the PID variables to veto combinatorics from wrongly identified particles. Selection training has shown that PID DLL variables possess the greatest discrimination between signal and combinatoric background (compared to track/vertex quality, event kinematic info etc.). These are simultaneously optimised using the CROP tool, and performed in both the prompt and the semileptonic selections. The optimisations use the training figure of merit  $S/\sqrt{S+B}$ , where  $S$  and  $B$  are the sums of the signal and background weights respectively.

The efficiencies of some stages of the selection must be evaluated on an event-by-event basis. The stripping selection efficiency, for example, must be calculated by assigning a per-candidate local efficiency depending on the candidate's location in the phase space parameterising the resonant  $\Lambda_c^+ \rightarrow phh'$  decay (see Section 5.1.5). The *sPlots* method is

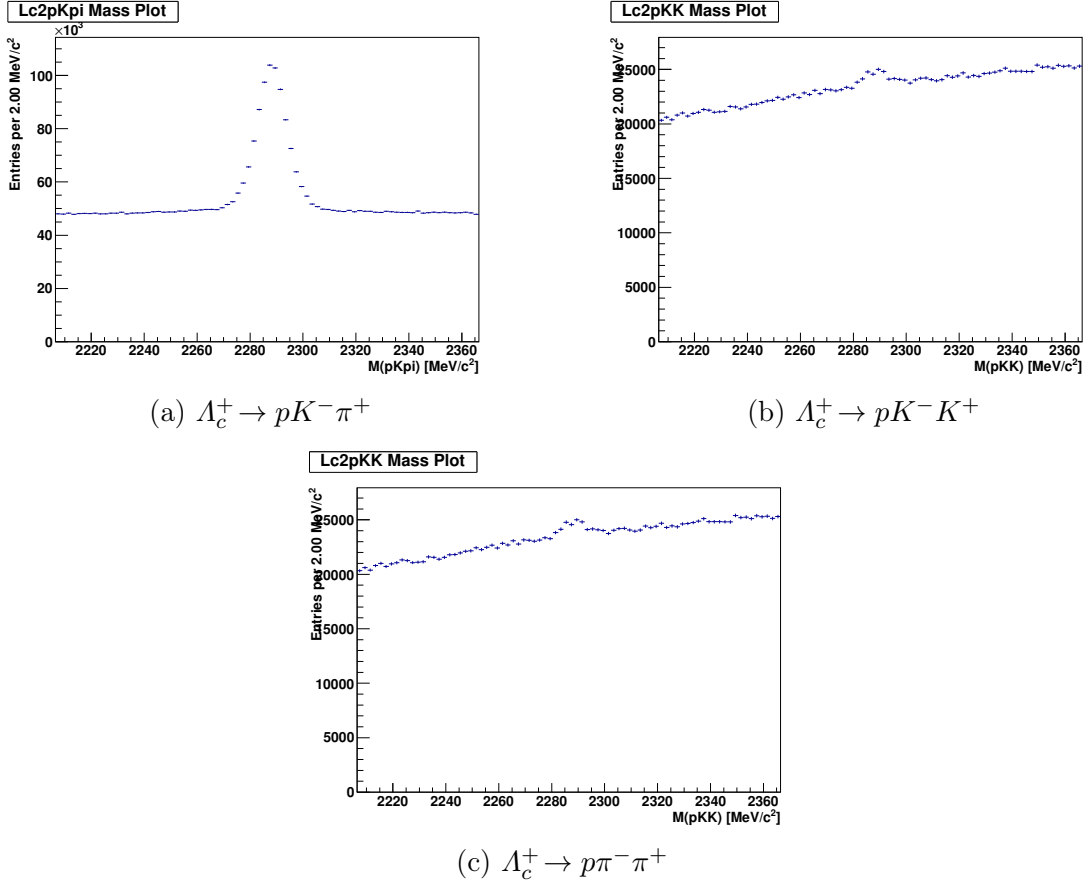


Figure 4.1: The mass distributions of the raw prompt stripping output, before the application of trigger cuts.

used for background subtraction in all yield extractions. In order to preserve the event weight normalisation, each selected  $\Lambda_c$  candidate must have daughter kinematics which correspond to a valid region of the decay phase space, such that a valid stripping efficiency may be assigned to the event.

To ensure each  $\Lambda_c$  candidate has valid daughter kinematics the DecayTreeFitter tool [134] is employed. In contrast to typical pattern reconstructions, which begin with the final daughters and work backwards to form parent particles, this tool simultaneously fits the entire decay chain using information on the momenta and vertex positions, and is able to utilise constraints using nominal particle masses. Our implementation uses a constraint on the  $\Lambda_c$  mass and no primary-vertex constraint. Convergence of the DecayTreeFitter algorithm is made necessary for an event to pass the selection. This has a minimal effect on the signal region, and primarily vetos events in the high mass sideband. The effect

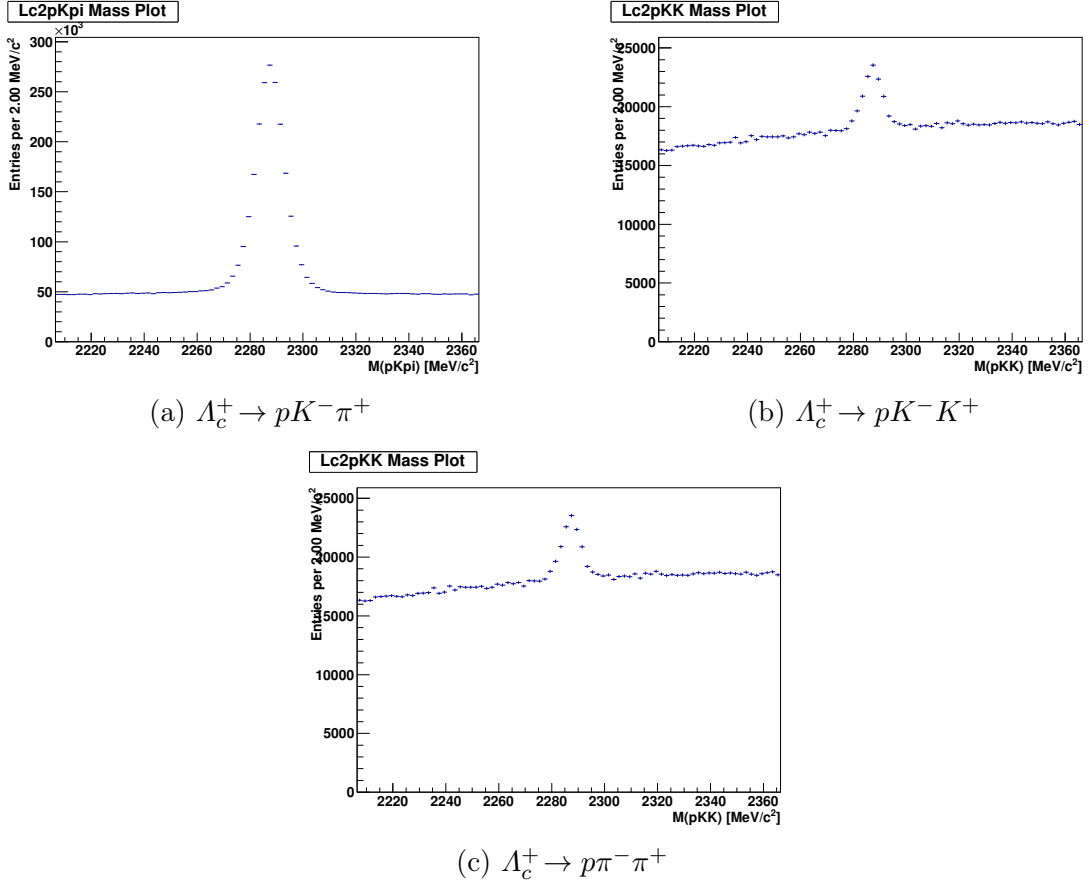


Figure 4.2: The mass distributions of the raw semileptonic stripping output, before the application of trigger cuts.

of this convergence criterion is demonstrated in the promptly selected  $\Lambda_c^+ \rightarrow pK^- \pi^+$  in Figure 4.4. This criterion is applied to both the prompt and semileptonic selections.

In order to ascertain the efficiencies of the PID DLL cuts used in the selections it is necessary to utilise the data-driven `PIDCaLib` technique. This technique uses calibration tracks from decay modes which may be cleanly reconstructed without the use of the PID discriminants. These tracks are binned in  $p$  and  $\eta$  to derive local PID efficiencies, which are then used to ascribe event-by-event PID efficiencies to the signal decays in this analysis (this procedure is outlined more fully in Section 5.1.6). There exist regions of the  $p - \eta$  phase space for which  $\Lambda_c^+ \rightarrow phh'$  signal tracks exist, but for which no calibration data exists. This is due to the lower  $p_T$  of protons in  $\Lambda^0 \rightarrow p\pi^-$  decays than those protons in  $\Lambda_c^+ \rightarrow phh'$  decays. In such regions it is impossible to attribute a PID efficiency to the signal data. It is therefore necessary to include a variety of fiducial cuts on the kinematics

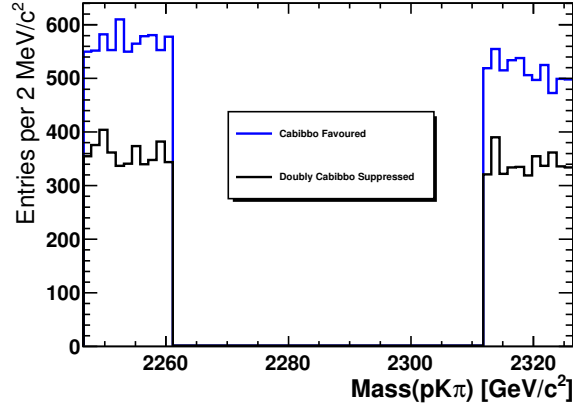


Figure 4.3: The mass sidebands from data of the promptly selected  $\Lambda_c^+ \rightarrow pK^- \pi^+$  and  $\Lambda_c^+ \rightarrow p\pi^- K^+$ , after the final selection. Integrating these distributions and taking the ratio of the doubly-Cabibbo suppressed over the Cabibbo favoured gives combinatoric background ratio of 0.67.

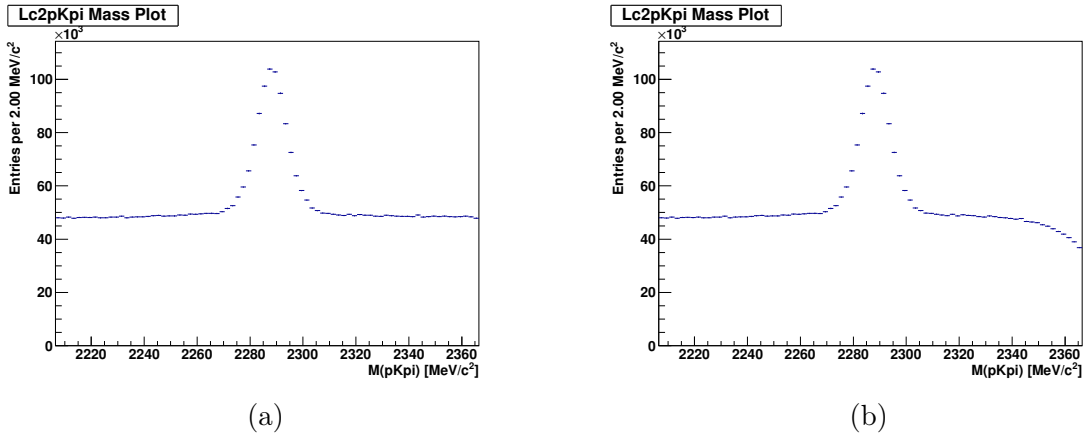


Figure 4.4: Mass distributions of promptly selected  $\Lambda_c^+ \rightarrow pK^- \pi^+$  before (a) and after (b) the application of the DTF configuration and convergence criterion.

of the daughter tracks in the  $\Lambda_c^+ \rightarrow phh'$  signal decays to exclude  $\Lambda_c$  candidates with daughter particles falling in such regions. This ensures a reliable PID efficiency is ascribed to each event of the signal data. The vetoed regions are given in Table 4.4, and illustrated in Figure 4.5. The vetoes exclude between 15 – 30 % of signal candidates varying on a per-mode basis.

Daughter Particle	Vetoed Regions
$\pi$	$\eta < 2.0, \eta > 4.5, p < 5\text{GeV}/c^2, p > 100\text{GeV}/c^2$
$K$	$\eta < 2.0, \eta > 4.5, p < 5\text{GeV}/c^2, p > 100\text{GeV}/c^2$
$p$	$\eta < 2.0, \eta > 4.5, p < 15.6\text{GeV}/c^2, p > 100\text{GeV}/c^2,$ $(2.0 < \eta < 2.625 \text{ and } p > 29.3\text{GeV}/c^2),$ $(2.625 < \eta < 3.25 \text{ and } p > 44.83\text{GeV}/c^2)$

Table 4.4: Kinematically vetoed regions of the  $p$  and  $\eta$  phase space such that the data-driven PIDCalib method may be properly utilised.

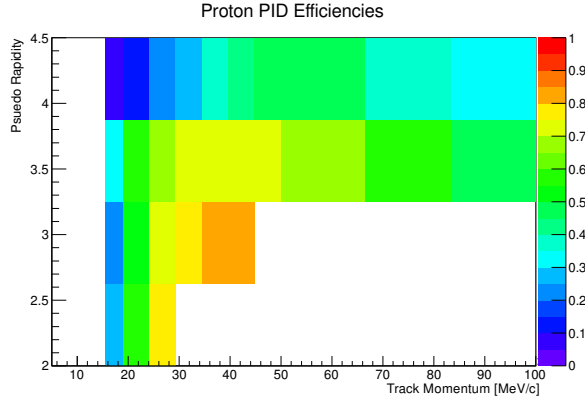


Figure 4.5: Kinematically vetoed regions of the  $p$  and  $\eta$  phase space for promptly selected protons. White bins indicate vetoed regions, coloured bins give the average efficiency of the PID DLL cuts on proton tracks in that region, as evaluated using the  $\Lambda^0 \rightarrow p\pi^-$  PID calibration samples.

### Offline selection of prompt candidates

The  $\Lambda_c$  mean lifetime is 200fs [10], which is much lower than that of charmed mesons (for example, the  $D^+$  mean lifetime is 1040ps). Due to the resultant low separation of the  $\Lambda_c$  decay vertex with respect to the primary vertex, combinatoric backgrounds resulting from combinations of unrelated tracks are large in the case of promptly produced  $\Lambda_c$ . In order to suppress these backgrounds, a multivariate selection is used in tandem with the offline PID DLL cuts in the selection of  $\Lambda_c^+ \rightarrow p\pi^- K^+$  candidates.

Multivariate selections combine information from numerous input variables describing a process and combine it to form one variable. When attempting to discriminate between multiple species in a sample, a simple selection placed on the multivariate can possess much greater discriminatory power than simple selections placed upon the input variables. A decision tree (BDT, [135]) consists of a branching tree of nodes. Starting from one node, a simple selection requirement is made on one or a combination of the input variables with

a binary output. Each output leads to a separate node whereby another requirement is made. Ultimately at the final nodes signals are assigned a value corresponding to their likelihood of being each species. A boosted decision tree (BDT [136]) consists of a series of trees in a “forest”, whereby the architecture of each tree is informed by the outcomes of the previous trees. Several algorithms exist to dictate the development of the forest, or the “boosting”. One such algorithm, ADABOOST [137], assigns greater weights for a given tree in the training phase to events which were misclassified in previous trees.

A boosted decision tree was trained using the ADABOOST adaptive boosting algorithm on the  $\Lambda_c^+ \rightarrow pK^-\pi^+$  data. The *sPlots* technique is utilised to disentangle the signal and background input variable distributions. The training and testing of the BDT was performed in TMVA [138]. Initially the TMVA default values for BDT architecture were utilised. The input variables were chosen such that the selection possesses minimum sensitivity to the kinematics of the daughter particles in the  $\Lambda_c$  decay to ensure the BDT’s selection of events has a uniform efficiency across the decay modes. These variables are:

- Reconstructed  $\Lambda_c$   $p_T$ .
- $\Lambda_c$  maximum *DoCA*, the distance of closest approach between any of the possible pairs of particles in the  $\Lambda_c$  decay.
- $\Lambda_c$  *DIRA*, the direction angle of the reconstructed  $\Lambda_c$  momentum w.r.t. the direction of flight to the best primary vertex.
- $\Lambda_c$  end vertex  $\chi^2$ .
- $\Lambda_c$  flight distance  $\chi^2$  with respect to the primary vertex.
- $\Lambda_c$  *IP* $\chi^2$ , the impact parameter  $\chi^2$  w.r.t. the best primary vertex, or the increase to the  $\chi^2$  of the associated primary vertex when the reconstructed  $\Lambda_c$  momentum is included in the primary vertex fit.

The distributions of these variables for signal and background for the prompt selection training sample, before the offline PID cuts, are given in Figure 4.6. These are acquired using the *sPlots* technique to extract the signal and combinatoric distributions.

In the selection of the Cabibbo favoured and singly-Cabibbo suppressed modes, we do not apply any MVA offline selection but do apply offline PID cuts. In the selection of  $\Lambda_c^+ \rightarrow p\pi^-K^+$  candidates, the offline PID cuts and the BDT itself are optimised in tandem recursively to attain the most powerful discrimination attainable. This procedure involves the following steps:

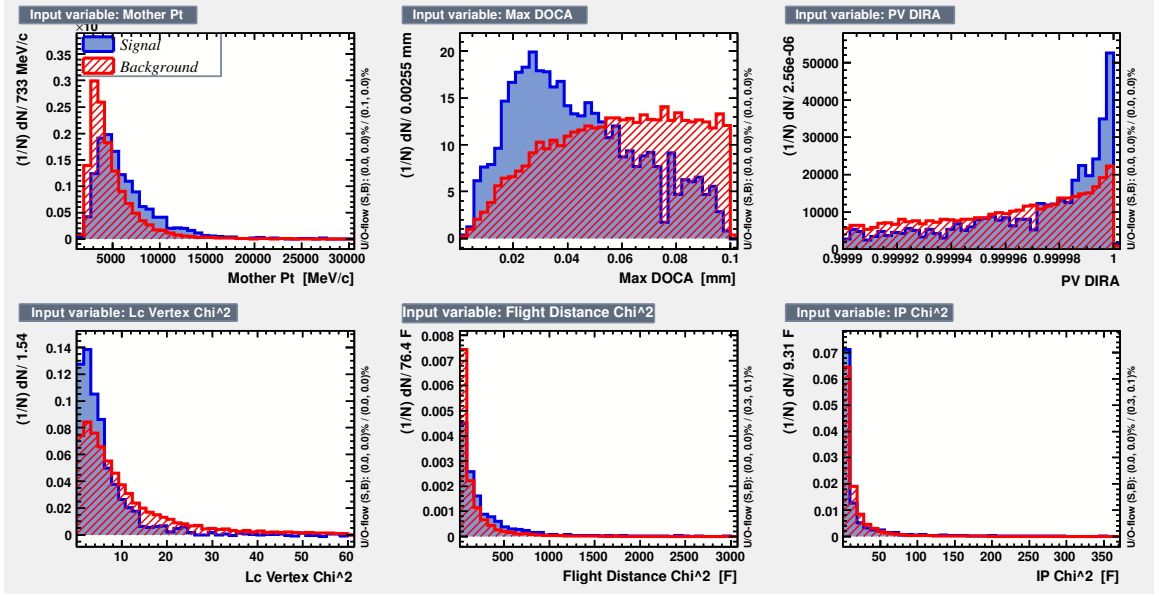


Figure 4.6: BDT input variables distributions for signal and combinatoric background, from the promptly selected  $\Lambda_c^+ \rightarrow pK^-\pi^+$  training sample.

1. A BDT is trained on the training sample without any offline PID cuts applied.
2. The BDT response cut is then optimised in CROP with the cuts on the PID DLL variables, using  $S/\sqrt{S+B}$  as a figure of merit. As the PID cuts will exclude some background events which the BDT is trained to exclude, the BDT will not be optimally trained for a selection in conjunction with the PID DLL cuts.
3. A new BDT is then trained on a data sample which has had the optimum PID DLL cuts as found in step 2 applied as a preselection. The new BDT response cut is then optimised in CROP in tandem with the cuts on the PID DLL variables to find new optimum PID cuts for this tree architecture.
4. This process is repeated, with new BDTs being trained until the optimum PID response as found by CROP converges.

At this point we can at the very least say that a local maximum in the N-dimensional cutspace has been found. A cross check is carried out to look for higher maxima of signal significance. A set of arbitrary PID cuts are applied to the training sample initially, and the simultaneous PID/BDT optimisation is reperformed. The arbitrary PID cuts used are:

- proton  $DLL(p - \pi) > 10$ .

- proton  $DLL(p - K) > 10$ .
- kaon  $DLL(K - \pi) > 8$ .

The same optimum PID and BDT cuts are attained, demonstrating that the maximum found is likely a global maximum.

At this stage an optimisation of the tree architecture takes place. The optimisation process takes into account both signal and background discrimination and the compatibility of the BDT response between the training and testing phases (as evaluated with a Kolmogorov Smirnov test [139] by TMVA). The former should be maximised for obvious reasons. The latter gives an indication of the level of overtraining, where the training phase becomes sensitive to the statistical fluctuations in the training sample, leading to a sub-optimal MVA architecture. The variables defining the tree architecture which were optimised are:

$N_{\text{trees}}$  - The number of trees in the forest.

**Boost type** - The algorithm which determines the boosting procedure.

**Adaptive Boost  $\beta$**  - The learning rate for the adaptive boost algorithm.

**Maximum Tree Depth** - The maximum depth of the trees, or depth of nodes per tree.

**Steps in Node Optimisation** - At each node in the tree the data is split according to a binary decision based on the input variable of interest at the node. This variable is the number of steps in the variable range used to find the optimum splitting point at each node.

The optimum values of these parameters are given in Table 4.5.

The final BDT classifier output, overtraining check and ROC curve are shown in Figure 4.7. The final PID DLL and BDT response cuts are given in Table 4.6. Assuming the naive expected ratio of doubly-Cabibbo suppressed to Cabibbo favoured decays, the maximum  $S/\sqrt{S+B}$  significance of the promptly selected  $\Lambda_c^+ \rightarrow p\pi^-K^+$  may be estimated. After the final PID cuts, this is done by summing the signal and background weights and varying the BDT response to find the optimum cut.

The tighter offline PID cuts used in the selection of all prompt modes (along with the semileptonic PID cuts) are given in Table 4.6.

Table 4.5: The BDT architecture variables which were optimised, showing the default and optimum values.

Architecture Variable	Default Value	Tested Values	Optimum Value
Boosting Type	Adaptive	Adaptive, Gradient, Bagging	Adaptive
Adaptive Boost $\beta$	0.5	0.1, 0.2, 0.3, 0.4, 0.5, 0.6, 0.7, 1.0	0.3
$N_{\text{trees}}$	400	10, 20, 40, 50, 80, 100, 150, 200, 300, 400	50
Maximum tree depth	3	2, 3, 4, 5	3
Steps in Node Optimisation	20	10, 12, 14, 16, 18, 20, 22, 24, 26	20

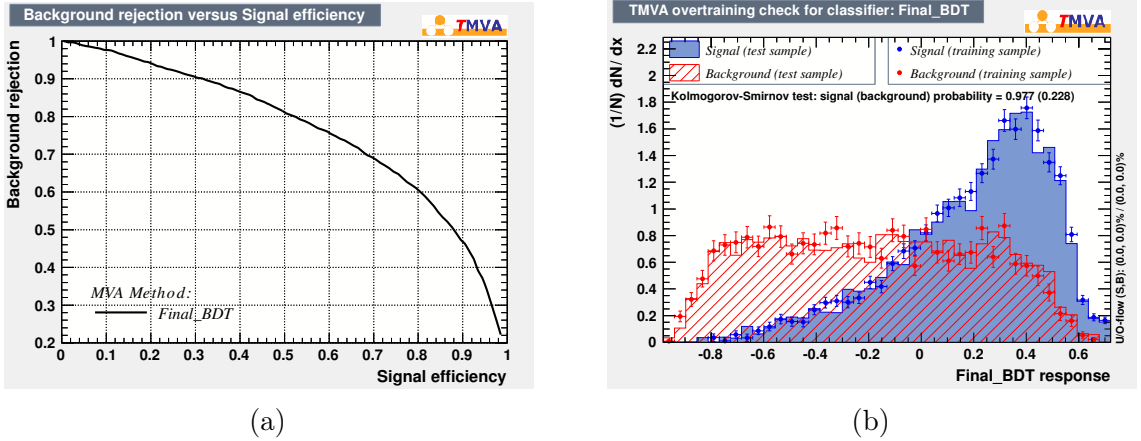


Figure 4.7: The receiver operating characteristic (ROC) curve (a) and the classifier output distributions for the training/testing phases (b) for the final BDT. The Kolmogorov-Smirnov tests for compatibility in the training and testing phases indicate that the training and testing sample distributions agree in both signal and background.

### Offline selection of semileptonic candidates

The higher separation from the primary vertex in semileptonically produced  $A_c$  over those produced promptly, due to the high mean lifetime of the  $A_b^0$  (approximately 1500 fs), results in a much lower combinatoric background in the semileptonic data. Investigation of multivariate analysis and of further rectangular cuts on kinematic properties of the  $A_b^0$  and  $A_c^+$  decays over those in the stripping demonstrated no significant gains in discrimination between signal and combinatoric backgrounds. Tighter cuts on the PID DLL variables compared to those in the stripping were shown to offer significant discrimination. As such PID DLL cuts were optimised in CROP for maximum sensitivity to the  $A_c^+ \rightarrow p\pi^- K^+$  mode, with the optimum cuts shown in Table 4.6. It should be noted that the tighter PID cuts in the semileptonic  $A_c^+ \rightarrow p\pi^- \pi^+$  come from the stripping line for this mode, and are very sub-optimal for the other  $A_c^+ \rightarrow phh'$  modes. As such these are the only differences in

offline selection between the semileptonic modes.

Selection	Particle	PID Cuts
Prompt $\Lambda_c^+ \rightarrow phh'$	$p$	$DLL_{(p-\pi)} > 20, DLL_{(p-K)} > 12$
	$K$	$DLL_{(K-\pi)} > 10, DLL_{(K-p)} > -8$
	$\pi$	$DLL_{(K-\pi)} < 0$
SL $\Lambda_c^+ \rightarrow p\pi^-\pi^+$	$p$	$DLL_{(p-\pi)} > 20, DLL_{(p-K)} > 9$
	$\pi$	$DLL_{(K-\pi)} < 0$
Other SL $\Lambda_c^+ \rightarrow phh'$	$p$	$DLL_{(p-\pi)} > 20, DLL_{(p-K)} > 9$
	$K$	$DLL_{(K-\pi)} > 10$
	$\pi$	$DLL_{(K-\pi)} < 10$

Table 4.6: The final PID cuts used in each of the selections in the analysis.

### 4.3.4 Mass spectra

The mass spectra at each stage of selection are given herein to demonstrate the effects of the selection at each stage. These are given in Figure 4.8 – Figure 4.13. The mass range is centred on the nominal  $\Lambda_c$  mass  $\pm 80 \text{ MeV}/c^2$ . The terms in the legend are as follows:

**Raw** - The mass spectra of all stripped candidates, i.e. the raw output of the stripping selections.

**Trigger** - The mass spectra of the stripped candidates which pass the trigger requirements.

**Trigger and PID** - The mass spectra of the stripped candidates which pass the trigger requirements and the tight offline PID cuts.

**Full Selection** - The mass spectra of the stripped candidates passing the trigger, offline PID, kinematic vetoes and DTF convergence requirement.

In the prompt, the TIS trigger chain vetoes very few candidates. This is expected due to the lack of dedicated Hlt2 lines for the Cabibbo-suppressed modes and the inefficiency of the Cabibbo-favoured dedicated Hlt2 line - what prompt  $\Lambda_c^+ \rightarrow phh'$  LHCb recorded in 2011 was almost entirely triggered independently of the  $\Lambda_c$  decay. In the semileptonic, the effect of the TOS chain is to veto a large amount of background while vetoing a relatively lower signal fraction - this is to be expected given the signal-enhancing cuts in the topological trigger. In both analyses the background is reduced considerably with the application of the PID cuts. The kinematic vetoes can be seen to veto signal and background indiscriminately, while the DTF convergence requirement results in candidates at high masses being vetoed in those channels with kaons in the final state.

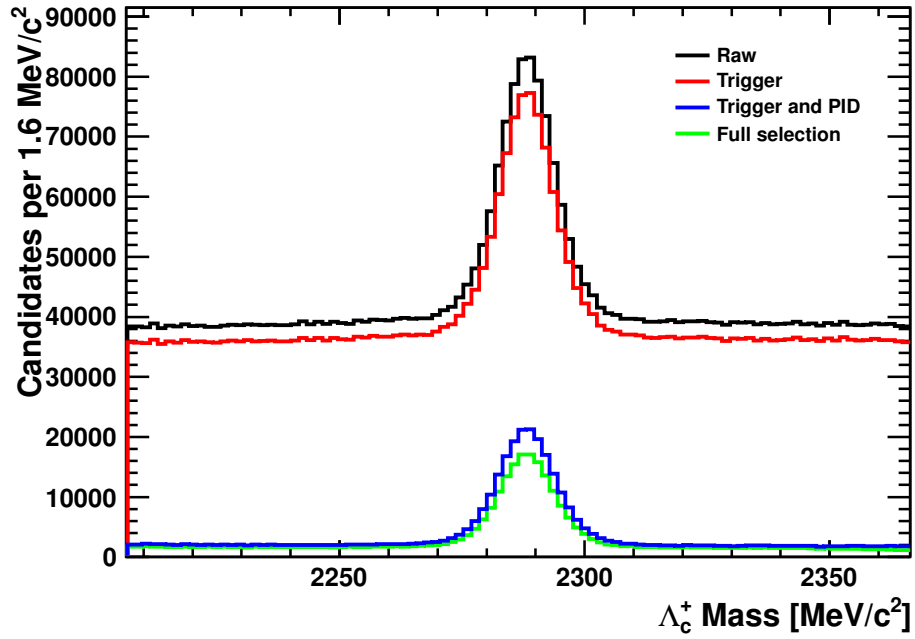


Figure 4.8: The mass distributions of the prompt  $\Lambda_c^+ \rightarrow pK^-\pi^+$  for each stage of selection.

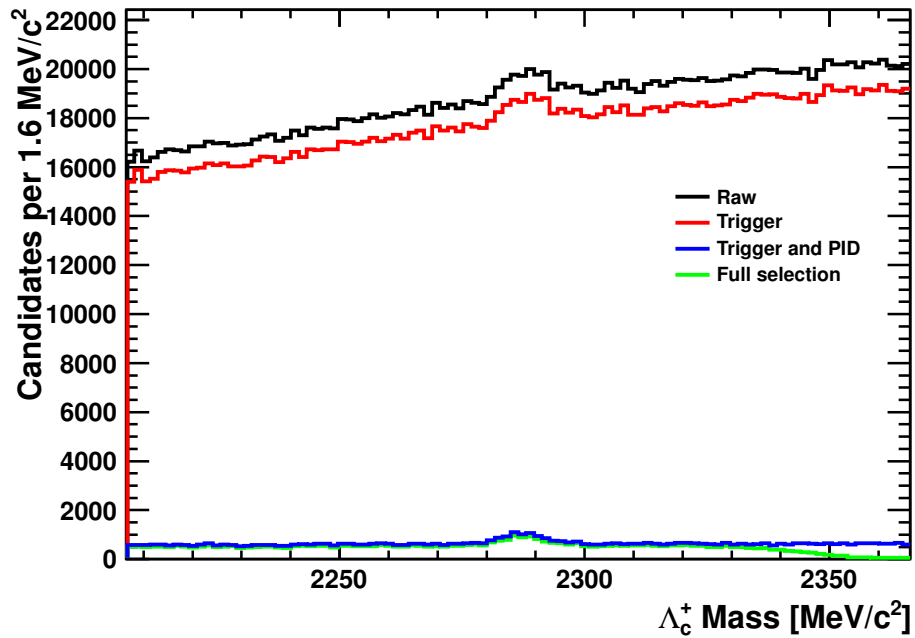


Figure 4.9: The mass distributions of the prompt  $\Lambda_c^+ \rightarrow pK^-K^+$  for each stage of selection.

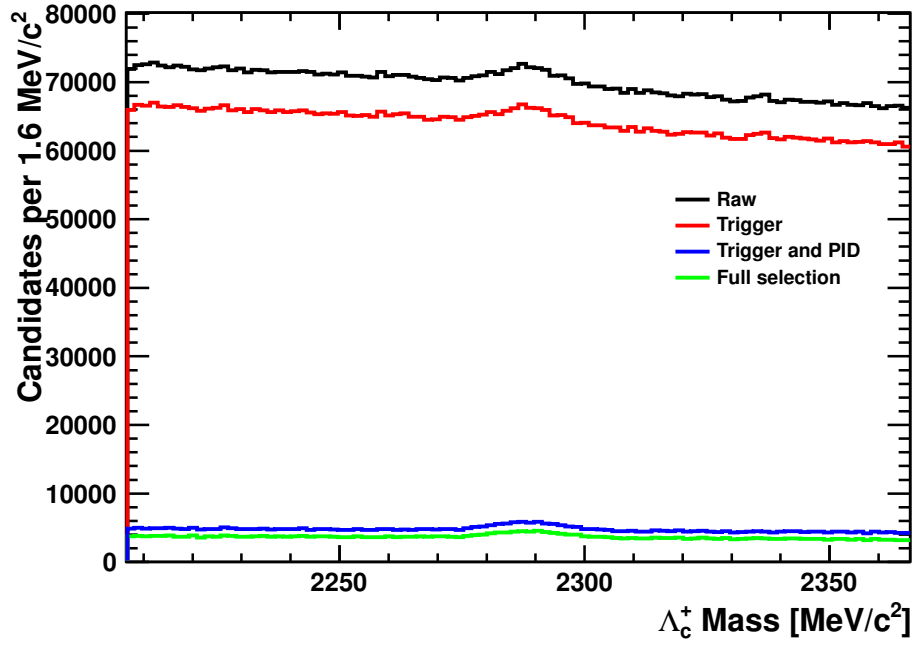


Figure 4.10: The mass distributions of the prompt  $\Lambda_c^+ \rightarrow p\pi^-\pi^+$  for each stage of selection.

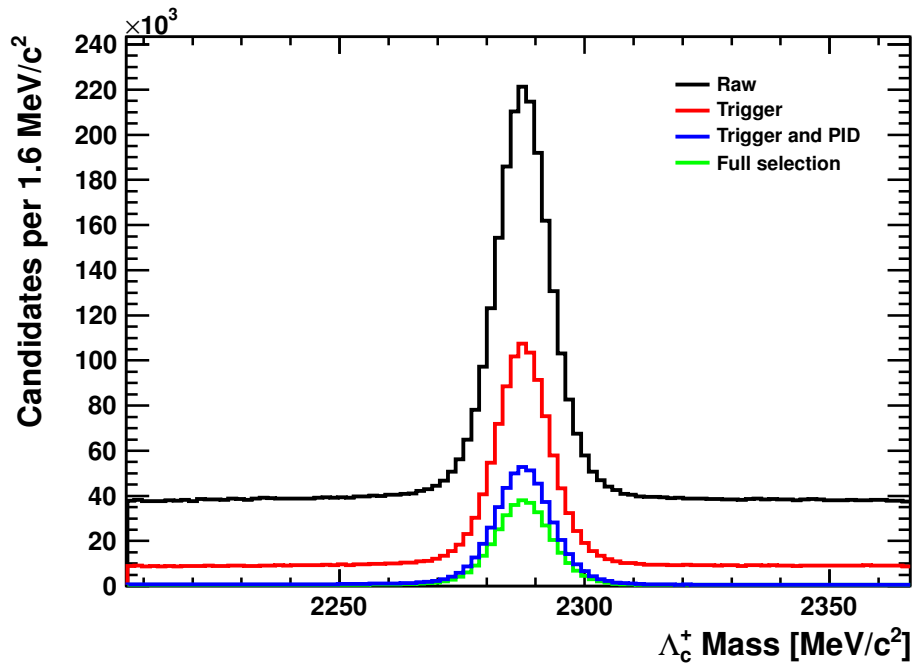


Figure 4.11: The mass distributions of the SL  $\Lambda_c^+ \rightarrow pK^-\pi^+$  for each stage of selection.

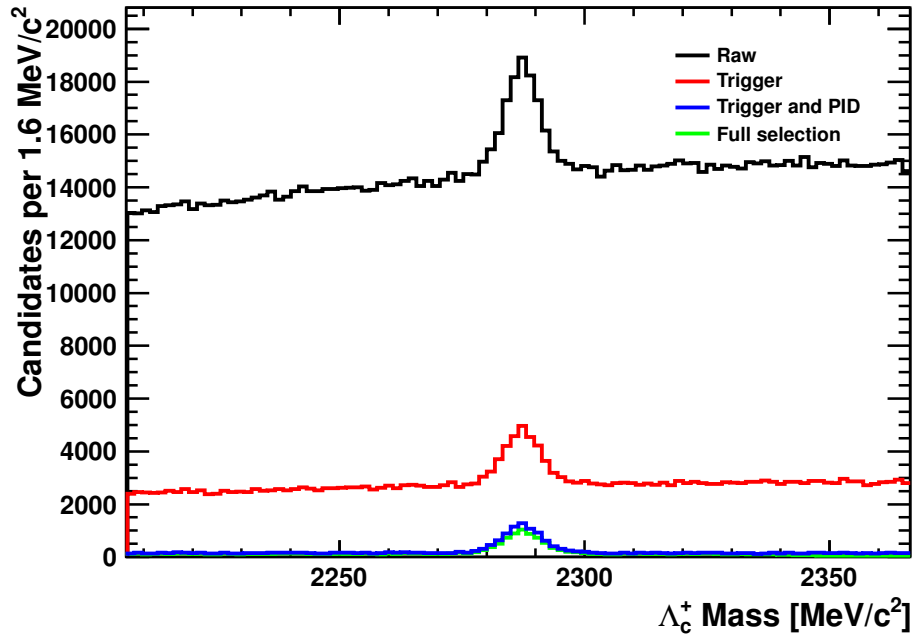


Figure 4.12: The mass distributions of the SL  $\Lambda_c^+ \rightarrow pK^-K^+$  for each stage of selection.

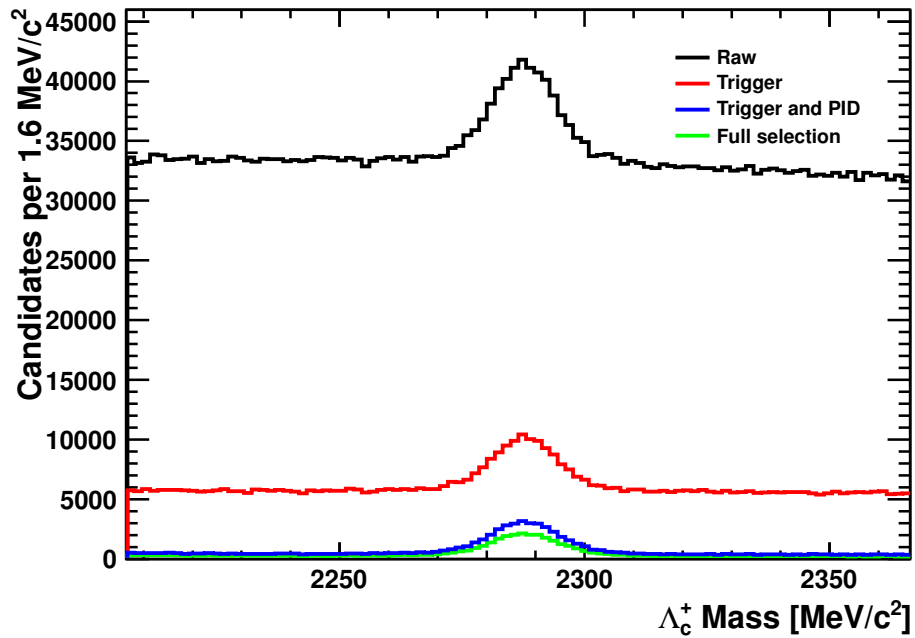


Figure 4.13: The mass distributions of the SL  $\Lambda_c^+ \rightarrow p\pi^-\pi^+$  for each stage of selection.

## 4.4 Prompt backgrounds

Herein we discuss the potential backgrounds in the prompt analysis. There are two broad categories of backgrounds that our selections may be prone to: reflections from  $D^+$  decays and  $\Lambda_c$  decays. There are a number of charmed meson decays which, if mis-reconstructed in some fashion, may result in peaking backgrounds in the  $|\Delta c|$  candidate mass window around the nominal. A brief summation of these are as follows (in all cases  $h$  refers to any permutation of charged kaons and pions):

$D^+ \rightarrow hhh/D_s^+ \rightarrow hhh$  **reflections** - all the  $D^+/D_s^+$  daughters are reconstructed, but at least one of the daughters are misidentified as another charged hadron.

$D^+ \rightarrow hhhh^0/D_s^+ \rightarrow hhhh^0$  **partial reconstruction** - the neutral daughter hadron, for example a  $\pi^0$  or  $K_s^0$ , is not reconstructed and at least one of the charged daughters is misidentified as another charged hadron.

$D^0 \rightarrow hhhh$  **partial reconstruction** - one charged daughter is not reconstructed, and at least one of the charged daughters is misidentified as another charged hadron.

The misidentification has the effect of smearing the candidate mass distribution and shifting it from the nominal  $\Lambda_c$  mass in non-trivial ways depending on the decay kinematics. To parametrise these distributions we apply our selection to simulated  $D$  decays while forcing the required mass hypotheses on the set of  $D$  daughters such that candidates manifest with a final state corresponding to one of the  $\Lambda_c^+ \rightarrow phh'$  modes under investigation.

### 4.4.1 $D_s^+ \rightarrow hhh/D^+ \rightarrow hhh$ mis-reconstructions

#### Method

There are a large number of  $D^+/D_s^+$  decays which, with a single final state kaon or pion mis-identified as a proton, can lead to their manifestation in the same final state as one of the  $\Lambda_c^+ \rightarrow phh'$  modes. To account for these  $D^+ \rightarrow hhh/D_s^+ \rightarrow hhh$  reflections, we consider the mis-identifications which can arise which will likely result in candidates in the region of the  $\Lambda_c$  mass.

The possible reflections are constrained by one of the same-sign daughters being mis-identified as a proton, resulting in only four generic cases whereby single mis-identification reflections are relevant. As the number of decays which can result in

such a mis-identification are numerous, we investigate first the modes which have the highest branching fractions corresponding to these general cases of mis-identification.

These decays are outlined in Table 4.7. The most abundantly produced  $D^+$  mode in which a pion mis-identification as proton is possible is  $D^+ \rightarrow \pi^+\pi^+K^-$ , with a measured branching fraction of  $(9.13 \pm 0.19) \%$  [140].  $D^+$  decays with a same-sign kaon in the final state require at least one Cabibbo-suppressed transition, and their branching fractions are correspondingly lower. The most abundant of these is the decay  $D^+ \rightarrow \pi^+K^-K^+$ , with a branching fraction of  $(9.54 \pm 0.26) \times 10^{-3}$  [140]. The highest branching fraction of a  $D_s^+$  with a same-sign pion or kaon in the final state is in both cases the decay  $D_s^+ \rightarrow \pi^+K^-K^+$ , with a branching fraction of  $(5.49 \pm 0.27) \%$  [141], [142].

$D^+ \rightarrow hhh$ Mode	$D^+$ decay $\mathcal{B}$ [%]	mis-ID	$\Lambda_c^+ \rightarrow phh'$ Mode
$D^+ \rightarrow \pi^+\pi^+K^-$	$(9.13 \pm 0.19) \times 10^{-2}$	$\pi^+ \rightarrow p$	$\Lambda_c^+ \rightarrow pK^-\pi^+$
$D^+ \rightarrow K^+K^-\pi^+$	$(9.54 \pm 0.26) \times 10^{-3}$	$K^+ \rightarrow p$	$\Lambda_c^+ \rightarrow pK^-\pi^+$
$D_s^+ \rightarrow K^+K^-\pi^+$	$(5.49 \pm 0.27) \times 10^{-2}$	$\pi^+ \rightarrow p$	$\Lambda_c^+ \rightarrow pK^-K^+$
$D_s^+ \rightarrow K^+K^-\pi^+$		$K^+ \rightarrow p$	$\Lambda_c^+ \rightarrow pK^-\pi^+$

Table 4.7: The decays which correspond to a  $D^+ \rightarrow hhh/D_s^+ \rightarrow hhh$  reflection where a positive charged kaon or pion is mis-identified as a proton. We provide the branching fractions and the mis-ID corresponding to the  $\Lambda_c^+ \rightarrow phh'$  modes in which the reflections manifest. The decays given possess some of the highest branching fractions of the  $D^+/D_s^+$  decays which can result in a  $\Lambda_c^+ \rightarrow phh'$  final state under a single misidentification.

## Efficiency and yield estimations

The numbers of simulated events passing the various stages of our selection are detailed in Table 4.8. For all modes, zero events pass the full selection. A finite number of candidates pass just the trigger and stripping, and a finite number of candidates pass just the stripping and PID. As the trigger chain in the prompt analysis is TIS, the subset of events passing the TIS requirement should not be dependent on the PID response. We can therefore factorise the individual efficiencies to better estimate the overall efficiency of our selection on the backgrounds. The full efficiency of the selection is therefore given as:

$$\epsilon_{total} = \frac{\epsilon_{(\text{strip,PID})}\epsilon_{(\text{strip,trig})}}{\epsilon_{\text{strip}}} \quad (4.2)$$

where  $\epsilon_{\text{strip}}$  is the efficiency of the stripping selection alone,  $\epsilon_{(\text{strip,PID})}$  is the efficiency of the stripping and PID selections and  $\epsilon_{(\text{strip,trig})}$  is the efficiency of the stripping and trigger

selections (as the stripping selection is applied to the baseline already it is necessary to include it in both the expressions for the PID and trigger efficiencies and factor it out). The efficiencies for the modes are shown in Table 4.9. Where non-zero numbers of events pass orthogonal selection, we provide an efficiency as per Equation 4.2. If no events survive any orthogonal selections, we provide upper limits. These efficiencies are rough calculations - the PID efficiency is derived using the PID response in the simulation, which is known to be poorly modelled. The numbers of events surviving the selections are very low, such that the binomial errors on the efficiencies are high. Nonetheless, they serve as a reasonable approximation when estimating the orders of magnitude of the efficiencies of our prompt selection on the  $D$  decays. The efficiencies for the full prompt selection are estimated to be of order  $\mathcal{O}(10^{-9}) - \mathcal{O}(10^{-8})$  for the various  $D$  decays considered.

The prompt charm cross sections at  $\sqrt{s} = 7$  TeV at LHCb have been measured in [130]. Integrated over the LHCb acceptance, those relevant to this analysis are:

- $\sigma(\Lambda_c) = 230 \pm 77 \mu\text{b}$
- $\sigma(D^+) = 676 \pm 137 \mu\text{b}$
- $\sigma(D_s^+) = 194 \pm 38 \mu\text{b}$
- $\sigma(D^0) = 1488 \pm 182 \mu\text{b}$

Taking these, with the estimated efficiencies of our selection on the above  $D$  decays, we can estimate the number of charged  $D$  reflections surviving the prompt  $\Lambda_c$  selection in the 2011 dataset. The typical expected  $D$  candidates passing our selection are estimated as:

$$N_{\text{pass}} = \mathcal{L}\sigma\mathcal{B}\epsilon_D \quad (4.3)$$

where  $\mathcal{L}$  is the integrated luminosity of the 2011 dataset,  $\sigma$  is the production cross section in the LHCb acceptance of the parent  $D$ ,  $\mathcal{B}$  is the branching fraction of the  $D$  decay leading to the reflection and  $\epsilon_D$  is the estimated efficiency of the prompt  $\Lambda_c$  selection on the  $D$  decay. These are summarised in Table 4.10. The estimations for  $N_{\text{pass}}$  are of the order of 1000 for the decays considered.

This somewhat low yield is to be expected given our selection's design. Tight PID cuts are used on every final state daughter in the prompt selection. In addition to suppressing combinations of unrelated tracks (of which there are many, due to the short  $\Lambda_c$  mean lifetime and low PV displacement), these serve to eliminate the majority of mis-identified reflections. The maximum lifetime cut on the reconstructed  $\Lambda_c$  candidate of 1.2 ps removes

a significant fraction (approximately 35 %) of genuine  $D$  decays, which have a mean lifetime of around 1 ps compared to 0.2 ps for the  $\Lambda_c$ . The minimum momentum requirement on the proton of 15.6 GeV/ $c$  and the requirement that at least one daughter have a transverse momentum above 1.2 GeV/ $c$  suppress the kaon/pion tracks which come from  $D$  decays (the proton momenta in genuine  $\Lambda_c$  decays are typically greater than those of the  $D$  decay daughters).

There are many components of our selection which will apply equally well to excluding other  $D$  decays. The lifetime cut will uniformly veto the same fraction of all  $D$  decays. The number of kaons and pions in the final state of each  $D$  decay will affect the momenta of the final state particles, although this is not expected to be a large effect. As such, to first order the efficacy of the momentum and PID requirements in vetoing other  $D$  decays which have not been directly examined should be comparable to the modes which were investigated. All other  $D$  decays which can result in final state reflections in the  $\Lambda_c$  reconstruction have lower branching fractions than the decays investigated herein, resulting in lower expected contamination in the 2011  $\Lambda_c$  data. In the case of reflections arising from two or three mis-identifications, we may assume that the tight PID cuts make it significantly less likely that a  $D$  decay with multiple incorrectly identified daughter tracks will pass our selection than in the case of a single mis-identification.

The number of reflection candidates expected to pass the selection for the highest  $D^+$  and  $D_s^+$  branching fractions should not be a significant factor in our fitting procedure if, as expected, they are spread across the full  $\Lambda_c$  mass window. We also provide the ratio of the number of reflection candidates expected to pass full selection in 2011 to the number of candidates in the corresponding  $\Lambda_c^+ \rightarrow phh'$  signal mode in which the reflection manifests. Given that 3 of the 4 reflections possible from the high branching ratio  $D^+/D_s^+$  decays considered manifest in the Cabibbo-favoured mode these reflection over signal ratios are generally at the per-cent level, and negligible in this analysis given other limiting systematics.

$D^+ \rightarrow hhh$ Mode	$N_{total}$	mis-ID	$N_{strip}$	$N_{strip,PID}$	$N_{strip,trig}$	$N_{strip,trig,pid}$
$D^+ \rightarrow \pi^+ \pi^+ K^-$	5128979	$\pi^+ \rightarrow p$	37492	40	125	0
$D^+ \rightarrow K^+ K^- \pi^+$	10150948	$K^+ \rightarrow p$	15141	41	329	0
$D_s^+ \rightarrow K^+ K^- \pi^+$	1007498	$\pi^+ \rightarrow p$	332	0	2	0
		$K^+ \rightarrow p$	41	0	7	0

Table 4.8: The simulated data used in the single mis-identification background studies. Shown are the numbers of events within 90 MeV/ $c^2$  of the  $A_c$  mass passing the prompt  $A_c$  selection at each stage of selection.

$D^+ \rightarrow hhh$ Mode	mis-ID	$\epsilon_{strip}$	$\epsilon_{(PID,strip)}$	$\epsilon_{(trig,strip)}$	$\epsilon_{total}$
$D^+ \rightarrow \pi^+ \pi^+ K^-$	$\pi^+ \rightarrow p$	$(7.309 \pm 0.037) \times 10^{-3}$	$(7.8 \pm 1.2) \times 10^{-6}$	$(2.4 \pm 0.2) \times 10^{-5}$	$(2.6 \pm 0.5) \times 10^{-8}$
$D^+ \rightarrow K^+ K^- \pi^+$	$K^+ \rightarrow p$	$(1.491 \pm 0.001) \times 10^{-3}$	$(4.0 \pm 0.6) \times 10^{-6}$	$(3.2 \pm 0.2) \times 10^{-5}$	$(8.8 \pm 1.5) \times 10^{-8}$
$D_s^+ \rightarrow K^+ K^- \pi^+$	$\pi^+ \rightarrow p$	$(3.295 \pm 0.181) \times 10^{-4}$	$< 1.3 \times 10^{-7} @ 95 \% \text{ CL}$	$(2.0 \pm 1.4) \times 10^{-6}$	$< 1.3 \times 10^{-7} @ 95 \% \text{ CL}$
	$K^+ \rightarrow p$	$(4.069 \pm 0.635) \times 10^{-5}$	$< 1.3 \times 10^{-7} @ 95 \% \text{ CL}$	$(7.0 \pm 2.6) \times 10^{-6}$	$< 1.3 \times 10^{-7} @ 95 \% \text{ CL}$

Table 4.9: The simulated data used in the single mis-identification background studies. Shown are the efficiencies for the various stages of the selection and the calculated efficiency of the full selection.

$D^+ \rightarrow hhh$ Mode	$\sigma(\text{mother})/\sigma(\Lambda_c)$	Decay $\mathcal{B}$	mis-ID	$N_{\text{final}}$	$\Lambda_c^+ \rightarrow phh'$ signal fraction [%]
$D^+ \rightarrow \pi^+ \pi^+ K^-$	$2.939 \pm 1.150$	$(9.13 \pm 0.19) \times 10^{-2}$	$\pi^+ \rightarrow p$	$(1.6 \pm 0.5) \times 10^3$	1.2
$D^+ \rightarrow K^+ K^- \pi^+$		$(9.54 \pm 0.26) \times 10^{-3}$	$K^+ \rightarrow p$	$(0.6 \pm 0.2) \times 10^3$	0.5
$D_s^+ \rightarrow K^+ K^- \pi^+$	$0.084 \pm 0.327$	$(5.49 \pm 0.27) \times 10^{-2}$	$\pi^+ \rightarrow p$	$< 1.4 \times 10^3 @ 95\% \text{ CL}$	51
			$K^+ \rightarrow p$	$< 1.4 \times 10^3 @ 95\% \text{ CL}$	1.1

Table 4.10: The estimated number of candidates from each charged  $D$  decay mode expected to pass the prompt  $\Lambda_c$  selection in the 2011 dataset. Also given are the ratio of this number of candidates to the number of candidates in the corresponding  $\Lambda_c^+ \rightarrow phh'$  signal mode in which the reflection manifests.

## Simulated mass distributions

We use the simulated data to investigate the shapes of the mass distributions of misreconstructed candidates. If the distributions do not peak within the  $\Lambda_c$  mass window, and have shapes which can be well modelled by a first order polynomial, it may be safely assumed that even if the number of  $D$  decays which pass our selection in this mass region is much higher in reality than our calculations say, this contribution will be accounted for by the fit model for the combinatoric background component.

As no simulated  $D$  decays pass our full selection, we investigate the shape of the mass distribution of the mis-reconstructed  $D$  candidates at various stages of the selection. We investigate the mass distribution after the stripping selection only, the mass distribution after the stripping and PID selections, and the mass distribution after the trigger and stripping selections.

An example of the  $D^+$  reflection mass distribution,  $D^+ \rightarrow K^-\pi^+\pi^+$ ,  $\pi^+$  mis-ID as  $p$ , is given in Figure 4.14 for the full candidate mass distribution, with equivalent plots of these quantities in just the  $\Lambda_c^+$  stripping mass window given in Figure 4.15. As can be seen, the candidates after stripping have mass distributions which either peak in the  $\Lambda_c$  mass region (albeit with very broad peaks) or which are not flat in this region. As can be seen in the distributions for candidates after stripping and PID and the distributions after stripping and trigger these structures become flatter as the selection is applied. It is therefore expected that the distributions of charged  $D$  reflections passing the full  $\Lambda_c$  selection will be well modelled by a first order polynomial. Our combinatoric background is also well described by a first order polynomial, and so any sum of these will simply be a new first order polynomial, for which our fit model will account.

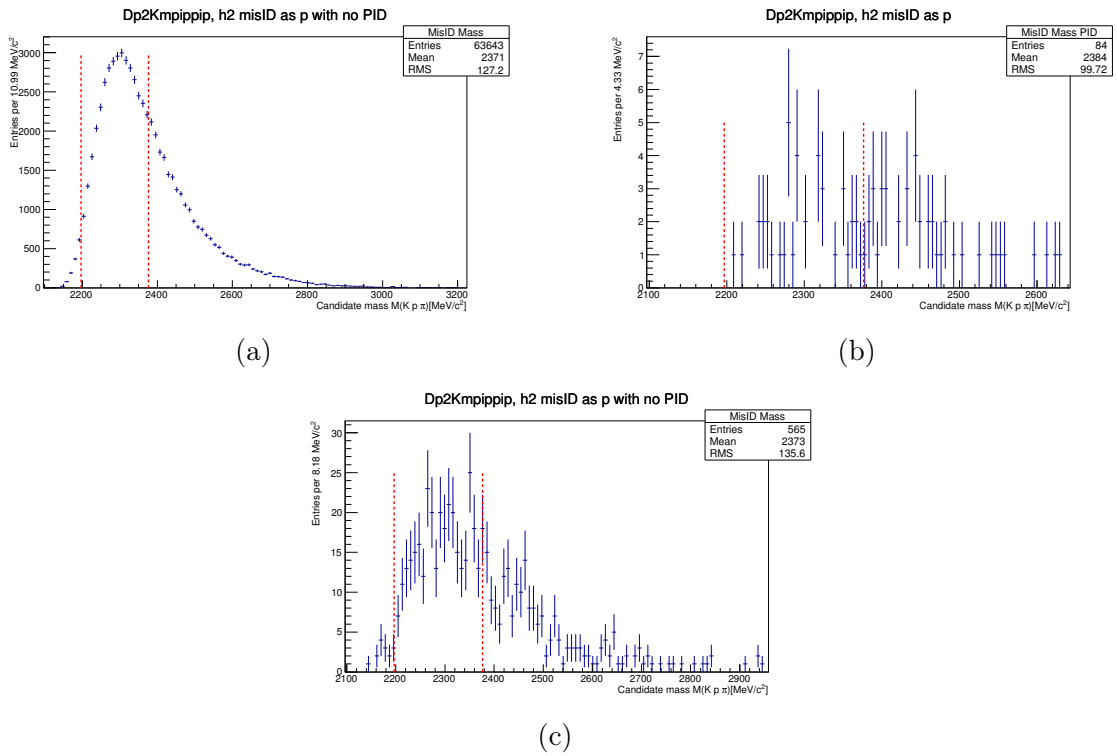


Figure 4.14: The mass distributions of simulated  $D^+ \rightarrow K^- \pi^+ \pi^+$  candidates with the proton mass hypothesis forced upon one of the daughter pions. Shaded red lines show the  $\Lambda_c$  mass region from the stripping. (a) has applied the stripping selection alone, (b) the stripping and PID, (c) the stripping and trigger.

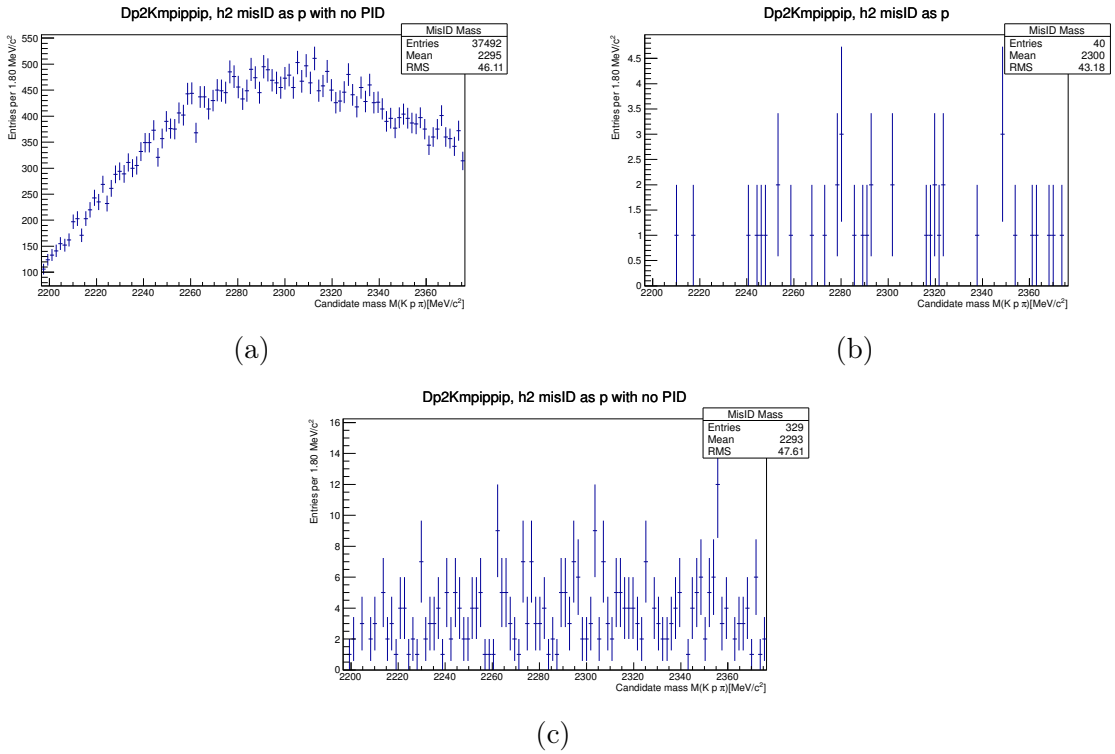


Figure 4.15: The mass distributions of simulated  $D^+ \rightarrow K^- \pi^+ \pi^+$  candidates with the proton mass hypothesis forced upon one of the daughter pions. The mass region shown is that applied in the  $\Lambda_c^+ \rightarrow phh'$  stripping. (a) has applied the stripping selection alone, (b) the stripping and PID, (c) the stripping and trigger.

## 4.4.2 Mis-ID in $\Lambda_c$ decays

In the case of cross-feed between the different  $\Lambda_c^+ \rightarrow phh'$  modes, single mis-identification of any daughter hadron is expected to result in a reconstructed mass distribution peaking away from the  $\Lambda_c$  mass. Double and triple mis-identification in the singly Cabibbo-suppressed modes is also expected to take the reconstructed candidate outside the mass range of interest. For the Cabibbo favoured and doubly-Cabibbo suppressed modes, when the pion is mis-identified as a kaon and the kaon is mis-identified as a pion, the mass distribution peaks close to the  $\Lambda_c$  mass, although the distribution will be highly smeared from the double mis-identification.

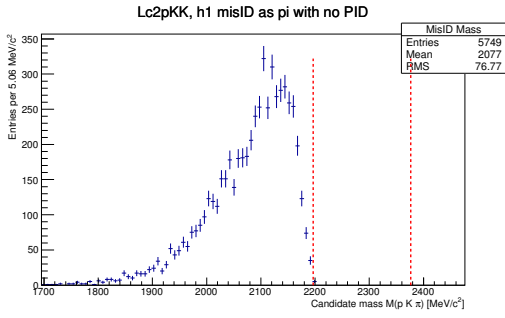
As the  $\Lambda_c^+ \rightarrow phh'$  real data has PID cuts applied at the stripping level, we use simulated  $\Lambda_c^+ \rightarrow phh'$  decays for these studies. The samples have undergone the stripping selection with PID cuts removed as described in Section 4.2.2. As in the case of the studies of  $D$  reflections, we force the wrong mass hypothesis on one or more of the truth matched signal decay daughters and recompute the invariant mass of the parent candidate.

### Single mis-ID

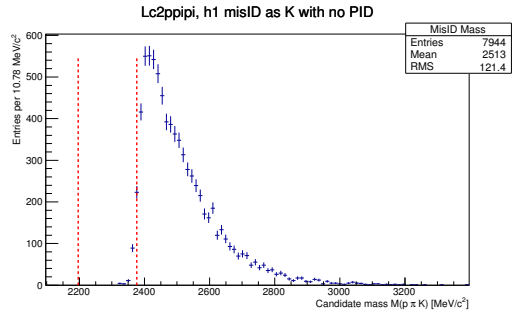
The case of a single daughter mis-identification, as expected, results in mass distributions outside of the signal region. These cases are shown in Figure 4.16, where no PID or trigger requirements are placed on the samples. As the mass distributions all peak outwith the range of interest we conclude that such cross feed between the  $\Lambda_c^+ \rightarrow phh'$  modes is not a concern.

### Double mis-ID

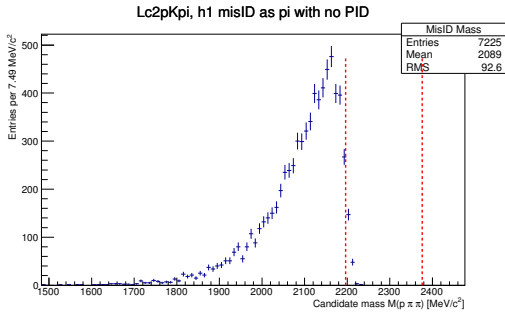
Considering that a single mis-identification of a daughter meson will result in a mass outside the range of interest, it is expected that double mis-ID in the singly Cabibbo-suppressed modes will result in a reconstructed candidate mass far from the true  $\Lambda_c$  mass, and are of no concern. We investigate the case of double mis-ID in the Cabibbo favoured mode, where both daughter mesons are incorrectly identified. Again, we find that no simulated events survive the full selection. As such, we consult the mass distributions of simulated  $\Lambda_c^+ \rightarrow pK^-\pi^+$  events with a mis-identification forced on both mesons in the decay after the stripping selection only. Candidate mass distributions are given in Figure 4.17, and demonstrated to be smeared uniformly over the stripping mass window. These candidates are well-modelled by a first-order polynomial. We conclude that in the case of possible Cabibbo-favoured decay contamination of the doubly-Cabibbo suppressed



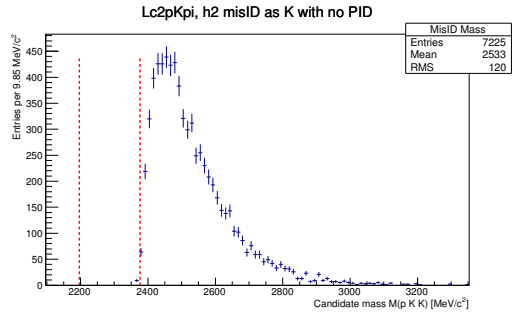
(a)  $\Lambda_c^+ \rightarrow pK^-K^+, K^- \rightarrow \pi^-$



(b)  $\Lambda_c^+ \rightarrow p\pi^-\pi^+\pi^- \rightarrow K^-$



(c)  $\Lambda_c^+ \rightarrow pK^-\pi^+, K^- \rightarrow \pi^-$



(d)  $\Lambda_c^+ \rightarrow pK^-\pi^+, \pi^+ \rightarrow K^+$

Figure 4.16: The mass distributions of simulated  $\Lambda_c^+ \rightarrow phh'$ , with the wrong mass hypothesis forced on one of the daughter mesons. The mass window indicated in red is that applied in the  $\Lambda_c^+ \rightarrow phh'$  stripping. The selection applied is a version of the stripping with all PID cuts removed, and no trigger requirements have been made.

decay, the candidates are sufficiently spread over the mass window that they will be included in the background fit. We also conclude that it will be impossible for reflections from a double mis-identification of  $\Lambda_c^+ \rightarrow pK^-\pi^+$  to imitate a narrow  $\Lambda_c^+ \rightarrow p\pi^-K^+$  peak.

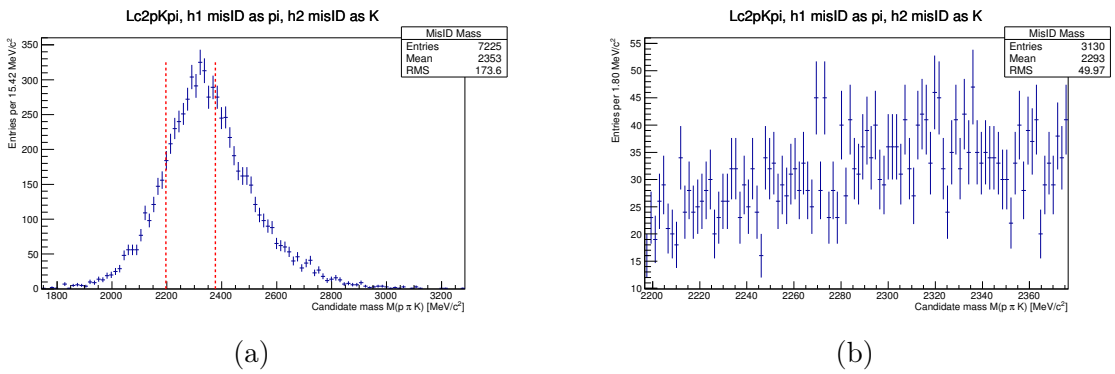


Figure 4.17: The mass distributions of simulated  $\Lambda_c^+ \rightarrow p K^- \pi^+$ , with the wrong mass hypothesis forced on both of the daughter mesons. The mass region indicated in red in (a) is that applied in the  $\Lambda_c^+ \rightarrow p h h'$  stripping, (b) shows just this region. The selection applied is a version of the stripping with all PID cuts removed, and no trigger cuts have been applied.

### 4.4.3 Reassigning mass hypotheses in data

As a more direct check we reassign the mass hypotheses of the daughter particles in the prompt  $\Lambda_c^+ \rightarrow phh'$  data, to those mass hypotheses which correspond to the final states of all possible  $D$  reflections. We show an example of these checks for  $\Lambda_c^+ \rightarrow pK^-\pi^+$  with the proton mass hypothesis changed to a kaon in Figure 4.18. No sharply peaking structures at either the  $D^+$  or  $D_s^+$  mass are found in any of the  $\Lambda_c^+ \rightarrow phh'$  data. We take this as evidence that our final datasets correspond to only candidates which are genuine  $\Lambda_c$  signal and candidates which are formed from unrelated tracks, and that reflection misreconstructions of  $D$  decays are sufficiently suppressed in our selections.

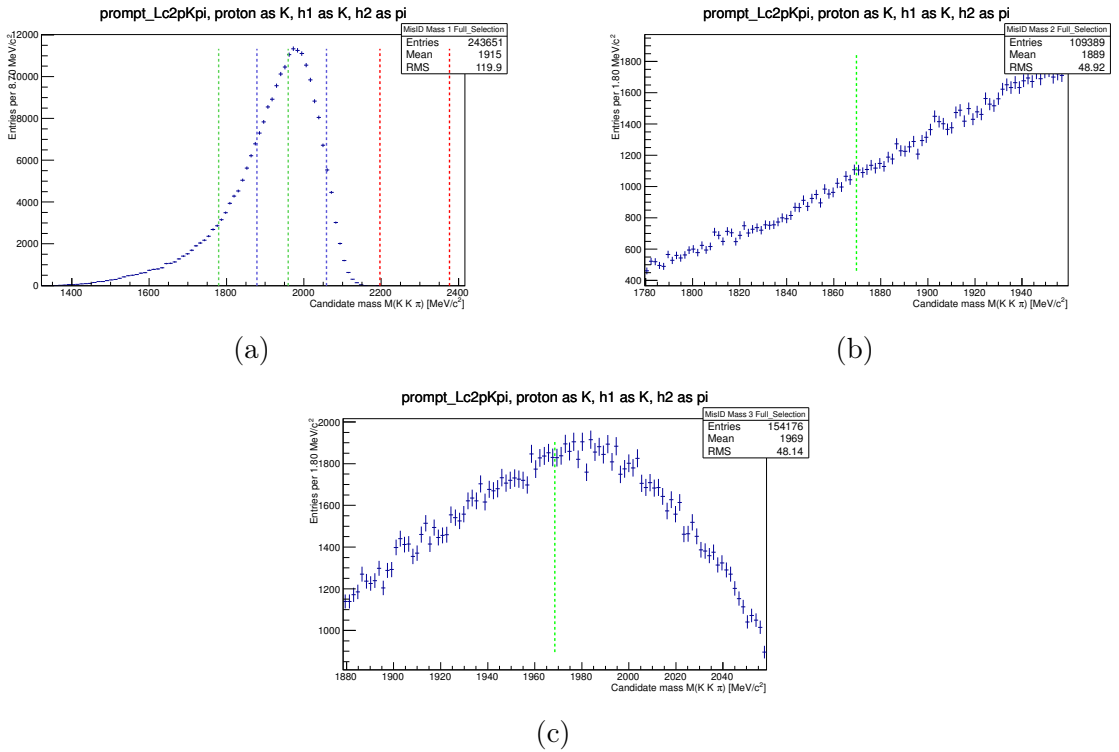


Figure 4.18: The candidate mass distribution of prompt  $\Lambda_c^+ \rightarrow pK^-\pi^+$  data after final selection, where the  $p$  mass hypothesis is changed to that of the  $K^+$ . Shown in (a) is the whole mass distribution, with the  $D^+$  mass region denoted in green with a zoom of this region in (b) and the  $D_s^+$  mass region denoted in blue with a zoom of this region in (c). This probes for the presence of reflections from mis-identified  $D^+/D_s^+ \rightarrow K^+K^-\pi^+$ .

#### 4.4.4 Summary

The likely peaking backgrounds from misidentified  $D^+ \rightarrow hhh/D_s^+ \rightarrow hhh$  and  $\Lambda_c^+ \rightarrow phh'$  decays have been investigated. We do not also explicitly investigate the case of partially reconstructed  $D^+ \rightarrow hhhh^0/D_s^+ \rightarrow hhhh^0$ - the missing neutral particle's momentum will result in mass distributions which are lower compared to those resulting from misidentification of fully reconstructed charged  $D$  decays. The variation in the missing neutral's momentum will also result in a higher smearing of the mass distributions. The branching fractions of four-body  $D$  decays are generally significantly lower than their three-body counterparts, leading to further suppression of possible candidates resulting from this misreconstruction. These factors indicate that any cross-feed from  $D^+ \rightarrow hhhh^0/D_s^+ \rightarrow hhhh^0$  decays will be less significant than in the case of  $D^+ \rightarrow hhh/D_s^+ \rightarrow hhh$  decays.

Our investigations using simulated data of the mass shapes indicate that distributions of any prominent reflections should be approximately linear across the  $\Lambda_c$  signal region. Our estimations using simulation of reflection yields passing the prompt selection place estimates on the number of  $D^+$  reflections passing the selection. These numbers are of the order  $10^3$ , although the errors on these estimates are of order 35 %. We are only able to place conservative upper limits on  $D_s^+$  reflections using simulation of  $10^5$ . As such we investigate the mass shapes of our real data with candidate mass hypotheses reassigned. We find no evidence of  $D$  reflection backgrounds contaminating our final data sets.

We do not explicitly investigate the corresponding cases of misidentified  $D^0 \rightarrow hhhh$  decays where one charged daughter is not reconstructed. The features of the prompt selection which make it so robust against charged  $D$  reflections also make it robust against partial reconstruction of neutral  $D$  mesons. The only difference between the two is that the reconstructed charged daughter kinematics will be lower in the case of neutral  $D$  decays due to the missing charged daughter's missing momentum. Our selection should therefore have a lower efficiency in the selection of these candidates compared to the investigated charged  $D$  decays due to the minimum daughter momentum requirements. While the measured cross section for  $D^0$  is higher than that of  $D^+$  or  $D_s^+$ , we still estimate that the number of reflection candidates from these sources is negligible.

We investigate cross-feed between the  $\Lambda_c^+ \rightarrow phh'$  modes. In single mis-ID cases we expect this to be negligible due to the shifting of the reconstructed candidate mass outside the signal mass window. In the case of  $\Lambda_c^+ \rightarrow pK^-\pi^+$  contamination of the  $\Lambda_c^+ \rightarrow p\pi^-K^+$  mode, we conclude that it is impossible for such contamination to mimic a narrow peak characteristic of the  $\Lambda_c^+ \rightarrow phh'$  decays.

## 4.5 Semileptonic backgrounds

Herein we discuss the potential backgrounds in the main semileptonic TOS analysis.

### 4.5.1 Mis-ID in $\Lambda_c$ decays

As in the case of the prompt analysis, we investigate cross-feed between the  $\Lambda_c^+ \rightarrow phh'$  decay modes.

#### Single mis-ID

The case of a single daughter mis-identification, as in the prompt analysis, results in mass distributions outside of the signal region. These cases are shown in Figure 4.19, where no PID or trigger requirements are placed on the samples. As the mass distributions all peak outwith the range of interest we conclude that such cross feed between the  $\Lambda_c^+ \rightarrow phh'$  modes is not a concern.

#### Double mis-ID

As in the prompt analysis, we investigate the case of double mis-ID in the Cabibbo favoured mode, where both daughter mesons are incorrectly identified. Again, no candidates survive the full stripping selection. The full mass distribution of these candidates and a close-up of the  $\Lambda_c$  mass window in the stripping selection is shown in Figure 4.20, where no PID or trigger requirements have been placed on the reconstructed candidates. As in the prompt analysis, we conclude that this Cabibbo favoured to doubly-Cabibbo suppressed mis-identification cannot mimic the narrow peaks typical of  $\Lambda_c^+ \rightarrow phh'$  decays.

### 4.5.2 Reassigning mass hypotheses in data

As a more direct check we reassign the mass hypotheses of the daughter particles on the semileptonic  $\Lambda_c^+ \rightarrow phh'$  data to check for sharply peaking structures, which would be indicative of  $D$  reflections surviving the selection. No structures are observed. We show an example of these checks for  $\Lambda_c^+ \rightarrow pK^-\pi^+$  with the proton mass hypothesis changed to a kaon in Figure 4.21.

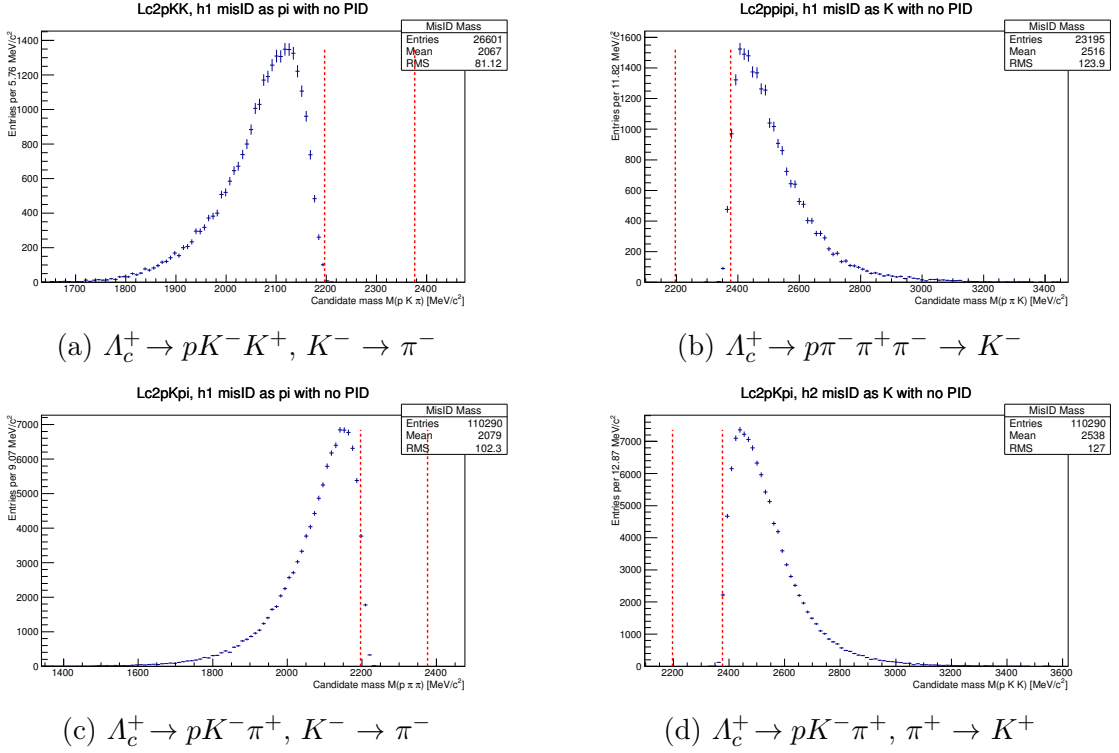


Figure 4.19: The mass distributions of simulated  $\Lambda_b^0 \rightarrow \Lambda_c^+ \mu^- \bar{\nu}_\mu$ ,  $\Lambda_c^+ \rightarrow phh'$ , with the wrong mass hypothesis forced on one of the daughter mesons. The mass region indicated in red is that applied in the  $\Lambda_b^0 \rightarrow \Lambda_c^+ \mu^- \bar{\nu}_\mu$ ,  $\Lambda_c^+ \rightarrow phh'$  stripping. The selection applied is a version of the stripping with all PID cuts removed, and no trigger cuts have been applied.

### 4.5.3 Summary

It was considered unnecessary to investigate in simulation the case whereby a  $\bar{B}^0 \rightarrow D^+ \mu^- \bar{\nu}_\mu, D^+ \rightarrow hhh$  decay is mis-reconstructed as the charge conjugate of a  $\Lambda_b^0 \rightarrow \Lambda_c^+ \mu^- \bar{\nu}_\mu, \Lambda_c^+ \rightarrow phh'$  decay. The shape of the candidate mass spectra resulting from such a mis-ID should be similar to the equivalent reflections in the prompt analysis. Despite the higher TOS trigger efficiencies of  $D$  mesons and the lower PID cuts no evidence of reflections from  $\bar{B}^0 \rightarrow D^+ \mu^- \bar{\nu}_\mu, D^+ \rightarrow hhh$  decays was found in checks with the real data. As such we assume that our selection suppresses reflections from other charm decays such that they are negligible. Upon unblinding the DCS mode we will investigate the mass distributions of double mis-ID candidates to check for contamination.

The conclusions we make regarding the SL backgrounds are broadly similar to those we state for the prompt in Section 4.4.4. We conclude that we have through examination of simulated and real data shown that our selections sufficiently suppress the backgrounds

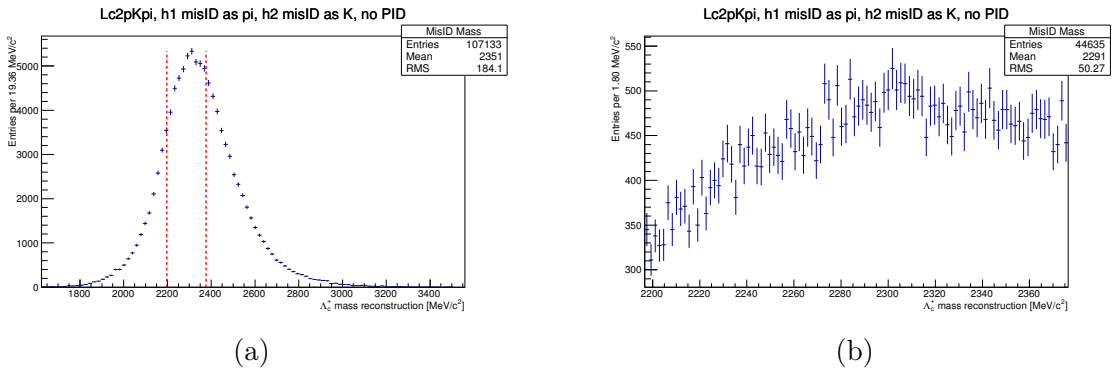


Figure 4.20: The mass distributions of simulated  $\Lambda_b^0 \rightarrow \Lambda_c^+ \mu^- \bar{\nu}_\mu, \Lambda_c^+ \rightarrow p K^- \pi^+$ , with the wrong mass hypothesis forced on both of the daughter mesons. The mass region indicated in red in (a) is that applied in the  $\Lambda_b^0 \rightarrow \Lambda_c^+ \mu^- \bar{\nu}_\mu, \Lambda_c^+ \rightarrow p h h'$  stripping, (b) shows just this region. The selection applied is a version of the stripping with all PID cuts removed, and no trigger cuts have been applied.

under consideration to a level whereby they may be considered negligible in the semileptonic analysis.

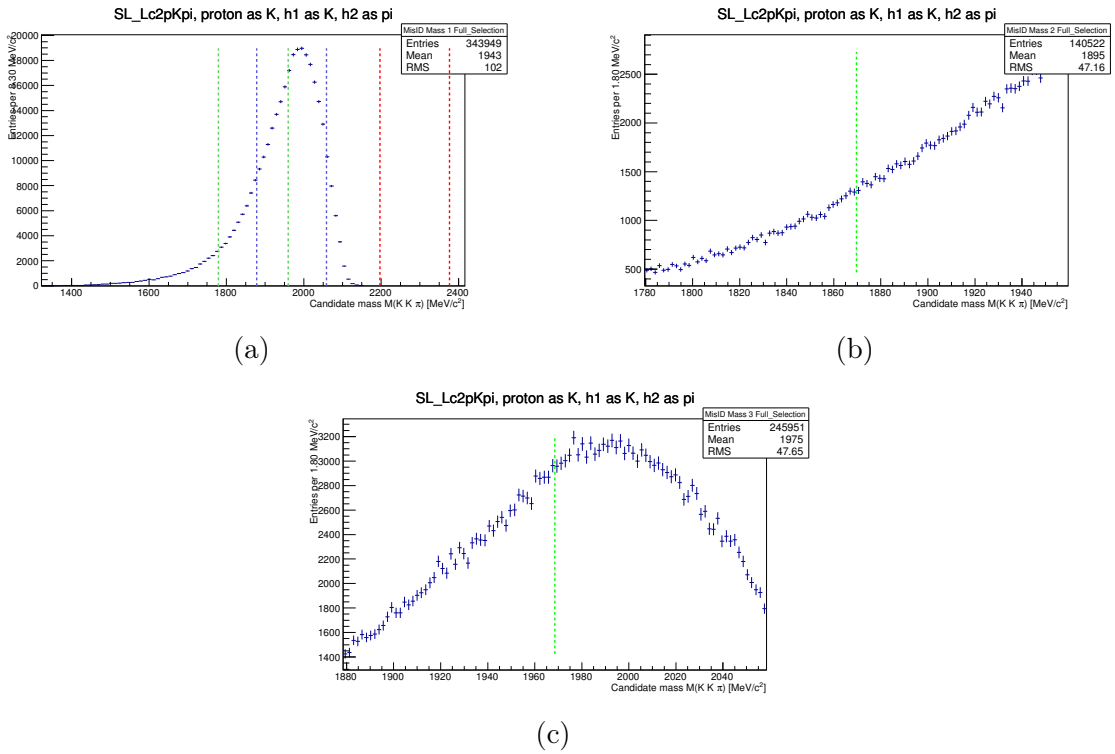


Figure 4.21: The mass distribution of SL  $A_c^+ \rightarrow pK^-\pi^+$  data after final selection, where the  $p$  has been mis-identified as a  $K^+$ . Shown top is the whole mass distribution, with the  $D^+$  mass region denoted in green (bottom left plot) and the  $D_s^+$  mass region denoted in blue (bottom right plot). This probes for the presence of reflections from mis-identified  $D^+/D_s^+ \rightarrow K^+K^-\pi^+$ .

# Chapter 5

## $\Lambda_c^+ \rightarrow phh'$ selection efficiencies and yield extractions

### 5.1 Efficiencies and efficiency corrections

#### 5.1.1 Overview

The correct determination of efficiencies for each stage of the selection is vital to the analysis. Starting from the  $\Lambda_c$  production, we define the selection and associated efficiencies as follows:

$$\epsilon_{acc|gen} = \frac{N_{acc}}{N_{gen}}$$

This is the fraction of candidates which decay with all daughters produced inside the detector acceptance.

$$\epsilon_{reco|acc} = \frac{N_{reco}}{N_{acc}}$$

The fraction of candidates generated within the detector acceptance which are fully reconstructible.

$$\epsilon_{trig|reco} = \frac{N_{trig}}{N_{reco}}$$

The fraction of reconstructible candidates which pass the trigger requirements.

$$\epsilon_{strip|trig} = \frac{N_{strip}}{N_{trig}}$$

The fraction of triggered candidates which are then stripped, pass the DTF convergence requirement and also pass our kinematic vetoes required for the PIDCalib calibration, excluding any PID selection in the stripping selection.

$$\epsilon_{PID|strip} = \frac{N_{PID}}{N_{strip}}$$

The fraction of events passing the full PID selection with respect to the number passing the rest of the stripping selection.

$$\epsilon_{BDT|PID} = \frac{N_{BDT}}{N_{PID}}$$

The fraction of events passing the BDT selection with respect to the number passing the full PID selection.

We now make a number of assumptions to simplify this chain. The first is that the trigger selection in the prompt analysis is independent of the stripping selection - a strong assumption given the TIS trigger selection. We also assume the trigger selection in the SL analysis is also independent of the stripping selection, which is a weaker assumption and so is explicitly verified. This is a necessary assumption as when the TOS trigger requirements are applied on the SL simulation very few events survive, and the stripping efficiency calculations become very statistically limited.

These assumptions let us remove the intermediary trigger step from the acceptance, reconstruction and stripping steps and we may now consider the following efficiency factor:

$$\epsilon_{strip|acc} = \frac{N_{strip}}{N_{acc}}$$

This is the fraction of  $\Lambda_c$  candidates decaying with all daughters in the detector acceptance which are reconstructed and stripped.

Now the final expression for the per-mode adjusted yield becomes:

$$M = \frac{N}{\epsilon_{trig|reco} \times \epsilon_{acc|gen} \times \epsilon_{strip|acc} \times \epsilon_{PID|strip} \times \epsilon_{BDT|PID}} \quad (5.1)$$

where the terms are:

N - The extracted raw yield for the mode.

$\epsilon_{trig|reco}$  - The per-mode trigger efficiency with respect to the reconstruction. In the prompt analysis we use a TIS chain, so the ratio of these efficiencies is expected to be 1. In the SL analysis the efficiencies are instead evaluated with simulated data. This is described in Section 5.1.3.

$\epsilon_{acc|gen}$  - The per-mode acceptance of the detector geometry. This is calculated in both analyses using generator-level simulation, as described in Section 5.1.4.

$\epsilon_{\text{strip|acc}}$  - The per-mode stripping efficiency with respect to the candidates falling in the detector acceptance. This efficiency must be calculated from simulation. The PID cuts in the stripping are removed from the selection of simulated candidates, and the PID cut efficiency correction is treated in a separate data-driven efficiency. The no-PID stripping efficiency calculation is detailed in Section 5.1.5.

$\epsilon_{\text{PID|strip}}$  - The per-mode PID selection efficiency with respect to the stripped candidates. This is calculated using a novel, entirely data-driven variation of the PIDCalib method, and described in Section 5.1.6.

$\epsilon_{\text{BDT|PID}}$  - The per-mode BDT efficiency w.r.t. the rest of the selection. The BDT selection is only applied in the selection of prompt  $\Lambda_c^+ \rightarrow p\pi^- K^+$  events, so is equal to 1 for all branching fraction ratios not involving the DCS mode. Its efficiency is extracted by fitting the signal yields of the Cabibbo-favoured distribution before and after the application of the BDT. Cross checks are performed to verify that the efficiency of the BDT selection will be uniform in the  $\Lambda_c^+ \rightarrow pK^-\pi^+$  and  $\Lambda_c^+ \rightarrow p\pi^- K^+$ . This is described in Section 5.1.7.

The full selection efficiencies for each analysis on a per-mode basis are then given in Section 5.1.8.

### 5.1.2 MC efficiencies and resonance modelling

It is necessary to take efficiency corrections for several of the described stages from simulated data. Poor modelling of any variable used in the selection has the potential to bias the calculated efficiency for any given stage of the selection. The simulated data used in the prompt analysis is generated with a phase-space distribution and ignores the complex resonant structure of  $\Lambda_c^+ \rightarrow phh'$  decays, while the semileptonic simulated data uses a pseudo-resonance model which attempts to account for the dominant resonant contributions (as was more fully outlined in Section 4.2.2).

As described previously within this document in Section 3.5.8, three-body baryonic decays to hadrons can be parameterised by five variables, shown in Figure 5.1. These variables are:

$M(ph_1)$  **and**  $M(h_1h_2)$  - The invariant mass of the proton and opposite sign meson, and the invariant mass of the meson pair. Decays through intermediate resonances (such as  $K^*$ ,  $\Lambda(1520)$ ,  $\phi$ ,  $f^0(980)$  etc.) will result in local enhancements in these quantities not present in a phase-space generated distribution.

$\cos \theta_p$  - In the  $\Lambda_c$  rest frame, the angle between the proton momentum vector and the polarisation axis of the  $\Lambda_c$ .

$\cos \phi_p$  - In the  $\Lambda_c$  rest frame, the angle between the component of proton momentum perpendicular to the  $\Lambda_c$  polarisation and the direction of the lab frame  $\Lambda_c$  momentum vector.

$\phi_{h_1 h_2}$  - In the  $\Lambda_c$  rest frame, the angle between the plane containing the proton momentum vector and the  $\Lambda_c$  polarisation vector, and the plane containing the two meson momentum vectors.

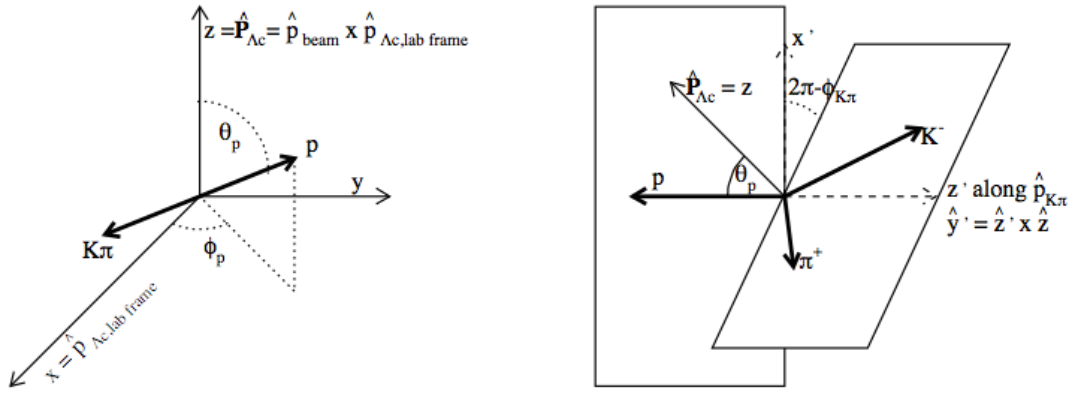


Figure 5.1: The angular variables characterising the  $\Lambda_c$  resonance structure. From [86].

The simulation used in this analysis does not properly account for the resonance structures in  $\Lambda_c$  decays. The data and MC distributions of the above variables are therefore expected to disagree to varying extents which are difficult to estimate given the poorly understood nature of  $\Lambda_c^+ \rightarrow phh'$  decays. The data and MC populations of promptly selected  $\Lambda_c^+ \rightarrow pK^-\pi^+$  in bins of the invariant mass resonant variables are shown in Figure 5.2 to illustrate such disagreements. It is therefore necessary to investigate each stage of the selection whereby the efficiency is taken from simulation for the following:

- Variations in acceptance across each of the five resonant quantities.
- Disagreements in the data/MC distributions in each of the five resonant quantities.

If both of these criteria are true for any variable at any given stage of the selection, phase-space averaged efficiencies from simulation may not be naively utilised for that stage of the selection.

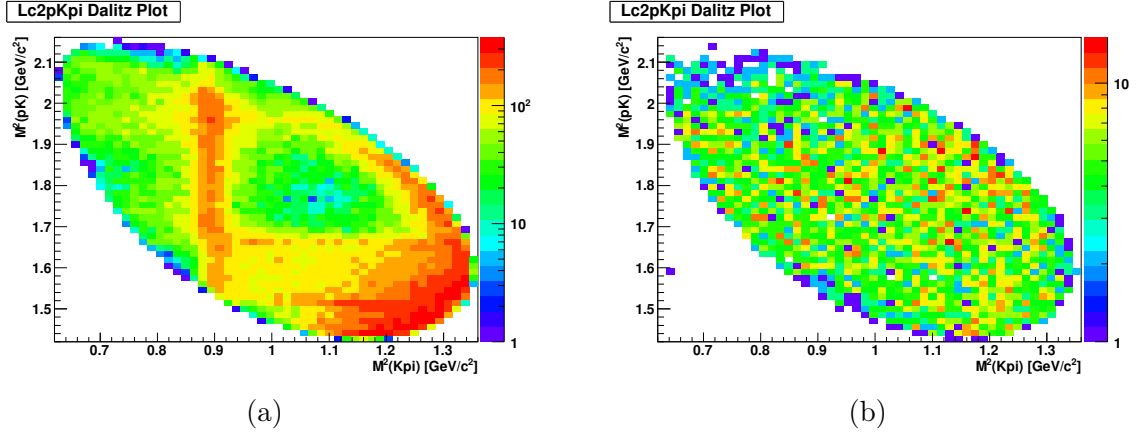


Figure 5.2: Comparison of the invariant mass of the systems of charge-opposite daughter pairs in promptly selected  $\Lambda_c^+ \rightarrow pK^-\pi^+$  decays, in stripped data (a) and stripped simulation (b).

We also note that in both the prompt and semileptonic analyses, for the Cabibbo favoured and doubly-Cabibbo suppressed modes the only differences in selection efficiency will arise from different kinematics due to the different resonances which are possible in the decays. We therefore exploit that the ratios of their selection efficiencies for a given stage of selection should be unity if the acceptance of the selection is flat with respect to the phase-space characterising the resonant structure of the  $\Lambda_c$  decay.

### 5.1.3 Trigger efficiencies

This efficiency is defined as the fraction of reconstructed candidates which pass the trigger selection. The requirement that the  $\Lambda_c$  decay is independent of the event triggering in the selection of prompt candidates is expected to result in efficiency ratios between modes which are not very different from one. These efficiencies are evaluated using simulated data, however due to the low TIS efficiency of the MC this calculation is imprecise. An algorithm is run over the simulation which uses the truth information to record all reconstructible  $\Lambda_c$  decays. The fraction of these candidates that pass the trigger selection is equivalent to the trigger efficiency, and was investigated in each decay mode.

In the semileptonic selection a trigger requirement is utilised such that the  $\Lambda_b^0$  decay itself must trigger the event. While at L0 and H1t1 the  $\mu$  in the  $\Lambda_b^0$  decay must be TOS, at H1t2 the full decay has a TOS requirement. As such, the differing  $\Lambda_c$  daughter kinematics will result in different H1t2 efficiencies. These are calculated using simulated data via the same procedure utilised in the prompt trigger checks.

#### Acceptance variations in resonant quantities

The trigger efficiencies are calculated with simulated data. Given the complexity of the trigger selection algorithms it was considered possible that the SL candidate trigger acceptance may vary with respect to the poorly modelled resonant quantities. This was investigated by evaluating the trigger efficiencies in bins of the resonant variables. The resonant quantities proved to be broadly uncorrelated with the trigger efficiency for all decay modes. Some example acceptances are given in Figure 5.3 in the invariant mass systems  $m_{pK}$  and  $m_{KK}$  in semileptonically produced  $\Lambda_c^+ \rightarrow pK^-K^+$ . As such, we take the ratio of efficiencies for the doubly-Cabibbo suppressed and Cabibbo-favoured modes to be unity.

#### Average full trigger efficiencies

The final results are taken with an average of the simulated efficiencies from the different magnet polarities weighted with the luminosities of the real data magnet polarities, with equal weighting given to  $\Lambda_c^+$  and  $\Lambda_c^-$ . The final average trigger efficiencies are given in Table 5.1. The subscript ‘‘Reco’’ refers to the condition of being reconstructible, while ‘‘Trig’’ refers to the subset of these passing the trigger selection.

We emphasise that in the prompt analysis, these are not used in the final calculations of the relative branching fractions and only serve as a cross check that the TIS efficiencies

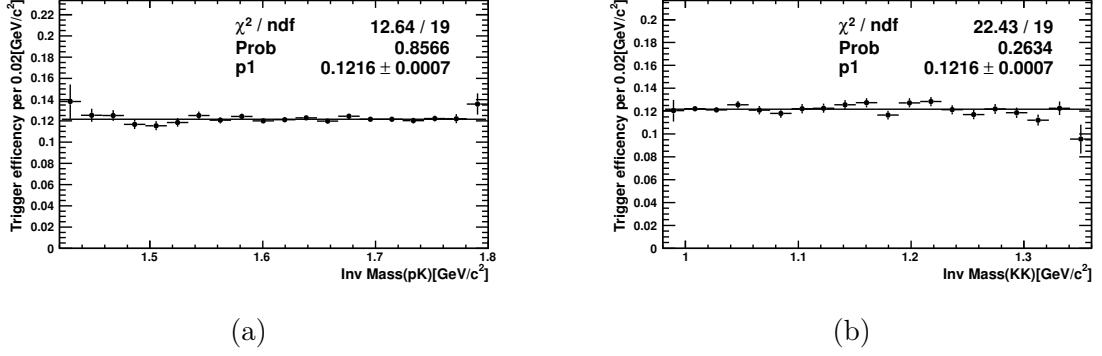


Figure 5.3: The trigger acceptance in semileptonically produced  $\Lambda_c^+ \rightarrow pK^-K^+$  with respect to resonant variables, demonstrating that the acceptance is broadly uncorrelated with the invariant masses  $m_{pK}$  (a) and  $m_{KK}$  (b).

of the different modes are uniform. We also emphasise that the ratio of efficiencies is demonstrated to be unity in the measurement of  $\mathcal{B}(\Lambda_c^+ \rightarrow p\pi^-K^+)/\mathcal{B}(\Lambda_c^+ \rightarrow pK^-\pi^+)$ . The errors provided are the statistical uncertainty arising from limited MC statistics.

Analysis	Mode	$\epsilon_{\text{Trig Reco}} [\%]$
Prompt	$\Lambda_c^+ \rightarrow pK^-\pi^+$	$0.47 \pm 0.01$
	$\Lambda_c^+ \rightarrow pK^-K^+$	$0.47 \pm 0.01$
	$\Lambda_c^+ \rightarrow p\pi^-\pi^+$	$0.44 \pm 0.01$
	$\Lambda_c^+ \rightarrow p\pi^-K^+$	$0.46 \pm 0.01$
SL	$\Lambda_c^+ \rightarrow pK^-\pi^+$	$14.21 \pm 0.03$
	$\Lambda_c^+ \rightarrow pK^-K^+$	$12.61 \pm 0.07$
	$\Lambda_c^+ \rightarrow p\pi^-\pi^+$	$14.67 \pm 0.08$

Table 5.1: The final per-mode phase-space averaged trigger efficiencies for the full trigger selection.

#### 5.1.4 Generator level efficiencies

The simulation utilised in the analyses employ one of two generator-level cuts. These are:

**DaughtersInLHCb** - This requires all charged daughters in the generated decay to be produced in the range  $0.01 \text{ rad} < \theta_{\text{charged}} < 0.4 \text{ rad}$  of the  $z$ -axis and all neutral daughters to be produced in the range  $0.005 \text{ rad} < \theta_{\text{neutral}} < 0.4 \text{ rad}$  of the  $z$ -axis.

**LHCbAcceptance** - This requires the head particle/mother of the specified signal decay to be produced in the range  $0 < \theta_{\text{signal}} < 0.4 \text{ rad}$  of the  $z$ -axis.

All generated MC samples utilise the `DaughtersInLHCb` cut, with the exception of the semileptonic CF  $\Lambda_c^+ \rightarrow pK^-\pi^+$  which utilises the `LHCbAcceptance` cut. Because of the differing daughter kinematics in the  $\Lambda_c^+ \rightarrow phh'$  modes it is natural to expect that the `DaughtersInLHCb` efficiency will not cancel out when a ratio of efficiencies is taken. As such, an efficiency correction must be applied.

### Acceptance variations in resonant quantities

The generator level efficiencies have a weak dependence on the daughter kinematics. Therefore at this stage of the selection there exists potential for the existence of acceptance variations with respect to resonant quantities. This was investigated with the use of a generator-level simulation with no acceptance cuts employed. 100k events were generated for each permutation of mode and polarity. By examining the decay kinematics it is determined for each simulated decay whether or not the two generator level requirements are met.

Histograms were then constructed by binning the samples in bins of the resonant variables and counting the candidates in each bin passing the cuts to construct efficiencies. We fit a first order polynomial with a gradient fixed at zero to the distribution to check for acceptance flatness. In these checks the fits to the distributions yielded acceptable p-values and reduced  $\chi^2$  values. As such it was concluded that there was no significant variation in acceptance at this stage of the selection, and that phase-space averaged efficiencies were appropriate. Example tests for the promptly produced  $\Lambda_c^+ \rightarrow p\pi^-\pi^+$  magnet-up efficiency distributions are shown in Figure 5.4. As such, we take the ratio of efficiencies for the doubly-Cabibbo suppressed and Cabibbo-favoured modes to be unity in the prompt and semileptonic analyses.

### Calculated efficiencies

Given that the generator-level acceptances do not appear correlated to the resonant variables, we can confidently use phase-space averaged efficiencies. In the semileptonic analysis the logs of the simulation production are used to record the generator requirement efficiencies, which are compared against the less precise checks calculated with the smaller samples generated with no generator requirements. In the prompt analysis the simulation has a significant non-prompt component which we remove from the samples after production. Therefore in the final results we use our smaller generator-level only samples where the  $\Lambda_c$  ancestry is verified as prompt. We calculate efficiencies by magnet polarity and by  $\Lambda_c$

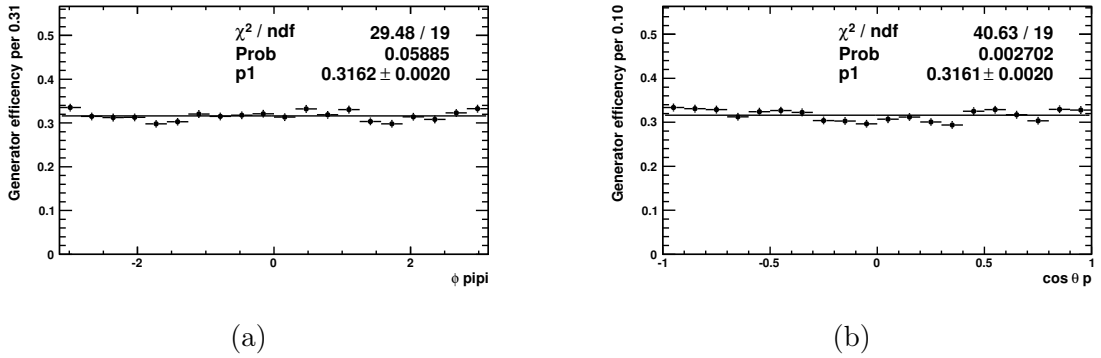


Figure 5.4: Generator cut acceptance in semileptonically produced  $\Lambda_c^+ \rightarrow p\pi^-\pi^+$  with respect to  $\theta_{hh}$  (a) and  $\cos \phi_p$  (b).

charge. The prompt efficiencies are given in Table 5.2, and the semileptonic efficiencies given in Table 5.3, for both the logfile efficiencies from the sample generation and from our own generator-level samples. While we provide both, the latter are used in the final results for the prompt and the former for the semileptonic.

We note that as the generator level acceptances are flat across the space characterising the resonant decay, the selection efficiencies cancel between the Cabibbo-favoured and the doubly-Cabibbo suppressed. We therefore take the relative efficiencies as unity for the measurements of  $\mathcal{B}(\Lambda_c^+ \rightarrow p\pi^-K^+)/\mathcal{B}(\Lambda_c^+ \rightarrow pK^-\pi^+)$ .

We also note that in the prompt there is a clear trend for the generator-level efficiency of  $\Lambda_c^-$  to be 3 – 5 % higher depending on the decay mode than the corresponding  $\Lambda_c^+$ . This is attributable to the differing hadronisation of  $\Lambda_c^+$  and  $\Lambda_c^-$  given the proton – proton collision and underlying event. The majority of prompt  $\Lambda_c$  production comes from  $c\bar{c}$  production, which in turn predominately comes from  $gg$  interactions. As such, independently of the underlying event we would expect symmetric hadronisation of  $\Lambda_c^+$  and  $\Lambda_c^-$ . However, the  $c$  quark can hadronise with the highly boosted proton remnants in the underlying event to form a boosted  $\Lambda_c^+$ , while the  $\bar{c}$  quark cannot form a  $\Lambda_c^-$  similarly. This results in a higher proportion of  $\Lambda_c^+$  being produced at high  $\eta$  and being lost in the beampipe, outwith the generator level acceptance. This is demonstrated in Figure 5.5 for the MagDown prompt  $\Lambda_c^+ \rightarrow pK^-\pi^+$  generator-level sample. The excess in  $\Lambda_c^+$  in the high  $\eta$  region (at around  $\eta = 9$ ) demonstrates this effect, and it is fully expected given the LHC’s production environment.

We provide in Table 5.4 the average efficiencies on a per-mode basis used in the final results. These are taken from an average of the simulated efficiencies from the different

Polarity	Part/Antipart	Decay mode	Logfile Eff	True Prompt Eff
MagUp	Particle	$\Lambda_c^+ \rightarrow pK^- \pi^+$	$0.208 \pm 0.001$	$0.211 \pm 0.002$
		$\Lambda_c^+ \rightarrow pK^- K^+$	$0.234 \pm 0.001$	$0.237 \pm 0.002$
		$\Lambda_c^+ \rightarrow p\pi^- \pi^+$	$0.194 \pm 0.001$	$0.199 \pm 0.003$
		$\Lambda_c^+ \rightarrow p\pi^- K^+$	$0.211 \pm 0.001$	$0.213 \pm 0.002$
	Antiparticle	$\Lambda_c^- \rightarrow \bar{p}K^+ \pi^-$	$0.219 \pm 0.001$	$0.218 \pm 0.002$
		$\Lambda_c^- \rightarrow \bar{p}\pi^+ \pi^-$	$0.242 \pm 0.001$	$0.244 \pm 0.002$
		$\Lambda_c^- \rightarrow \bar{p}K^+ K^-$	$0.200 \pm 0.001$	$0.201 \pm 0.004$
		$\Lambda_c^- \rightarrow \bar{p}\pi^+ K^-$	$0.217 \pm 0.001$	$0.218 \pm 0.003$
MagDown	Particle	$\Lambda_c^+ \rightarrow pK^- \pi^+$	$0.210 \pm 0.001$	$0.210 \pm 0.002$
		$\Lambda_c^+ \rightarrow pK^- K^+$	$0.234 \pm 0.001$	$0.235 \pm 0.002$
		$\Lambda_c^+ \rightarrow p\pi^- \pi^+$	$0.193 \pm 0.001$	$0.195 \pm 0.002$
		$\Lambda_c^+ \rightarrow p\pi^- K^+$	$0.211 \pm 0.001$	$0.210 \pm 0.002$
	Antiparticle	$\Lambda_c^- \rightarrow \bar{p}K^+ \pi^-$	$0.214 \pm 0.001$	$0.220 \pm 0.002$
		$\Lambda_c^- \rightarrow \bar{p}\pi^+ \pi^-$	$0.243 \pm 0.001$	$0.242 \pm 0.002$
		$\Lambda_c^- \rightarrow \bar{p}K^+ K^-$	$0.199 \pm 0.001$	$0.203 \pm 0.002$
		$\Lambda_c^- \rightarrow \bar{p}\pi^+ K^-$	$0.217 \pm 0.001$	$0.217 \pm 0.002$

Table 5.2: The prompt generator-level efficiencies both from the logfiles of the simulation production and a small sample of generator-level MC where the  $\Lambda_c$  is verified as being produced promptly. All efficiencies correspond to the `DaughtersInLHCb` requirement. The latter efficiencies correspond to only those candidates which are prompt, the former includes secondary contamination and is not used but provided for comparison.

magnet polarities weighted with the luminosities of the real data magnet polarities, with

Polarity	Part/Antipart	Decay mode	Logfile Eff	Calculated Eff
MagUp	Particle	$\Lambda_b^0 \rightarrow \Lambda_c^+ \mu^- \bar{\nu}_\mu, \Lambda_c^- \rightarrow \bar{p}K^+ \pi^-$	$0.334 \pm 0.001$	$0.339 \pm 0.002$
		$\Lambda_b^0 \rightarrow \Lambda_c^+ \mu^- \bar{\nu}_\mu, \Lambda_c^- \rightarrow \bar{p}K^+ K^-$	$0.182 \pm 0.001$	$0.182 \pm 0.002$
		$\Lambda_b^0 \rightarrow \Lambda_c^+ \mu^- \bar{\nu}_\mu, \Lambda_c^- \rightarrow \bar{p}\pi^+ \pi^-$	$0.157 \pm 0.001$	$0.158 \pm 0.002$
	Antiparticle	$\Lambda_b^0 \rightarrow \Lambda_c^- \mu^+ \nu_\mu, \Lambda_c^- \rightarrow \bar{p}K^+ \pi^-$	$0.332 \pm 0.001$	$0.331 \pm 0.002$
		$\Lambda_b^0 \rightarrow \Lambda_c^- \mu^+ \nu_\mu, \Lambda_c^- \rightarrow \bar{p}K^+ K^-$	$0.181 \pm 0.001$	$0.182 \pm 0.002$
		$\Lambda_b^0 \rightarrow \Lambda_c^- \mu^+ \nu_\mu, \Lambda_c^- \rightarrow \bar{p}\pi^+ \pi^-$	$0.158 \pm 0.001$	$0.159 \pm 0.002$
MagDown	Particle	$\Lambda_b^0 \rightarrow \Lambda_c^+ \mu^- \bar{\nu}_\mu, \Lambda_c^- \rightarrow \bar{p}K^+ \pi^-$	$0.334 \pm 0.001$	$0.337 \pm 0.002$
		$\Lambda_b^0 \rightarrow \Lambda_c^+ \mu^- \bar{\nu}_\mu, \Lambda_c^- \rightarrow \bar{p}K^+ K^-$	$0.183 \pm 0.001$	$0.181 \pm 0.002$
		$\Lambda_b^0 \rightarrow \Lambda_c^+ \mu^- \bar{\nu}_\mu, \Lambda_c^- \rightarrow \bar{p}\pi^+ \pi^-$	$0.157 \pm 0.001$	$0.158 \pm 0.002$
	Antiparticle	$\Lambda_b^0 \rightarrow \Lambda_c^- \mu^+ \nu_\mu, \Lambda_c^- \rightarrow \bar{p}K^+ \pi^-$	$0.333 \pm 0.001$	$0.330 \pm 0.002$
		$\Lambda_b^0 \rightarrow \Lambda_c^- \mu^+ \nu_\mu, \Lambda_c^- \rightarrow \bar{p}K^+ K^-$	$0.181 \pm 0.001$	$0.182 \pm 0.002$
		$\Lambda_b^0 \rightarrow \Lambda_c^- \mu^+ \nu_\mu, \Lambda_c^- \rightarrow \bar{p}\pi^+ \pi^-$	$0.156 \pm 0.001$	$0.154 \pm 0.002$

Table 5.3: The semileptonic generator-level efficiencies both from the logfiles of the simulation production and a sample of generator-level MC. The logfile efficiencies are valid in this case and use higher statistics in their calculations so are used, the ‘‘Calculated Eff’’ serves merely as a cross check. All  $\Lambda_c^+ \rightarrow pK^- \pi^+$  modes use the `LHCbAcceptance` cut, all other modes use the `DaughtersInLHCb` cut. Some cross check efficiencies are missing due to processing errors.

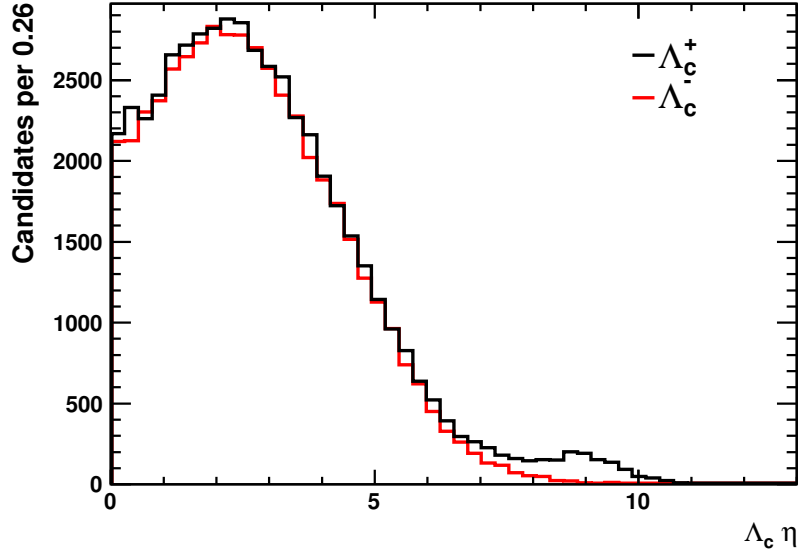


Figure 5.5: The  $\eta$  distributions of generator-level  $\Lambda_c^+$  (black) and  $\Lambda_c^-$  (red). Distributions are taken from the generator-level samples of  $\Lambda_c^+ \rightarrow pK^- \pi^+$  data. Shown is the excess in high  $\eta$   $\Lambda_c^+$  corresponding to  $c$  quarks which have hadronised with the proton remnants and fall outside the detector acceptance.

equal weighting given to  $\Lambda_c^+$  and  $\Lambda_c^-$ .

Stream	Mode	$\epsilon_{\text{Acc Gen}} [\%]$
Prompt	$\Lambda_c^+ \rightarrow pK^- \pi^+$	$21.27 \pm 0.05$
	$\Lambda_c^+ \rightarrow pK^- K^+$	$23.84 \pm 0.05$
	$\Lambda_c^+ \rightarrow p\pi^- \pi^+$	$19.66 \pm 0.05$
	$\Lambda_c^+ \rightarrow p\pi^- K^+$	$21.35 \pm 0.05$
Semileptonic	$\Lambda_c^+ \rightarrow pK^- \pi^+$	$33.31 \pm 0.07$
	$\Lambda_c^+ \rightarrow pK^- K^+$	$18.15 \pm 0.04$
	$\Lambda_c^+ \rightarrow p\pi^- \pi^+$	$15.66 \pm 0.04$

Table 5.4: The average per-mode generator level efficiencies used in the final analysis. The subscript “Gen” refers to the condition of being generated, “Acc” refers to the condition of passing the generator level cut for that mode.

## 5.1.5 Stripping efficiencies

### Overview

The stripping selections in prompt and semileptonic, as outlined in Section 4.3.1, use a suite of kinematic cuts and PID information to reduce the combinatoric background. The stripping efficiency may be factorised into the efficiency of the PID cuts and the efficiency of the rest of the stripping selection. This is useful as the PID response is not well modelled in the LHCb simulation, and is better evaluated with the use of data-driven techniques.

The efficiency of the remainder of the stripping selection may be evaluated with simulated data. Further kinematic cuts on the daughter particles in the decay - specifically track  $p$  and  $\eta$  - are necessary for PID calibration (this was elaborated in Section 4.3.3, and the full suite of kinematic cuts was previously given in Table 4.4). As the real data candidates with daughters falling in the kinematically vetoed region do not have valid PID efficiencies, we cannot derive an efficiency correction in a data-driven way. Instead the efficiency of these cuts must be evaluated with simulated data. For convenience the evaluation of the efficiency of these kinematic cuts is performed in tandem with the no-PID stripping efficiency.

We factorise out the PID cuts by running a version of the stripping selection algorithm which has had all PID cuts removed on the simulated data. We also apply the kinematic vetoes and DTF convergence requirement on this dataset. The fraction of generated, truth-matched candidates which pass the no-PID stripping, DTF convergence requirement and kinematic vetoes is defined as the stripping efficiency. We repeat the point that the stripping efficiency in this analysis is defined as the efficiency of the no-PID stripping, DTF convergence requirement and kinematic vetoes together - we do not treat the latter separately as an “offline” efficiency as these cuts are necessary for the PID selection efficiency correction to be valid.

The selections used in both prompt and semileptonic samples sculpt the distributions of signal kinematics. The effect this has on the stripping acceptance with respect to the resonant variables was investigated. Strong local variation in acceptance was observed in a number of variables, especially in bins of invariant masses of the daughter pairs. Such variation is displayed in Figure 5.6 for the invariant mass variables in prompt  $\Lambda_c^+ \rightarrow pK^-\pi^+$ .

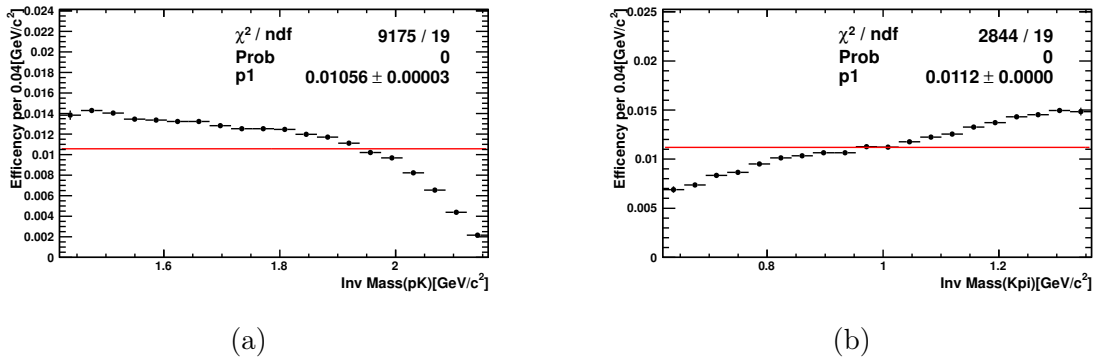


Figure 5.6: Stripping efficiency in bins of the invariant mass variables for semileptonically selected  $\Lambda_c^+ \rightarrow pK^-\pi^+$ . Unlike the checks for acceptance bias at the generator and trigger levels of the selection, strong variation is observed at the stripping level.

### Local efficiencies and re-weighting procedure

The stripping efficiency bias with respect to the resonant variables necessitates a re-weighting of the simulation and of the efficiency for the stripping selection. This is achieved by dividing the simulation in multidimensional bins of the resonant variables. We count the generated candidates in each bin and the truth-matched candidates surviving the no-PID stripping selection and kinematic veto selection to acquire local efficiencies in the 5D space. We then use these local efficiencies to assign per-candidate efficiencies to the real data, extracting the adjusted yield  $M$  by summing over the bins:

$$M = \sum_j \frac{N_j}{\epsilon_j} \quad (5.2)$$

where  $N_j$  is the number of data candidates in bin  $j$  and  $\epsilon_j$  is the efficiency in bin  $j$ . The ratio of the raw number of data candidates passing selection over the adjusted yield gives the re-weighted efficiency  $\bar{\epsilon}$ :

$$\bar{\epsilon} = \frac{N}{M} \quad (5.3)$$

In such a procedure the following systematic uncertainties arise:

1. The finite simulation statistics result in a binomial uncertainty on the bin efficiency. As we further subdivide our sample this uncertainty becomes larger in magnitude.
2. The bins in the schema have a finite width. As we know, the efficiency varies across the variable space. This means that for each bin in the schema, the average bin efficiency is dependent on the distributions of the resonant variables within the bin.

These are different between data and MC and so can result in biases if the binning is too coarse.

These are clearly opposing trends - to minimise the overall systematic contribution we must therefore find the optimum choice of binning.

Due to the low efficiency of both the prompt and semileptonic selections, a low proportion of the generated candidates survive the stripping selection. The number of MC events which survive the selection are given in Table 5.5. This makes attaining a sufficiently fine-grained 5D binning problematic, and initial efforts to construct a full 5D binning schema yielded results with a high disagreement between the prompt and semileptonic measurements. As such, we use a "reduced dimensionality" method to re-weight the efficiency within the 5D space only where necessary by discounting variables from the binning schema where the acceptance is flat or the data-MC agreement is good.

Mode	$N_{\text{Acc}}$	$N_{\text{Strip Acc}}$	$\epsilon_{\text{Strip Acc}} [\%]$
$\Lambda_c^+ \rightarrow pK^- \pi^+$	2308801	7225	$3.131 \pm 0.037 \times 10^{-3}$
$\Lambda_c^+ \rightarrow pK^- K^+$	2230984	5598	$2.510 \pm 0.033 \times 10^{-3}$
$\Lambda_c^+ \rightarrow p\pi^- \pi^+$	2305682	7945	$3.448 \pm 0.039 \times 10^{-3}$
$\Lambda_b^0 \rightarrow \Lambda_c^+ \mu^- \bar{\nu}_\mu, \Lambda_c^+ \rightarrow pK^- \pi^+$	9585315	110290	$1.118 \pm 0.003 \times 10^{-2}$
$\Lambda_b^0 \rightarrow \Lambda_c^+ \mu^- \bar{\nu}_\mu, \Lambda_c^+ \rightarrow pK^- K^+$	1017068	26601	$2.611 \pm 0.016 \times 10^{-2}$
$\Lambda_b^0 \rightarrow \Lambda_c^+ \mu^- \bar{\nu}_\mu, \Lambda_c^+ \rightarrow p\pi^- \pi^+$	990964	23194	$2.342 \pm 0.015 \times 10^{-2}$

Table 5.5: The number of MC events generated and the number of MC events passing the no-PID stripping selection. The subscript ‘‘Acc’’ refers to the condition of passing the generator level cuts, and the subscript ‘‘Strip’’ refers to the condition of passing the no-PID stripping selection. For prompt, the number generated corresponds to the number of true prompt decays, excluding those  $\Lambda_c$  produced from long-lived particles. The ratio of the stripped to generated candidates cannot be naively interpreted as an average stripping efficiency due to the poor data/MC agreement in the resonant structure, but are given here for completeness. We also remind the reader that the SL  $\Lambda_c^+ \rightarrow pK^- \pi^+$  simulation has different generator level cuts and therefore has a markedly different stripping efficiency with respect to the generator-level accepted candidates.

### Propagating bin errors to errors on $\bar{\epsilon}$

In any binned efficiency schema, each bin efficiency has a binomial uncertainty associated to it. To propagate this error through to the final re-weighted efficiency, we utilise a toy approach. In this method, we take a particular binning schema and evaluate efficiencies and binomial errors for each bin, where as usual the subscript ‘‘Acc’’ refers to the condition

of passing generator level cuts:

$$\begin{aligned}\epsilon &= \frac{N_{\text{Strip}}}{N_{\text{Acc}}} \\ \sigma_\epsilon &= \sqrt{\frac{\epsilon(1-\epsilon)}{N_{\text{Acc}}}}.\end{aligned}\tag{5.4}$$

We then generate 1000 toy binning schemas based on the original. For every toy, in each bin we randomly resample the number of events which pass the selection from a binomial distribution, using the original number of candidates generated in said bin and the efficiency of the original bin as the  $n$  and  $p$  of the binomial distribution respectively. We then use each binning schema to assign a stripping efficiency to each real data candidate, and then from the efficiency-corrected yield extract a new stripping efficiency for the mode using the candidate sWeights:

$$\begin{aligned}M &= \sum_{i=1}^n \frac{w_i}{\epsilon_i} \\ \bar{\epsilon} &= N/M\end{aligned}\tag{5.5}$$

where  $w_i$  is the candidate sWeight,  $\epsilon_i$  the candidate stripping efficiency,  $M$  the adjusted yield,  $N$  the extracted raw yield and  $\bar{\epsilon}$  the re-weighted average efficiency. In such a fashion, for each toy an  $\bar{\epsilon}$  is calculated. We then take the standard deviation of the  $\bar{\epsilon}$  distribution for all toys over the original re-weighted efficiency as a fractional systematic uncertainty on the efficiency.

### The $\kappa$ binning statistic

There is no standard way to find the optimum bin granularity given a specific simulated dataset. The efficiency within a given bin should be as close to uniform as possible. If there is significant variation in efficiency across a kinematic bin then differences in kinematics between the data and simulation can result in the average efficiency in the bin being markedly different in data and simulation. However, binning too finely inflates the statistical error and eventually can cause biases.

It is difficult to visualise an efficiency space in more than 2 dimensions - as such the candidate developed a method of parameterising the efficiency variation between adjacent bins relative to the statistical uncertainty on the adjacent bin efficiencies. This weighted

difference in efficiency between bin  $a$  and bin  $b$ ,  $\kappa_{ab}$ , may be expressed as:

$$\kappa_{ab} = \frac{|\epsilon_a - \epsilon_b|}{\sqrt{\sigma_a^2 + \sigma_b^2}}. \quad (5.6)$$

We consult the mean  $\kappa$  over multidimensional binning schemas. If this mean value is too large, the schema is too coarse given the simulation statistics available, and the variation of bin efficiency relative to the binomial error is too large. If the mean is too small, the schema is too fine given the statistics available, and the statistical uncertainty on the bin efficiencies is too high relative to the efficiency variation. We use the mean  $\kappa$  value of the bin schemas to determine which schemas provide the best description of the efficiency space - those binnings with a mean  $\kappa$  close to one are determined to be suitable. A full description of this test statistic and a justification of the optimum mean  $\kappa$  is given in Appendix A, which can be read as a standalone chapter.

### **Efficiency biases in re-weighting**

A bias in the stripping efficiency re-weighting due to finite simulation statistics was also identified when using our expression for the adjusted yield. This bias results in the re-weighted efficiencies being biased downward, and is proportional to the ratio of the statistical uncertainty on the bin efficiencies divided by the bin efficiencies. For a set number of simulated events, this bias therefore becomes worse as the number of bins increases. Investigations with toy simulation determined the magnitude of this bias for each stripping efficiency. This allows an upper limit on the number of bins in a schema to be derived, which is defined as the number of bins where the magnitude of the bias is larger than the binomial uncertainty on the integrated simulation sample. The statistical motivation for this bias and the full results of our toy studies are presented in Appendix B, which can also be read as a standalone chapter.

### **Recipe for reduced dimensionality efficiencies**

We describe the steps to obtain the final stripping selection efficiency and the associated systematics for each mode as follows:

1. We consult the data/MC distributions for each resonant variable. If there is good agreement, we discount the variable from the re-weighting schema.

2. We consult the stripping acceptance with respect to each resonant variable. If the acceptance is flat, we discount the variable from the re-weighting schema.
3. From steps 1 and 2 we arrive at a list of resonant variables for which we must re-weight.
4. At this stage we begin to construct local efficiencies using a variety of uniformly binned schemas, with different numbers of bins in each variable. We bin the simulated sample in the required variables and, by counting the numbers of generated and stripped candidates in each bin, assign an efficiency and binomial error on said efficiency to each bin in the schema. We construct binnings with 5 – 15 bins in each variable.
5. We then perform the following for each schema:
  - (a) Ensure that the binning granularity is low enough, and the binomial errors on the bin efficiencies low enough, that the bias identified in Section 5.1.5 is not statistically significant. If it is, we discount the schema from those considered suitable.
  - (b) Calculate the mean  $\kappa$  value for the schema. We make the ansatz that binnings with mean  $\kappa$  above 1.5 should be discounted because the efficiency variation across the individual bins in the schema are too high. We also discount binnings with mean  $\kappa$  below 0.9 because the statistical fluctuations in the individual bin efficiencies begin to dominate over the genuine efficiency structure.
  - (c) For each of the surviving schemas which satisfy the above stability criteria, we re-weight the real data using the efficiency bin schema to assign per-candidate efficiencies to the data. We then use these to extract average re-weighted per-mode efficiencies.
  - (d) We use the toy method outlined in Section 5.1.5 to propagate the statistical uncertainty from finite simulation statistics on the individual bins (and therefore the per-candidate efficiencies) to the final re-weighted average efficiency.
6. At this point we have arrived at a set of efficiency binning schemas for the mode which satisfy the stability criteria with different binning granularities. We have used each of these schemas to assign a set of per-candidate efficiencies to the real data, and used each of these to evaluate average re-weighted efficiencies for the mode.

Each of these efficiencies has a statistical uncertainty ascribed to it due to limited MC statistics.

7. In steps 1 and 2 we have discounted variables from the schema based on data/MC compatibility or acceptance flatness. These checks are, however, 1D checks while integrating over all other resonant variables, and are insensitive to local variations with respect to the excluded variable in the multidimensional space which average out when the integration occurs. As a cross check:
  - (a) If a variable has been discounted from the schema, we construct new binning schemas using the variables which have not been discounted with an arbitrary number of bins in the discounted variable under investigation. We then repeat the re-weighting procedure with this new schema to acquire an average re-weighted efficiency and associated statistical error.
  - (b) We then compare this new efficiency with an efficiency determined from a binning schema and re-weighting without the discounted variable.
  - (c) If the average re-weighted efficiencies are consistent within error, we take this as evidence that the discounting of the variable from the schema is well motivated. If they are not in agreement, then we take this as evidence that there is some local structure with respect to the discounted variable, and that the discounting of the variable from the schema is not valid. As such, we re-include the discounted variable into the schema.
8. Now we have a final list of re-weighted efficiencies which are derived only from those schemas satisfying the stability criteria. Each of these will have different granularities. Therefore each will be subject to slightly different statistical fluctuations in each bin, but this is largely taken into account by the toy method to evaluate statistical uncertainties.
9. The foremost reason for considering an ensemble of efficiencies from valid binning schemas stems from the consideration of the systematic uncertainty which arises due to the finite bin size; this finite size means that the efficiency in each bin is not single valued. Between schemas in our ensemble of binnings, the bin boundaries have different locations. This gives us some sensitivity to the variation of efficiency across individual bins in the schemas, and its contribution to the systematic uncertainty on

the re-weighted efficiency, when we consider the variation in the extracted re-weighted efficiencies in the ensemble.

10. We therefore take the median value of the ensemble of re-weighted efficiencies as the final re-weighted efficiency, with the highest and lowest efficiencies forming upper and lower bounds on the systematic uncertainty due to binning effects. We take the maximum statistical uncertainty of the efficiencies as the systematic uncertainty from finite simulation statistics.

This allows the derivation of efficiencies which are re-weighted to take account of the resonant structures in data, in such a way which allows us to estimate and minimise systematic uncertainties from limited statistics and the limitations of the binning schema.

We note that for the efficiency correction for the  $\Lambda_c^+ \rightarrow p\pi^-K^+$  mode in the semileptonic, we use the simulation of  $\Lambda_c^+ \rightarrow pK^-\pi^+$  to derive local efficiencies in the resonant space. Various resonances are modelled in the Cabibbo favoured simulation. We therefore bin finely in the invariant mass resonant variables, such that the efficiency in each bin should be very close to single-valued. This results in valid bin efficiencies across the phase space for the doubly-Cabibbo suppressed mode, even with the resonances modelled in the Cabibbo-favoured simulation.

### Final re-weighted efficiencies

We present in Table 5.6 the final re-weighted stripping efficiencies for each analysis on a per-mode basis. We also present a comparison between the phase-space average efficiencies and the re-weighted efficiencies for each mode in the two analyses in Table 5.7. The re-weighting procedure alters most of the stripping efficiencies at statistically significant levels.

### 5.1.6 PID efficiencies from a fully data-driven PIDCalib

#### PIDCalib outline

PID DLL cuts are included in all prompt and semileptonic  $\Lambda_c^+ \rightarrow phh'$  stripping selections, but the PID response is known to be poorly modelled in the LHCb simulation. This is caused by the lower detector occupancy in simulated events and the changing operating conditions in real data (the gas radiator temperature and pressure fluctuates over time) that are difficult to model. The PIDCalib package is used to assign event-by-event PID efficiencies to each candidate in a data-driven fashion.

Stream	Mode	Final $\epsilon_{\text{rw}}$ [%]	Fractional systematic [%]
Prompt	$\Lambda_c^+ \rightarrow pK^- \pi^+$	$(0.289 \pm 0.006 \pm 0.003)$ %	2.1 / 1.0 / 2.3
	$\Lambda_c^+ \rightarrow pK^- K^+$	$(0.266 \pm 0.008 \pm 0.003)$ %	3.0 / 1.1 / 3.2
	$\Lambda_c^+ \rightarrow p\pi^- \pi^+$	$(0.334 \pm 0.008 \pm 0.001)$ %	2.4 / 0.3 / 2.4
SL	$\Lambda_c^+ \rightarrow pK^- \pi^+$	$(1.194 \pm 0.004 \pm 0.016)$ %	0.3 / 1.3 / 1.4
	$\Lambda_c^+ \rightarrow pK^- K^+$	$(2.612 \pm 0.018 \pm 0.038)$ %	0.7 / 1.5 / 1.6
	$\Lambda_c^+ \rightarrow p\pi^- \pi^+$	$(2.229 \pm 0.025 \pm 0.046)$ %	1.1 / 2.1 / 2.3

Table 5.6: The final re-weighted efficiencies for each analysis. The first errors on the efficiencies are those from the propagated binomial uncertainties from limited simulation statistics as evaluated by our toy method. The second errors on the efficiencies are the additional systematic from the discounted variables and the finite bin width. The first fractional errors given are those from limited statistics, the second are those from the finite bin width and discounted resonant variables, the third are the sum of these in quadrature.

Stream	Mode	$\epsilon_{\text{ave}}$ [%]	$\epsilon_{\text{rw}}$ [%]	Difference ( $\sigma$ )
Prompt	$\Lambda_c^+ \rightarrow pK^- \pi^+$	$(0.313 \pm 0.004)$ %	$(0.289 \pm 0.007)$ %	3.0
	$\Lambda_c^+ \rightarrow pK^- K^+$	$(0.251 \pm 0.003)$ %	$(0.266 \pm 0.009)$ %	1.6
	$\Lambda_c^+ \rightarrow p\pi^- \pi^+$	$(0.345 \pm 0.004)$ %	$(0.334 \pm 0.008)$ %	1.2
SL	$\Lambda_c^+ \rightarrow pK^- \pi^+$	$(1.118 \pm 0.013)$ %	$(1.194 \pm 0.016)$ %	3.7
	$\Lambda_c^+ \rightarrow pK^- K^+$	$(2.611 \pm 0.016)$ %	$(2.612 \pm 0.042)$ %	0.0
	$\Lambda_c^+ \rightarrow p\pi^- \pi^+$	$(2.342 \pm 0.015)$ %	$(2.229 \pm 0.052)$ %	2.1

Table 5.7: The phase-space averaged per-mode stripping efficiencies and the re-weighted per-mode efficiencies. The errors on the phase-space averages are from finite simulation statistics, the errors on the re-weighted values are the full systematics, or the errors from finite simulation and the binning errors taken in quadrature. Also given are the differences between the phase-space averaged and re-weighted values in terms of the error in quadrature of the two efficiencies (ignoring correlations between the statistical uncertainties).

The PID response of a given daughter is dependent on the daughter’s mass, momentum and  $\eta$ . It is also dependent on the number of particles passing through the RICH in the complete event. The PIDCalib method assumes that the PID response of a given track may be characterised by a finite suite of kinematic and event variables. There exist two commonly used suites of variables within typical LHCb analyses:

- $p$ ,  $p_T$ , and the number of tracks in the event,  $N_{\text{Tracks}}$ .
- $p$ ,  $\eta$  and the number of tracks in the event,  $N_{\text{Tracks}}$ .

Both of these suites of variables are assumed to fully characterise the PID DLL response to a given track.

The method exploits the use of decay channels, which may be cleanly reconstructed purely with kinematic constraints, and without PID cuts of any form. Reconstruction of these modes allows for samples of  $p$ ,  $\pi$  and  $K$  tracks to be acquired which have not been subjected to any PID cuts. The decay modes corresponding to each type of charged daughter are:

$$p : \Lambda \rightarrow p\pi^-$$

$$K/\pi : D^*(2010)^+ \rightarrow D(K^-\pi^+)\pi_s^+$$

By binning the data from these modes in schemas composed of one of the above sets of variables, and then applying the PID DLL cuts used in the analysis, it is possible to acquire local PID efficiencies within the variable space in an entirely data-driven way. Signal data is assigned an event-by-event PID efficiency based on its position within said variable space.

### Data reference samples

Usually in `PIDCalib`, the end-user utilises a simulated signal, or reference, sample which has had no PID cuts applied to it. This entails passing the sample to `PIDCalib`, where the application assigns each simulated candidate's tracks a PID efficiency from the performance histograms generated with the calibration data tracks. For decays with multiple daughter tracks with PID requirements, the candidate PID efficiency is then the product of the track PID efficiencies - in this way the kinematic correlations between daughter tracks are accounted for. The per-mode signal PID efficiency is therefore simply the average candidate PID efficiency, as no PID cuts have been applied to the sample.

In the case of  $\Lambda_c$  decays, it is known that the daughter kinematics, and especially the correlations between daughter kinematics due to intermediate resonances, are badly modelled in the LHCb simulation. In some cases where poor kinematic modelling is known to be an issue, a solution is to re-weight the simulation kinematics to match the data and then to use the simulated sample in `PIDCalib`. The inclusion of PID cuts in all stripping selections in this analysis precludes this option, as we do not have access to the unbiased PID distribution before cuts. As such, the proponents have developed an implementation of `PIDCalib` where a data-driven reference sample with PID cuts is utilised.

The calibration data is used to assign per-candidate efficiencies in the usual way to the real data reference sample. Then, to extract a per-mode average PID efficiency we

calculate the PID-adjusted yield by weighting the signal candidate sWeights with the per-candidate PID weights. The expression for the PID-adjusted yield  $M$  is

$$M = \sum_{i=1}^n \frac{w_i}{\epsilon_i} \quad (5.7)$$

where there are  $n$  candidates, each with an sWeight  $w_i$  and a PIDCalib determined per-candidate efficiency  $\epsilon_i$ . The per-mode PID efficiency is then

$$\bar{\epsilon}_{PID} = \frac{\sum_{i=1}^n w_i}{M}. \quad (5.8)$$

This is simply the raw yield over the PID-adjusted yield, and is functionally identical to the determination of the re-weighted stripping efficiencies. As such, we can correct for the PID efficiency of the  $\Lambda_c$  decay modes without utilising any simulation data.

### Binning schema and kinematic vetoes

The choice of binning schema in this analysis is influenced by two factors. Firstly, the  $p_T$  distributions of protons from charm decays are much higher than in the calibration  $\Lambda \rightarrow p\pi^-$  sample. The  $\eta$  distributions, however, have similar coverage. As such,  $\eta$  is favoured over  $p_T$ .

A 3D binning will inflate the statistical uncertainty in each bin compared to a 2D binning. As can be seen in Figure 5.7, the distributions for event nTracks between the  $\Lambda_c^+ \rightarrow phh'$  decay modes are similar. Discounting nTracks from the binning schema will result in the derived PID efficiencies becoming biased by a constant factor, which will be identical between the decay modes in the case of equal distributions of nTracks.

Therefore a 2D binning schema is chosen using  $p$  and  $\eta$ , detailed in full in Table 5.8. PID efficiency histograms with this binning schema are constructed using the calibration data, and are used to assign event-by-event local PID efficiencies. The histograms of PID efficiency in bins of track  $\eta$  and track  $p$  are shown in Figure 5.8 for the prompt selection and in Figure 5.9 for the semileptonic selection. The same plots for the semileptonically selected pions in the SL  $\Lambda_c^+ \rightarrow p\pi^-\pi^+$ , on which different PID cuts are placed compared to the pions in the other semileptonic modes, are shown in Figure 5.10.

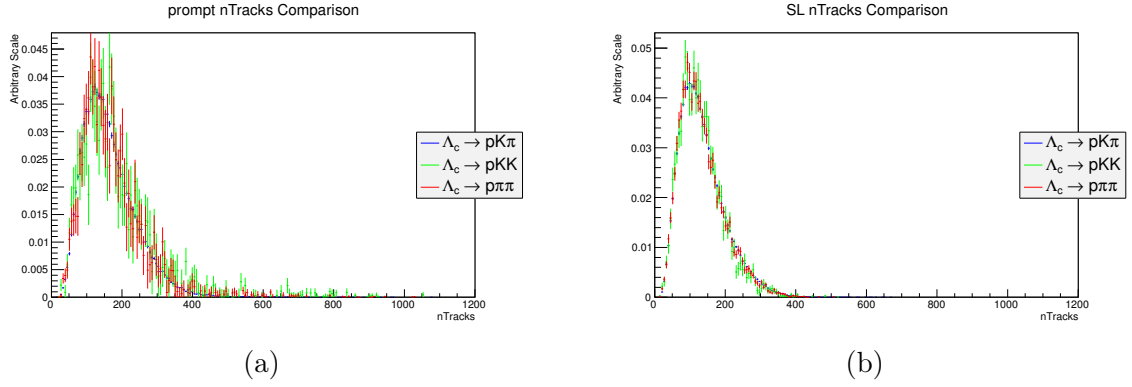


Figure 5.7: The background subtracted event nTrack distributions in the prompt (a) and semileptonic (b) selections. The distributions are compatible in all  $\Lambda_c^+ \rightarrow phh'$  decay modes.

Selection	Var	Bin Schema
All $\Lambda_c^+ \rightarrow phh'$	$p$ [MeV/ $c^2$ ]	5000 : 9300 : 15600 : 19000 : 24166.7 : 29333.3 : 34500 : 39666.7 : 44833.3 : 50000 : 66666.7 : 83333.3 : 100000
	$\eta$	2 : 2.625 : 3.25 : 3.875 : 4.5

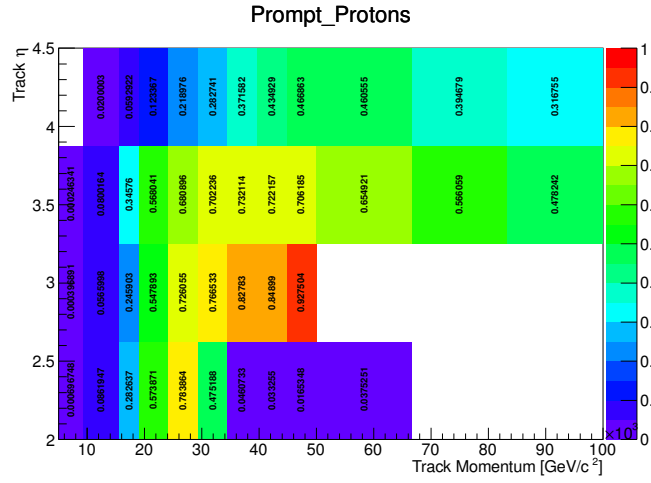
Table 5.8: The binning schemas used in the PID Calibration procedure.

## Final PID efficiencies

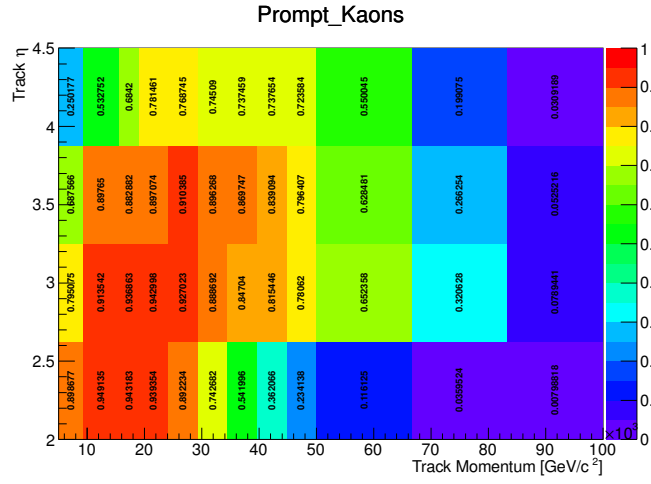
The average per-mode PID efficiencies are given in Table 5.9. The subscript ‘‘PID’’ refers to the condition of passing the PID cuts used in the mode, and ‘‘Strip’’ refers to the condition of passing the no-PID stripping selection (including the DTF convergence criteria and the kinematic vetoes).

Stream	Mode	$\epsilon_{\text{PID Strip}} [\%]$
Prompt	$\Lambda_c^+ \rightarrow pK^- \pi^+$	$42.74 \pm 0.04$
	$\Lambda_c^+ \rightarrow pK^- K^+$	$38.62 \pm 0.04$
	$\Lambda_c^+ \rightarrow p\pi^- \pi^+$	$45.35 \pm 0.05$
SL	$\Lambda_c^+ \rightarrow pK^- \pi^+$	$47.95 \pm 0.05$
	$\Lambda_c^+ \rightarrow pK^- K^+$	$43.34 \pm 0.04$
	$\Lambda_c^+ \rightarrow p\pi^- \pi^+$	$43.21 \pm 0.04$

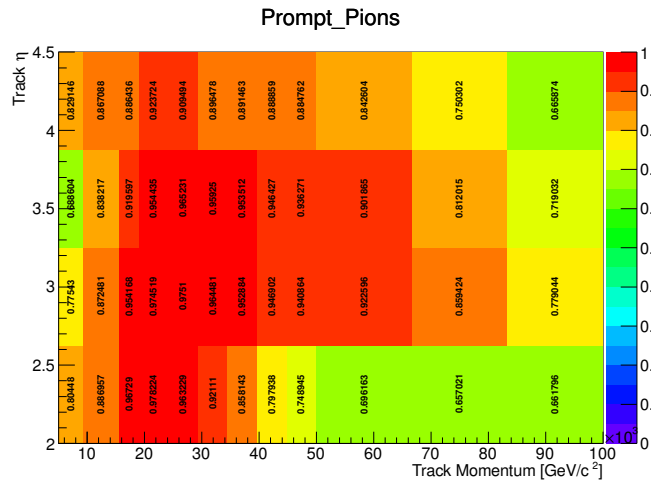
Table 5.9: The per-mode average PID efficiencies.



(a)  $p$  :  $\log(\mathcal{L}_p/\mathcal{L}_\pi) > 20$ ,  $\log(\mathcal{L}_p/\mathcal{L}_K) > 12$

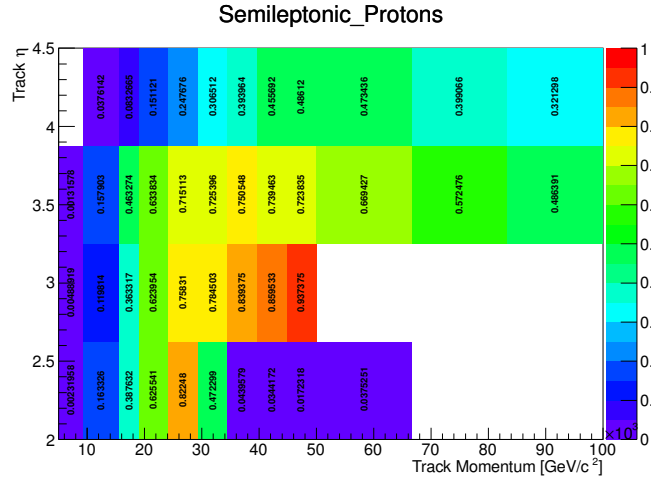


(b)  $K$  :  $\log(\mathcal{L}_K/\mathcal{L}_\pi) > 10$ ,  $\log(\mathcal{L}_K/\mathcal{L}_p) > -8$

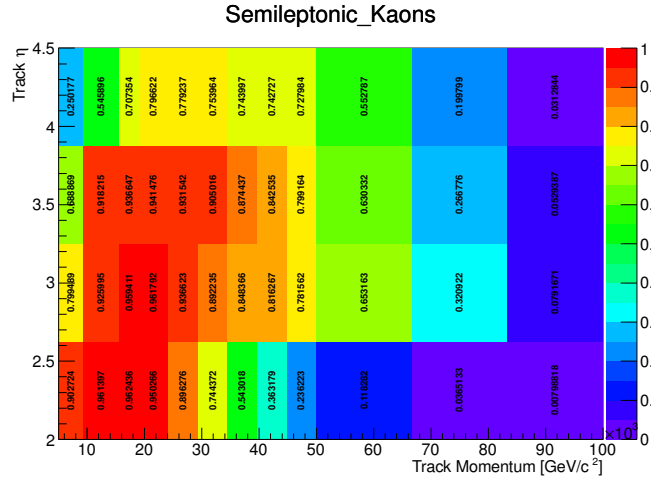


(c)  $\pi$  :  $\log(\mathcal{L}_K/\mathcal{L}_\pi) < 0$

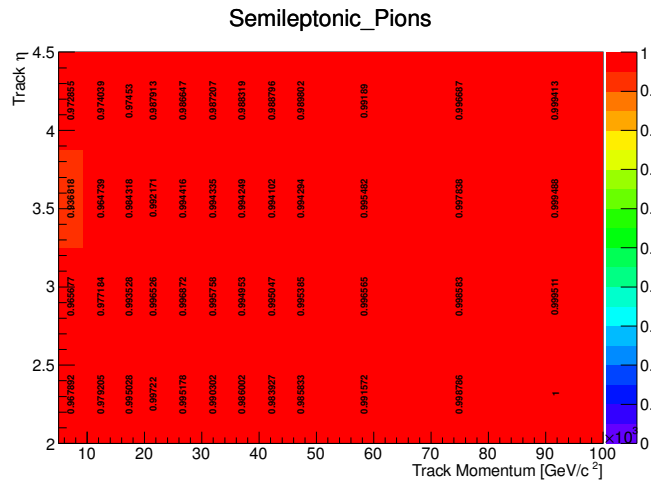
Figure 5.8: The prompt PID efficiencies in bins of track  $\eta$  and track  $p$ , as obtained from PIDCaLib.



(a)  $p : \log(\mathcal{L}_p/\mathcal{L}_\pi) > 20, \log(\mathcal{L}_p/\mathcal{L}_K) > 9$

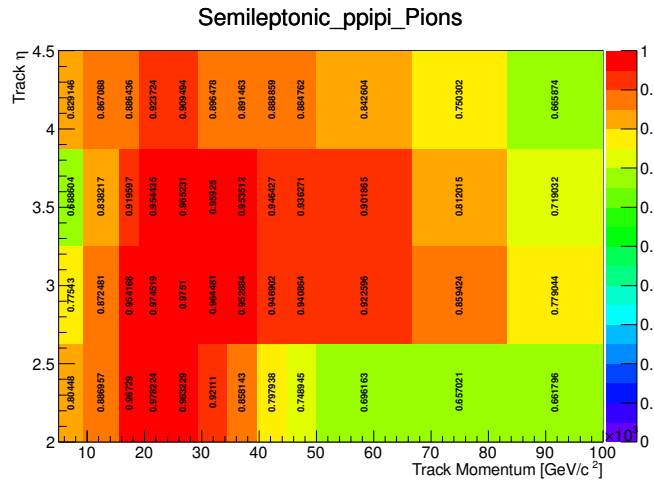


(b)  $K : \log(\mathcal{L}_K/\mathcal{L}_\pi) > 10$



(c)  $\pi : \log(\mathcal{L}_K/\mathcal{L}_\pi) < 10$

Figure 5.9: The semileptonic PID efficiencies in bins of track  $\eta$  and track  $p$ , as obtained from PIDCalib.



(a)  $\pi : \log(\mathcal{L}_K/\mathcal{L}_\pi) < 0$

Figure 5.10: The semileptonic  $\Lambda_c^+ \rightarrow p\pi^-\pi^+$  pion PID efficiencies in bins of track  $\eta$  and track  $p$ .

### 5.1.7 BDT efficiency

A BDT is applied in the offline selection of prompt  $\Lambda_c^+ \rightarrow p\pi^- K^+$  events. It is likely that upon unblinding the channel that the extraction of a signal yield before the application of the BDT will be impossible. As the BDT is trained to be agnostic to the daughter kinematics in the  $\Lambda_c$  decay, the responses to the BDT of the CF and DCS modes should be equivalent despite the different intermediate resonances which are expected to occur in the two modes. We utilise the stripped MC to verify this, with the calculated efficiencies given in Table 5.10. The efficiencies for the  $\Lambda_c^+ \rightarrow pK^-\pi^+$  and  $\Lambda_c^+ \rightarrow p\pi^- K^+$  modes agree within errors. We investigate in  $\Lambda_c^+ \rightarrow pK^-\pi^+$  the distributions of input variables to investigate the modelling of the BDT input variables. The Cabibbo-favoured is utilised in these checks for the higher statistics in the mode. We observe in all cases good agreement between data and simulation.

As a final check we verify that the efficiency of the BDT selection is compatible between the  $\Lambda_c^+ \rightarrow pK^-\pi^+$  data and simulation. The large statistics of the sample mean we can extract the efficiency of the selection on the real  $\Lambda_c^+ \rightarrow pK^-\pi^+$  data simply by fitting the  $\Lambda_c$  mass before and after the BDT selection. The selection efficiency on the simulated data is  $80.0 \pm 0.5$ , while for the real data the selection efficiency is evaluated to be  $79.5 \pm 0.5$ , and as such the two are compatible. As such we may confidently take from simulation the BDT efficiency for the DCS, verified by the identical Cabibbo-favoured response in simulation, and the matching response of the Cabibbo-favoured data.

Stream	Mode	N <sub>Strip</sub>	N <sub>BDT Strip</sub>	$\epsilon_{\text{BDT Strip}} [\%]$
Prompt	$\Lambda_c^+ \rightarrow pK^-\pi^+$	6507	5206	$80.0 \pm 0.5$
	$\Lambda_c^+ \rightarrow p\pi^- K^+$	7172	5771	$80.5 \pm 0.5$

Table 5.10: The efficiencies of the BDT selection when applied to the prompt MC.

### 5.1.8 Full selection efficiencies and summary

The efficiencies of the full selections for each mode are given in Table 5.11. In these figures the trigger efficiencies in the prompt analysis are included to better illustrate the efficiencies of the full selections, though the trigger efficiency correction is not included in the final prompt relative branching fraction results as the efficiencies are demonstrated to be equal across the prompt modes. These are the final efficiencies used to derive the adjusted yields in the final branching fraction results.

Stream	Mode	$\epsilon_{\text{Total}}$
Prompt	$\Lambda_c^+ \rightarrow pK^- \pi^+$	$(1.24 \pm 0.04) \times 10^{-6}$
	$\Lambda_c^+ \rightarrow pK^- K^+$	$(1.15 \pm 0.04) \times 10^{-6}$
	$\Lambda_c^+ \rightarrow p\pi^- \pi^+$	$(1.40 \pm 0.04) \times 10^{-6}$
SL	$\Lambda_c^+ \rightarrow pK^- \pi^+$	$(2.71 \pm 0.01) \times 10^{-4}$
	$\Lambda_c^+ \rightarrow pK^- K^+$	$(2.59 \pm 0.04) \times 10^{-4}$
	$\Lambda_c^+ \rightarrow p\pi^- \pi^+$	$(2.21 \pm 0.03) \times 10^{-4}$

Table 5.11: The total selection efficiencies in the analyses. The errors are the statistical errors from finite signal simulation and PIDCalib calibration data only.

## 5.2 Yield extraction

The analysis procedure relies on the extraction of genuine  $\Lambda_c^+ \rightarrow phh'$  candidates from those candidates formed from combinatorics. We outline the present yield extraction, and conclude this section by detailing a planned update to the prompt yield extractions to account for secondary  $\Lambda_c^+ \rightarrow phh'$  backgrounds.

### 5.2.1 Prompt

The species identified in the prompt sample are as follows:

**Prompt**  $\Lambda_c^+ \rightarrow phh'$  - decays of  $\Lambda_c^+ \rightarrow phh'$  where the  $\Lambda_c$  is produced either directly at the primary interaction or from a decay from a short-lived excited charm hadron. This is classed as the “signal”. The mass distribution of these candidates is modelled by a Crystal Ball function [143] and a Gaussian function constrained to a shared mean in the Cabibbo-favoured mode, and a Gaussian function in all other modes. <sup>1</sup>

**Secondary**  $\Lambda_c^+ \rightarrow phh'$  - decays of  $\Lambda_c^+ \rightarrow phh'$  where the  $\Lambda_c$  is produced in the decay of a long-lived  $b$ -hadron. This is classed as a background. At present this background is not properly accounted for in the prompt analysis.

**Combinatorics** - combinations of unrelated tracks which mimic  $\Lambda_c^+ \rightarrow phh'$  decays. The mass distribution of these candidates is modelled by a first order polynomial.

We utilise an unbinned extended maximum likelihood fit to the data candidates. All parameters in the mass models are allowed to float. The fit takes place over  $-80 - +45 \text{ MeV}/c^2$  of the nominal  $\Lambda_c$  mass of  $2286.46 \text{ MeV}/c^2$ .

The fit results after the final selection are shown for the semileptonically produced candidates in Figure 5.11 – Figure 5.13. In all plots, the total combined pdf is indicated in blue, the combined signal pdf is indicated in green, any individual signal components are indicated in cyan, and the background component is indicated in red.

---

<sup>1</sup>The Crystal Ball function is a Gaussian function with a power law low-end tail. It is of particular use in parameterising the mass distributions of candidates formed from combinations of tracks from a decaying particle, whereby unreconstructed final state radiation (FSR) results in a lower computed invariant mass of the system which manifests in a low end power law tail.

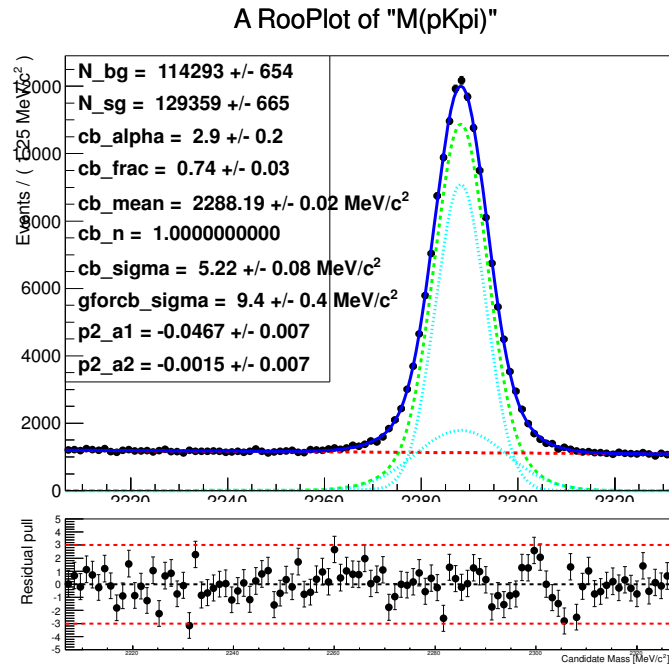


Figure 5.11:  $\Lambda_c$  mass fit and pull distribution for the prompt  $\Lambda_c^+ \rightarrow pK^-\pi^+$ .

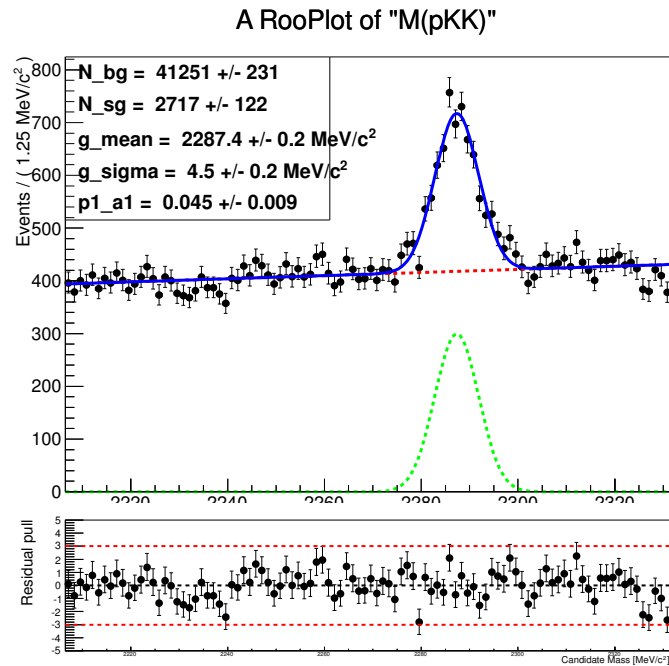


Figure 5.12:  $\Lambda_c$  mass fit and pull distribution for the prompt  $\Lambda_c^+ \rightarrow pK^-K^+$ .

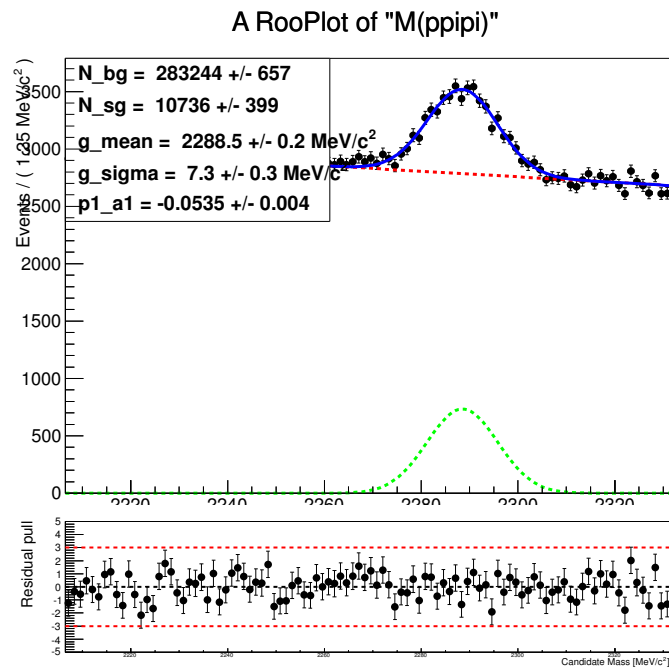


Figure 5.13:  $\Lambda_c^+$  mass fit and pull distribution for the prompt  $\Lambda_c^+ \rightarrow p\pi^-\pi^+$ .

## 5.2.2 Semileptonic

The species identified in the semileptonic sample are as follows:

$\Lambda_b^0 \rightarrow \Lambda_c^+ \mu^- \bar{\nu}_\mu$ ,  $\Lambda_c^+ \rightarrow phh'$  - decays of  $\Lambda_c^+ \rightarrow phh'$  where the  $\Lambda_c$  is produced in a semileptonic decay of a  $\Lambda_b^0$ . This is classed as the “signal”. The mass distribution of these candidates is modelled by a Crystal Ball function [143] and Gaussian function constrained to a shared mean in the Cabibbo-favoured mode, and a Gaussian function in all other modes.

**Combinatorics** - combinations of unrelated tracks which mimic  $\Lambda_c^+ \rightarrow phh'$  decays. The mass distribution of these candidates is modelled by a first order polynomial.

We utilise an unbinned extended maximum likelihood function in the fit to the data candidates. All parameters in the mass models are allowed to float. The fit takes place over  $-80 - +45$  MeV/ $c^2$  of the nominal  $\Lambda_c$  mass of 2286.46 MeV/ $c^2$ .

The fit results after the final selection are shown for the semileptonically produced candidates in Figure 5.14 – Figure 5.16. In all plots, the total combined pdf is indicated in blue, the combined signal pdf is indicated in green, any individual signal components are indicated in cyan, and the background component is indicated in red.

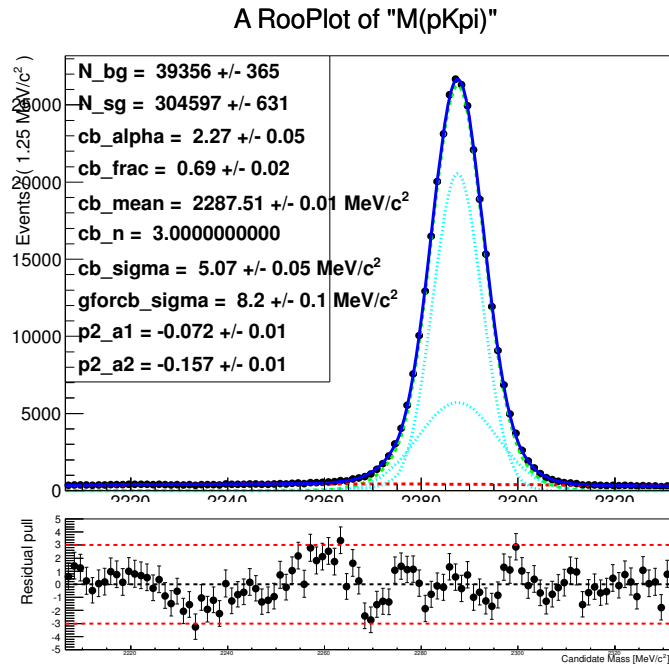


Figure 5.14:  $\Lambda_c$  mass fit and pull distribution for the semileptonic  $\Lambda_c^+ \rightarrow pK^-\pi^+$ .

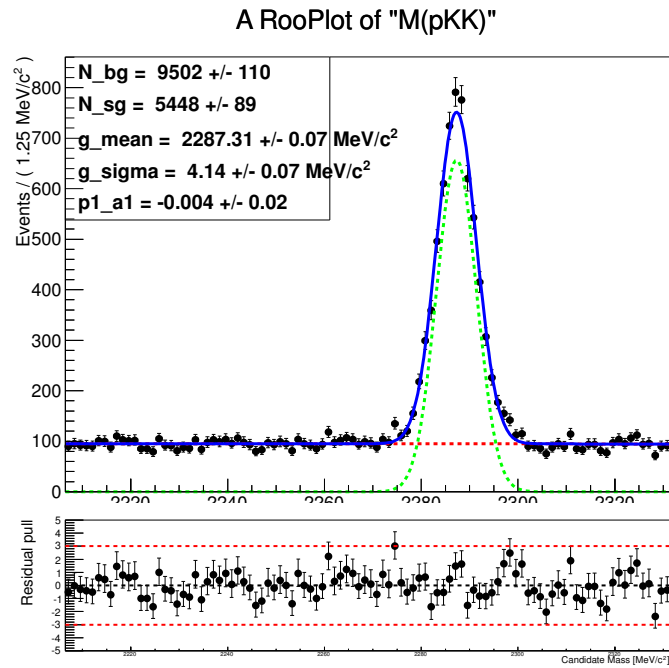


Figure 5.15:  $\Lambda_c$  mass fit and pull distribution for the semileptonic  $\Lambda_c^+ \rightarrow pK^-K^+$ .

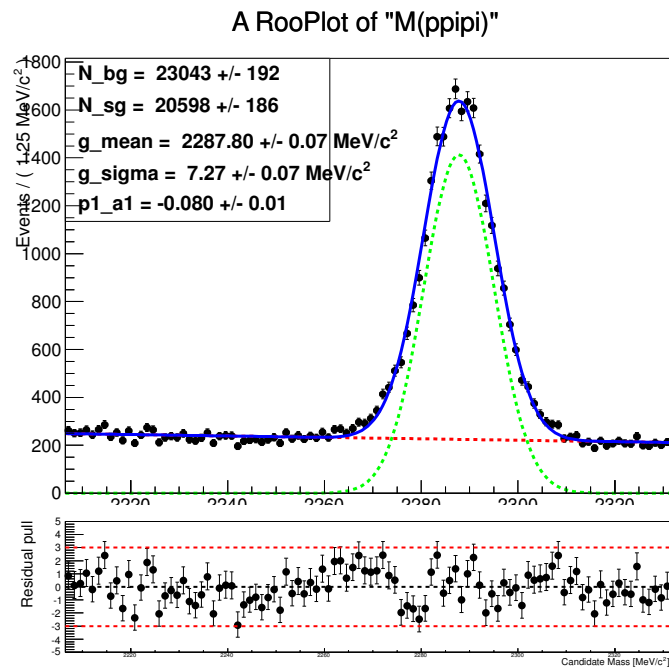


Figure 5.16:  $\Lambda_c$  mass fit and pull distribution for the semileptonic  $\Lambda_c^+ \rightarrow p\pi^-\pi^+$ .

### 5.2.3 Raw and adjusted yields

The raw and adjusted yields for each channel are given in Table 5.12. We do not provide errors on the adjusted yields, as these numbers when not taken as ratios fold in a number of detection and production uncertainties - their meaning in isolation is limited and they are merely given for illustration. We also note that the prompt adjusted yields fold in trigger efficiencies, which are demonstrated to cancel between the  $\Lambda_c^+ \rightarrow phh'$  modes and therefore not included in the final branching fraction results. The full systematic and statistical uncertainties are derived in Section 6. We note that the adjusted yields given also include the scaling factor of  $\frac{1}{0.9}$  for the Cabibbo-favoured yields, to account for the 10 % of the data which is used in the training.

Stream	Mode	Raw Yield	Adjusted Yield
Prompt	$\Lambda_c^+ \rightarrow pK^- \pi^+$	$129359 \pm 665$	$1.17 \times 10^{11}$
	$\Lambda_c^+ \rightarrow pK^- K^+$	$2717 \pm 122$	$2.36 \times 10^9$
	$\Lambda_c^+ \rightarrow p\pi^- \pi^+$	$10736 \pm 399$	$8.19 \times 10^9$
SL	$\Lambda_c^+ \rightarrow pK^- \pi^+$	$304597 \pm 631$	$1.24 \times 10^9$
	$\Lambda_c^+ \rightarrow pK^- K^+$	$5448 \pm 89$	$2.10 \times 10^7$
	$\Lambda_c^+ \rightarrow p\pi^- \pi^+$	$20598 \pm 186$	$9.31 \times 10^7$

Table 5.12: The raw yields for each of the prompt and semileptonically selected modes. The errors on the adjusted yields are the errors on the extracted yields, which accounts for the statistical uncertainty on the fitting procedure.

### 5.2.4 Planned update to prompt fits

The analysis procedure relies on the extraction of genuine  $\Lambda_c^+ \rightarrow phh'$  candidates from those candidates formed from combinatorics. This was first accomplished through a fit to the  $\Lambda_c$  candidate mass, however investigations of the promptly selected  $\Lambda_c^+ \rightarrow phh'$  signal  $IP\chi^2$  distributions revealed a significant high end tail. Such a tail is consistent with contamination from those  $\Lambda_c$  produced from decays of long-lived  $b$ -hadrons. We give a comparison of the data and simulation for the  $\Lambda_c^+ \rightarrow pK^- \pi^+$  prompt and semileptonic  $\log_e(IP\chi^2)$  in Figure 5.17, where the signal distributions of the data are extracted from fits to the  $\Lambda_c$  candidate mass.

Simulation of secondary  $\Lambda_c$  candidates was used to investigate the per-mode phase-space averaged stripping acceptance. The  $\Lambda_c$  candidates in the sample were all verified to have a long-lived  $b$ -hadron mother. In all cases the acceptances are higher than the prompt

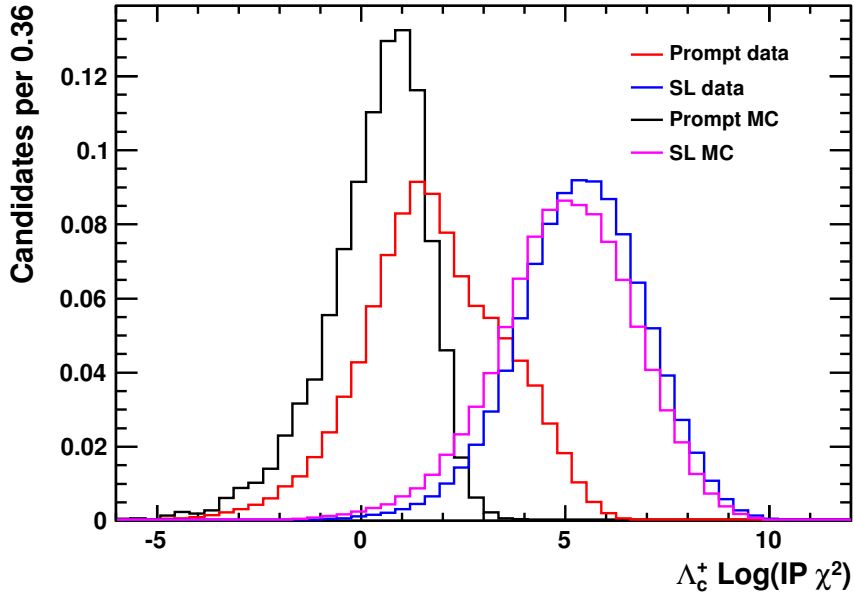


Figure 5.17: Data and simulation distributions for  $\Lambda_c$   $IP\chi^2$  distributions in both prompt and SL  $\Lambda_c^+ \rightarrow pK^-\pi^+$ . While the SL  $IP\chi^2$  are generally well modelled (albeit with a slight downward shift of the distribution in simulation), the prompt distributions do not agree. The high end tail in the prompt data is strong evidence of secondary  $\Lambda_c$  contamination.

$\Lambda_c$ . Importantly, the ratios of the secondary efficiencies between the  $\Lambda_c^+ \rightarrow phh'$  modes are not consistent with the ratios of the prompt efficiencies. As such, using purely prompt simulation to use the efficiency to correct for the candidate distributions extracted with only a fit to the  $\Lambda_c$  mass will yield biased relative branching fraction results in the prompt analysis.

Mode	Prompt		Secondary	
	$N_{\text{Acc}}$	$\epsilon_{\text{Strip} \text{Acc}}$	$N_{\text{Acc}}$	$\epsilon_{\text{Strip} \text{Acc}}$
$\Lambda_c^+ \rightarrow pK^-\pi^+$	2308801	$0.313 \pm 0.004$	225139	$0.701 \pm 0.018$
$\Lambda_c^+ \rightarrow pK^-K^+$	2289265	$0.251 \pm 0.003$	226432	$0.693 \pm 0.017$
$\Lambda_c^+ \rightarrow p\pi^-\pi^+$	2305682	$0.345 \pm 0.004$	223950	$0.686 \pm 0.017$

Table 5.13: The statistics and phase-space averaged stripping efficiencies for the prompt and secondary  $\Lambda_c$  in the “prompt” simulation. We note that the subscript “Acc” refers to the condition of passing the generator level cuts, and “Strip” refers to the condition of passing the no-PID stripping selection (including the kinematic vetoes and DTF convergence criterion).

This informs a planned update to the yield extraction in the analyses. The prompt yield extraction utilises a simultaneous 2D fit to the  $\Lambda_c$  mass and the  $\Lambda_c \log_e(IP\chi^2)$  to

extract the distribution for prompt signal candidates such that the secondary  $\Lambda_c^+ \rightarrow phh'$  component may be discriminated and treated as a background. We do not attempt to conduct a measurement with the data in the prompt selections identified as secondary - the muon tagged samples in the semileptonic analysis enjoy a higher selection efficiency and greater purity, and can provide a more precise measurement of the relative branching fractions. In the semileptonic analysis no evidence for significant prompt contamination in the data samples is observed. Therefore the signal extraction in the semileptonic analysis will still be accomplished with a fit to the  $\Lambda_c$  mass.

The species identified in the prompt sample are as follows:

**Prompt**  $\Lambda_c^+ \rightarrow phh'$  - decays of  $\Lambda_c^+ \rightarrow phh'$  where the  $\Lambda_c$  is produced either directly at the primary interaction or from a decay from a short-lived excited charm hadron. This is classed as the “signal”. The mass distribution of these candidates is modelled by a Crystal Ball function [143] and a Gaussian function constrained to a shared mean in the Cabibbo-favoured mode, and a Gaussian function in all other modes. <sup>2</sup>

**Secondary**  $\Lambda_c^+ \rightarrow phh'$  - decays of  $\Lambda_c^+ \rightarrow phh'$  where the  $\Lambda_c$  is produced in the decay of a long-lived  $b$ -hadron. This is classed as a background. The mass distribution of these candidates is modelled by a Crystal Ball function and a Gaussian function constrained to a shared mean in the Cabibbo-favoured mode, and a Gaussian function in all other modes.

**Combinatorics** - combinations of unrelated tracks which mimic  $\Lambda_c^+ \rightarrow phh'$  decays. The mass distribution of these candidates is modelled by a first order polynomial.

In all modes the  $\log_e(IP\chi^2)$  candidate distributions are modelled by a Bukin function, which is a modified Novosibirsk function with tail extended tail functions. The Bukin functional form is

$$B(x; \mu; \sigma; \xi; \rho_1; \rho_2) = \begin{cases} \exp \left[ \rho_1 \frac{(x-x_1)^2}{(x-x_1)^2} + \frac{(x-x_1)\xi\sqrt{\xi^2+1}\cdot\sqrt{2\log 2}}{1} - \log 2 \right] & x < x_1 \\ \exp \left[ -\log 2 \cdot \left[ \frac{\log \left( 1+2\xi\sqrt{\xi^2+1}\cdot\frac{x-\mu}{\sigma\sqrt{2\log 2}} \right)}{\log \left( 1+2\xi(\xi-\sqrt{\xi^2+1}) \right)} \right]^2 \right] & x_1 < x < x_2 \\ \exp \left[ \rho_2 \frac{(x_2-x)^2}{(x_2-\mu)^2} + \frac{(x_2-x)\xi\sqrt{\xi^2+1}\cdot\sqrt{2\log 2}}{1} - \log 2 \right] & x > x_2 \end{cases} \quad (5.9)$$

---

<sup>2</sup>The Crystal Ball function is a Gaussian function with a power law low-end tail. It is of particular use in parameterising the mass distributions of candidates formed from combinations of tracks from a decaying particle, whereby unreconstructed final state radiation (FSR) results in a lower computed invariant mass of the system which manifests in a low end power law tail.

where  $\xi$  is the Novosibirsk asymmetry parameter,  $\sqrt{2\log 2}\sigma$  is the full width half maximum (FWHM),  $\mu$  is the position of the mode, and  $\rho_1$  and  $\rho_2$  are the left and right tail parameters respectively.  $x_1$  and  $x_2$  are the turnover points where the function has half of its maximum value - they are defined as:

$$x_1 \equiv \mu + \sigma \sqrt{2\log 2} \left( \frac{\xi}{\sqrt{\xi^2 + 1}} - 1 \right) \quad (5.10)$$

$$x_2 \equiv \mu + \sigma \sqrt{2\log 2} \left( \frac{\xi}{\sqrt{\xi^2 + 1}} + 1 \right) \quad (5.11)$$

The function and its first derivative are continuous at  $x_1$  and  $x_2$ .

The fit is a simultaneous 2D fit to the  $\Lambda_c$  mass and the  $\Lambda_c$   $IP\chi^2$ . We utilise an unbinned extended maximum likelihood fit to the data candidates. All parameters in the mass models are allowed to float. The fit takes place over  $-80 - +45$  MeV/ $c^2$  of the nominal  $\Lambda_c$  mass of 2286.46 MeV/ $c^2$ . In the  $IP\chi^2$  models we take the shape of the combinatoric from a fit to the mass sidebands in data and fixing all Bukin parameters in the full fit to the results of this fit. For the prompt candidates we take initial values for the Bukin parameters from fits to simulated candidates, allowing all parameters to float with the exception of the  $\rho_2$  high-end tail, which lies in a region dominated by the secondaries and so is fixed to the value extracted from simulation. The secondary shape has its tail and asymmetry parameters fixed to values determined from fits to simulated data, while its mean is allowed to float.

The updated fits in the prompt analysis are currently under collaboration review, and any yields extracted using the current fit models will be updated in the future.

# Chapter 6

## $\Lambda_c^+ \rightarrow phh'$ branching fraction systematic uncertainties and results

### 6.1 Systematic uncertainties

The systematic uncertainties in the analyses are discussed herein. The primary sources of uncertainty are associated with the determination of selection efficiencies and the yield extraction.

#### 6.1.1 PID calibration uncertainty

There are two sources of systematic uncertainty associated with the PIDCalib procedure: the finite calibration statistics and the variation in PID efficiency across individual calibration bins. These are opposing trends with respect to granularity, and are described below.

##### Calibration statistics

The calibration procedure involves binning the calibration data in kinematic bins. This results in a statistical uncertainty that increases as the bin schema becomes more granular. Along with a PID weight associated with the calibration bin dictated by the event track kinematics, each signal event is ascribed a PID weight error. For a calibration bin  $i$ , the efficiency and associated error are given by:

$$\epsilon_i = k_i/n_i \tag{6.1}$$

$$\sigma(\epsilon_i) = \sqrt{\left| \frac{\epsilon_i(1 - \epsilon_i)}{n_i} \right|} \quad (6.2)$$

where  $n_i$  is the total number of calibration tracks in bin  $i$  and  $k_i$  is the number of calibration tracks in bin  $i$  surviving the PID cut.

In order to propagate this uncertainty in terms of final adjusted yields we utilise a toy simulation approach. The PID performance histograms have their bin efficiencies reassigned with a random number generated from a normal distribution with the measured bin efficiency as the mean and the error on the measured efficiency as the variance. The PID weights are then reassigned and an adjusted yield is recalculated. This procedure is repeated 1000 times. The toy simulation adjusted yield distribution is then fitted with a Gaussian function and the variance over the nominal adjusted yield is taken as a fractional systematic. Example adjusted yield distributions of the toy simulations are shown in Figure 6.1 for the prompt and semileptonic  $\Lambda_c^+ \rightarrow pK^-\pi^+$  decay channels.

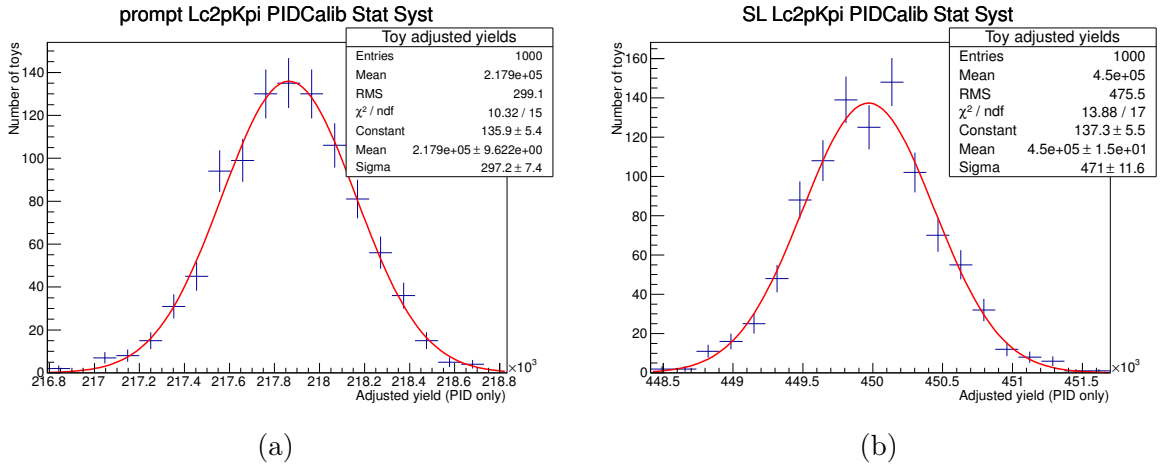


Figure 6.1: The  $\Lambda_c^+ \rightarrow phh'$  adjusted yields of the toy simulation, fitted with a Gaussian function. The variance over the mean of the Gaussian function is taken to be the fractional systematic on the individual adjusted yields. The only efficiency correction applied is the PID weighting.

### Efficiency variation across calibration bins

As the width of bins in the calibration sample increases, so does the variation of PID response within a given bin. If the kinematic distribution of the signal sample is not the same as that of the calibration sample, this can result in average PID cut efficiencies that are not the same between the signal and calibration modes within individual calibration bins. This systematic uncertainty is dependent on the binning schema utilised and on

the kinematic distribution of the signal sample. As such, this must be evaluated with simulated signal and calibration data. As the simulated calibration and signal samples both have the same poorly modelled PID distributions, any discrepancy between the true cut efficiency and that evaluated from `PIDCalib` will be due to binning effects.

No simulated  $\Lambda \rightarrow p\pi^-$  samples existed in the `PIDCalib` framework at the time the analysis was conducted, so MC samples were prepared by the candidate. These samples are outlined in [144]. PID performance histograms are constructed from the calibration simulation, and the calibration procedure is repeated with the simulated signal samples with a PID cut applied. This is then compared to the true efficiency of the PID cut as evaluated using the MC truth information. Our calibration procedure does not account for the number of tracks in the event because the distributions of this quantity in the individual modes is consistent. This results in our PID efficiencies being inaccurate by a constant factor when taken in isolation, but they cancel when the ratio of the efficiencies is taken for the relative branching fraction results. As such, we take the ratio of the `PIDCalib` efficiencies and compare these to the ratio of the true efficiencies of the PID cuts. The discrepancy in this quantity is dependent on the PID cut used, and to account for this the procedure is repeated for DLL values  $\pm 3$  of the nominal value used in the analysis.

The binning systematic is defined as:

$$\sigma_{bins} = \left| \frac{\epsilon_{true|pK\pi}}{\epsilon_{true|phh}} - \frac{\epsilon_{PIDCalib|pK\pi}}{\epsilon_{PIDCalib|phh}} \right| \quad (6.3)$$

where  $\epsilon_{true|phh}$  is the true efficiency of a given PID cut on the  $\Lambda_c^+ \rightarrow phh'$  mode in question, and  $\epsilon_{PIDCalib|phh}$  is the efficiency of the PID cut on the mode in question as evaluated with the `PIDCalib` method. This discrepancy is shown for the prompt relative branching fraction measurements in Figure 6.2. It should be noted that the large errors on these points are due to the low numbers of simulated events which survive our selection.

It was found that the proton PID response in this analysis varies much more rapidly across the kinematic phase space than the kaon or pion PID response - this is a result of both the RICH characteristics and also the harsher PID cuts placed upon protons in these analyses than kaons or pions. This resulted in a measured discrepancy in the individual proton track efficiencies that was significantly higher than the individual kaon and pion track efficiencies. As such, the maximum discrepancy while varying the proton  $\log(\mathcal{L}_p/\mathcal{L}_K)$  response was used as the basis for the quoted systematic. A systematic uncertainty is assigned as the combination in quadrature of the statistical uncertainty of the discrepancy

at the nominal value and the largest difference between the nominal discrepancy and any other discrepancy value in the scanned  $\log(\mathcal{L}_p/\mathcal{L}_K)$  range.

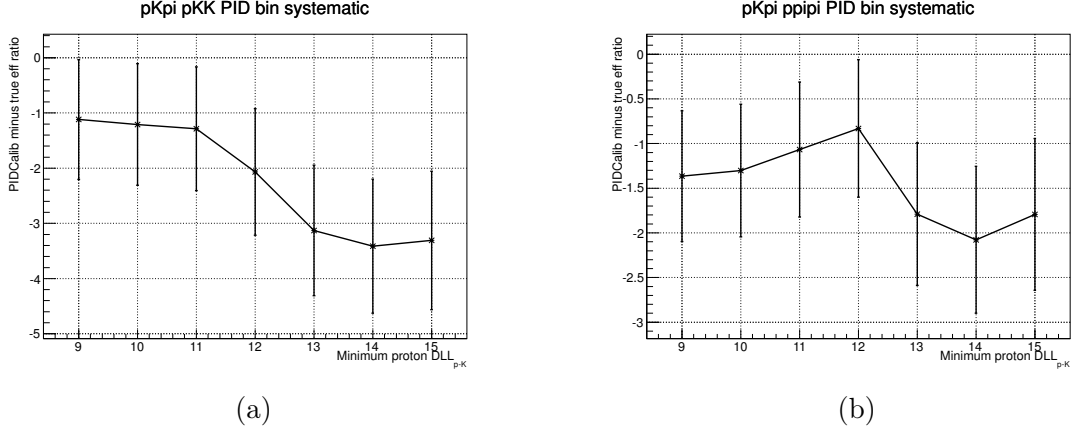


Figure 6.2: The discrepancy in simulation for the true and PIDCalib evaluated PID efficiencies for the promptly produced  $\Lambda_c^+ \rightarrow pK^-K^+$  to  $\Lambda_c^+ \rightarrow pK^-\pi^+$  ratio (left) and the  $\Lambda_c^+ \rightarrow p\pi^-\pi^+$  to  $\Lambda_c^+ \rightarrow pK^-\pi^+$  ratio (right). The discrepancy is given in %.

The systematic errors are shown for the relative semileptonic Cabibbo-suppressed measurements in Figure 6.3. These discrepancies are considerably lower than the corresponding discrepancies in the prompt measurements. This is explained by the looser PID cuts applied in the semileptonic selection. Generally, as PID cuts become tighter, variation of the PID efficiency over the  $p - \eta$  space becomes more rapid, leading to higher variation of PID response over individual bins in our schema.

### 6.1.2 Selection efficiency uncertainty

The uncertainty in the selection efficiency is dominated by the stripping efficiency uncertainty - the evaluation of the stripping efficiency systematic uncertainty is given in Section ???. The remaining contributions from the binomial uncertainty on the generator and trigger level uncertainties are much smaller, as we do not need to subdivide the samples to account for resonant contributions to the  $\Lambda_c$  decay.

### 6.1.3 Uncertainty due to fit model

There is a systematic uncertainty associated with our yield extraction and fit model to the  $\Lambda_c$  mass and  $\log_e(IP\chi^2)$ . To evaluate the dependence of the extracted yields on the fit model we vary the components of the fit to check for significant variations in extracted

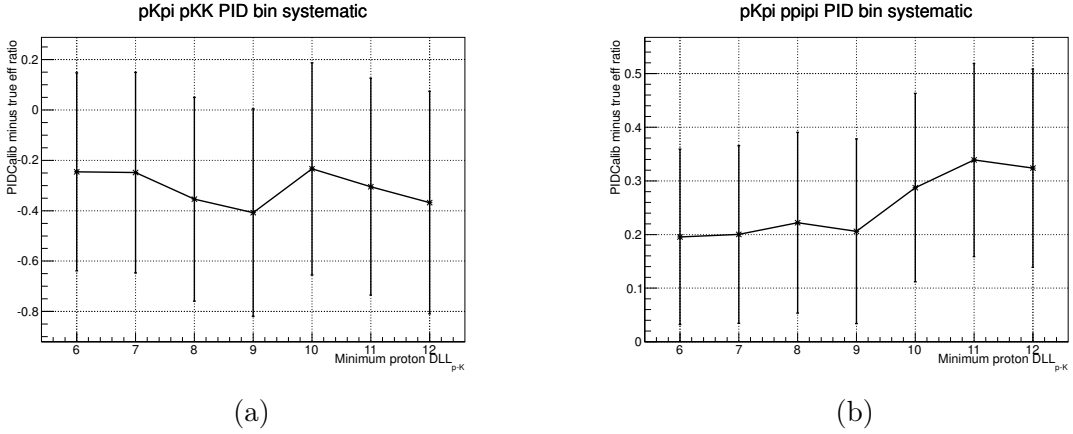


Figure 6.3: The discrepancy in simulation for the true and `PIDCalib` evaluated PID efficiencies for the semileptonically produced  $\Lambda_c^+ \rightarrow pK^- K^+$  to  $\Lambda_c^+ \rightarrow pK^- \pi^+$  ratio (left) and the  $\Lambda_c^+ \rightarrow p\pi^- \pi^+$  to  $\Lambda_c^+ \rightarrow pK^- \pi^+$  ratio (right). The discrepancy is given in %.

signal. In the fits to the  $\Lambda_c$  mass, we use both Crystal Ball functions and Gaussian functions for the signal (and secondary component in prompt), while we utilise exponential functions, first and second order polynomial functions to parameterise the combinatoric background component. In the prompt fits to the  $\Lambda_c \log_e(IP\chi^2)$  we substitute the Bukin functions for bifurcated Gaussian functions.

We take the standard deviation of the ensemble of extracted signal yields using all permutations of the combined models as the systematic uncertainty associated with the yield extraction. The standard deviation in extracted yield over the mean of the extracted yield is quoted as a per-mode systematic error. These are combined in quadrature to give systematic errors on the relative branching fraction measurements.

#### 6.1.4 Uncertainty from input parameters

A systematic uncertainty will arise from our use of input parameters to extract the absolute branching fractions using our relative values, specifically the absolute value of  $\mathcal{B}(\Lambda_c^+ \rightarrow pK^- \pi^+)$ . The PDG's current listings for the branching fraction provide a measurement taken as an average of a series of model-dependent results [10]. Their currently quoted value for  $\mathcal{B}(\Lambda_c^+ \rightarrow pK^- \pi^+)$  is  $(5.0 \pm 1.3)\%$ .

To extract absolute branching fractions for the Cabibbo-suppressed modes using our relative measurements we instead use a recent model independent measurement by the Belle Collaboration [145]. The measurement adopts a model-independent ap-

proach by reconstructing the recoiling momentum of the  $D^{*-}p\pi^+$  system in the decay  $e^+e^- \rightarrow D^{*-}p\pi^+ \Lambda_c^+$  to acquire  $\Lambda_c^+$  without reconstructing the  $\Lambda_c^+$  decay. They measure  $\mathcal{B}(\Lambda_c^+ \rightarrow pK^-\pi^+) = (6.84 \pm 0.24 \pm 0.21) \%$  where the first errors are statistical and the second are systematic. As such, we use the Belle result, which represents a significant improvement over the previous PDG average of model-dependent results.

### 6.1.5 Systematic uncertainties summary

The systematic uncertainties associated with the measurements are outlined in Table 6.1 through Table 6.4. We note that the systematic errors assigned for “Other finite MC stats” is that arising from limited MC statistics only in the determination of the generator level and trigger level efficiencies. Both calculations enjoy significantly larger statistics than the calculations for the stripping efficiency (due to the low stripping efficiencies and also the division of the stripping simulation into kinematic bins for efficiency reweighting). As such, both are small compared to other systematic errors in the analysis. The systematic uncertainties in Table 6.1 – Table 6.4 are either attributed to individual modes, or are derived with some combination of the modes (for example our `PIDCalib` systematics which are based on the ratio of efficiencies between modes) and indicated as such. The “total” systematics are the sum in quadrature of the individual systematic components.

Systematic	Mode	Magnitude [%]
Stripping reweighting - MC stats	$\Lambda_c^+ \rightarrow pK^- \pi^+$	2.1
	$\Lambda_c^+ \rightarrow pK^- K^+$	3.0
Stripping reweighting - binning	$\Lambda_c^+ \rightarrow pK^- \pi^+$	1.0
	$\Lambda_c^+ \rightarrow pK^- K^+$	1.1
Fit model uncertainty	$\Lambda_c^+ \rightarrow pK^- \pi^+$	0.2
	$\Lambda_c^+ \rightarrow pK^- K^+$	2.1
PIDCalib - Calib Stats	Combined	0.2
PIDCalib - binning	Combined	1.8
Other finite MC stats	Combined	0.2
Total	-	4.8

Table 6.1: Prompt  $\mathcal{B}(\Lambda_c^+ \rightarrow pK^- K^+)/\mathcal{B}(\Lambda_c^+ \rightarrow pK^- \pi^+)$  systematics

Systematic	Mode	Magnitude [%]
Stripping reweighting - MC stats	$\Lambda_c^+ \rightarrow pK^- \pi^+$	2.1
	$\Lambda_c^+ \rightarrow p\pi^- \pi^+$	2.4
Stripping reweighting - binning	$\Lambda_c^+ \rightarrow pK^- \pi^+$	1.0
	$\Lambda_c^+ \rightarrow p\pi^- \pi^+$	0.3
Fit model uncertainty	$\Lambda_c^+ \rightarrow pK^- \pi^+$	0.2
	$\Lambda_c^+ \rightarrow p\pi^- \pi^+$	3.0
PIDCalib - Calib Stats	Combined	0.1
PIDCalib - binning	Combined	1.5
Other finite MC stats	Combined	0.2
Total	-	4.8

Table 6.2: Prompt  $\mathcal{B}(\Lambda_c^+ \rightarrow p\pi^- \pi^+)/\mathcal{B}(\Lambda_c^+ \rightarrow pK^- \pi^+)$  systematics

Systematic	Mode	Magnitude [%]
Stripping reweighting - MC stats	$\Lambda_c^+ \rightarrow pK^- \pi^+$	0.3
	$\Lambda_c^+ \rightarrow pK^- K^+$	0.7
Stripping reweighting - binning	$\Lambda_c^+ \rightarrow pK^- \pi^+$	1.3
	$\Lambda_c^+ \rightarrow pK^- K^+$	1.5
Fit model uncertainty	$\Lambda_c^+ \rightarrow pK^- \pi^+$	0.5
	$\Lambda_c^+ \rightarrow pK^- K^+$	0.5
PIDCalib - Calib Stats	Combined	0.1
PIDCalib - binning	Combined	0.4
Other finite MC stats	Combined	0.4
Total	-	2.3

Table 6.3: SL  $\mathcal{B}(\Lambda_c^+ \rightarrow pK^- K^+)/\mathcal{B}(\Lambda_c^+ \rightarrow pK^- \pi^+)$  systematics

Systematic	Mode	Magnitude [%]
Stripping reweighting - MC stats	$\Lambda_c^+ \rightarrow pK^- \pi^+$	0.3
	$\Lambda_c^+ \rightarrow p\pi^- \pi^+$	1.1
Stripping reweighting - binning	$\Lambda_c^+ \rightarrow pK^- \pi^+$	1.3
	$\Lambda_c^+ \rightarrow p\pi^- \pi^+$	2.1
Fit model uncertainty	$\Lambda_c^+ \rightarrow pK^- \pi^+$	0.5
	$\Lambda_c^+ \rightarrow p\pi^- \pi^+$	1.5
PIDCalib - Calib Stats	Combined	0.1
PIDCalib - binning	Combined	0.4
Other finite MC stats	Combined	0.7
Total	-	3.2

Table 6.4: SL  $\mathcal{B}(\Lambda_c^+ \rightarrow p\pi^- \pi^+)/\mathcal{B}(\Lambda_c^+ \rightarrow pK^- \pi^+)$  systematics

## 6.2 $\Lambda_c^+ \rightarrow p\pi^- K^+$ significance extraction and confidence intervals

The statistical significances of the unobserved  $\Lambda_c^+ \rightarrow p\pi^- K^+$  modes are calculated from the change in the logarithm of the likelihood profiles ( $\Delta \ln L$ ) of the nominal mass fit with varying fixed values of signal yield. Therefore, the significance is given, in accordance with Wilks' theorem [146], by:

$$\text{Significance} = \sqrt{-2\Delta \ln L} \quad . \quad (6.4)$$

As the systematic errors have proven much smaller than the statistical errors in the analysis of the doubly-Cabibbo suppressed decays, we will ignore systematic errors in the calculation of Wilks' theorem. In the event of observing a  $\Lambda_c^+ \rightarrow p\pi^- K^+$  signal consistent with zero we utilise Wilks' theorem to derive upper limits on the signal yields, and correspondingly on the relative branching fractions.

## 6.3 $\Lambda_c^+ \rightarrow p\pi^- K^+$ results

### 6.3.1 Yield extractions

In this section we give the yield extractions for the doubly-Cabibbo suppressed modes. We remained ignorant of the candidate masses in the signal region until the selection, yield extraction, efficiency determinations and systematic uncertainties had been evaluated. The fit models to the  $\Lambda_c$  candidate mass are identical to those used in the singly-Cabibbo suppressed modes. The fits to the data and the pull distributions are shown in Figure 6.4 for the prompt channel and in Figure 6.5 for the semileptonic channel. The extracted signal yields are consistent with zero in the prompt analysis and  $539 \pm 64$  for the semileptonic analysis.

### 6.3.2 Efficiency corrections

We remind the reader that the generator-level and the trigger efficiencies cancel between the Cabibbo-favoured and the doubly-Cabibbo suppressed modes, as the acceptance is flat across the variable space characterising the resonant decay. We are able to successfully distinguish the  $\Lambda_c^+ \rightarrow p\pi^- K^+$  data in the semileptonic analysis, and so are sensitive to the

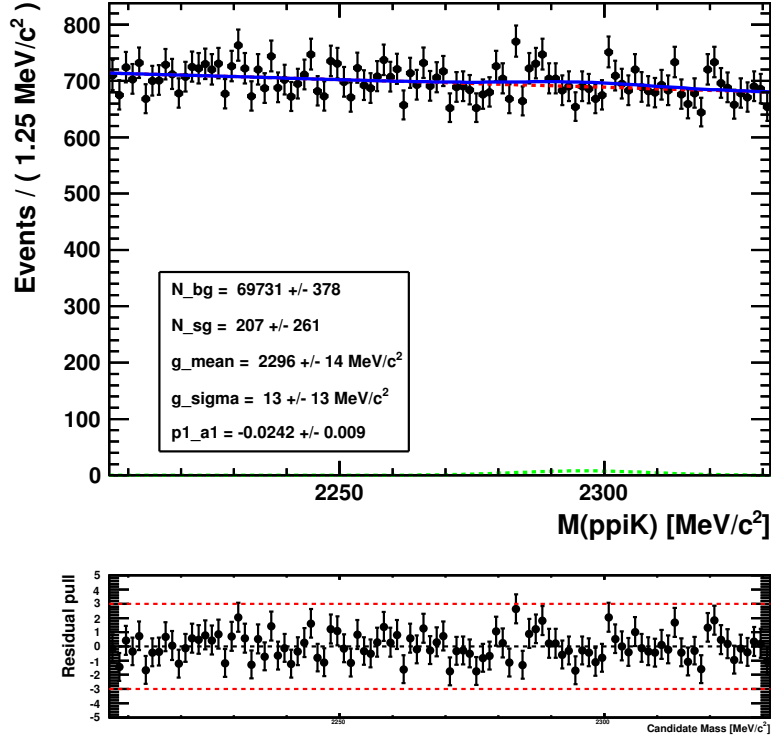


Figure 6.4:  $\Lambda_c$  mass fit and pull distribution for the promptly selected  $\Lambda_c^+ \rightarrow p\pi^-K^+$ .

different resonance structure of the decay compared to the Cabibbo-favoured. As we are not sensitive to the kinematics of any promptly-produced  $\Lambda_c^+ \rightarrow p\pi^-K^+$ , we must assume that its efficiency is the same as the promptly-produced  $\Lambda_c^+ \rightarrow pK^-\pi^+$ .

Herein we provide the selection efficiencies for the semileptonic  $\Lambda_c^+ \rightarrow p\pi^-K^+$ . The efficiencies of the PID selection and the stripping selection are data-driven and informed by the data kinematics respectively, and as such could only be evaluated prior to unblinding the signal windows. The stripping selection efficiencies for  $\Lambda_c^+ \rightarrow pK^-\pi^+$  and  $\Lambda_c^+ \rightarrow p\pi^-K^+$  are given in Table 6.5, while the PID efficiencies are given in Table 6.6. The full selection efficiencies are given in Table 6.7.

### 6.3.3 Systematic uncertainties

The systematic uncertainties are evaluated in the same fashion as the relative branching ratios of the Cabibbo-suppressed measurements. The systematic ‘‘Finite MC stats’’ which was present in those measurements is not present here, as the trigger and generator-level

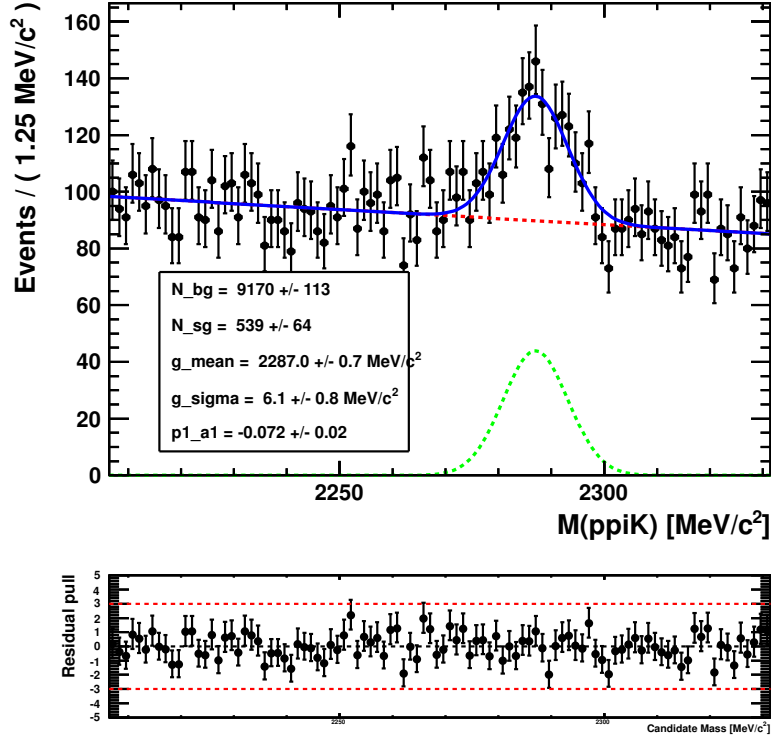


Figure 6.5:  $\Lambda_c$  mass fit and pull distribution for the semileptonically selected  $\Lambda_c^+ \rightarrow p\pi^- K^+$ .

Analysis	Mode	$\epsilon_{\text{Strip Acc}}$ [%]
Semileptonic	$\Lambda_c^+ \rightarrow pK^- \pi^+$	$(1.194 \pm 0.016)\%$
	$\Lambda_c^+ \rightarrow p\pi^- K^+$	$(1.111 \pm 0.020)\%$

Table 6.5: The  $\Lambda_c^+ \rightarrow p\pi^- K^+$  stripping efficiencies after the re-weighting procedure is applied to the  $\Lambda_c^+ \rightarrow pK^- \pi^+$  simulation.

efficiencies cancel. The systematic uncertainties summaries are provided in Table 6.8.

Analysis	Mode	$\epsilon_{\text{PID Strip}}$ [%]
Semileptonic	$\Lambda_c^+ \rightarrow pK^- \pi^+$	$47.95 \pm 0.05$
	$\Lambda_c^+ \rightarrow p\pi^- K^+$	$50.48 \pm 0.05$

Table 6.6: The  $\Lambda_c^+ \rightarrow p\pi^- K^+$  PID efficiencies, as calculated using the PIDCalib technique.

Analysis	Mode	$\epsilon_{\text{Total}}$
Semileptonic	$\Lambda_c^+ \rightarrow pK^- \pi^+$	$(2.71 \pm 0.01) \times 10^{-4}$
	$\Lambda_c^+ \rightarrow p\pi^- K^+$	$(2.67 \pm 0.01) \times 10^{-4}$

Table 6.7: The total selection efficiencies in the Cabibbo-favoured and doubly-Cabibbo suppressed channels. The errors are the statistical errors from finite signal simulation and PIDCalib calibration data only.

Systematic	Mode	Magnitude [%]
Stripping reweighting - MC stats	$\Lambda_c^+ \rightarrow pK^- \pi^+$	0.3
	$\Lambda_c^+ \rightarrow p\pi^- K^+$	0.4
Stripping reweighting - binning	$\Lambda_c^+ \rightarrow pK^- \pi^+$	1.3
	$\Lambda_c^+ \rightarrow p\pi^- K^+$	1.8
Fit model uncertainty	$\Lambda_c^+ \rightarrow pK^- \pi^+$	0.5
	$\Lambda_c^+ \rightarrow p\pi^- K^+$	2.1
PIDCalib - Calib Stats	Combined	0.2
PIDCalib - binning	Combined	2.0
Total	-	3.3

Table 6.8: SL  $\mathcal{B}(\Lambda_c^+ \rightarrow p\pi^- K^+)/\mathcal{B}(\Lambda_c^+ \rightarrow pK^- \pi^+)$  systematics

### 6.3.4 Signal significance extractions

The significance of the semileptonic signal is taken from Wilks' theorem. The semileptonic  $-\Delta$  Log-likelihood as a function of signal yield is shown in Figure 6.6. The significance is found to be  $11.1\sigma$  for the semileptonic channel. This corresponds to a significant discovery, the first of this mode. We note that this is the first doubly-Cabibbo suppressed mode of a charmed baryon to be observed.

We use Wilks' theorem to set upper limits on the prompt  $\Lambda_c^+ \rightarrow p\pi^- K^+$  yield, and in turn set upper limits on the relative branching fraction  $\mathcal{B}(\Lambda_c^+ \rightarrow p\pi^- K^+)/\mathcal{B}(\Lambda_c^+ \rightarrow pK^- \pi^+)$ . We do not have access to the  $\Lambda_c$  daughter kinematics for the doubly-Cabibbo suppressed mode, and so must assume a constant efficiency between the two samples. The prompt  $-\Delta$  Log-likelihood as a function of signal yield is shown in Figure 6.7. The 95 % upper limit on the signal yield is 350, corresponding to an upper limit on the relative branching fraction  $\mathcal{B}(\Lambda_c^+ \rightarrow p\pi^- K^+)/\mathcal{B}(\Lambda_c^+ \rightarrow pK^- \pi^+)$  of  $< 2.71 \times 10^{-3}$  @ 95 % C.L..

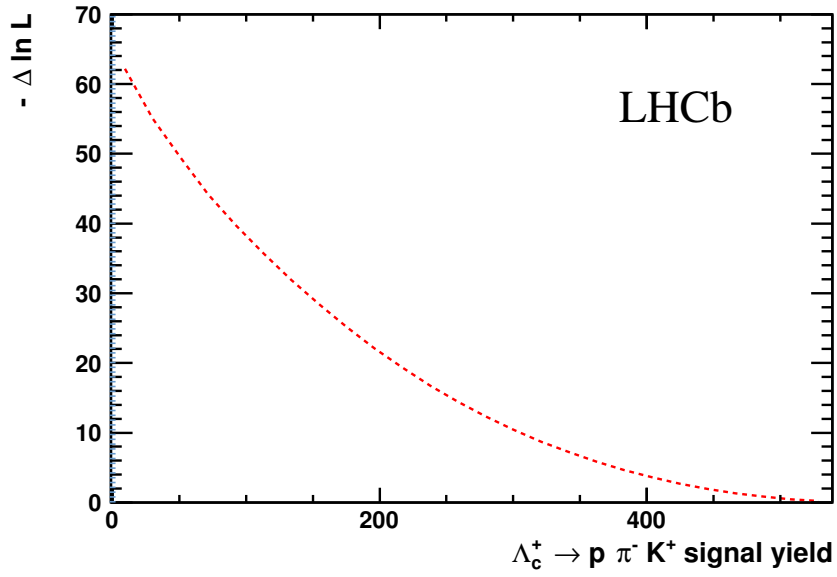


Figure 6.6: The  $-\Delta$  Log-likelihood as a function of the semileptonic  $\Lambda_c^+ \rightarrow p\pi^- K^+$  signal yield. The  $-\Delta$  Log-likelihood with respect to the null hypothesis is 62.2, corresponding to an observed significance of 11.1  $\sigma$ .

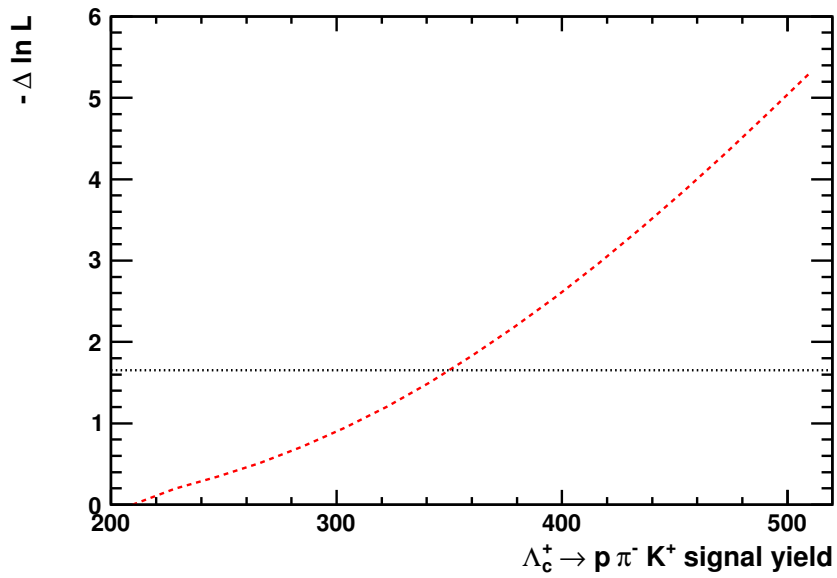


Figure 6.7: The  $-\Delta$  Log-likelihood as a function of the prompt  $\Lambda_c^+ \rightarrow p\pi^- K^+$  signal yield. The lowest signal yield corresponding to an increase in  $-\Delta$  Log-likelihood of 1.645, or a 95 % one-sided confidence interval, is 350.

## 6.4 Relative branching fraction results

Now that we have determined full per-mode selection efficiencies and raw yields the expression for the relative branching fraction of a given  $\Lambda_c^+ \rightarrow phh'$  mode is:

$$\frac{\mathcal{B}(\Lambda_c^+ \rightarrow phh')}{\mathcal{B}(\Lambda_c^+ \rightarrow pK^-\pi^+)} = \frac{N_{[\Lambda_c^+ \rightarrow phh']}}{N_{[\Lambda_c^+ \rightarrow pK^-\pi^+]}} \times \frac{\epsilon_{[\Lambda_c^+ \rightarrow pK^-\pi^+]}}{\epsilon_{[\Lambda_c^+ \rightarrow phh']}} \quad (6.5)$$

where  $N$  indicates the raw yield and  $\epsilon$  the full selection efficiency of the designated mode. The final relative branching fractions for the prompt and semileptonic analyses are given in Table 6.10. The first errors are statistical (the sum of weights squared errors on the respective yields combined in quadrature), the second are the full systematics in the analysis.

Measurement	Prompt	Semileptonic
$\frac{\mathcal{B}(\Lambda_c^+ \rightarrow pK^-K^+)}{\mathcal{B}(\Lambda_c^+ \rightarrow pK^-\pi^+)}$	$(2.03 \pm 0.07 \pm 0.10) \times 10^{-2}$	$(1.68 \pm 0.03 \pm 0.07) \times 10^{-2}$
$\frac{\mathcal{B}(\Lambda_c^+ \rightarrow p\pi^-\pi^+)}{\mathcal{B}(\Lambda_c^+ \rightarrow pK^-\pi^+)}$	$(7.04 \pm 0.19 \pm 0.34) \times 10^{-2}$	$(7.45 \pm 0.06 \pm 0.24) \times 10^{-2}$
$\frac{\mathcal{B}(\Lambda_c^+ \rightarrow p\pi^-K^+)}{\mathcal{B}(\Lambda_c^+ \rightarrow pK^-\pi^+)}$	$< 2.71 \times 10^{-3} @ 95 \% \text{ C.L.}$	$(1.62 \pm 0.15 \pm 0.05) \times 10^{-3}$

Table 6.9: Final relative branching fractions for  $\Lambda_c^+ \rightarrow pK^-K^+$ ,  $\Lambda_c^+ \rightarrow p\pi^-\pi^+$  and  $\Lambda_c^+ \rightarrow p\pi^-K^+$  with respect to  $\Lambda_c^+ \rightarrow pK^-\pi^+$ . The first errors are statistical, the second are the full systematic errors in the analysis.

## 6.5 Extraction of absolute branching fractions

These results are obtained by combining the relative results with the model independent measurement of the absolute  $\Lambda_c^+ \rightarrow pK^-\pi^+$  branching fraction from the Belle collaboration [145] to extract the absolute branching fractions of the Cabibbo-suppressed modes for  $\Lambda_c^+ \rightarrow pK^-K^+$ ,  $\Lambda_c^+ \rightarrow p\pi^-\pi^+$  and  $\Lambda_c^+ \rightarrow p\pi^-K^+$  in both the prompt and semileptonic analyses. The external uncertainty quoted comes from the uncertainty on the absolute  $\Lambda_c^+ \rightarrow pK^-\pi^+$  branching fraction.

Measurement	Analysis	Value
$\mathcal{B}(\Lambda_c^+ \rightarrow pK^- K^+)$	Prompt	$(1.39 \pm 0.05 \text{ (stat)} \pm 0.07 \text{ (syst)} \pm 0.07 \text{ (ext)}) \times 10^{-3}$
	SL	$(1.15 \pm 0.03 \text{ (stat)} \pm 0.06 \text{ (syst)} \pm 0.05 \text{ (ext)}) \times 10^{-3}$
$\mathcal{B}(\Lambda_c^+ \rightarrow p\pi^- \pi^+)$	Prompt	$(4.82 \pm 0.13 \text{ (stat)} \pm 0.23 \text{ (syst)} \pm 0.23 \text{ (ext)}) \times 10^{-3}$
	SL	$(5.10 \pm 0.04 \text{ (stat)} \pm 0.16 \text{ (syst)} \pm 0.24 \text{ (ext)}) \times 10^{-3}$
$\mathcal{B}(\Lambda_c^+ \rightarrow p\pi^- K^+)$	Prompt	$< 1.85 \times 10^{-4} @ 90 \% \text{ C.L.}$
	SL	$(1.11 \pm 0.10 \text{ (stat)} \pm 0.04 \text{ (syst)} \pm 0.05 \text{ (ext)}) \times 10^{-4}$

Table 6.10: Final absolute branching fractions for  $\Lambda_c^+ \rightarrow pK^- K^+$ ,  $\Lambda_c^+ \rightarrow p\pi^- \pi^+$  and  $\Lambda_c^+ \rightarrow p\pi^- K^+$  with respect to  $\Lambda_c^+ \rightarrow pK^- \pi^+$ . The first errors are statistical, the second are the full systematic errors in the analysis, the third are the external uncertainties from our use of the BELLE measurement of the absolute  $\Lambda_c^+ \rightarrow pK^- \pi^+$  branching fraction.

# Chapter 7

## Summary and conclusions

### 7.1 Summary

This thesis began with a theory review of the Standard Model (SM) of particle physics in Chapter 1. Therein the development of the quark model was described, along with the theory of the Cabibbo-Kobayashi-Maskawa quark mixing matrix underpinning the coupling of quarks via the weak interaction. This was followed by a review of recent charmed baryon calculations from theory, specifically from lattice Quantum Chromodynamics (QCD) and the Heavy Quark Effective Theory (HQET). The chapter concluded by discussing experimental results in charmed hadron spectroscopy, including recent efforts in identifying new states and amplitude analysis of charmed baryon decays.

In Chapter 2, the design and performance of the Large Hadron Collider beauty (LHCb) experiment at the Large Hadron Collider (LHC) was presented. The systems responsible for particle tracking, particle identification (PID), and particle calorimetry were described. The functionality and performance of the LHCb trigger system was given, along with a description of the Monte Carlo generators used by LHCb to simulate proton collisions, heavy-flavour decays, and particle transport through the detector.

In Chapter 3, the RICH system at LHCb was detailed, including the design and operation of the RICH1 and RICH2 detectors. A track-based reconstruction method is detailed, which is used to assign relative likelihoods of the identities of charged particles which radiate Cherenkov photons in the RICH. A data-driven correction for selections utilising these PID estimators is outlined, along with the datasets of cleanly reconstructed decays used to perform the correction. The development of new heavy-flavour samples of calibration protons from  $\Lambda_c^+ \rightarrow pK^-\pi^+$  decays is described. The helicity information of

the  $\Lambda_c$  decay is used as a powerful discriminant between signal decays and combinatoric backgrounds. A series of cross checks are described to monitor the systematic uncertainties in the extraction of the kinematic distributions of the signal protons.

The results of a study of the RICH1 aerogel performance were presented. This study demonstrated that, despite a notable improvement in the performance in 2012 relative to 2011, the discrimination between charged species provided by the aerogel is at a far lower level than that afforded by the gas radiators. These results were of key influence in the decision by the LHCb collaboration to remove the aerogel from the RICH1 detector for the upcoming LHC run II.

In Chapters 4 – 6, the results of an analysis to measure the relative branching fractions of  $\Lambda_c^+ \rightarrow phh'$ , where  $hh' \in \{K^-\pi^+, K^-K^+, \pi^-\pi^+, \pi^-K^+\}$ , was presented. The analysis used a dataset gathered with the LHCb detector in 2011, corresponding to an integrated luminosity of  $1 \text{ pb}^{-1}$ . This analysis utilised  $\Lambda_c$  produced from two sources -  $\Lambda_c$  produced promptly at the primary interaction and  $\Lambda_c$  produced in the decay  $\Lambda_b^0 \rightarrow \Lambda_c^+(pK^-\pi^+)\mu^-\bar{\nu}_\mu$ .

The measurements of the branching fractions of the singly-Cabibbo suppressed channels relative to the Cabibbo favoured were:

$$\begin{aligned} \mathcal{B}(\Lambda_c^+ \rightarrow pK^-K^+)/\mathcal{B}(\Lambda_c^+ \rightarrow pK^-\pi^+) &= (2.03 \pm 0.07 \text{ (stat)} \pm 0.10 \text{ (syst)}) \times 10^{-2}, \\ \mathcal{B}(\Lambda_c^+ \rightarrow p\pi^-\pi^+)/\mathcal{B}(\Lambda_c^+ \rightarrow pK^-\pi^+) &= (7.04 \pm 0.19 \text{ (stat)} \pm 0.34 \text{ (syst)}) \times 10^{-2} \end{aligned}$$

while in the semileptonic analysis they were

$$\begin{aligned} \mathcal{B}(\Lambda_c^+ \rightarrow pK^-K^+)/\mathcal{B}(\Lambda_c^+ \rightarrow pK^-\pi^+) &= (1.68 \pm 0.03 \text{ (stat)} \pm 0.04 \text{ (syst)}) \times 10^{-2}, \\ \mathcal{B}(\Lambda_c^+ \rightarrow p\pi^-\pi^+)/\mathcal{B}(\Lambda_c^+ \rightarrow pK^-\pi^+) &= (7.45 \pm 0.06 \text{ (stat)} \pm 0.24 \text{ (syst)}) \times 10^{-2}, \end{aligned}$$

These results are the most precise measurements of both relative branching fractions made to date. The two measurements of  $\mathcal{B}(\Lambda_c^+ \rightarrow pK^-K^+)/\mathcal{B}(\Lambda_c^+ \rightarrow pK^-\pi^+)$  show a discrepancy of  $2.6 \sigma$ . It is believed that a small amount of non-prompt background in the prompt signal accounts for this difference. The  $\mathcal{B}(\Lambda_c^+ \rightarrow p\pi^-\pi^+)/\mathcal{B}(\Lambda_c^+ \rightarrow pK^-\pi^+)$  measurements are compatible within  $0.9 \sigma$ .

The analysis also included a search for the hitherto unobserved doubly-Cabibbo suppressed decay  $\Lambda_c^+ \rightarrow p\pi^-K^+$ . The decay was found unambiguously in the semileptonic analysis, with a signal significance of  $11.1\sigma$ . The branching fraction of the mode relative

to the Cabibbo-favoured was measured to be:

$$\mathcal{B}(\Lambda_c^+ \rightarrow p\pi^- K^+)/\mathcal{B}(\Lambda_c^+ \rightarrow pK^-\pi^+) = (1.62 \pm 0.15 \text{ (stat)} \pm 0.05 \text{ (syst)}) \times 10^{-3} .$$

Utilising the recent BELLE measurement of the absolute  $\Lambda_c^+ \rightarrow pK^-\pi^+$  branching fraction, we extract the absolute branching fraction:

$$\mathcal{B}(\Lambda_c^+ \rightarrow p\pi^- K^+) = (1.11 \pm 0.10 \text{ (stat)} \pm 0.04 \text{ (syst)} \pm 0.05 \text{ (ext)}) \times 10^{-4}$$

We note that this is the lowest recorded branching fraction of any charmed baryon decay to date. While we do not observe the decay in the prompt analysis, we are able to place an upper limit on the decay of:

$$\mathcal{B}(\Lambda_c^+ \rightarrow p\pi^- K^+) < 1.85 \times 10^{-4} @ 90 \% \text{ C.L.}$$

which is compatible with our observation of this decay mode in the semileptonic analysis.

## 7.2 Outlook

There still remain a great many observations to be recorded in the field of charmed baryon spectroscopy, and LHCb has the potential to make a great many of these. The plentiful production of charm in LHC collisions, along with the detector's versatility in recording heavy-flavour decays, provides the detector with the ability to gather unprecedented datasets on a variety of charmed baryons.

In the observation of the decay  $\Lambda_c^+ \rightarrow p\pi^- K^+$ , the dominant errors in the analysis are statistical in nature. With more data, more precise measurements of the relative branching fractions can be made. A significant amount of valid signal in the analysis was lost due to the lack of PIDCalib calibration data. Thanks to the new datasets described in Chapter 3, future analyses of decays containing protons in the final state will be able to retain greater signal yields. In future  $\Lambda_c^+ \rightarrow phh'$  analyses, the lack of any kinematic vetoes on the candidates will also lessen the sculpting of the acceptance with respect to the variables characterising the resonant  $\Lambda_c$  decay. As a consequence, the selection efficiencies of future analyses will be better understood.

This analysis has demonstrated that the LHCb datasets of the Cabibbo-suppressed  $\Lambda_c$  decays are abundant enough that a first amplitude analysis of these decays can be conducted at LHCb. With the precise vertexing and decay-time resolution achievable at

the experiment, the charmed baryon lifetimes will be measured to a very high precision at LHCb. These endeavours will be bolstered by the large dataset LHCb is expected to gather in the upcoming LHC run II, and provide the experiment with the ability to continue to make charmed baryon discoveries throughout its lifetime.

LHCb continues to search for doubly-charmed baryon production, such that the nature of the SELEX observation might finally be confirmed. Recent theory calculations suggest that with  $10 \text{ fb}^{-1}$  of LHCb data, around the order of  $10^5$  decays of triple-heavy baryons can be recorded at LHCb [147].

# Appendix A

## Optimum descriptions of efficiency spaces

A common problem in LHCb analyses, and in HEP analyses in general, is poor modelling in the simulation of a signal decay, where the simulation must be used to apply an efficiency correction that cannot be determined using some data-driven method. This usually necessitates some re-weighting approach, such that the simulation candidates are re-weighted according to the real data distributions relevant to the acceptance of the selection. A common solution to this problem is to identify variables which are both badly modelled and on which the acceptance of the selection depends - the simulation should then be binned in these variables, and by counting the numbers of simulated candidates that survive the selection and the number of simulated candidates generated in each bin, local efficiencies in the variable space can be derived. The data candidates are then assigned per-candidate efficiencies dependent on their location in the variable space. In this way the efficiencies of each simulation bin are re-weighted by the data population in the corresponding bin .

### A.1 Systematics in efficiency re-weightings

This approach raises another concern: how should the simulation be binned? The systematic uncertainties of the re-weighting procedure are highly dependent on the choice of binning schema. The binning schema should be informed by considerations of:

- The distributions of the simulated data in the re-weighting variables. In local variable space regions of high simulation population, statistical uncertainties become lower,

and more granular binnings may be considered.

- The relative distributions of both the data and the simulation. In regions of the variable space where the data and simulation agree, little to no re-weighting is required. Where the distributions disagree, high granularity is desirable.
- The distributions of the selection acceptance. In regions where the acceptance is constant, there is no need to locally divide the simulation into bins. Where the acceptance varies rapidly, it is desirable to increase the binning granularity in that region of the variable space. If the binning granularity is not fine enough, information on the efficiency structure is lost.

These considerations directly pertain to the systematic uncertainties and biases that are incurred during the re-weighting procedures. Systematic uncertainties - and biases - can arise from several sources:

**Limited calibration statistics.** As the binning schema becomes more granular, the statistics in each bin become lower. This results in a higher binomial error on the bin efficiency. This can also result in biases to the re-weighted efficiencies. The bias is only relevant when statistical fluctuations become very high, and is fully outlined in Appendix B.

**Variations in efficiency over individual bins.** The re-weighting relies on the bins being small enough that the efficiency in each bin is approximately single-valued. Due to the finite bin size, there is some finite variation in efficiency over the individual bins. As the kinematics of the data and MC are different, the average efficiency in one particular bin can be different in the data and MC, leading to potential biases. This effect becomes more severe with larger bins.

The first may be evaluated with a toy simulation approach, provided certain conditions are met. The second is more problematic to evaluate, but the use of multiple schemas may give an idea of the magnitude of the systematic error, motivated by a meta-analysis of the bin efficiencies (which will be outlined later).

### A.1.1 Limited MC statistics - inflation of error

In any binning schema, each bin has a binomial uncertainty associated to it. To propagate this error through to the final extracted efficiency, we utilise a toy approach. In this

method, we take a particular binning schema and evaluate efficiencies and binomial errors for each bin:

$$\begin{aligned}\epsilon &= \frac{N_{strip}}{N_{gen}} \\ \sigma_\epsilon &= \sqrt{\frac{\epsilon(1-\epsilon)}{N_{gen}}}\end{aligned}\tag{A.1}$$

We then generate a large number of toy efficiency histograms based on the original. For every toy, in each bin we randomly resample the number of events which pass the selection from a binomial distribution, using the original number of candidates generated in said bin and the efficiency of the original bin such that  $N_{gen}$  is the mean and  $\epsilon$  is the probability of the binomial distribution. We then use each binning schema to assign a stripping efficiency to each real data candidate, and then from the efficiency-corrected yield extract a new stripping efficiency for the mode using the candidate sWeights:

$$\begin{aligned}M &= \sum_{i=1}^n \frac{w_i}{\epsilon_i} \\ \bar{\epsilon} &= N/M\end{aligned}\tag{A.2}$$

where  $w_i$  is the candidate sWeight,  $\epsilon_i$  the candidate stripping efficiency,  $M$  the adjusted yield,  $N = \sum_{i=1}^n w_i$  the extracted raw yield and  $\bar{\epsilon}$  the re-weighted average efficiency.

In such a fashion, for each toy an  $\bar{\epsilon}$  is calculated. We then take the standard deviation of the  $\bar{\epsilon}$  distribution over the original efficiency as a fractional systematic uncertainty. This method only provides an accurate systematic in the case whereby valid efficiencies will be returned after randomisation. In the case of errors resampled from a binomial distribution, this method breaks down when the probability of randomising zero stripped candidates is non-negligible. This provides a limit on the granularity of the bin schemas used in the re-weighting, although in practice this is less strict than the high granularity boundary imposed by the efficiency bias outlined in Appendix B.

### A.1.2 Variations in efficiency over individual bins

In any binned re-weighting approach, it is necessary that the granularity of the binning schema be fine enough that it sufficiently accounts for the true variation in the underlying efficiency. Parameterising this in a proper fashion is problematic - the only way to assess whether or not there is finer structure in the efficiency than a given binning can account

for is to adopt a finer binning and check for regions whereby new structure appears, or to check if the re-weighted average efficiency is altered outwith the statistical uncertainty. Naturally, the number of subdivisions that can be made locally is limited by the low statistics thresholds mentioned in the previous section - eventually either the statistical uncertainty on the extracted efficiency becomes so large as to obscure any genuine changes in local efficiency or to bias the efficiency, or the the probability of the toy bins not being assigned a valid efficiency becomes non-negligible (i.e. when the likelihood of returning zero new events passed in a given bin becomes non-negligible in our binomial resampling).

### A.1.3 The $\kappa$ statistic

### A.1.4 The $\kappa$ bin boundary parameter

Ultimately we wish to minimise the overall systematic uncertainty arising from these opposing trends. For better or worse, this is usually done visually by analysts. By investigating the acceptance in different binning granularities and examining the statistical errors on each bin an optimum can be loosely determined. This is problematic in two ways:

1. This is a subjective approach, and lacks a quantitative statement of what constitutes the optimum binning.
2. This only applies to multidimensional structures which can be easily visualised. Any re-weightings of dimensionality 3 or higher are almost impossible to judge “by eye”.

As such, we seek a quantitative method of assessing the choice of a bin schema, which is applicable for any dimensionality, regardless of ease of visualisation.

We posit that while not mathematically equivalent to minimising the systematic, that providing the best description of the efficiency space possible with a given sample size of simulation statistics will ensure a close to optimum systematic when the efficiency bin schema is used in re-weightings. To this end we investigate the difference in efficiency relative to the statistical error on efficiency at each bin boundary. This weighted difference in efficiency between bin  $a$  and bin  $b$ ,  $\kappa_{ab}$ , may be expressed as:

$$\kappa_{ab} = \frac{|\epsilon_a - \epsilon_b|}{\sqrt{\sigma_a^2 + \sigma_b^2}} \quad (\text{A.3})$$

- If this quantity is small, then the variation in efficiency between the bins relative to the error on said bins' efficiencies is small. This may be interpreted that the binomial efficiency on the bin efficiencies is taken to be large relative to the necessary parametrisation of the local variations in efficiency, and that for an optimum description of the efficiency the bins should be merged at the boundary. This will entail a sufficiently granular binning to provide an accurate description of the efficiency in the local region but with a lowered binomial error on the merged bin efficiency.
- If this quantity is high, then there is a large, statistically significant difference in efficiency between the adjacent bins. This may be interpreted that the variation in efficiency across the bin boundary is very high, and that variation in efficiency across the bins themselves will be significant. This implies the assumption that the efficiency is approximately single-valued in the bins forming the boundary - which is necessary in the re-weighting procedure - is a poor one. As such, the description of the efficiency space may be further optimised by imposing a higher binning granularity in these regions.

This is complicated by the effects of genuine statistical fluctuation on individual bin efficiencies - as such, the single  $\kappa$  values of boundaries can be misleading. Instead, the relevance of  $\kappa$  values lies in their distributions across an entire schema. By looking at these instead of individual bin boundaries, this mitigates the effects of efficiency fluctuation and gives a more meaningful description of the suitability of the schema.

This is not a perfect panacea to binning problems, nor does it give a definite estimate of the systematic uncertainty incurred in any re-weighting using a particular schema - this is still very much dependent on the distributions of the data which are re-weighted using the schema.

It is also still possible to conceive of local variations within a given bin which average out, leading to the overall bin efficiency satisfying this criteria with its neighbours. The only way to investigate potential local variations is to divide the bins and check for emergent structure - something which ultimately becomes unfeasible as the statistical limitations of the simulation sample come into play.

We may, however, confidently say that the  $\kappa$  statistic provides a method of quantitatively finding the best description of a multidimensional efficiency space *with the statistics available*. This may be loosely interpreted as the most granular binning schema permitted with the statistics available before statistical uncertainties on the individual bins dominate

over genuine efficiency structure.

### A.1.5 Optimum $\kappa$ distributions

We posit that for an optimum binning schema the distribution of  $\kappa$  for all combinations of bins should be normally distributed about 1. This will result in each adjacent bin possessing an efficiency approximately 1 standard error from its neighbours. The width on the  $\kappa$  distribution would arise from genuine statistical fluctuation of bin efficiencies - it is expected that some adjacent bins will have efficiencies which fluctuate away from one another and that some adjacent bins will conversely fluctuate towards one another.

Practically, such a perfect schema is almost impossible for the following reasons:

- Assuming that the genuine efficiency structure has efficiency isobars which do not vary orthogonally with respect to the binning variables, one requires polygonal bins to achieve a perfect binning. We are practically restricted to bins which are rectangular (or some n-orthotope/hyperrectangle in higher dimensions). As such the bins will likely not align with the genuine efficiency isobars in the variable space, and will be sub-optimal.
- For simplicity we generally consider binning schemas with uniform divisions. If the efficiencies do not vary uniformly, as is very likely the case, the schema is sub-optimal.

### A.1.6 Practical $\kappa$ distributions

Given we deal with uniform binning schemas with rectangular bins, we consider what the  $\kappa$  distributions would look like for uniform schemas in the cases of those that are extremely finely binned and extremely coarsely binned. This should aid in our interpretation of the distributions.

- For a schema which is too coarse, we give the example of the SL  $\Lambda_c^+ \rightarrow pK^-\pi^+$  stripping efficiency in  $5 \times 5$  bins of  $\cos\theta_p$  and  $\phi_{h_1h_2}$  (this quantity is demonstrated in the next section to be optimally binned at much higher granularity).
- For a schema which is too fine we give the  $\kappa$  distribution for a full 5D re-weighting of the SL  $\Lambda_c^+ \rightarrow pK^-\pi^+$  stripping efficiency in all  $\Lambda_c^+$  resonant variables, with 9 bins per variable. This results in the 100 k events we have for this mode passing the stripping selection being split over approximately 60 k bins - clearly this will result

in the order of one event passing selection in each bin and correspondingly large efficiency uncertainties.

The two distributions are given in Figure A.1. It can be seen that in the low granularity case, the mean  $\kappa$  is very high, around 7.5. This indicates that the average difference in bin efficiencies is around  $7.5 \sigma$ . At this low granularity the bins are demonstrably large enough that the efficiency across them relative to the binomial error is very high. This suggests that a more complete description of the efficiency space may be achieved by increasing the granularity given the statistics available.

In the case for which the granularity is too high, we can see that the distribution looks approximately normally distributed around zero and positive definite. We can interpret this as the efficiency structure being “washed out” by the high binomial uncertainty on the individual bin efficiencies. In such a case any variation in efficiency between bins will be dominated by statistical fluctuations. As the  $\kappa$  value is the difference in efficiency normalised to the error, we would expect an approximately normal distribution of  $\kappa$  values. In such a situation, clearly a more meaningful efficiency description can be attained by decreasing the binning granularity.

As such, we might expect that our uniformly binned efficiency schemas will possess  $\kappa$  distributions with elements from both these extremes. Contributions from regions where the efficiency does not vary significantly will have  $\kappa$  normally distributed around zero, and contributions from regions where the efficiency varies too rapidly will result in bin boundaries with outliers of high  $\kappa$ . Our aim is to balance these contributions. We make the ansatz that for uniform bin schemas with rectangular boundaries, mean  $\kappa$  values which are close to 1 will indicate binning schemas which represent a good balance between the two opposing systematic trends.

### A.1.7 A practical case in 2D

To properly introduce the  $\kappa$  statistic we use an example which serves to demonstrate these properties of  $\kappa$  distributions. We possess more MC for SL  $\Lambda_c^+ \rightarrow pK^-\pi^+$  than the other decay modes in the analyses, so let us use this as an example.

The stripping efficiency is known to vary with all resonant variables in this mode. It is easy to visualise the efficiency distribution in up to two dimensions, so we will investigate a two-dimensional efficiency space. We pick two of the resonant variables at random, in this case  $\cos \theta_p$  and  $\phi_{h_1 h_2}$ , and plot their efficiency using various granularities of uniform binning schemas. We utilise  $5 \times 5$ ,  $10 \times 10$ ,  $20 \times 20$ ,  $30 \times 30$  and  $40 \times 40$  binnings. We

then calculate the  $\kappa$  values for the binning schemas, such that all pairs of adjacent bins are accounted for. These are then plotted to examine the distribution shapes.

The efficiency histograms and corresponding  $\kappa$  distributions are shown in Figure A.2 and Figure A.3. It can be seen that a  $5 \times 5$  description of the efficiency space is clearly too coarse to resolve the fine structure. The  $\kappa$  values are correspondingly high, with a mean around 7.5. This indicates that the average bin efficiency separation in terms of the efficiency error is  $7.5 \sigma$ , and that across each bin there is a large efficiency variation - the approximation that the efficiency is single-valued in the bin is clearly not a good one.

As we increase the granularity we see more of the efficiency structure is resolved. The low efficiency regions centred at  $\cos \phi_p = 0$ ,  $\phi_{h1h2} = \pm\pi/2$  become clearly elliptic in shape. The  $\kappa$  distribution begins to take on lower values until it averages approximately 1.0 at  $20 \times 20$  bins. At higher granularities the average  $\kappa$  drops below 1. In these cases we note many regions of statistical fluctuation in those regions where we expect the acceptance to vary smoothly. We take this as evidence that the bin schema is too granular and the statistical error on the bins is beginning to dominate over the genuine efficiency structure.

In this case an analyst would probably, by eye, consider  $20 \times 20$  to be the optimal binning of all those examined - although the reader may come to different conclusions given the subjectivity of judging shapes in this fashion. The  $20 \times 20$  binning schema is the binning with a mean  $\kappa$  value of the schema closest to one. We take this as some indication that our ansatz of ideal mean  $\kappa$  in a uniform distribution is somewhat well motivated.

## A.2 Concluding remarks

It is perhaps worth repeating why examinations of  $\kappa$  are so useful for our re-weightings. While examining 2D efficiency distributions by eye, one could broadly come to a similar conclusion - that  $20 \times 20$  bins is probably the most suitable, or at least among the most suitable, of the granularities considered. This would be very impractical in the case of greater binning dimensionalities than 2, where visualisation with the human brain becomes impractical - this is certainly so in the case of 5D. The  $\kappa$  distributions give us the means to broadly quantify how well suited a multi-dimensional schema is given the statistics at hand. It also enables, by looking at the shape of the  $\kappa$  distribution, an estimation of the fraction of the variable space which is too coarsely binned and the fraction which is too finely binned. Naturally an adaptive algorithm could exploit this more capably in higher dimensions than manually setting the bin limits.

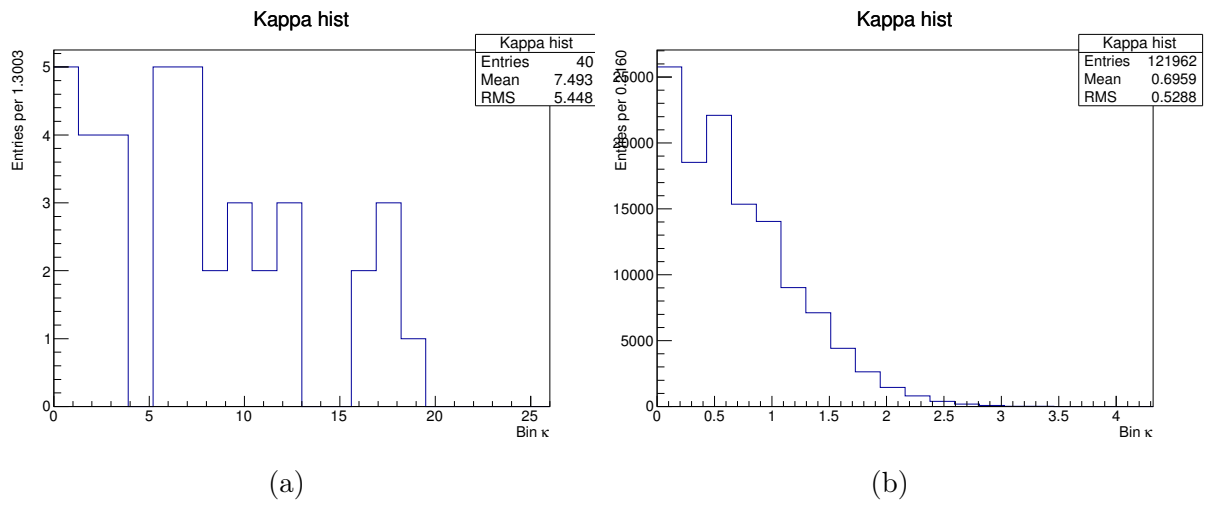


Figure A.1: The  $\kappa$  distributions for the cases of efficiency binnings which are too coarse, (a), and too granular, (b).

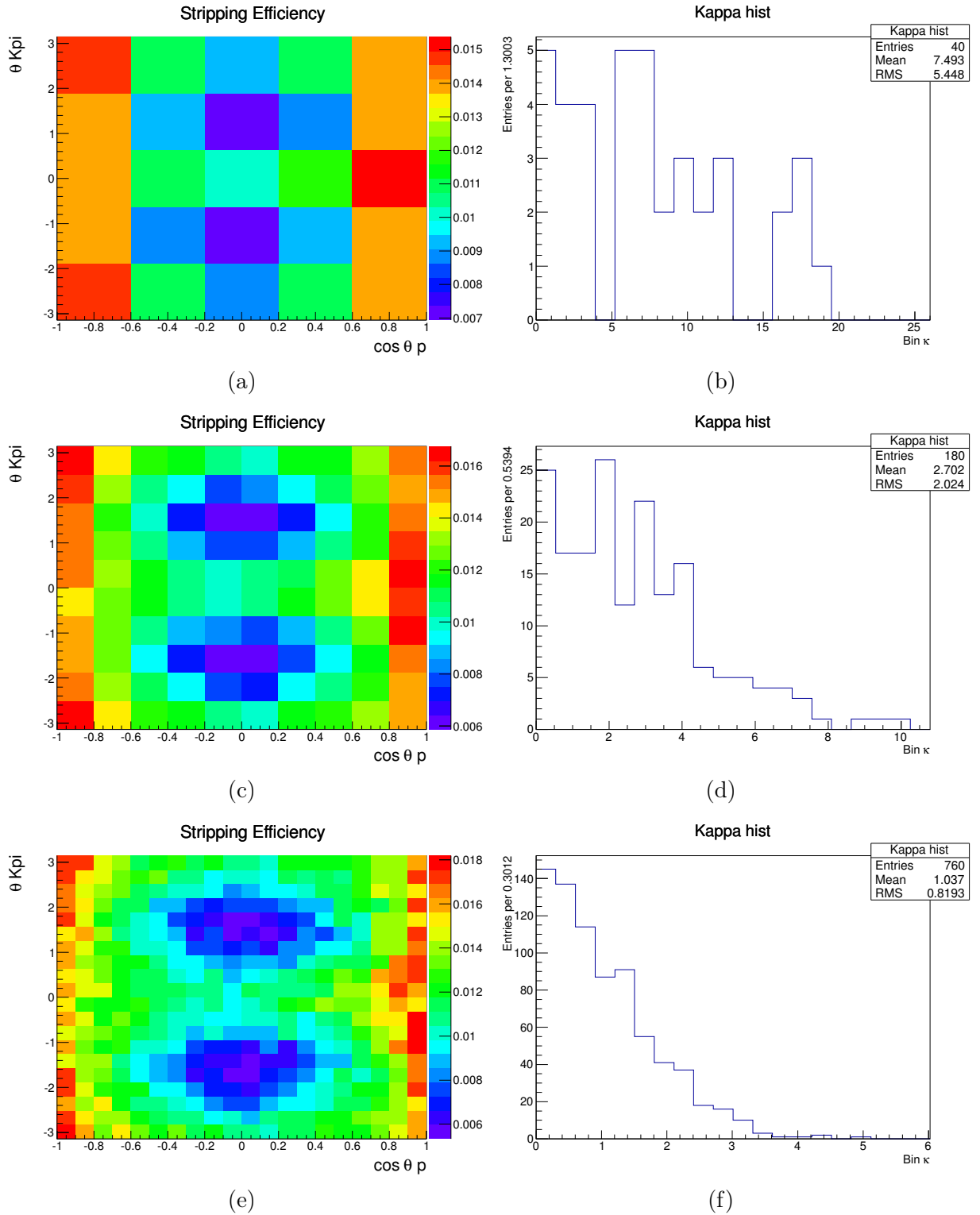


Figure A.2: The SL  $\Lambda_c^+ \rightarrow pK^-\pi^+$  stripping efficiency for  $\cos \phi_p$  vs.  $\phi_{h_1h_2}$  and the corresponding  $\kappa$  distributions for  $5 \times 5$ ,  $10 \times 10$  and  $20 \times 20$  binning granularities.

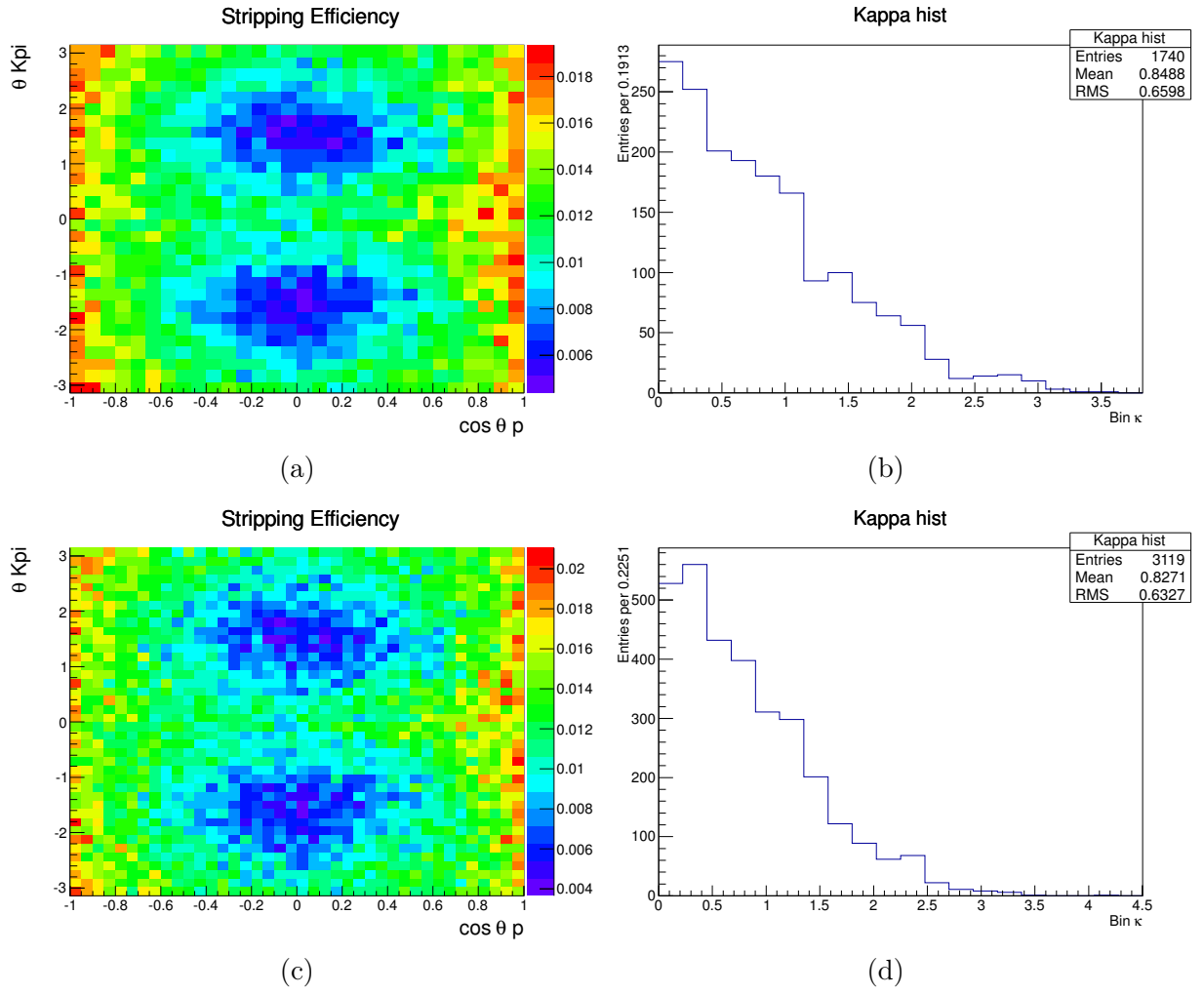


Figure A.3: The SL  $\Lambda_c^+ \rightarrow pK^-\pi^+$  stripping efficiency for  $\cos \phi_p$  vs.  $\phi_{h_1h_2}$  and the corresponding  $\kappa$  distributions for  $30 \times 30$  and  $40 \times 40$  binning granularities.

# Appendix B

## Biases in efficiency re-weightings from limited simulated/calibration statistics

### B.1 Stripping efficiency correction

A very crude description of the stripping efficiency re-weighting in our analyses is as follows:

1. The stripping selection is applied to the data candidates.
2. Samples of simulated signal decays are generated for each mode.
3. A version of the stripping selection with no PID cuts is applied to the simulated candidates.
4. The total number of truth matched candidates which survive the selection over the total number of simulated candidates is taken as the phase-space averaged stripping efficiency.
5. The poor modelling of the  $\Lambda_c^+$  decay resonant variables in the MC, and the dependence of the selection efficiency on said variables, necessitates that we bin the MC in these variables to construct schemas of local stripping efficiencies in the variable space.
6. These efficiencies are then used to assign per-candidate efficiencies to the data candidates dependent on their position in the variable space.

As to what binnings of the simulated data should be utilised, we are in part motivated by a form of statistical bias which appears in this form of re-weighting procedure. This

appendix motivates this bias and contains investigations into its magnitude in the stripping efficiency re-weighting procedure, and in the use of the fully data-driven PIDCalib method. This is accomplished with toy simulation experiments.

## B.2 Source of bias

While conducting the stripping efficiency re-weighting in the analysis, the candidate noted a disturbing trend: that generally, as the number of bins in our efficiency schemas increased, that the extracted per-mode re-weighted efficiencies generally became lower. At first this was attributed to genuine efficiency structures, but it became clear that no matter the re-weighted variables, that the extracted efficiencies became lower - even when the re-weighting variables were known to have a very weak dependence on the stripping selection.

After some consideration, the nature of this bias was understood; its origins are purely statistical in nature, and not pertaining to the efficiency structures or features of the resonant structure of  $\Lambda_c^+ \rightarrow phh'$  decays. The ultimate effect is that when using a sample of data to derive local, binned efficiencies for some arbitrary selection, higher binning granularities in the schema result in higher adjusted yields being derived when said efficiency schema is used to assign event-by-event weights to another data sample. This is an effect of the inflation of binomial uncertainty on the bin efficiencies that is implicit with higher granularity.

This bias is easily illustrated when we consider the implications of finite MC statistics. Each bin in the schema will have a calculated efficiency and error. We posit that there is some “true” efficiency value for each bin. Through statistical fluctuations, some calculated efficiencies are above and below the true value. Roughly equal numbers of bins will fluctuate above and below their true values. It can be shown that when the efficiency schema is used to re-weight another dataset, contributions from candidates falling in bins with efficiency fluctuations downwards from the true value are given higher weight than those candidates falling in bins with efficiency fluctuations upwards from the true value.

In a phase-space integrated approach, all events are assigned the average efficiency and the adjusted yield is then simply

$$M = \frac{N}{\epsilon}. \tag{B.1}$$

To illustrate the bias we consider binning the MC in some control variable  $x$  on which the efficiency does not depend. If  $x$  is uniformly distributed in the simulation, each bin will have

roughly the same efficiency and binomial error on said efficiency. Statistical fluctuations will result in a Gaussian distribution of bin efficiencies, with a width approximately equal to the average binomial error. By construction, approximately equal numbers of bins have efficiencies with upward fluctuations from the integrated efficiency value as downward fluctuations.

We then use these binned efficiencies to assign per-candidate efficiencies to the data, extracting the adjusted yield  $M$  by summing over the bins:

$$M = \sum_j \frac{N_j}{\epsilon_j} \quad (\text{B.2})$$

where  $N_j$  is the number of data candidates in bin  $j$ . The ratio of the number of data candidates passing selection over the adjusted yield gives the re-weighted efficiency  $\bar{\epsilon}$ :

$$\bar{\epsilon} = \frac{N}{M} \quad (\text{B.3})$$

With a uniform reference sample in  $x$ , there will be roughly Gaussian distributed per-candidate efficiencies assigned to the data sample. So for one set of candidates  $N_{j-}$  falling in bins with efficiency fluctuation  $y$  below the average effective efficiency, there is a roughly equal number of candidates  $N_{j+}$  falling in bins with efficiency fluctuation  $y$  above the average. With uniform distributions in  $x$ ,  $N_{j-} = N_{j+} = 2N_j$ . Under a phase-space averaged treatment these data candidates are assigned the adjusted yield:

$$M = \frac{2N_j}{\epsilon} \quad (\text{B.4})$$

In the binned approach they are instead assigned the adjusted yield:

$$\begin{aligned} M &= \frac{N_j}{\epsilon + y} + \frac{N_j}{\epsilon - y} \\ &= \frac{N_j(\epsilon - y) + N_j(\epsilon + y)}{(\epsilon + y)(\epsilon - y)} \\ &= \frac{2N_j\epsilon}{\epsilon^2 - y^2} \\ &= \frac{2N_j}{\epsilon - \frac{y^2}{\epsilon}} \end{aligned} \quad (\text{B.5})$$

In the case of zero statistical fluctuations this reduces to the phase-space averaged adjusted yield. For contributions from bins with non-zero fluctuation  $y$ , this always results in an

adjusted yield which is larger. We will therefore always extract a re-weighted  $\bar{\epsilon}$  which is biased downwards.

Even when the  $x$  variable is some resonant variable on which the stripping efficiency depends, we expect that some bin efficiencies will fluctuate above their “true” value and some fluctuate down. We have demonstrated that contributions from downward fluctuating efficiencies dominate over upwardly fluctuating efficiencies when the binomial uncertainties on the bin efficiencies are high relative to the bin efficiencies. This is a downward bias in the re-weighted efficiencies which is purely statistical in nature.

As can also be seen, the magnitude of this bias is determined by the factor  $\frac{y^2}{\epsilon}$ . This states that the larger the statistical fluctuations on the bin efficiencies relative to said bin efficiencies, the larger the bias. This explains why as we increase the granularity of our efficiencies we extract increasingly lower  $\bar{\epsilon}$  values. While in this example we bin in a variable uncorrelated with the selection efficiency, this effect is still present even when the binning variable is correlated with efficiency.

### B.3 Toy estimations

We demonstrate this effect using toy MC, by generating a simulated population of  $N_t$  candidates. Let this distribution be known as the calibration sample - it is analogous to the simulated data in our analysis. Each candidate is randomly assigned a value in a control variable,  $x$ , which is uniformly distributed between 0 and 1. A random selection is applied to this dataset, with a true efficiency  $\epsilon_{\text{true}}$ . As such, the efficiency of the selection is independent of the control variable  $x$ . We calculate the effective efficiency of the selection by counting the number of candidates surviving the selection. We divide the sample into  $j$  equal bins in  $x$ , and derive an effective efficiency for each bin,  $\epsilon_j$ .

We generate a second sample of  $k$  events with the same uniform distribution in  $x$ . Let this second sample be known as the re-weighting sample - it is analogous to the real data in our analysis. We use the binned efficiencies constructed using the calibration data to assign per-event efficiencies to the re-weighting sample. We then calculate the adjusted yield for the re-weighting sample, and use this to extract the effective efficiency  $\epsilon_{\text{RW}}$ . With  $k_j$  as the number of re-weighting events in bin  $j$ , the extracted yield  $M$  is then:

$$M = \sum_j \frac{k_j}{\epsilon_j} \tag{B.6}$$

and the extracted efficiency is then

$$\epsilon_{\text{RW}} = \frac{k}{M}. \quad (\text{B.7})$$

This has applications in several of our efficiency corrections. The most relevant are in the determinations of the re-weighted per-mode stripping efficiencies and in our MC evaluations of the PIDCalib systematic uncertainties. We note that in the following sections there will be some rounding errors from floating point operations.

### B.3.1 PIDCalib

In the PID correction of the data, we possess sufficient calibration statistics to safely avoid this bias. However, our evaluations of the systematic errors arising from variation in efficiency use simulated calibration data - in the case of protons the statistics are much lower, around  $10^5$ . The selection efficiency is conservatively set at 0.1, and the number of generated calibration events is 100000. We run the procedure described in the previous section for a varying number of bins. The re-weighted efficiencies are shown in Table B.1. Naturally, as the number of bins increases, the fractional binomial efficiency error increases, and the width of the distribution of bin efficiencies becomes larger. This leads to larger biases being introduced. Examples of the distributions of bin efficiencies for different numbers of bins are given in Figure B.1. The magnitude of the bias in extracted efficiency is plotted against the number of bins in the re-weighting in Figure B.2. At around the level of 50 bins, our PIDCalib granularity, this bias is around half the binomial uncertainty on the integrated efficiency. This is taken into account in our systematic error evaluations.

### B.3.2 Prompt stripping efficiencies

We now make estimations of the biases in our stripping efficiency re-weightings - where this bias becomes significant gives us a rough idea of the granularities we can safely attain in our re-weighting schemas. We use the phase-space averaged efficiencies as a rough guide to the typical magnitude on the bin efficiencies. The prompt modes have comparable simulation statistics and comparable efficiencies. Using the prompt  $\Lambda_c^+ \rightarrow pK^-K^+$  as an example, taking an efficiency of  $2.5 \times 10^{-3}$  and a number of simulated candidates of  $2.3 \times 10^6$ . The re-weighted efficiencies are shown in Table B.2. Examples of the distributions of bin efficiencies for different numbers of bins are given in Figure B.3. The magnitude of the bias in extracted efficiency is plotted against the number of bins in the re-weighting in

Figure B.4.

As can be seen, severe biases manifest at much lower granularities due to the low efficiency of the prompt selections. In order to suppress the bias, we posit that the granularity should not exceed the threshold whereby the bias is greater than the binomial uncertainty on the efficiency of the integrated sample. This seems to indicate that in the case of the prompt sample our schemas should not exceed 80 bins - a far lower granularity upper limit than was previously expected.

### B.3.3 SL Cabibbo-suppressed stripping efficiencies

For each of the SL Cabibbo suppressed modes, there are around  $10^6$  simulated candidates, with phase-space averaged efficiencies of around 2.5 %. We take the least efficient of these, the SL  $\Lambda_c^+ \rightarrow p\pi^-\pi^+$ , as a conservative example. Now the efficiency in the toy model is 2.3 %, and the number of generated candidates 1m. The re-weighted efficiencies are shown in Table B.3. Examples of the distributons of bin efficiencies for different numbers of bins are given in Figure B.5. The magnitude of the bias in extracted efficiency is plotted against the number of bins in the re-weighting in Figure B.6.

In this case, the bias approaches the magnitude of the binomial uncertainty on the integrated sample at around 120 bins. We take this as an upper limit on our binning granularities for the SL Cabibbo-suppressed modes.

### B.3.4 SL $\Lambda_c^+ \rightarrow pK^-\pi^+$ stripping efficiencies

We have considerably higher simulation statistics for this mode. Now the efficiency is taken as 1.1 %, and the total number of generated candidates is  $10^6$ . The re-weighted efficiencies are shown in Table B.3. Examples of the distributons of bin efficiencies for different numbers of bins are given in Figure B.7. The magnitude of the bias in extracted efficiency is plotted against the number of bins in the re-weighting in Figure B.6.

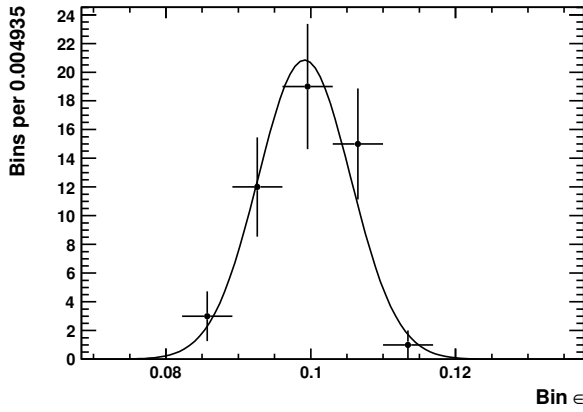
In this case, the bias appraoches the size of the binomial uncertainty on the efficiency of the integrated sample at around 300 bins - we take this as the granularity limit in this case.

## B.4 Summary

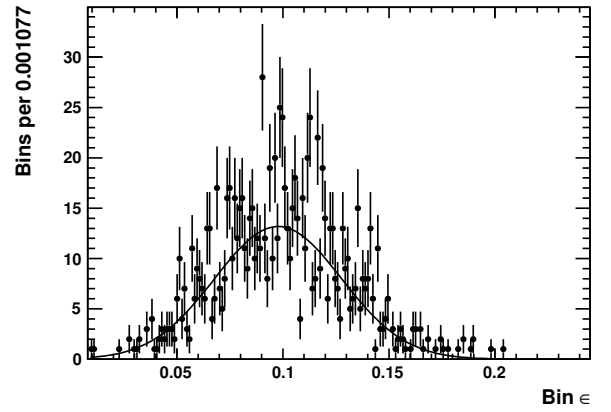
We identify a bias that appears when data candidates are assigned per-candidate efficiencies using a simulated sample of candidates with finite statistics. We motivate this bias by considering the effects of statistical fluctuations on bin efficiencies due to finite MC statistics on the extracted adjusted yields of data distributions. We conclude that this bias will be negligible in the case of our use of `PIDCalib`, and derive maximum limits on the numbers of bins to be used in the stripping efficiency re-weighting bin schemas, as indicated by our investigations using toy MC.

Table B.1: The extracted efficiencies for a variety of binning schemas. In this example,  $\epsilon_{\text{true}} = 10\%$ ,  $N_t = 100000$ ,  $\epsilon_{\text{ave}} = 9.94 \pm 0.09\%$ .  $\epsilon_{\text{RW}}$  refers to the re-weighted efficiency,  $\epsilon_{\text{ave}}$  refers to the integrated efficiency, and the “Bias” in the final column is the fractional change in re-weighted efficiency compared to the average efficiency in percent, or  $(|\epsilon_{\text{ave}} - \epsilon_{\text{RW}}| / \epsilon_{\text{ave}}) * 100$ .

N Bins	$\epsilon_{\text{RW}} [\%]$	$ \epsilon_{\text{RW}} - \epsilon_{\text{ave}}  [\%]$	Average bin $\sigma_\epsilon [\%]$	Bias [%]
10	9.92	0.01	0.30	0.15
25	9.91	0.03	0.47	0.26
50	9.89	0.05	0.67	0.46
100	9.84	0.10	0.95	0.97
200	9.73	0.21	1.34	2.13
300	9.66	0.28	1.64	2.77
400	9.55	0.39	1.89	3.94
500	9.41	0.53	2.12	5.32
600	9.33	0.61	2.32	6.14
700	9.11	0.83	2.50	8.33
800	9.08	0.86	2.68	8.65
900	8.91	1.02	2.84	10.31
1000	8.80	1.14	2.99	11.45



(a)



(b)

Figure B.1: The bin efficiency distributions distributions for 50 bins (a) and 1000 bins (b).

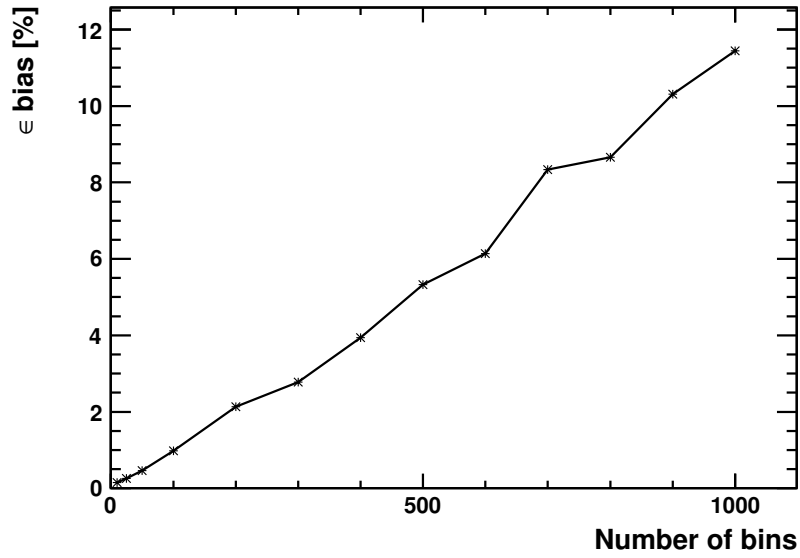


Figure B.2: The efficiency bias versus number of bins for the PIDCalib systematic evaluation.

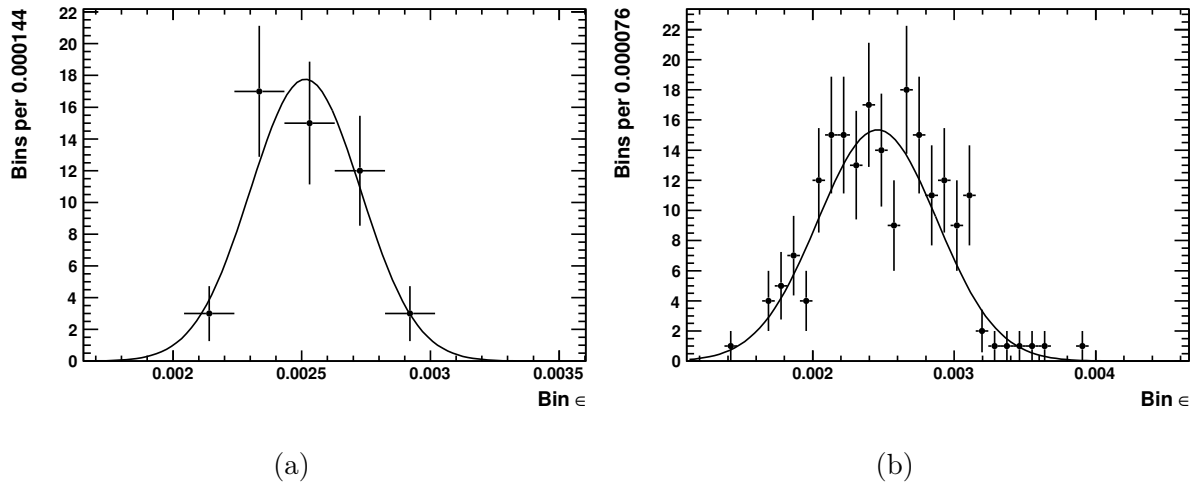


Figure B.3: The prompt stripping bin efficiency distributions distributions for 50 bins (a) and 200 bins (b).

Table B.2: The extracted efficiencies for a variety of binning schemas. In this example,  $\epsilon_{\text{true}} = 0.25\%$ ,  $N_t = 100000$ ,  $\epsilon_{\text{ave}} = 0.251 \pm 0.003\%$ .  $\epsilon_{RW}$  refers to the re-weighted efficiency,  $\epsilon_{\text{ave}}$  refers to the integrated efficiency, and the “Bias” in the final column is the fractional change in re-weighted efficiency compared to the average efficiency in percent, or  $(|\epsilon_{\text{ave}} - \epsilon_{RW}| / \epsilon_{\text{ave}}) * 100$ .

N Bins	$\epsilon_{RW}$ [%]	$ \epsilon_{RW} - \epsilon_{\text{ave}} $ [%]	Average bin $\sigma_\epsilon$ [%]	Fractional bias on $\epsilon$ [%]
10	0.25071	0.00024	0.01043	0.09664
20	0.25031	0.00065	0.01475	0.25708
30	0.24993	0.00103	0.01807	0.40895
40	0.24980	0.00116	0.02087	0.46146
50	0.24937	0.00158	0.02333	0.63023
60	0.24853	0.00243	0.02555	0.96692
70	0.24855	0.00241	0.02760	0.95948
80	0.24799	0.00296	0.02951	1.18129
90	0.24751	0.00345	0.03130	1.37493
100	0.24668	0.00428	0.03299	1.70358
120	0.24714	0.00381	0.03614	1.51964
240	0.24301	0.00794	0.05111	3.16494
160	0.24485	0.00611	0.04173	2.43493
180	0.24397	0.00699	0.04426	2.78447
200	0.24399	0.00697	0.04666	2.77587
250	0.24106	0.00989	0.05216	3.94184
300	0.24010	0.01086	0.05714	4.32571
400	0.23383	0.01713	0.06598	6.82564
500	0.22644	0.02451	0.07377	9.76844
600	0.22424	0.02671	0.08081	10.64506
700	0.21283	0.03812	0.08728	15.19186
800	0.21104	0.03992	0.09331	15.90675
900	0.20150	0.04946	0.09897	19.70693
1000	0.20602	0.04494	0.10433	17.90618
1500	0.19493	0.05603	0.12777	22.32690
2000	0.19439	0.05656	0.14754	22.53896

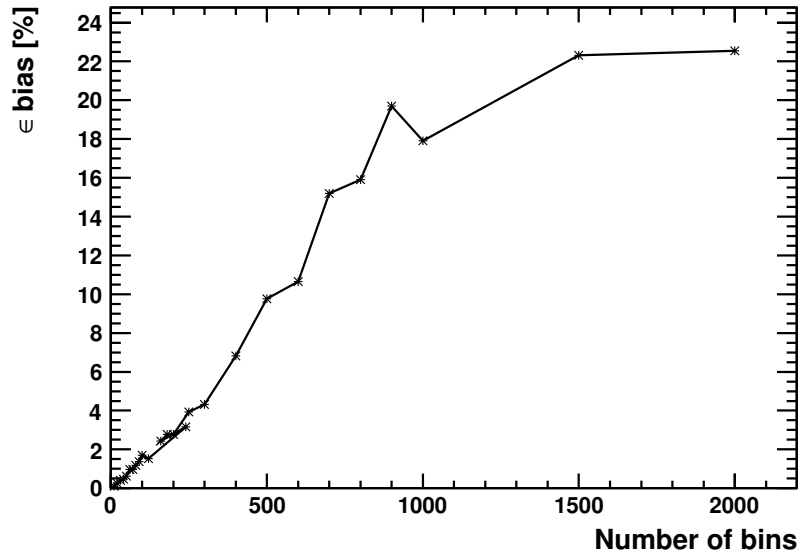


Figure B.4: The efficiency bias versus number of bins for the prompt stripping efficiency re-weighting.

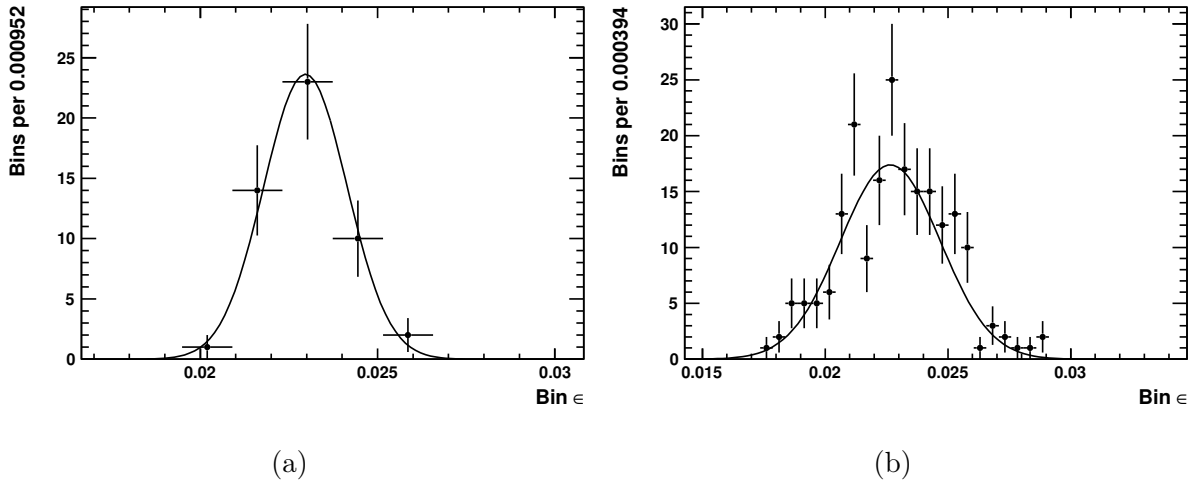


Figure B.5: The SL CS stripping bin efficiency distributions distributions for 50 bins (a) and 200 bins (b).

Table B.3: The extracted efficiencies for a variety of binning schemas. In this example,  $\epsilon_{\text{true}} = 2.3\%$ ,  $N_t = 1000000$ ,  $\epsilon_{\text{ave}} = 2.284 \pm 0.015\%$ .  $\epsilon_{RW}$  refers to the re-weighted efficiency,  $\epsilon_{\text{ave}}$  refers to the integrated efficiency, and the “Bias” in the final column is the fractional change in re-weighted efficiency compared to the average efficiency in percent, or  $(|\epsilon_{\text{ave}} - \epsilon_{RW}| / \epsilon_{\text{ave}}) * 100$ .

N Bins	$\epsilon_{RW}$ [%]	$ \epsilon_{RW} - \epsilon_{\text{ave}} $ [%]	Average bin $\sigma_\epsilon$ [%]	Fractional bias on $\epsilon$ [%]
10	2.28249	0.00091	0.04724	0.03977
20	2.28181	0.00159	0.06680	0.06945
30	2.27954	0.00386	0.08182	0.16908
40	2.27775	0.00565	0.09447	0.24751
50	2.27867	0.00473	0.10562	0.20720
60	2.27569	0.00771	0.11570	0.33774
70	2.27283	0.01057	0.12498	0.46293
80	2.27341	0.00999	0.13360	0.43738
90	2.27406	0.00934	0.14171	0.40919
100	2.26873	0.01467	0.14937	0.64255
120	2.26997	0.01343	0.16363	0.58795
240	2.25765	0.02575	0.23141	1.12788
160	2.26496	0.01844	0.18894	0.80764
180	2.26368	0.01972	0.20041	0.86354
200	2.26161	0.02179	0.21125	0.95427
250	2.25681	0.02659	0.23618	1.16451
300	2.25153	0.03187	0.25872	1.39569
400	2.24260	0.04080	0.29875	1.78701
500	2.23096	0.05244	0.33401	2.29640
600	2.22359	0.05981	0.36589	2.61912
700	2.20935	0.07405	0.39521	3.24313
800	2.20159	0.08181	0.42249	3.58285
900	2.18692	0.09648	0.44812	4.22531
1000	2.17322	0.11018	0.47236	4.82505
1500	2.12974	0.15366	0.57852	6.72955
2000	2.05782	0.22558	0.66802	9.87900

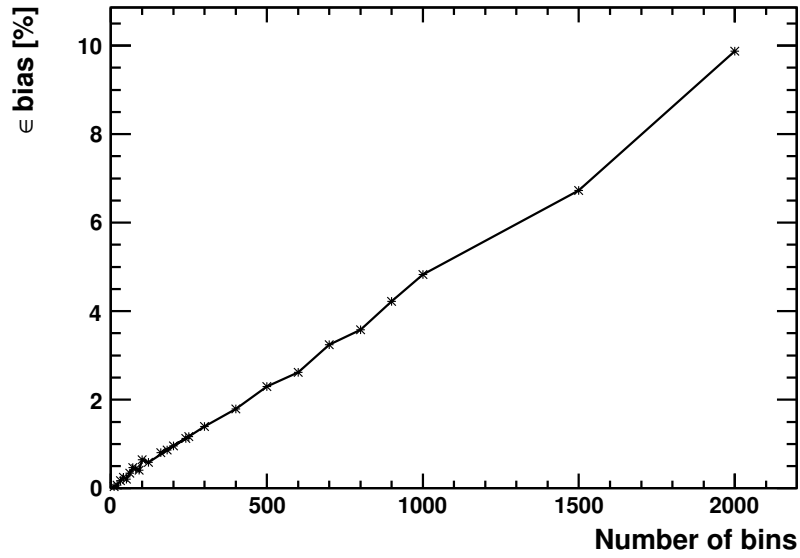


Figure B.6: The efficiency bias versus number of bins for the SL CS stripping efficiency re-weighting.

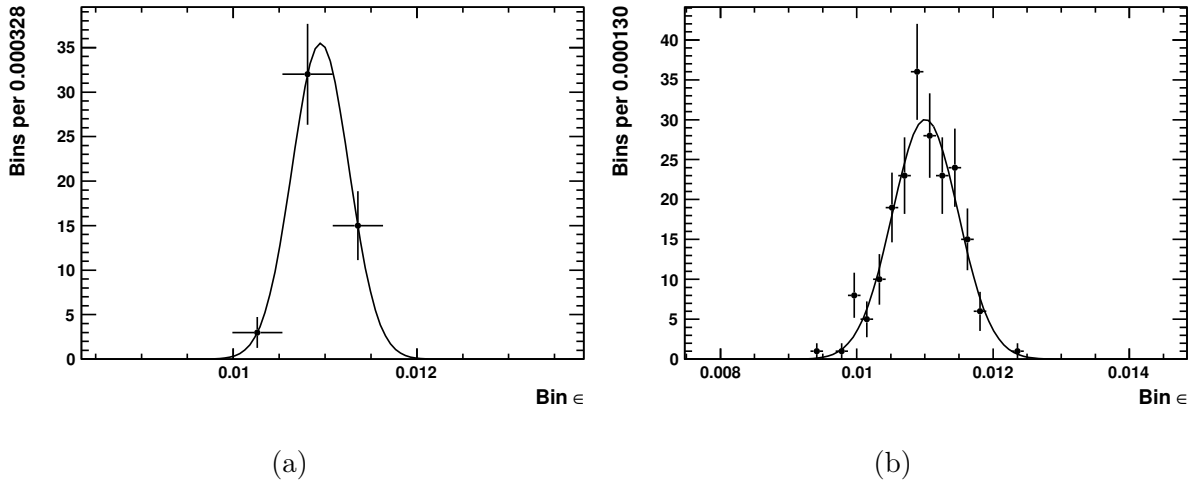


Figure B.7: The SL  $A_c^+ \rightarrow pK^-\pi^+$  stripping bin efficiency distributions for 50 bins (a) and 200 bins (b).

Table B.4: The extracted efficiencies for a variety of binning schemas. In this example,  $\epsilon_{\text{true}} = 1.1\%$ ,  $N_t = 10^6$ ,  $\epsilon_{\text{ave}} = 1.096 \pm 0.003\%$ .  $\epsilon_{\text{RW}}$  refers to the re-weighted efficiency,  $\epsilon_{\text{ave}}$  refers to the integrated efficiency, and the “Bias” in the final column is the fractional change in re-weighted efficiency compared to the average efficiency in percent, or  $(|\epsilon_{\text{ave}} - \epsilon_{\text{RW}}| / \epsilon_{\text{ave}}) * 100$ .

N Bins	$\epsilon_{\text{RW}}$ [%]	$ \epsilon_{\text{RW}} - \epsilon_{\text{ave}} $ [%]	Average bin $\sigma_\epsilon$ [%]	Fractional bias on $\epsilon$ [%]
10	1.09596	0.00007	0.01041	0.00662
20	1.09578	0.00025	0.01472	0.02302
30	1.09575	0.00028	0.01803	0.02575
40	1.09562	0.00041	0.02082	0.03764
50	1.09552	0.00051	0.02328	0.04647
60	1.09535	0.00068	0.02550	0.06221
70	1.09533	0.00070	0.02755	0.06344
80	1.09503	0.00100	0.02945	0.09093
90	1.09484	0.00119	0.03123	0.10839
100	1.09478	0.00125	0.03292	0.11397
120	1.09440	0.00163	0.03607	0.14901
240	1.09319	0.00284	0.05101	0.25884
160	1.09412	0.00191	0.04165	0.17384
180	1.09385	0.00218	0.04417	0.19897
200	1.09396	0.00207	0.04656	0.18932
250	1.09361	0.00242	0.05206	0.22118
300	1.09286	0.00317	0.05703	0.28954
400	1.09216	0.00387	0.06585	0.35354
500	1.09088	0.00515	0.07362	0.47019
600	1.08971	0.00632	0.08065	0.57664
700	1.08886	0.00717	0.08711	0.65373
800	1.08824	0.00779	0.09312	0.71088
900	1.08647	0.00956	0.09877	0.87251
1000	1.08627	0.00976	0.10412	0.89025
1500	1.08022	0.01581	0.12752	1.44272
2000	1.07646	0.01957	0.14724	1.78528

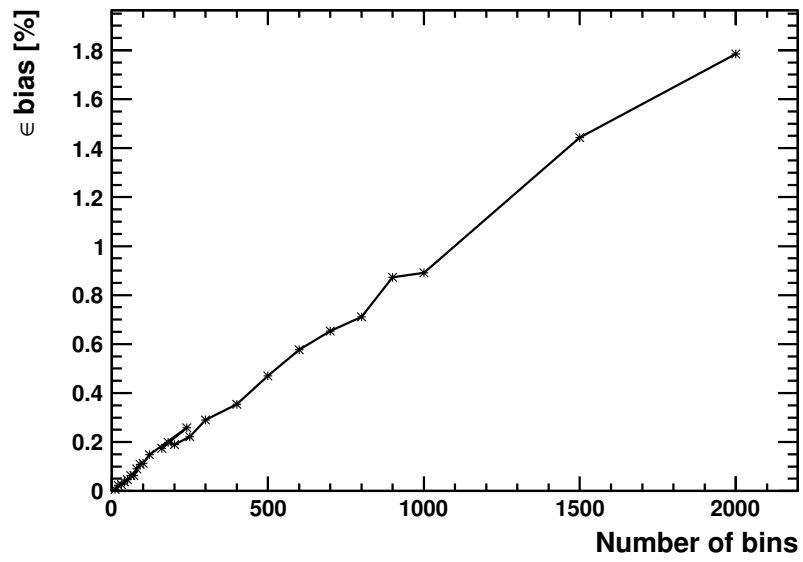


Figure B.8: The efficiency bias versus number of bins for the SL  $\Lambda_c^+ \rightarrow pK^-\pi^+$  stripping efficiency re-weighting.

# Bibliography

- [1] Super-Kamiokande Collaboration, Y. Fukuda *et al.*, *Evidence for oscillation of atmospheric neutrinos*, Phys. Rev. Lett. **81** (1998) 1562.
- [2] ATLAS Collaboration, G. Aad *et al.*, *Observation of a new particle in the search for the Standard Model Higgs boson with the ATLAS detector at the LHC*, Phys. Lett. **B716** (2012) 1, [arXiv:1207.7214](#).
- [3] CMS Collaboration, S. Chatrchyan *et al.*, *Observation of a new boson at a mass of 125 GeV with the CMS experiment at the LHC*, Phys. Lett. **B716** (2012) 30, [arXiv:1207.7235](#).
- [4] LHCb Collaboration, R. Aaij *et al.*, *First Evidence for the Decay  $B_s^0 \rightarrow \mu^+ \mu^-$* , Phys. Rev. Lett. **110** (2013) 021801, [arXiv:1211.2674](#).
- [5] CMS Collaboration, S. Chatrchyan *et al.*, *Measurement of the  $B(s)$  to  $\mu^+ \mu^-$  branching fraction and search for  $B^0$  to  $\mu^+ \mu^-$  with the CMS Experiment*, Phys. Rev. Lett. **111** (2013) 101804, [arXiv:1307.5025](#).
- [6] *Combination of results on the rare decays  $B_{(s)}^0 \rightarrow \mu^+ \mu^-$  from the CMS and LHCb experiments*, 2013.
- [7] Cheng, Xiao-Dong, Yang, Ya-Dong, and Yuan, Xing-Bo, *Phenomenological discriminations of the Yukawa interactions in two-higgs doublet models with  $z_2$  symmetry*, Eur. Phys. J. C **74** (2014), no. 10 3081.
- [8] X.-Q. Li, J. Lu, and A. Pich,  *$B_{s,d}^0 \rightarrow \ell^+ \ell^-$  Decays in the Aligned Two-Higgs-Doublet Model*, JHEP **1406** (2014) 022, [arXiv:1404.5865](#).
- [9] T. Hermann,  *$B_s \rightarrow \mu^+ \mu^-$  in the SM and  $\bar{B} \rightarrow X_s \gamma$  in the 2HDM at NNLO in QCD*, PoS **RADCOR2013** (2013) 002, [arXiv:1311.5342](#).

- [10] Particle Data Group, J. Beringer *et al.*, *Review of particle physics*, Phys. Rev. **D86** (2012) 010001.
- [11] D. J. Gross and F. Wilczek, *Ultraviolet behavior of non-abelian gauge theories*, Phys. Rev. Lett. **30** (1973) 1343.
- [12] P. W. Anderson, *Coherent excited states in the theory of superconductivity: gauge invariance and the Meissner effect*, Phys. Rev. **110** (1958) 827.
- [13] Y. Nambu, *Quasi-particles and gauge invariance in the theory of superconductivity*, Phys. Rev. **117** (1960) 648.
- [14] J. Goldstone, *Field theories with superconductor solutions*, Il Nuovo Cimento **19** (1961), no. 1 154.
- [15] F. Englert and R. Brout, *Broken symmetry and the mass of gauge vector mesons*, Phys. Rev. Lett. **13** (1964) 321.
- [16] G. S. Guralnik, C. R. Hagen, and T. W. B. Kibble, *Global conservation laws and massless particles*, Phys. Rev. Lett. **13** (1964) 585.
- [17] P. W. Higgs, *Broken symmetries and the masses of gauge bosons*, Phys. Rev. Lett. **13** (1964) 508.
- [18] S. Glashow, *Partial Symmetries of Weak Interactions*, Nucl. Phys. **22** (1961) 579.
- [19] A. Salam and J. Ward, *Weak and electromagnetic interactions*, Il Nuovo Cimento Series 10 **11** (1959), no. 4 568.
- [20] S. Weinberg, *A Model of Leptons*, Phys. Rev. Lett. **19** (1967) 1264.
- [21] C. Lattes, H. Muirhead, G. Occhialini, and C. Powell, *Processes involving charged mesons*, Nature **159** (1947) 694.
- [22] H. Yukawa, *On the interaction of elementary particles*, Proc. Phys. Math. Soc. Jap. **17** (1935) 48.
- [23] M. Gell-Mann, *Isotopic spin and new unstable particles*, Phys. Rev. **92** (1953) 833.
- [24] K. Nishijima, *Charge Independence Theory of V Particles*, Progress of Theoretical Physics **13** (1955) 285.

- [25] Y. Ne'eman, *Derivation of strong interactions from a gauge invariance*, Nuclear Physics **26** (1961), no. 2 222 .
- [26] V. E. Barnes *et al.*, *Observation of a hyperon with strangeness minus three*, Phys. Rev. Lett. **12** (1964) 204.
- [27] N. Cabibbo, *Unitary Symmetry and Leptonic Decays*, Phys. Rev. Lett. **10** (1963) 531.
- [28] S. L. Glashow, J. Iliopoulos, and L. Maiani, *Weak interactions with lepton-hadron symmetry*, Phys. Rev. D **2** (1970) 1285.
- [29] J. Aubert *et al.*, *Experimental observation of a heavy Particle J*, Adv. Exp. Phys. **5** (1976) 128.
- [30] SLAC-SP-017 Collaboration, J. Augustin *et al.*, *Discovery of a Narrow Resonance in  $e^+ e^-$  Annihilation*, Phys. Rev. Lett. **33** (1974) 1406.
- [31] E. Cazzoli *et al.*, *Evidence for  $\Delta S = -\Delta Q$  Currents or Charmed Baryon Production by Neutrinos*, Phys. Rev. Lett. **34** (1975) 1125.
- [32] G. Goldhaber *et al.*, *Observation in  $e^+ e^-$  Annihilation of a Narrow State at  $1865 \text{ MeV}/c^2$  Decaying to  $K\pi$  and  $K\pi\pi\pi$* , Phys. Rev. Lett. **37** (1976) 255.
- [33] I. Peruzzi *et al.*, *Observation of a Narrow Charged State at  $1876 \text{ MeV}/c^2$  Decaying to an Exotic Combination of  $K\pi\pi$* , Phys. Rev. Lett. **37** (1976) 569.
- [34] S. Neddermeyer and C. Anderson, *Note on the Nature of Cosmic Ray Particles*, Phys. Rev. **51** (1937) 884.
- [35] M. L. Perl *et al.*, *Evidence for anomalous lepton production in  $e^+ - e^-$  annihilation*, Phys. Rev. Lett. **35** (1975) 1489.
- [36] S. Herb *et al.*, *Observation of a Dimuon Resonance at  $9.5 \text{ GeV}$  in  $400 \text{ GeV}$  Proton-Nucleus Collisions*, Phys. Rev. Lett. **39** (1977) 252.
- [37] J. H. Kuhn, *Weak Decays of Open and Hidden Top*, Acta Phys. Austriaca Suppl. **24** (1982) 203.
- [38] CDF Collaboration, F. Abe *et al.*, *Observation of top quark production in  $\bar{p}p$  collisions with the collider detector at fermilab*, Phys. Rev. Lett. **74** (1995) 2626.

- [39] D0 Collaboration, S. Abachi *et al.*, *Search for high mass top quark production in  $p\bar{p}$  collisions at  $\sqrt{s} = 1.8$  TeV*, Phys. Rev. Lett. **74** (1995) 2422.
- [40] LHCb collaboration, R. Aaij *et al.*, *Observation of overlapping spin-1 and spin-3  $\bar{D}^0 K^-$  resonances at mass 2.86 GeV/ $c^2$* , Phys. Rev. Lett. **113** (2014) 162001, [arXiv:1407.7574](#).
- [41] C. S. Wu *et al.*, *Experimental test of parity conservation in beta decay*, Phys. Rev. **105** (1957) 1413.
- [42] J. H. Christenson, J. W. Cronin, V. L. Fitch, and R. Turlay, *Evidence for the  $2\pi$  decay of the  $K_2^0$  meson*, Phys. Rev. Lett. **13** (1964) 138.
- [43] M. Kobayashi and T. Maskawa, *CP Violation in the Renormalizable Theory of Weak Interaction*, Prog. Theor. Phys. **49** (1973) 652.
- [44] L.-L. Chau and W.-Y. Keung, *Comments on the Parametrization of the Kobayashi-Maskawa Matrix*, Phys. Rev. Lett. **53** (1984) 1802.
- [45] J. Charles *et al.*, *CP Violation and the CKM matrix: assessing the impact of the asymmetric  $b$  factories*, The European Physical Journal C - Particles and Fields **41** (2005), no. 1 1.
- [46] G. P. Lepage *et al.*, *Improved nonrelativistic QCD for heavy quark physics*, Phys. Rev. **D46** (1992) 4052, [arXiv:hep-lat/9205007](#).
- [47] H. D. Politzer and M. B. Wise, *Leading Logarithms of Heavy Quark Masses in Processes with Light and Heavy Quarks*, Phys. Lett. **B206** (1988) 681.
- [48] H. D. Politzer and M. B. Wise, *Effective Field Theory Approach to Processes Involving Both Light and Heavy Fields*, Phys. Lett. **B208** (1988) 504.
- [49] N. Isgur and M. B. Wise, *Weak transition form-factors between heavy mesons*, Phys. Lett. **B237** (1990) 527.
- [50] Z. S. Brown, W. Detmold, S. Meinel, and K. Orginos, *Charmed bottom baryon spectroscopy from lattice QCD*, Phys. Rev. D **90** (2014) 094507.
- [51] D. Ebert, R. Faustov, V. Galkin, and A. Martynenko, *Masses and weak decay rates of doubly heavy baryons*, [arXiv:hep-ph/0411082](#).

- [52] K. Sharma and R. Verma, *A Study of weak mesonic decays of  $\Lambda_c$  and  $\Xi_c$  baryons on the basis of HQET results*, Eur. Phys. J. **C7** (1999) 217, [arXiv:hep-ph/9803302](#).
- [53] C. Jin, *Calculation of the semileptonic decay width of the  $\Lambda_b$  baryon*, Phys. Rev. **D56** (1997) 7267, [arXiv:hep-ph/9709457](#).
- [54] B. Guberina, R. Ruckl, and J. Trampetic, *Charmed Baryon Lifetime Differences*, Z. Phys. **C33** (1986) 297.
- [55] M. A. Shifman and M. Voloshin, *Hierarchy of Lifetimes of Charmed and Beautiful Hadrons*, Sov. Phys. JETP **64** (1986) 698.
- [56] M. A. Shifman and M. Voloshin, *Preasymptotic Effects in Inclusive Weak Decays of Charmed Particles*, Sov. J. Nucl. Phys. **41** (1985) 120.
- [57] K. G. Wilson, *Confinement of quarks*, Phys. Rev. D **10** (1974) 2445.
- [58] P. Perez Rubio, *Charmed Baryon Spectroscopy from lattice QCD for  $N_f = 2 + 1$  flavours*, PoS **ConfinementX** (2012) 141, [arXiv:1302.5774](#).
- [59] L. Liu, H.-W. Lin, K. Orginos, and A. Walker-Loud, *Singly and Doubly Charmed  $J=1/2$  Baryon Spectrum from Lattice QCD*, Phys. Rev. **D81** (2010) 094505, [arXiv:0909.3294](#).
- [60] PACS-CS Collaboration, Y. Namekawa *et al.*, *Charmed baryons at the physical point in 2+1 flavor lattice QCD*, Phys. Rev. **D87** (2013), no. 9 094512, [arXiv:1301.4743](#).
- [61] K. Orginos, *Charmed and Bottom Baryon Spectrum from Lattice QCD*, eCONF **C0906083** (2009) 01.
- [62] Z. S. Brown, W. Detmold, S. Meinel, and K. Orginos, *Charmed bottom baryon spectroscopy from lattice QCD*, Phys. Rev. **D90** (2014), no. 9 094507, [arXiv:1409.0497](#).
- [63] CMS Collaboration, S. Chatrchyan *et al.*, *Observation of a new  $\Xi_b$  baryon*, Phys. Rev. Lett. **108** (2012) 252002, [arXiv:1204.5955](#).
- [64] LHCb collaboration, R. Aaij *et al.*, *Measurement of the  $\Lambda_b^0$ ,  $\Xi_b^-$  and  $\Omega_b^-$  baryon masses*, Phys. Rev. Lett. **110** (2013), no. 18 182001, [arXiv:1302.1072](#).
- [65] BELLE Collaboration, R. Chistov *et al.*, *Observation of new states decaying into  $\Lambda_c^+ K^- \pi^+$  and  $\Lambda_c^+ K_0^S \pi^-$* , Phys. Rev. Lett. **97** (2006) 162001, [arXiv:hep-ex/0606051](#).

- [66] Belle Collaboration, T. Lesiak, *Charmed baryon spectroscopy with Belle*, arXiv:hep-ex/0605047.
- [67] Belle Collaboration, R. Mizuk *et al.*, *Observation of an isotriplet of excited charmed baryons decaying to  $\Lambda_c^+\pi$* , Phys. Rev. Lett. **94** (2005) 122002, arXiv:hep-ex/0412069.
- [68] BaBar Collaboration, B. Aubert *et al.*, *A Study of Excited Charm-Strange Baryons with Evidence for new Baryons  $\Xi_c^+(3055)$  and  $\Xi_c^+(3123)$* , Phys. Rev. **D77** (2008) 012002, arXiv:0710.5763.
- [69] Belle Collaboration, T. Lesiak *et al.*, *Measurement of masses of the  $\Xi_c(2645)$  and  $\Xi_c(2815)$  baryons and observation of  $\Xi_c(2980) \rightarrow \Xi_c(2645)\pi$* , Phys. Lett. **B665** (2008) 9, arXiv:0802.3968.
- [70] BaBar Collaboration, B. Aubert *et al.*, *Production and decay of  $\Omega_c^0$* , Phys. Rev. Lett. **99** (2007) 062001, arXiv:hep-ex/0703030.
- [71] BaBar Collaboration, B. Aubert *et al.*, *Observation of an excited charm baryon  $\Omega_c^*$  decaying to  $\Omega_c^0\gamma$* , Phys. Rev. Lett. **97** (2006) 232001, arXiv:hep-ex/0608055.
- [72] E. Solovieva *et al.*, *Study of  $\Omega_c^0$  and  $\Omega_c^{*0}$  Baryons at Belle*, Phys. Lett. **B672** (2009) 1, arXiv:0808.3677.
- [73] B. Guberina, B. Melic, and H. Stefancic, *Inclusive decays and lifetimes of doubly charmed baryons*, Eur. Phys. J. **C9** (1999) 213, arXiv:hep-ph/9901323.
- [74] C.-H. Chang, T. Li, X.-Q. Li, and Y.-M. Wang, *Lifetime of doubly charmed baryons*, Commun. Theor. Phys. **49** (2008) 993, arXiv:0704.0016.
- [75] Z.-G. Wang, *Analysis of the  $\frac{1}{2}^+$  doubly heavy baryon states with QCD sum rules*, Eur. Phys. J. **A45** (2010) 267, arXiv:1001.4693.
- [76] D. Ebert, R. Faustov, V. Galkin, and A. Martynenko, *Mass spectra of doubly heavy baryons in the relativistic quark model*, Phys. Rev. **D66** (2002) 014008, arXiv:hep-ph/0201217.
- [77] D.-H. He *et al.*, *Evaluation of spectra of baryons containing two heavy quarks in bag model*, Phys. Rev. **D70** (2004) 094004, arXiv:hep-ph/0403301.

- [78] W. Roberts and M. Pervin, *Heavy baryons in a quark model*, Int. J. Mod. Phys. **A23** (2008) 2817, [arXiv:0711.2492](#).
- [79] SELEX Collaboration, M. Mattson *et al.*, *First observation of the doubly charmed baryon  $\Xi_{cc}^+$* , Phys. Rev. Lett. **89** (2002) 112001, [arXiv:hep-ex/0208014](#).
- [80] SELEX Collaboration, A. Ocherashvili *et al.*, *Confirmation of the double charm baryon  $\Xi_{cc}^+(3520)$  via its decay to  $pD^+K^-$* , Phys. Lett. **B628** (2005) 18, [arXiv:hep-ex/0406033](#).
- [81] BaBar Collaboration, B. Aubert *et al.*, *Search for doubly charmed baryons  $\Xi_{cc}^+$  and  $\Xi_{cc}^{++}$  in BABAR*, Phys. Rev. **D74** (2006) 011103, [arXiv:hep-ex/0605075](#).
- [82] LHCb collaboration, R. Aaij *et al.*, *Search for the doubly charmed baryon  $\Xi_{cc}^+$* , JHEP **1312** (2013) 090, [arXiv:1310.2538](#).
- [83] E791 Collaboration, E. Aitala *et al.*, *Multidimensional resonance analysis of  $\Lambda_c^+ \rightarrow pK^-\pi^+$* , Phys. Lett. **B471** (2000) 449, [arXiv:hep-ex/9912003](#).
- [84] J.-M. Richard, *Double charm physics*, [arXiv:hep-ph/0212224](#).
- [85] E687 Collaboration, P. Frabetti *et al.*, *Analysis of three  $D \rightarrow K\pi\pi$  Dalitz plots*, Phys. Lett. **B331** (1994) 217.
- [86] E791 Collaboration, E. Aitala *et al.*, *Multidimensional resonance analysis of  $\Lambda_c^+ \rightarrow pK^-\pi^+$* , Phys. Lett. **B471** (2000) 449, [arXiv:hep-ex/9912003](#).
- [87] ACCMOR Collaboration, A. Bozek *et al.*, *A Study of  $\Lambda_c^+$  decays into  $pK^-\pi^+$ ,  $pK^-\pi^+\pi^0$  and  $pK^-\pi^+\pi^0\pi^0$* , Phys. Lett. **B312** (1993) 247.
- [88] M. Basile *et al.*, *A Measurement of two resonant contributions in the  $\Lambda_c^+$  branching ratios*, Nuovo Cim. **A62** (1981) 14.
- [89] ACCMOR Collaboration, S. Barlag *et al.*, *Measurement of frequencies of various decay modes of charmed particles  $D^0$ ,  $D^+$ ,  $D_s^+$  and  $\Lambda_c^+$  including the observation of new channels*, Z. Phys. **C48** (1990) 29.
- [90] Belle Collaboration, K. Abe *et al.*, *Observation of Cabibbo suppressed and W exchange  $\Lambda_c^+$  baryon decays*, Phys. Lett. **B524** (2002) 33, [arXiv:hep-ex/0111032](#).

- [91] CLEO Collaboration, J. Alexander *et al.*, *Observation of the Cabibbo suppressed charmed baryon decay  $\Lambda_c^+ \rightarrow p\phi$* , Phys. Rev. **D53** (1996) 1013, [arXiv:hep-ex/9508005](#).
- [92] FOCUS Collaboration, J. Link *et al.*, *Search for  $\Lambda_c^+ \rightarrow pK^+\pi^-$  and  $D_s^+ \rightarrow K^+K^+\pi^-$  using genetic programming event selection*, Phys. Lett. **B624** (2005) 166, [arXiv:hep-ex/0507103](#).
- [93] F. Fayette, *Strategies for precision measurements of the charge asymmetry of the  $W$  boson mass at the LHC within the ATLAS experiment*, [arXiv:0906.4260](#).
- [94] L. Evans and P. Bryant, *LHC Machine*, JINST **3** (2008) S08001.
- [95] CMS Collaboration, S. Chatrchyan *et al.*, *The CMS experiment at the CERN LHC*, JINST **3** (2008) S08004.
- [96] ATLAS Collaboration, G. Aad *et al.*, *The ATLAS Experiment at the CERN Large Hadron Collider*, JINST **3** (2008) S08003.
- [97] ALICE Collaboration, K. Aamodt *et al.*, *The ALICE experiment at the CERN LHC*, JINST **3** (2008) S08002.
- [98] LHCb collaboration, A. A. Alves Jr. *et al.*, *The LHCb detector at the LHC*, JINST **3** (2008) S08005.
- [99] M. Gersabeck, *Alignment of the LHCb vertex locator*, Nuclear Instruments and Methods in Physics Research A **598** (2009) 71, [arXiv:0807.3525](#).
- [100] C. Farinelli, *Performance of the LHCb vertex locator*, in *Nuclear Science Symposium and Medical Imaging Conference (NSS/MIC), 2012 IEEE*, pp. 1498–1502, Oct, 2012. doi: 10.1109/NSSMIC.2012.6551360.
- [101] J. Gassner, M. Needham, and O. Steinkamp, *Layout and Expected Performance of the LHCb TT Station*, Tech. Rep. LHCb-2003-140, CERN-LHCb-2003-140, 2004.
- [102] LHCb Collaboration, *LHCb: Inner tracker technical design report*, Tech. Rep. CERN-LHCC-2002-029, 2002.
- [103] *LHCb: Outer tracker technical design report*, Tech. Rep. CERN-LHCC-2001-024, 2001.

- [104] LHC-B Collaboration, *LHCb magnet: Technical design report*, Tech. Rep. CERN-LHCC-2000-007, 2000.
- [105] F. Archilli *et al.*, *Performance of the muon identification at LHCb*, JINST **8** (2013) P10020, [arXiv:1306.0249](#).
- [106] R. Aaij *et al.*, *The LHCb trigger and its performance in 2011*, JINST **8** (2013) P04022, [arXiv:1211.3055](#).
- [107] LHCb HLT project, J. Albrecht, V. Gligorov, G. Raven, and S. Tolk, *Performance of the LHCb High Level Trigger in 2012*, J. Phys. Conf. Ser. **513** (2014) 012001, [arXiv:1310.8544](#).
- [108] LHCb Collaboration, M. Clemencic *et al.*, *The LHCb simulation application, Gauss: Design, evolution and experience*, J. Phys. Conf. Ser. **331** (2011) 032023.
- [109] LHCb Collaboration, I. Belyaev *et al.*, *Handling of the generation of primary events in Gauss, the LHCb simulation framework*, .
- [110] M. Dobbs and J. B. Hansen, *The HepMC C++ Monte Carlo event record for High Energy Physics*, Comput. Phys. Commun. **134** (2001) 41.
- [111] T. Sjostrand, S. Mrenna, and P. Z. Skands, *A Brief Introduction to PYTHIA 8.1*, Comput. Phys. Commun. **178** (2008) 852, [arXiv:0710.3820](#).
- [112] E. Barberio, B. van Eijk, and Z. Was, *PHOTOS: A Universal Monte Carlo for QED radiative corrections in decays*, Comput. Phys. Commun. **66** (1991) 115.
- [113] D. J. Lange, *The EvtGen particle decay simulation package*, Nucl. Instrum. Meth. **A462** (2001) 152.
- [114] BaBar Collaboration, B. Aubert *et al.*, *The BaBar detector*, Nucl. Instrum. Meth. **A479** (2002) 1, [arXiv:hep-ex/0105044](#).
- [115] GEANT4 collaboration, J. Allison *et al.*, *Geant4 developments and applications*, IEEE Trans. Nucl. Sci. **53** (2006) 270.
- [116] GEANT4 collaboration, S. Agostinelli *et al.*, *GEANT4: A simulation toolkit*, Nucl. Instrum. Meth. **A506** (2003) 250.

- [117] LHCb collaboration, R. Aaij *et al.*, *Measurement of b-hadron branching fractions for two-body decays into charmless charged hadrons*, JHEP **10** (2012) 037, [arXiv:1206.2794](#).
- [118] T. Bellunato *et al.*, *Performance of aerogel as Cherenkov radiator*, Nuclear Instruments and Methods in Physics Research Section A: Accelerators, Spectrometers, Detectors and Associated Equipment **519** (2004), no. 3 493 .
- [119] A. A. Alves Jr. *et al.*, *Performance of the LHCb muon system*, JINST **8** (2013) P02022, [arXiv:1211.1346](#).
- [120] O. Ullaland, *Fluid systems for RICH detectors*, Nuclear Instruments and Methods in Physics Research Section A: Accelerators, Spectrometers, Detectors and Associated Equipment **553** (2005), no. 1 107, Proceedings of the fifth International Workshop on Ring Imaging Detectors Fifth International Workshop on Ring Imaging Detectors.
- [121] M. Bosteels, F. Hahn, and S. Haider, *LHCb RICH gas system proposal*, Tech. Rep. LHCb-2000-079, CERN, Geneva, Apr, 2001.
- [122] A. A. Macgregor, *The laser mirror alignment system for the LHCb RICH detectors*, PhD thesis, University of Glasgow, 2006.
- [123] P. D. Sail, *Lifetime measurements of the  $B_s \rightarrow KK$  system and RICH studies at LHCb*, PhD thesis, University of Glasgow, 2013.
- [124] M. Alesia *et al.*, *First operation of a hybrid photon detector prototype with electrostatic cross-focussing and integrated silicon pixel readout*, Nuclear Instruments and Methods in Physics Research Section A: Accelerators, Spectrometers, Detectors and Associated Equipment **449** (2000), no. 1 48.
- [125] LHCb Collaboration, R. Forty, *RICH pattern recognition for LHCb*, Nucl. Instrum. Meth. **A433** (1999) 257.
- [126] M. Pivk and F. L. Diberder, *A statistical tool to unfold data distributions*, Nuclear Instruments and Methods in Physics Research Section A: Accelerators, Spectrometers, Detectors and Associated Equipment **555** (2005), no. 1 356.
- [127] CDF Collaboration, T. Aaltonen *et al.*, *Observation of new charmless decays of bottom hadrons*, Phys. Rev. Lett. **103** (2009) 031801.

- [128] LHCb Collaboration, R. Aaij *et al.*, *Measurement of  $b$ -hadron branching fractions for two-body decays into charmless charged hadrons*, JHEP **1210** (2012) 037, [arXiv:1206.2794](#).
- [129] L. Gladilin, *Charm hadron production fractions*, 1999.
- [130] LHCb collaboration, R. Aaij *et al.*, *Prompt charm production in  $pp$  collisions at  $\sqrt{s} = 7$  TeV*, Nucl. Phys. **B871** (2013) 1, [arXiv:1302.2864](#).
- [131] LHCb Collaboration, R. Aaij *et al.*, *Precision measurement of the ratio of the  $\Lambda_b^0$  to  $\bar{B}^0$  lifetimes*, Phys. Lett. **B734** (2014) 122, [arXiv:1402.6242](#).
- [132] J. D. Bjorken, *Spin Dependent Decays of the Lambda( $c$ )*, Phys. Rev. **D40** (1989) 1513.
- [133] M. Needham, *Clone track identification using the Kullback-Liebler distance*, Tech. Rep. CERN-LHCB-2008-002, LPHE-2008-02, 2008.
- [134] W. D. Hulsbergen, *Decay chain fitting with a Kalman filter*, Nucl. Instrum. Meth. **A552** (2005) 566, [arXiv:physics/0503191](#).
- [135] L. Breiman, J. Friedman, R. Olshen, and C. Stone, *Classification and Regression Trees*, Wadsworth and Brooks, Monterey, CA, 1984. new edition [?]?
- [136] L. Breiman, J. H. Friedman, R. A. Olshen, and C. J. Stone, *Classification and regression trees*, Wadsworth international group, Belmont, California, USA, 1984.
- [137] R. E. Schapire and Y. Freund, *A decision-theoretic generalization of on-line learning and an application to boosting*, Jour. Comp. and Syst. Sc. **55** (1997) 119.
- [138] A. Hoecker *et al.*, *TMVA: Toolkit for Multivariate Data Analysis*, PoS **ACAT** (2007) 040, [arXiv:physics/0703039](#).
- [139] J. Massey, Frank J., *The Kolmogorov-Smirnov Test for Goodness of Fit*, Journal of the American Statistical Association **46** (1951), no. 253 pp. 68.
- [140] CLEO Collaboration, S. Dobbs *et al.*, *Measurement of absolute hadronic branching fractions of  $D$  mesons and  $e^+ e^- \rightarrow D$  anti- $D$  cross-sections at the  $\psi(3770)$* , Phys. Rev. **D76** (2007) 112001, [arXiv:0709.3783](#).

- [141] CLEO Collaboration, P. Onyisi *et al.*, *Improved Measurement of Absolute Hadronic Branching Fractions of the  $D_s^+$  Meson*, Phys. Rev. **D88** (2013), no. 3 032009, [arXiv:1306.5363](#).
- [142] Belle Collaboration, A. Zupanc *et al.*, *Measurements of branching fractions of leptonic and hadronic  $D_s^+$  meson decays and extraction of the  $D_s^+$  meson decay constant*, JHEP **1309** (2013) 139, [arXiv:1307.6240](#).
- [143] T. Skwarnicki, *A study of the radiative cascade transitions between the Upsilon-prime and Upsilon resonances*, PhD thesis, Institute of Nuclear Physics, Krakow, 1986, DESY-F31-86-02.
- [144] S. Ogilvy, *PIDCalib MC for  $\Lambda^0 \rightarrow p^+\pi^-$* , Tech. Rep. LHCb-INT-2013-028. CERN-LHCb-INT-2013-028, CERN, Geneva, Jun, 2013.
- [145] (Belle Collaboration), A. Zupanc *et al.*, *Measurement of the branching fraction  $\mathcal{B}(\Lambda_c^+ \rightarrow pk^-\pi^+)$* , Phys. Rev. Lett. **113** (2014) 042002.
- [146] S. S. Wilks, *The Large-Sample Distribution of the Likelihood Ratio for Testing Composite Hypotheses*, The Annals of Mathematical Statistics **9** (1938), no. 1 pp. 60.
- [147] Y.-Q. Chen and S.-Z. Wu, *Production of Triply Heavy Baryons at LHC*, JHEP **1108** (2011) 144, [arXiv:1106.0193](#).